

AN ABSTRACT OF THE THESIS OF

George R. Halliwell, Jr. for the degree of Doctor of Philosophy
in Oceanography presented on October 14, 1986.

Title: The Large-Scale Coastal Wind Field and Sea Level Response
Along the West Coast of North America

Abstract approved: _____

Redacted for privacy

John S. Allen

Summer wind fluctuations (obtained from measurement stations and calculated from FNOC surface pressure analyses) along the west coast of North America are driven primarily by the interaction between two relatively stationary pressure systems, the North Pacific subtropical high and southwest U.S. thermal low, and by their interactions with propagating atmospheric systems to the north. Winter wind fluctuations are primarily driven by propagating cyclones and anticyclones, and tend to have larger variance and space scales than in summer. Coastal atmospheric boundary layer processes substantially modify winds within 100-200 km of the coast. The FNOC calculated winds represent fluctuations with alongshore wavelengths ≥ 900 km rather well, but poorly represent those with smaller wavelengths and those due to coastal atmospheric boundary layer effects. Fluctuations in alongshore wind stress (τ) are relatively energetic at alongshore wavenumbers $|k| \leq 1.1 \times 10^{-3}$ cpkm

$|\ell| \leq 1.1 \times 10^{-3}$ cpkm and frequencies $0.025 < \omega < 0.5$ cpd, and they effectively drive a coastal sea level (ζ) response within this (ℓ, ω) band. The ζ response is displaced poleward along the coast from regions of strong local τ forcing. Equatorward propagation ($\ell < 0$) dominates the winter wind and τ fluctuations for $\omega < 0.35$ cpd, and poleward propagation ($\ell > 0$) dominates in summer for $\omega < 0.1$ cpd. In contrast, poleward propagation strongly dominates the ζ fluctuations in both seasons, but more so in summer. The largest coherence between ζ and τ is observed for $0 \leq \ell \leq 1.1 \times 10^{-3}$ cpkm in summer and $-1.1 \times 10^{-3} \leq \ell < 0$ cpkm in winter. The ζ response at a given location can be predicted using theoretical models for wind-driven coastally trapped waves with reasonable accuracy given τ within 1000-2000 km equatorward of that location. Many, but not all, properties of the ζ response in (ℓ, ω) space are consistent with a response dominated by one coastally trapped wave mode governed by a forced, first-order wave equation with a linear friction term. Several possible reasons for the differences between predicted and observed response properties are discussed.

The Large-Scale Coastal Wind Field and Sea Level Response
Along the West Coast of North America

by

George R. Halliwell, Jr.

A THESIS

submitted to

Oregon State University

in partial fulfillment of
the requirements for the
degree of

Doctor of Philosophy

Completed October 14, 1986

Commencement June 1987

APPROVED:

Redacted for privacy

Professor of Oceanography in charge of major

Redacted for privacy

Dean of the College of Oceanography

Redacted for privacy

Dean of Graduate School

Date thesis is presented October 14, 1986
Typed by researcher for George R. Halliwell, Jr.

ACKNOWLEDGEMENTS

This research was performed with the support of the Oceanography section of the National Science Foundation under grants OCE-8014939 and OCE-8411613 as part of the Coastal Ocean Dynamics Experiment (CODE). I thank my thesis advisor, Dr. J. S. Allen, for his considerable help and assistance. For Chapter II, we thank Dr. D. B. Chelton, Dr. K. H. Brink, Dr. W. Crawford, and an anonymous referee for helpful comments. For Chapter III, we thank Drs. D. B. Enfield, S. Esbensen, K. H. Brink, and an anonymous referee for helpful comments. We express our gratitude to the organizations and people that have provided the wind data used in this study. We especially thank Mr. Andrew Bakun for help in obtaining the calculated wind set. Most figures were generated using the interactive graphics package PLOT5 developed by Dr. Donald W. Denbo. Chapter II is CODE contribution no. 33, Chapter III is CODE contribution no. 38, and Chapter IV will be assigned a CODE contribution no. in the future. I thank my wife Vicki for her assistance in assembling this thesis.

TABLE OF CONTENTS

CH. I: Introduction	1
CH. II: Large-Scale Sea Level Response to Atmospheric Forcing Along the West Coast of North America, Summer 1973	4
ABSTRACT	4
II.1 INTRODUCTION	5
II.2 THE DATA SET	8
II.2.1 Atmospheric Forcing	8
II.2.2 Adjusted Coastal Sea Level	11
II.3 COMPARISON OF CALCULATED AND MEASURED WIND	12
II.4 THE ALONGSHORE-TIME PROPERTIES OF WIND-STRESS FORCING AND RESPONSE	17
II.4.1 Basic Statistics of ζ and τ	17
II.4.2 Alongshore-time Contour Plots of ζ and τ	18
II.4.3 Time-domain EOFs of ζ and τ	20
II.5 THE ALONGSHORE-FREQUENCY PROPERTIES OF WIND-STRESS FORCING AND RESPONSE	22
II.5.1 Autospectra	22
II.5.2 Frequency-Domain EOFs	23
II.6 THE RELATIONSHIP OF SEA LEVEL RESPONSE TO THE LARGE- SCALE WIND STRESS FIELD	27
II.7 DYNAMICAL INTERPRETATION OF THE OBSERVED RESPONSE TO WIND STRESS FORCING	32
II.8 DISCUSSION	38
CH. III: The Large-Scale Coastal Wind Field Along the West Coast of North America, 1981-82	68
ABSTRACT	68
III.1 INTRODUCTION	69
III.2 THE DATA SET	73
III.2.1 Data and Data Processing	73
III.2.2 The Rotation Correction for Calculated Winds	77
III.3 BASIC STATISTICAL PROPERTIES OF THE WIND FIELD	79
III.3.1 Seasonal Means	79
III.3.2 Seasonal RMS Amplitudes	81
III.3.3 The Coastal Boundary Layer Influence on Wind Properties	84
III.3.4 Can Land Winds be Adjusted to Equal Offshore Winds?	88
III.3.5 Effects of the RMS Amplitude Distribution on Statistical Analyses	90
III.3.6 Correlation Scales and Wind Field Correlations	92
III.3.7 The Coastal Boundary Influence on Alongshore Wind Statistics	96

III.4 SPECTRUM ANALYSIS OF THE WIND FIELD	98
III.4.1 Frequency Domain Properties	98
III.4.2 Wavenumber-Frequency Domain Properties	104
III.5 CHARACTERISTICS OF WIND FLUCTUATION EVENTS	108
III.5.1 Space-Time Contour Plots of Alongshore Wind	108
III.5.2 Winter Event Properties	109
III.5.3 Summer Event Properties	112
III.6 DISCUSSION	117
CH. IV: Wavenumber-Frequency Domain Properties of Coastal Sea Level Response to Alongshore Wind Stress Along the West Coast of North America, 1980-84	149
ABSTRACT	149
IV.1 INTRODUCTION	150
IV.2 THE DATA	153
IV.3 BASIC STATISTICAL PROPERTIES OF THE WIND STRESS AND SEA LEVEL FIELDS	158
IV.3.1 Means and RMS Amplitudes	158
IV.3.2 Correlation/Coherence Scales and Alongshore Propagation	160
IV.4 WAVENUMBER-FREQUENCY AUTOSPECTRA OF WIND STRESS AND SEA LEVEL	166
IV.4.1 Summer and Winter Autospectra of τ and ζ	166
IV.4.2 Interannual Variability in the Autospectra of τ and ζ	169
IV.4.3 Comparison of Measured and Calculated τ Autospectra	172
IV.5 OBSERVED SEA LEVEL RESPONSE PROPERTIES IN WAVENUMBER- FREQUENCY SPACE	175
IV.5.1 Summer and Winter Response of ζ to τ	175
IV.5.2 Interannual Variability in the Response of ζ to τ	178
IV.5.3 The Response of ζ to Measured and Calculated τ	179
IV.6 PREDICTED SEA LEVEL RESPONSE PROPERTIES IN WAVENUMBER- FREQUENCY SPACE	181
IV.6.1 Response Properties Predicted by (IV.1.1) for One Mode	181
IV.6.2 Response Predicted by (IV.1.1) for More Than One Mode	188
IV.6.3 One Dimensional Response Properties Predicted by (IV.1.1)	190
IV.7 DISCUSSION	192
BIBLIOGRAPHY	230

APPENDIX A: THE LARGE-SCALE RELATIONSHIP OF CUE-II CURRENTS TO CALCULATED τ	236
APPENDIX B: THE LARGE-SCALE RELATIONSHIP OF ζ to MEASURED τ	240
APPENDIX C: CORRELATION SIGNIFICANCE LEVELS	243
APPENDIX D: SPACE-LAGGED CORRELATION, COHERENCE, AND PHASE FUNCTIONS	244
APPENDIX E: CALCULATION OF THE WAVENUMBER-FREQUENCY SPECTRUM ESTIMATES	248
APPENDIX F: SEA LEVEL RESPONSE PREDICTED BY FORCED, FIRST- ORDER WAVE EQUATIONS	251

LIST OF FIGURES

Figure	Page
II.1: Coastal meteorological stations available during summer 1973.	49
II.2: Coastal points of the CODE large-scale analysis grid and sea level stations.	50
II.3: Space-time contours of daily averaged calculated τ and daily averaged demeaned gridded ζ for summer 1973.	51
II.4: Wavenumber autospectra of gridded ζ and calculated τ , ensemble averaged over 4 months from six-hourly autospectra.	52
II.5: The two most significant time-domain EOFs of gridded ζ : rms amplitudes and percent variance explained; and correlation with local calculated τ that has been lagged by one day to approximately maximize the local correlation.	53
II.6: Time-varying amplitudes of the two most significant EOFs of gridded ζ from Fig. II.5 and autospectra of these amplitudes graphed as energy density and as cumulative energy density in percent.	54
II.7: The two most significant time-domain EOFs of calculated τ : rms amplitude and percent variance explained.	55
II.8: Autospectra of ζ and calculated τ contoured as a function of frequency and y .	56
II.9: The northern and southern frequency-domain EOFs of gridded ζ contoured as a function of frequency and y : rms amplitude in cm; percent variance explained; and phase lag in hr.	57
II.10: As in Fig. II.9 for the two most significant frequency-domain EOFs of calculated τ .	58
II.11: Coherence squared between the northern frequency-domain EOF of gridded ζ and the most significant frequency-domain EOF of calculated τ .	59
II.12: Contours of the space and time lagged correlation of ζ at each of six selected measurement stations with calculated τ at all grid points.	60
II.13: Contours of the space and time lagged correlation of	

calculated τ at each of the six grid points nearest to the six ζ stations in Fig. II.12 with calculated τ at all grid points.	61
II.14: As in Fig. II.13 for gridded ζ .	62
II.15: Contours of the space lagged coherence squared of ζ at the six measurement stations used in the correlation analysis with calculated τ at all grid points.	63
II.16: Space-time contours of six-hourly calculated τ in dy cm^{-2} and six-hourly gridded ζ in cm for 3 July through 19 July 1973, spanning τ events 4 and 5.	64
II.17: As in Fig. II.16 but for the time interval of 3-13 September 1973, spanning τ event 11.	65
II.18: Time series of measured and predicted ζ at SBC.	66
II.19: The fraction of the total variance of gridded ζ explained by the prediction from (II.7.2) and the squared correlation coefficients between measured and gridded ζ .	67
III.1: The coastal points of the CODE analysis grid and the wind measurement stations used in this study.	127
III.2: The rotation correction required to align the calculated wind fluctuations with measured wind fluctuations for grid points 2 through 17 for the three seasons.	128
III.3: Mean vectors for calculated and measured winds.	129
III.4: The means and rms amplitudes of the calculated and measured alongshore winds as a function of y for the three seasons.	130
III.5: Same as Fig. III.3, except for rms principal axis ellipses.	131
III.6: Zero time-lagged correlation matrices for calculated and measured winds contoured as a function of alongshore separation.	132
III.7: Correlation coefficients between measured and calculated winds.	133
III.8: Autospectra of calculated, adjusted measured, and measured alongshore winds for the three seasons.	134
III.9: Contours of rotary coefficients	

$[S_r(y, -\omega) - S_r(y, +\omega)] / [S_r(y, -\omega) + S_r(y, +\omega)]$ for calculated and measured vector winds for the three seasons.	135
III.10: The squared coherences between measured and calculated alongshore winds and squared rotary coherences between measured and calculated vector winds contoured as a function of frequency and y for the three seasons.	136
III.11: The space-frequency squared coherence γ^2 , calculated from space-averaged autospectra and cross-spectra for calculated and measured alongshore winds over grid points 4 through 13 for the three seasons.	137
III.12: Wavenumber-frequency autospectra of calculated, adjusted measured, and measured alongshore winds over grid points 4 through 13 for the three seasons.	138
III.13: Wavenumber-frequency propagating autospectra of calcu- lated, adjusted measured, and measured alongshore winds over grid points 4 through 13 for the three seasons.	139
III.14: Integrated wavenumber autospectra and integrated fre- quency autospectra for calculated, adjusted measured, and measured alongshore winds over grid points 4 through 13 for the three seasons.	140
III.15: Wavenumber-frequency squared coherences between adjusted measured and calculated, and between measured and calcu- lated, alongshore winds, over grid points 4 through 13 for the three seasons.	141
III.16: Calculated, adjusted measured, and measured alongshore wind contoured as a function of time and y for 17 May through 30 June 1981.	142
III.17: As in Fig. III.16, except for 15 February through 31 March 1982.	143
III.18: As in Fig. III.16, except for 1 May through 14 June 1982.	144
III.19: Surface atmospheric pressure charts for 11 to 14 March 1982.	145
III.20: As in Fig. III.19, except for 28 to 31 May 1981.	146
III.21: As in Fig. III.19, except for 15 to 18 May 1982.	147
III.22: As in Fig. III.19, except for 28 to 31 May 1982.	148

IV.1: The coastal points of the CODE analysis grid, the wind measurement stations, and the coastal sea level stations used in this study.	203
IV.2: The mean and rms amplitude envelopes of τ and ζ for summer and winter.	204
IV.3: The ratios of winter rms amplitude to summer rms amplitude for τ and ζ which has been interpolated to the CODE grid.	205
IV.4: The space-time correlation functions $R_{\tau\tau}(\eta_n, \tau_\ell)$, $R_{\zeta\zeta}(\eta_n, \tau_\ell)$, and $R_{\zeta\tau}(\eta_n, \tau_\ell)$, calculated from space-averaged covariances as described in Appendix IV.A, ensemble-averaged over the four summers (grid points 4 through 17) and four winters (grid points 2 through 17).	206
IV.5: The space-frequency coherence squared $\gamma_{\tau\tau}^2(\eta_n, \omega_\ell)$, $\gamma_{\zeta\zeta}^2(\eta_n, \omega_\ell)$, and $\gamma_{\zeta\tau}^2(\eta_n, \omega_\ell)$, calculated from space-averaged autospectra and cross-spectra and ensemble-averaged over the four summers (grid points 4 through 17) and four winters (grid points 2 through 17).	207
IV.6: The space-frequency phase lags $\theta_{\tau\tau}(\eta_n, \omega)$, $\theta_{\zeta\zeta}(\eta_n, \omega)$, and $\theta_{\zeta\tau}(\eta_n, \omega)$ contoured in days, and the phase speed functions $c_{\tau\tau}(\eta_n, \omega)$ and $c_{\zeta\zeta}(\eta_n, \omega)$ contoured in cm s^{-1} .	208
IV.7: Wavenumber-frequency autospectra and propagating autospectra of τ and ζ ensemble-averaged over the four summers (grid points 4 through 17) and four winters (grid points 2 through 17).	209
IV.8: Integrated wavenumber autospectra and integrated frequency autospectra for τ and ζ , ensemble-averaged over the four summers (grid points 4 through 17) and four winters (grid points 2 through 17).	210
IV.9: Wavenumber-frequency autospectra of τ for the individual four summers (grid points 4 through 17) and four winters (grid points 2 through 17).	211
IV.10: Wavenumber-frequency autospectra of ζ for the individual four summers (grid points 4 through 17) and four winters (grid points 2 through 17).	212
IV.11: Wavenumber-frequency propagating autospectra of τ and ζ for the individual four summers (grid points 4 through 17) and four winters (grid points 2 through 17).	213
IV.12: Wavenumber-frequency autospectra of calculated, adjusted	

- measured, and measured τ at grid points 4 through 13 for two summers and one winter. 214
- IV.13: Integrated wavenumber autospectra and integrated frequency autospectra for calculated winds, adjusted measured winds, and measured τ , at grid points 4 through 13 for two summers and one winter. 215
- IV.14: Wavenumber-frequency coherence squared between adjusted measured and calculated τ , and between measured and calculated τ , at grid points 4 through 13 for two summers and one winter. 216
- IV.15: Wavenumber-frequency coherence squared between τ and ζ , and the transfer function [gain in $\text{cm} (\text{dy cm}^{-2})^{-1}$ and phase in degrees] of the ζ response to τ , calculated from autospectra and cross-spectra ensemble-averaged over the four summers (grid points 4 through 17) and four winters (grid points 2 through 17). 217
- IV.16: Integrated wavenumber and frequency coherence squared between τ and ζ and the transfer function [gain in $\text{cm} (\text{dy cm}^{-2})^{-1}$ and phase in degrees] of the ζ response to τ , ensemble-averaged over four summers (grid points 4 through 17) and four winters (grid points 2 through 17). 218
- IV.17: Wavenumber-frequency coherence squared between τ and ζ for the individual four summers (grid points 4 through 17) and four winters (grid points 2 through 17). 219
- IV.18: Wavenumber-frequency gain in $\text{cm} (\text{dy cm}^{-2})^{-1}$ of the transfer function of the ζ response to τ for the individual four summers (grid points 4 through 17) and four winters (grid points 2 through 17). 220
- IV.19: Wavenumber-frequency phase in degrees of the transfer function of the ζ response to τ for the individual four summers (grid points 4 through 17) and four winters (grid points 2 through 17). 221
- IV.20: Wavenumber-frequency coherence squared between τ and ζ , and transfer functions [gain in $\text{cm} (\text{dy cm}^{-2})^{-1}$ and phase in degrees] of the ζ response to τ , at grid points 4 through 13 for calculated, adjusted measured, and measured τ during summer 1981. 222
- IV.21: Same as Fig. IV.20 for Winter 1981-82, except that gain > 2 is shaded for calculated and adjusted measured winds. 223

IV.22: Same as Fig. IV.20 for Summer 1982.	224
IV.23: Transfer functions (gain and phase) of the ζ response to τ in wavenumber-frequency space predicted by the forced, first-order wave equation with linear friction term (IV.1.1) for one coastally trapped wave mode.	225
IV.24: Transfer functions (gain and phase) of the ζ response to τ in wavenumber-frequency space predicted by (IV.1.1) for several coastally trapped wave modes calculated using the parameters in Table IV.7.	226
IV.25: Same as Fig. IV.24, except that the T_{fn} from Table II.7 have been reduced in magnitude as shown.	227
IV.26: Integrated wavenumber and frequency squared coherence between τ and ζ , and the transfer function [gain in $\text{cm} (\text{dy cm}^{-2})^{-1}$ and phase in degrees] of the ζ response to τ , calculated from (IV.1.1) as described in Appendix IV.C using the summer and winter autospectra of τ presented in Fig. IV.7.	228
IV.27: Same as Fig. IV.26, except for using $T_f = 3$ days.	229
A.1: Contours of the space and time lagged correlations of ζ at SBC with calculated τ at all grid points and the most significant u-v column time-domain EOFs of currents at the CUE-II cross-shelf array discussed by Huyer et al. (1978) with calculated τ at all grid points.	239
B.1: As in Fig. II.12 using measured τ at each of the 12 stations indicated in Table II.1.	241
B.2: As in Fig. II.15 using measured τ at each of the 12 stations indicated in Table II.1.	242

LIST OF TABLES

Table	Page
II.1 Meteorological station information and basic statistics of measured τ .	42
II.2 Coastal points of the CODE analysis grid and basic statistics of calculated τ .	43
II.3 Coastal sea level information and standard deviation of ζ .	44
II.4 Summary of the two comparisons of calculated and measured vector winds: II.4a The inner correlation and phase. II.4b Comparison of both wind sets to sea level.	45 46
II.5 Computation of the alongshore component of calculated wind stress.	47
II.6 Summary of the space and time lagged correlation analyses between ζ at each of six selected stations and τ at all grid points.	48
III.1 Coastal points of the CODE large-scale analysis grid.	122
III.2 Wind measurement stations used in the analysis of wind field properties. Additional wind measurement stations used in the filling of data gaps and in the comparison of land to offshore winds are listed at the bottom.	123
III.3 Regression of offshore vector wind speed U_o on nearby land vector wind speed U_l , $U_o = a + bU_l$, and the variance ratio of buoy alongshore winds to nearby land alongshore winds.	124
III.4 Integral correlation alongshore space scales and time scales for coastal alongshore winds between grid points 4 (34.6°N; y = -540 km) and 13 (48.2°N; y = 1080 km).	125
III.5 Percentage of total variance due to alongshore wind fluctuations with wavelengths ≥ 900 km determined from wave-number-frequency autospectra integrated over frequency.	126
IV.1 Coastal points of the CODE large-scale analysis grid.	196
IV.2 Coastal sea level stations used in this analysis.	197
IV.3 Wind measurement stations used in the intercomparison with	

- calculated winds. 198
- IV.4 Integral space and time correlation scales for summer (grid points 4 through 17) and winter (grid points 2 through 17) determined from the space-time correlation functions described in Appendix IV.A. 199
- IV.5 The total variance, the percentage of total variance with $|\lambda| \leq 1.1 \times 10^{-3}$ cpkm, and the percentage of total variance due to poleward-propagating fluctuations for summer (grid points 4 through 17) and winter (grid points 2 through 17) seasons. 200
- IV.6 The percentage of total variance with wavelengths ≥ 900 km and the percentage of total variance due to poleward-propagating fluctuations for calculated, adjusted measured, and measured τ over grid points 4 through 13 for summers 1981 and 1982 plus winter 1981-82. 201
- IV.7 Parameters of (IV.1.1) calculated by Brink (personal communication) for the CODE site and Chapman (1986) for the west coast between San Diego and the CODE site using the model of Brink (1982). 202

THE LARGE-SCALE COASTAL WIND FIELD AND SEA LEVEL RESPONSE ALONG
THE WEST COAST OF NORTH AMERICA

CHAPTER I

Introduction

The Coastal Ocean Dynamics Experiment (CODE) was designed to study the dynamics of the response of continental shelf currents to atmospheric forcing over periods between two days and two weeks, the dominant periods of fluctuations in the atmosphere and ocean caused by synoptic-scale atmospheric systems. Two extensively-instrumented experiments were conducted during the spring/summer upwelling seasons of 1981 and 1982 (CODE-1 and CODE-2) in an approximately 100 km segment of the continental shelf northwest of San Francisco located between Point Arena and Point Reyes (Winant, et al., 1986). The large-scale component of the CODE experiment was designed to study a much larger segment of the continental shelf that contained the site of the CODE experiments, and this thesis presents many of the results from this component.

Numerous observational and theoretical studies indicate that fluctuations in shelf currents with the above periods have large alongshore scales (\gg shelf/slope width) and propagate alongshore with the coast on the right in the Northern Hemisphere, or poleward along the west coast of North America [see Allen (1980) for a

review]. The alongshore component of wind stress is the most important forcing mechanism for shelf current fluctuations with large alongshore scales. Most studies of this response have used currents, coastal sea level, and wind stress in small alongshore segments of continental shelves. These studies concentrated on the response to local wind stress only, and did not explicitly consider that part of the observed response could be forced by alongshore wind stress at a distant alongshore location and propagate into the study area. The few studies that did investigate distant forcing in a very simple manner (Hamon, 1976; Clarke, 1977) indicated that it was probably important. A major goal of the large-scale component of the CODE experiment was to statistically characterize the properties of the large-scale coastal ocean response over a larger segment of continental shelf than used in earlier studies. This study was made possible by collecting wind stress data, plus coastal sea level as the response variable, along a 3600 km segment of the west coast of North America.

The results from three components of this study are presented here. First, a preliminary study of the response of coastal sea level to wind stress during summer 1973 is presented in Chapter II, the results of which helped in planning the analyses to be performed on the CODE large-scale data set. Many problems exist in assembling good wind data to use as the atmospheric forcing function, and it was necessary to characterize properties of the coastal wind field relevant to the forcing of the large-scale

coastal ocean response. Therefore, a study of the coastal wind field along the west coast of North America was the first to be undertaken using the CODE data set, and the results are presented in Chapter III. The study of the sea level response to alongshore wind stress using the CODE data set is presented in Chapter IV. Results from earlier studies indicated that the coastal ocean response should depend on the wavenumber and frequency domain properties of the atmospheric forcing, so the primary purpose of this analysis was to characterize the properties of the wind stress forcing and sea level response in wavenumber-frequency space. These three analyses have been published or submitted for publication in refereed journals, and information on these articles is summarized in the Bibliography (Halliwell and Allen, 1984, 1986a, 1986b). Note that Chapter II is copyright by the American Meteorological Society and that Chapters III and IV are copyright by the American Geophysical Union. At the time of this writing, the article presented in Chapter IV is undergoing review, so the final version that appears in the journal will differ somewhat from Chapter IV.

CHAPTER II

Large-Scale Sea Level Response to Atmospheric Forcing
along the West Coast of North America, Summer 1973

ABSTRACT

Along the west coast of North America, the response of sea level to fluctuations in alongshore wind stress at large alongshore scales (>1000 km) accounted for a substantial fraction of the total sea level variance during summer 1973. Space-time contour plots of sea level and alongshore stress show that the response of sea level to poleward-propagating wind stress events was generally stronger than the response to equatorward-propagating events. Atmospheric forcing was most effective in two regions along the coast, with relatively strong forcing and response along northern California and Oregon, and somewhat weaker forcing and response along northern Baja California. The forced fluctuations in sea level propagated poleward away from these forcing regions, causing local sea level to be most correlated with alongshore wind stress earlier in time and at a distant equatorward location. Along the southern and central California coast, fluctuations in sea level were partly forced along northern Baja California, although some of the energy may have entered the domain from the south. Poleward of Crescent City, fluctuations in sea level were dominated by the response to

alongshore stress in the northern forcing region, and were therefore poorly correlated with sea level to the south. Most of the sea level energy was contained in two frequency-domain modes representing the northern and southern fluctuations in sea level. The southern mode had proportionally more energy than the northern mode at a frequency of 0.043 cpd, while the opposite was true for frequencies between 0.086 and 0.22 cpd. Sea level apparently responded more effectively in frequency bands where fluctuations in wind stress propagated poleward and acted over a longer alongshore distance. Along the British Columbia coast, local atmospheric forcing was relatively ineffective, and fluctuations in sea level were apparently dominated by free wave energy propagating poleward from the northern forcing region. Predictions of sea level response made from simple theory of wind-forced coastally-trapped waves were similar to the observed response, and accounted for up to 70% of the total variance along Oregon and Washington, poleward of the northern forcing region.

II.1 INTRODUCTION

Theoretical models for wind-driven shelf currents (e.g., Gill and Schumann, 1974) illustrate the nature of the response to atmospheric forcing at large alongshore scales; i.e., at scales much larger than the width of the continental margin. In these models, the alongshore component of wind stress is the dominant forcing mechanism. Since midlatitude atmospheric systems typically

have spatial scales of several hundred to several thousand kilometers and time scales of 2 days to about 2 weeks, large-scale perturbations driven by coastal atmospheric forcing should be an important component of the variability of coastal currents at these time scales. In addition, a continental margin theoretically acts as a waveguide for subinertial frequency coastally-trapped waves, which are nondispersive for large alongshore scales and propagate poleward along eastern boundaries. Thus, large-scale current fluctuations at a given location along a continental margin can be partly or totally forced at distant locations, and the possibility of resonant forcing exists if a wind stress perturbation propagates along the coast at the free wave velocity of a coastally-trapped wave mode. These theoretical results indicate the importance of resolving large-scale forcing and response in order to understand the behavior of currents measured at any particular geographical location during shelf dynamics field experiments.

A primary objective of the Coastal Ocean Dynamics Experiment (CODE) is to determine the dynamics of wind-driven coastal currents along a 100 km segment of the California coast centered near $38^{\circ}42'N$ (Fig. II.1) during two time intervals: April through August 1981 (CODE-1) and April through August 1982 (CODE-2) (Allen, et al., 1983). As part of CODE, a large-scale study has been designed to determine the nature of the large-scale forcing and response along a 3600 km section of the coast from central Baja California to northern British Columbia ($26-54^{\circ}N$) for the

three-year interval April 1980 through March 1983, and to determine the influence of large-scale processes on currents observed at the CODE site. In the large-scale study, atmospheric forcing is represented by wind and pressure measured at continental United States and Canadian coastal stations and buoys, and by alongshore wind stress calculated from Fleet Numerical Oceanography Center (FNOC) atmospheric pressure analyses. Coastal sea level measurements from all available continental United States and Canadian stations are used to represent the response of coastal currents, based on the generally high correlation of sea level and alongshore currents established by previous observations (e.g., Smith, 1974). The use of sea level as the response variable in place of currents is discussed in Appendix A.

Prior to analyzing the large-scale response during CODE, it was deemed useful to perform a similar study for the United States west coast during the summer of 1973 to test the assumptions and analysis procedures. Summer 1973 was chosen because the Coastal Upwelling Experiment (CUE-II) was performed off Oregon (near 45°N) during July and August 1973, providing a well studied set of current measurements at one location along the coast. Also, limited aspects of the large-scale response during that time interval have been studied by Wang and Mooers (1977). Our more extensive analyses of data spanning longer space and time scales enable us to present many new results concerning the large-scale nature of the atmospheric forcing and response along the west coast

of North America during summer 1973. Our primary purpose in this paper is to characterize statistically the nature and interrelationship of the forcing and response independent of any dynamical models (Sections II.4 through II.6). We then briefly show that a simple linear model of wind-driven coastally-trapped waves qualitatively predicts the observed statistical relationship between the forcing and response (Section II.7).

II.2 THE DATA SET

In the following analyses, we use a right-handed curvilinear coordinate system with y parallel to the coast, increasing in the poleward direction, and x normal to the coast, increasing onshore. The alongshore direction at a given location along the coast is estimated by visually smoothing the coast over a sufficiently long segment to eliminate the irregularities due to small headlands and bays (typically 10 to 20 km). The origin is on the coast at the latitude of the central line of the CODE experiment ($38^{\circ}42'N$). The time variable is t .

II.2.1 Atmospheric Forcing

Atmospheric forcing is represented by measured data at selected coastal meteorological stations (Table II.1, Fig. II.1) and by analyzed fields obtained from FNOC (Bakun, 1975) that have been interpolated to coastal points of the CODE analysis grid (Table II.2, Fig. II.2). The 20 coastal CODE grid points are

separated by 180 km, with grid point 7 located at the origin of the coordinate system, $y = 0$. (This spacing is used because analyzed variables from the National Weather Service LFM-II forecast model are available on a grid with similar spacing at middle latitudes. LFM data are not used for summer 1973 because of substantial gaps.) Surface atmospheric pressure (p) and wind components along the east-west and north-south axes (u, v) are obtained from the coastal meteorological stations. Analyzed fields of p , u , and v are obtained at the CODE grid points. The variables obtained from FNOC will hereafter be referred to as calculated variables. Alongshore positions (y coordinates) of all meteorological stations and grid points are presented in Tables II.1 and II.2.

Calculated winds are obtained from the six-hourly FNOC pressure fields by the methods described by Bakun (1975). Pressures are interpolated to grid points separated by three degrees of latitude and longitude, resulting in a north-south spatial resolution of about 300 km at all latitudes, and an east-west resolution of about 240 km at the altitude of the CODE site. Geostrophic winds are calculated from these gridded pressures. To obtain estimates of surface winds, a simple boundary layer correction is applied by reducing wind speed by 30% and rotating wind vectors 15 degrees counterclockwise (Bakun, 1975).

The measured meteorological data are obtained from several sources at sampling rates between one and six hours. The data sources and editorial procedures are discussed by Halliwell and

Allen (1983,1985). After editing, the following major steps are performed on all measured and calculated time series:

1. gaps less than 24 hr in length within the time series are filled by linear interpolation,
2. measured wind speed is adjusted to an anemometer height of 10 m assuming a logarithmic velocity profile (neutral stability) (calculated winds are assumed to represent 10 m winds), and
3. time series are low-pass filtered using a Cosine-Lanzcos filter with a 40 hr cutoff and subsampled to 6 hr when necessary (Pittock, et al., 1982).

The filtered time series start at 0000 PST 4 June and end at 0600 PST 27 September 1973 and have a sampling rate of 6 hr. We computed wind stress for othe calculated and measured winds prior to filtering by using the bulk aerodynamic equation with a drag coefficient given by (Large and Pond, 1981):

$$\vec{\tau} = \rho_a C_d |\vec{V}_{10}| \vec{V}_{10} \quad (\text{II.2.1})$$

with

$$10^3 C_d = \begin{cases} 1.2 & |\vec{V}_{10}| \leq 11 \text{ m s}^{-1} \\ 0.49 + 0.065 |\vec{V}_{10}| & |\vec{V}_{10}| > 11 \text{ m s}^{-1} \end{cases} \quad (\text{II.2.2})$$

The axes are then rotated to compute stress components in the curvilinear coordinate system (Section II.3). The alongshore

component of stress is used as a forcing function, and hereafter referred to as τ .

II.2.2 Adjusted Coastal Sea Level

Coastal sea level data are obtained from the National Ocean Survey and the Canadian Marine Environment Service (Table II.3). These data are checked for datum shifts (Pittock, et al., 1982), then subjected to essentially the same editorial procedures as meteorological data (Halliwell and Allen, 1983). Adjusted sea level (ζ), corresponding to pressure beneath the sea surface, is formed by adding the equivalent of atmospheric pressure to the sea level data (in cm). The p time series used in this adjustment are listed in Table II.3. In cases where p is not available within about 50 km of the sea level station, it is estimated by linear interpolation using the two nearest p stations of the same type (i.e., both calculated or both measured), one equatorward of, and one poleward of, the ζ station. The mean values of ζ are then removed. The start and end times are the same as for the meteorological data. Time series of ζ are linearly interpolated to the coastal CODE analysis grid (points 2 through 16) with allowances made for time lags between the input time series of measured ζ caused by propagating disturbances. These lags are objectively determined using lagged cross-correlation analysis. Details of the interpolation procedures are presented by Halliwell and Allen (1983).

II.3. COMPARISON OF CALCULATED AND MEASURED WIND

Calculated winds form an attractive data set for analysis because they are spatially complete, available on a regular grid, and derived by uniform procedures over that grid. In contrast, available coastal measured winds have irregular spacing alongshore and are of variable quality because of differences in local topography, instrument location, etc. For these reasons, calculated winds are used extensively in the following analyses. A thorough comparison between calculated and measured winds is given by Halliwell and Allen (1986a). Several aspects of the comparison are important for the present study and are discussed here. We first compare fluctuations in calculated vector winds to fluctuations in measured vector windw, then quantify an additional rotation that must be performed on the calculated winds to bring their fluctuations into alignment with those of the measured winds. In Appendix B, we compare some of the analyses in Section II.6 performed using calculated τ with similar analyses using measured τ and show that reliable results are obtainable with calculated τ .

At each grid point, the inner correlation and phase between calculated vector winds and all measured vector winds within 90 km (Table II.4) show that the winds are rather well correlated in most cases, being greater than 0.7 for 17 out of 24 cases. The inner phase gives the difference in angular orientation between the fluctuations that is weighted by the amplitude of the instantaneous vectors (Kundu, 1976). All inner phases except one are positive,

and the largest is 76° . Positive inner phase means that calculated vector winds must be rotated counterclockwise to bring their fluctuations into alignment with the measured winds. The inner phase varies along the coast, being relatively small ($<25^\circ$) near Point Conception (grid point 4) and along the Oregon coast (grid points 10 and 11), and larger elsewhere.

Because of the possible influence of local topography on measured winds, we cannot assume that they accurately represent the orientation of wind fluctuations over the shelf. Therefore, we cannot assume that the inner phase between calculated and measured winds provides an accurate estimate of the rotation error in calculated winds. An independent estimate of the rotation error is obtained by comparing the relation of both calculated and measured vector winds to ζ . The orientations of the components of these winds most correlated with ζ are estimated by regressing sea level on wind components in the time domain, then using the regression coefficients to calculate the orientations (Garret and Toulany, 1982). The results are presented in Table II.4 for all measurement stations and grid points where the vector winds explain a statistically significant fraction of the ζ variance to 95% confidence. The maximum correlation orientations for the calculated winds are typically smaller than (rotated clockwise from) the orientations of the measured winds. This misalignment becomes very clear by inspecting the basic statistics of the difference between these computed orientations and the

corresponding geographical alongshore orientations. For the eleven measured wind orientations listed in Table II.4, this difference is $-9^\circ \pm 14^\circ$, and for the ten calculated wind orientations it is $-54^\circ \pm 17^\circ$. Thus, it is roughly the geographical alongshore component of measured wind that is most correlated with sea level, but a component of calculated wind that is, on average, more than 50° clockwise from the geographical alongshore orientation is most correlated with ζ . We therefore conclude that local topography does not seriously change the orientation of the fluctuations in measured wind and that the inner phase provides a reasonably good estimate of the rotation error. Calculated winds (and wind stress) must therefore be rotated counterclockwise to best represent the true coastal winds.

We emphasize that this correction may only apply to winds measured at or near the coast. The 15° counterclockwise rotation of the calculated winds performed during the boundary layer correction may be sufficient to best represent the true surface wind over the open ocean, but the marine coastal boundary layer is influenced by other factors, such as the presence of coastal mountains, surface horizontal temperature gradients, and diurnal wind fluctuations. These additional influences may substantially affect the veering of the wind vertically through the marine boundary layer near the coast and change the rotation required to align the calculated winds with the measured winds at the surface. Our results indicate that along most of the coast, a 15°

counterclockwise rotation is insufficient to correct for wind veering in the coastal marine boundary layer. Similar misalignments between calculated winds and coastal measured winds are also observed in the CODE large-scale data set (Halliwell and Allen, 1986a). Also, Thomson (1983), in a comparison of calculated winds to measured winds from two meteorological buoys along the British Columbia coast during two summer seasons 1979 and 1980, found that calculated wind vectors had to be rotated an additional 20° counterclockwise to be aligned properly with the measured wind.

The correlation coefficients between these components of calculated and measured winds and the nearby ζ measurements are also presented in Table II.4. The calculated winds are slightly better correlated with ζ than the measured winds along most of the coast between grid points 5 and 12. The measured winds may be substantially affected by factors such as small-scale wind fluctuations and local topography. Calculated winds apparently represent the large-scale wind fluctuations that drive oceanic response with enough accuracy to be an adequate forcing function for the purpose of this study. This conclusion is supported by the analyses presented in Appendix B.

Since the rotation correction is apparently a function of alongshore position, we estimate a separate correction at each grid point. We use both the inner phase and the differences in wind orientation most correlated with ζ to estimate these corrections, since very few estimates of the inner phase exist at each grid

point and therefore they alone cannot provide a good estimate of the rotation correction. Average values of the differences between measured and calculated winds in inner phase and in the wind orientation most correlated with ζ are presented in Table II.5. At grid points 6 through 12, where both could be computed, they have similar values, which increases our confidence that they both approximately measure the misalignment between fluctuations in calculated and measured winds.

We therefore estimate τ in the following manner: For measured τ , we simply compute the alongshore component of the measured vector stress. For calculated τ , we first rotate the calculated vector stress at each grid point by an amount determined by averages of the two differences presented in Table II.5 to correct for the misalignment. We then compute calculated τ in the same manner as measured τ . Estimates of the correction angles at each grid point are presented in Table II.5. At grid points 2 through 5 and 13, only the average inner phase difference could be used to estimate the correction angles. At grid points 1, 14, 15, and 16, there were no statistics upon which to estimate the correction angles. We determined the correction angles for grid point 1 by assuming that it is the same as for grid point 2. Similarly, the correction angles for grid points 14-16 are assumed to be the same as for grid point 13.

For the analyses performed in Appendix B using measured τ , we use a subset of the measured wind stations in Table II.1. These

stations are selected to be as evenly spaced as possible along the coast, with an effort made to use better-quality winds wherever possible. These stations are marked in Table II.1, where the basic statistics of τ are presented. Both the mean and standard deviation of measured τ are substantially smaller than those for calculated τ presented in Table II.2. The measured wind stations also vary irregularly from station to station along the coast while the calculated τ statistics vary smoothly. Apparently, both the mean values of measured τ and the amplitudes of its fluctuations are strongly influenced by factors such as local topography. Therefore, we rely only on the basic statistics of calculated τ in the following analyses.

II.4 THE ALONGSHORE-TIME PROPERTIES OF WIND STRESS FORCING AND RESPONSE

II.4.1 Basic Statistics of ζ and τ

The dominant features in the alongshore distribution of the means and standard deviations of τ (Table II.2) is that both have large magnitudes at grid point 8, which is located near Cape Mendocino. (Unless otherwise noted, τ will represent calculated τ for the remainder of this paper. Measured variables will always be prefixed by the word measured.) The mean at this point is equatorward, as it is everywhere south of northern Vancouver Island. The standard deviation at this point is four to five times

larger than it is along the coast of northern Baja California, southern California, and Washington. Smaller relative maxima in the standard deviation exist near Point Conception (grid point 4) and along the northern British Columbia coast. In contrast, the largest ζ standard deviation (Table II.3) occurs along the Washington coast, with minima located along the coasts of central California and southern British Columbia. In general, maxima and minima of ζ standard deviations are displaced poleward of corresponding maxima and minima of τ standard deviations, suggesting a poleward shift in the response of ζ to τ .

II.4.2 Alongshore-time Contour Plots of ζ and τ

Contours of daily averages of τ and gridded ζ are presented in Fig. II.3. Fluctuations of τ are largest near $y = 180$ km, the latitude of Cape Mendocino. Twelve τ events, some poleward (positive τ) extrema and some equatorward (negative τ) extrema, are labeled in Fig. II.3. (We use the term "event" to denote these 12 specific wind stress extrema, although they are not completely independent in time from other extrema.) Time lines of these events, defined here as the lines in the y - t plane tracing the location of the τ extrema as a function of time, are indicated by solid lines for equatorward extrema and dashed lines for poleward extrema. For most events, the τ extrema do not occur simultaneously along the coast, but propagate poleward or equatorward as indicated by the slopes of the time lines, which

provide estimates of propagation speeds.

The τ event time lines are reproduced on the ζ contour chart (Fig. II.3). The maximum ζ response is characteristically located poleward of, and later in time than, the τ event. In general, ζ appears to respond more effectively to poleward-propagating τ extrema. The ζ response to the poleward-propagating events in Fig. II.3 [2, 5, 7, 8, 9(northern part), 10(northern part), 11, and 12] is substantially larger than the response to the equatorward-propagating events [3, 4, 6, 9(southern part), and 10(southern part)]. A ζ response of intermediate amplitude occurs for event 1, for which the τ extremum is in-phase along the coast. To assess the ζ response to τ better, we examine events 4, 5 and 11 in more detail in Section II.7 and compare them with an idealized theoretical model response of ζ to the observed τ field.

It can be seen qualitatively from Fig. II.3 that both the τ and ζ fields are dominated by large-scale fluctuations with wavelengths greater than 1000 km. This is supported quantitatively by wavenumber autospectra of ζ and τ (four-month ensemble averages of six-hourly wavenumber spectra) plotted in Fig. II.4. Most of the energy in both ζ and τ exists in fluctuations with wavelengths greater than 1000 km. Only a very small fraction (about 0.03) of ζ variance exists at wavelengths smaller than the FNOC Nyquist wavelength for τ of about 600 km. Since we focus only on these dominant large-scale fluctuations in this report, the fact that calculated τ does not adequately represent fluctuations with

spatial scales less than several hundred kilometers should not lead to serious problems in using it as the wind stress forcing function.

II.4.3 Time-Domain EOFs of ζ and τ

Time-domain EOFs of gridded ζ (Figs. II.5 and II.6) are calculated to determine the alongshore structure of ζ . Mode 1 (56% of the total variance) essentially represents a northern mode, and mode 2 (23%) a southern mode, indicating that ζ fluctuations poleward of Crescent City (CCY) are poorly correlated with those equatorward of CCY. This discontinuity is very evident in the distribution of the percent variance explained for each mode. This agrees with the results of Osmer and Huyyer (1978), who discovered a discontinuity in ζ correlation located between CCY and Charleston (CHR) during the summers of 1973 through 1975. The EOFs presented here indicate that the boundary between the subdomains is located near CCY during the summer of 1973.

Time-varying amplitudes and their autospectra, plotted in Fig. II.6, indicate that the southern mode is relatively more energetic at lower frequencies than the northern mode, with 69% of the southern mode energy and 41% of the northern mode energy existing at frequencies less than 0.043 cycles per day (cpd), and 29% of the southern mode energy and 55% of the northern mode energy existing at frequencies between 0.043 and 0.22 cpd. A time scale equal to, or greater than, four months is also visually evident in

the southern mode. Therefore, some of the energy in the southern mode may have originated near the equator as discussed by Enfield and Allen (1980) and Chelton and Davis (1982).

The correlations between these time-varying amplitudes and local τ indicate that the northern mode is strongly related to τ along the coast between Northern California and Washington (Fig. II.5). The southern mode is marginally significantly correlated with τ to the south of the CODE site, with two correlation maxima located near $y = -180$ km [between San Francisco (SFO) and Monterey (MRY)] and $y = -1440$ km (northern Baja California). Therefore, the southern ζ mode may be forced in part by wind stress fluctuations. The correlations between the southern mode and local τ change sign poleward of Cape Mendocino and approach marginally significant levels along the Washington and British Columbia coast. This probably occurs because of large-scale correlation patterns in the τ fields.

Time-domain EOFs of τ are presented in Fig. II.7 to characterize the large-scale structure of the τ fluctuations. Mode 1 is dominated by the energetic τ fluctuations near Cape Mendocino, while mode 2 is dominated by large-scale fluctuations with wavelengths of at least 3000 km and a node near Cape Mendocino. Mode 1 explains almost all of the variance at the grid points near Cape Mendocino. Mode 2 explains about half of the variance at the grid points along the Washington coast and along the southern California and Baja California coasts. The northern ζ

mode is significantly correlated with both τ modes 1 and 2, with maximum correlation coefficients and time lags for the τ mode of, respectively, (0.63, 1.5 days) and (0.45, 0.75 days). The southern ζ mode is significantly correlated with τ mode 2 only (0.57, 1.5 days). There is no significant correlation between ζ modes 1 and 2 and higher τ modes. The northern ζ mode is apparently primarily forced by the energetic τ fluctuations centered near Cape Mendocino, although there is some contribution from the larger-scale τ fluctuations represented by mode 2. The τ fluctuations that are at least partly responsible for driving the southern ζ mode are apparently part of a large-scale atmospheric oscillation for which we have sampled less than one wavelength in the alongshore direction.

II.5 THE ALONGSHORE-FREQUENCY PROPERTIES OF WIND-STRESS FORCING AND RESPONSE

II.5.1 Autospectra

Autospectra of ζ and τ (Fig. II.8) are computed at each sea level station or grid point, then contoured as a function of y and frequency. The energy of ζ fluctuations generally increases poleward from the southern end of the domain over all frequencies, reaching a maximum along the southern Washington coast. The energy then decays rapidly poleward through central British Columbia, then slowly increases along the northern British Columbia coast.

Relatively energetic fluctuations in ζ also exist for $y \leq -500$ km near 0.4 cpd.

The distribution of ζ and τ energy along the coast shows the poleward displacement of the ζ response to τ noted in the discussion of basic statistics (Section II.4). Fluctuations in τ are most energetic near Cape Mendocino, and smaller alongshore energy maxima exist near Point Conception ($y = -575$ km) and along the northern British Columbia coast over all frequencies. The alongshore energy maximum of ζ is displaced poleward from the τ energy maximum near Cape Mendocino, and is located near the latitude of a τ energy minimum. A ζ energy minimum along the central British Columbia coast is displaced about 400 km poleward of this τ energy minimum.

II.5.2 Frequency-Domain EOFs

The two most significant frequency-domain EOFs (Wallace and Dickinson, 1972) of gridded ζ are presented in Fig. II.9. For each mode, rms amplitude, percent variance explained (which is 100 times the coherence squared with gridded ζ), and phase lag in hours are contoured as a function of y and frequency. The modes are computed for 10 frequency bands between 0.043 and 0.43 cpd, the same frequencies and frequency bandwidths used for the autospectra in Fig. II.8. The subdomains in y -frequency space dominated by the first two modes are sharply delineated by the contours of percent variance explained in Fig. II.9. The first mode represents most of

the ζ variance poleward of grid point 9 (near CCY), and the second mode represents most of the variance equatorward of point 9, consistent with the time-domain EOFs. However, a substantial percentage of sea level variance along the northern British Columbia coast is also contained in the second mode, which is not observed in the second time-domain EOF. For consistency, we refer to these frequency-domain EOFs as northern and southern modes.

The plots of amplitude and percent variance explained show that the northern mode increases rapidly in amplitude poleward of $y = 0$ km. It has maximum amplitude along the southern Washington coast at a frequency of 0.086 cpd. The southern mode generally decreases in amplitude poleward of San Francisco, then increases again in amplitude along the northern British Columbia coast, and is therefore smaller in amplitude than the northern mode from Northern California through central British Columbia. The energy of the southern mode increases enough along the northern British Columbia coast to explain as much variance as the northern mode near Bella Bella.

From the contours of phase lag in hours, the northern mode fluctuations poleward of Cape Mendocino propagate poleward at roughly 600 cm s^{-1} between 0.086 and 0.17 cpd, a frequency band where the northern mode has relatively large amplitude. The northern mode extends equatorward along the central and southern California coast near 0.13 cpd based on the coherence with measured ζ , where the fluctuations propagate poleward at about 250 cm^{-1} . At

frequencies greater than 0.22 cpd, the phase lags are irregular and consistent phase propagation cannot be identified. The ζ fluctuations in the southern mode propagate poleward at roughly 250 cm s^{-1} for frequencies equal to or less than 0.086 cpd, a frequency band where the mode has relatively large amplitude. The propagation speed increases to roughly 450 cm s^{-1} between 0.17 and 0.22 cpd, a frequency band where the mode has much smaller amplitude. Considering the properties of both modes, fluctuations in ζ poleward of Cape Mendocino tend to propagate substantially faster than fluctuations equatorward of the Cape.

Frequency-domain EOFs of τ , calculated for the same frequency bandwidths as the ζ EOFs, are presented in Fig. II.10. The most energetic mode represents the energetic fluctuations centered near Cape Mendocino plus some very low-frequency fluctuations located equatorward of the Cape and centered near Point Conception. The second mode is dominated by the relatively less energetic fluctuations located both poleward and equatorward of the Cape, consistent with the spatial structure of the first two time-domain EOFs of τ (Fig. II.7).

Phase contours of mode 1 display a banded structure over frequency. A band of equatorward-propagating fluctuations exists at frequencies near 0.043 cpd. Poleward of Cape Mendocino, poleward propagation exists over all frequencies equal to or greater than 0.086 cpd. Equatorward of Cape Mendocino, poleward propagation exists in the frequency bands centered near 0.086,

0.13, and 0.22 cpd, with equatorward propagation in the frequency band centered near 0.17 cpd and over all frequencies greater than 0.22 cpd. Thus, propagation is exclusively poleward throughout the alongshore domain of the mode in the three frequency bands centered near 0.086, 0.13, and 0.22 cpd. The computed phase lags for τ mode 2 are irregular and consistent phase propagation cannot be identified.

We compute the coherence squared (Fig. II.11) between the northern ζ mode and τ mode 1 using the method of Denbo and Allen (1984). The only coherences significant at the 95% level of confidence are observed at the same three frequencies (0.086, 0.13, and 0.22 cpd) where mode-1 τ fluctuations propagate exclusively poleward throughout the entire alongshore subdomain of the mode.

The largest amplitude of τ mode 1 is observed along the Oregon and northern California coast at two frequencies, 0.086 and 0.17 cpd. The largest amplitude of ζ mode 1 is observed along the Washington coast at 0.086 cpd, with no indication of a relative maximum near 0.17 cpd. At 0.086 cpd, the fluctuations in τ mode 1 propagate poleward at about 350 cm s^{-1} between Point Conception and Neah Bay. At 0.17 cpd, these fluctuations are nearly in-phase, implying very rapid alongshore propagation speeds ($> 1000 \text{ cm s}^{-1}$), with equatorward propagation south of Cape Mendocino. Thus, ζ mode 1 has its largest amplitude and is significantly coherent with τ mode 1 at the only frequency (0.086 cpd) where the τ mode has both a relative amplitude maximum and poleward propagation over its

entire alongshore domain at a speed relatively close to the observed propagation speed of fluctuations in ζ . At 0.17 cpd, the τ mode only possesses the first property, and it is not significantly coherent with the ζ mode (Fig. II.11). The response of ζ to fluctuations in τ is frequency-dependent, and at a given frequency it apparently depends on both the amplitude and alongshore propagation speed (hence the wavenumber) of the fluctuations in τ . Although it is not clearly demonstrated here, the response presumably also depends on the alongshore distance over which the τ field possesses these properties. Further studies using wavenumber-frequency decompositions of ζ and τ are in progress.

II.6 THE RELATIONSHIP OF SEA LEVEL RESPONSE TO THE LARGE-SCALE WIND STRESS FIELD

Space- and time-lagged correlations between ζ at six stations from Bella Bella to Long Beach and calculated τ at all grid points are analyzed to study the alongshore variability of the response of ζ to τ . These ζ - τ correlations are contoured as a function of lag time and y in Fig. II.12. It is evident that ζ tends to be more highly correlated with τ equatorward from, and earlier in time than, the location and time of the ζ measurements. These lags are estimated from Fig. II.12 and summarized in Table II.6. Correlations between τ at the six grid points closest to the six ζ stations used in the ζ - τ correlation analysis and τ at all grid

points are contoured in Fig. II.13, and correlations between ζ at these six grid points and ζ at all grid points are contoured in Fig. II.14.

From the ζ - τ correlation pattern (Fig. II.12), fluctuations in ζ at Bella Bella (BBL), Neah Bay (NBA) and Southbeach (SBC) are all most highly correlated with τ along the southern Oregon and extreme northern California coast. The lag times for these stations become more negative with increasing poleward separation from the northern forcing region, ranging from -0.75 days at SBC to -3.0 days at BBL. At BBL and NBA, the correlation of ζ with local τ is insignificant. The τ - τ correlation patterns relative to grid points 16 and 13 (Fig. II.13) do not show a corresponding correlation peak at negative lag times along Northern California and Oregon. The ζ - ζ correlation patterns relative to grid points 16 and 13 (Fig. II.14) show that ζ at these points is relatively well correlated with ζ along the Oregon coast, the apparent origin of much of the ζ energy observed at these grid points. Apparently, fluctuations in ζ along Washington and British Columbia are dominated by free wave energy that is forced along the Northern California and Oregon coast.

Near-local forcing is apparently much more important at SBC, where the ζ - τ correlation peak is located within 200 km equatorward of SBC. The corresponding τ - τ and ζ - ζ correlation patterns relative to grid point 11 both have positive slopes in the major axes of the central correlation peaks. The τ - τ correlation peak relative to grid point 9 (near CCY) also has positive slope.

Positive slopes are expected if poleward propagating energy exceeds equatorward-propagating energy. This indicates that near-resonant forcing may be relatively important along the Oregon and extreme northern California coast. In contrast, the central peaks of the τ - τ correlation patterns relative to grid points 16 and 13 do not have a noticeable slope, indicating that near-resonant forcing is less important along the Washington and British Columbia coast. This is probably one reason why near-local atmospheric forcing is not very important along this part of the coast.

The slopes of the ζ - ζ correlation peaks in Fig. II.14 from grid point 9 to the south are substantially smaller than the slopes at the northern grid points, except at grid point 2 where a slope cannot be discerned. The slope relative to grid point 9 is smaller equatorward of the point than poleward of the point. This indicates that propagation speeds are smaller along the California coast than to the north, in agreement with the results of the frequency-domain EOF analysis.

The existence of the southern forcing region along the Northern Baja California coast (near $y = -1080$ km) is evident in the ζ - τ correlations from the statistically significant correlation maxima between ζ at CCY, MRY, and Long Beach (LBC) and τ along Northern Baja California at negative lag times (Fig. II.12). Effects of this forcing region appear as far poleward as NBA, since weak correlation maxima between τ near $y = -1080$ km and ζ at NBA and SBC are also observed at negative lag times in Fig. II.12.

These correlation maxima again occur at increasingly negative lag times with increasingly poleward separation of the ζ station from $y = -1080$ km (Table II.6). However, part of the high correlation with τ near $y = -1080$ km may be due to correlation patterns in the τ field itself. At grid point 2, τ is relatively well correlated with τ at locations poleward of the grid point, giving a positive slope to the τ - τ correlation peak (Fig. II.13). Thus, τ fluctuations along Northern Baja California appear to propagate poleward to Northern California.

A characteristic speed of forced ζ fluctuations may be estimated from the lag distances (Δy) and lag times (Δt) of the correlation maxima denoted by the solid dots in Fig. II.12. A rough estimate of uncertainty is obtained by computing a range of speeds for a lag time uncertainty of ± 0.25 days. Most speed estimates range between 200 and 450 cm s^{-1} . The two exceptions are for the correlation maxima located within 100 km equatorward of MRY, where the speed is about 100 cm s^{-1} , and for the one correlation maximum located equatorward of LBC, where the speed is over 1000 cm s^{-1} .

We do not pursue a dynamical interpretation of these results here. The problem is addressed by Allen and Denbo (1984), who show that the space-time lagged ζ - ζ and τ - τ correlation patterns observed here are implied by the first-order wave equation of Gill and Schumann (1974). This equation is discussed in Section II.7.

The relationship of the ζ -response to the large-scale τ field is examined in the frequency-domain by contouring squared coherences between ζ at six stations and τ at all grid points as a function of frequency and y (Fig. II.15). The two forcing regions are evident in the τ - ζ coherence plots for BBL, NBA, and SBC. The coherence between SBC ζ and τ in the northern forcing region is large over a broad frequency band from 0.043 to about 0.4 cpd. The τ - ζ coherence patterns relative to NBA and BBL indicate that the coherent frequency band narrows and shifts toward very low frequencies (near 0.043 cpd relative to BBL ζ) with increasing alongshore separation from the northern forcing region. The coherence maximum between NBA and SBC ζ and τ in the southern forcing region is near 0.086 cpd, while the corresponding coherence maximum between BBL ζ and τ is near 0.043 cpd. Apparently, only the lowest-frequency component of the wind-forced ζ fluctuations from both forcing regions reaches BBL. At CCY and MRY, ζ is most coherent with τ between the alongshore locations of these stations and the southern end of the analysis domain for frequencies less than about 0.2 cpd. At LBC, ζ is most coherent with τ along northern Baja California at a frequency of 0.043 cpd. A coherence maximum also exists between LBC ζ and τ at $y = -900$ km at a frequency of about 0.4 cpd. This indicates that the relatively large ζ energy observed near the southern end of the analysis domain at this frequency (Fig. II.8) is probably wind-driven.

II.7 DYNAMICAL INTERPRETATION OF THE OBSERVED RESPONSE TO WIND STRESS FORCING

To assess the dynamics of the ζ response to τ fluctuations, we focus on τ events 4 and 5 (Fig. II.16) plus event 11 (Fig. II.17) by overlaying contours of six-hourly τ and gridded ζ . We compare these observations to ζ predicted from the observed τ using a simple theoretical model. Events 4 and 5 are both pulses of strong equatorward τ , with the pulse associated with event 5 propagating poleward at about 500 cm s^{-1} and evidently capable of more effective forcing of ζ than event 4, which propagates equatorward at about 650 cm s^{-1} . Event 4 depresses ζ by less than 3 cm, with the response occurring later in time and poleward of the time line of the τ extremum (Fig. II.16). Event 5 depresses ζ by up to 14 cm, more than four times greater than the response to event 4, even though the maximum amplitude of τ is only 1.5 times greater. The maximum response amplitude occurs at the poleward edge of the τ event.

Event 11 propagates poleward at about 550 cm s^{-1} , and it extends over a larger alongshore domain than the other events (Fig. II.17). The resulting depression in ζ propagates poleward along with, but occurring about one-half day later than, the location and time of the τ extremum. A large ζ maximum forced along the Oregon coast about three days prior to event 11 is also observed in Fig. II.17. A weak, poleward-propagating (at about 700 cm s^{-1}) τ maximum is apparently responsible for this response.

In linear models of wind-forced coastally-trapped waves, if the variables are expanded in terms of modes dependent on the cross-shelf and vertical coordinates, the alongshore and time-dependent behaviour $Y_n(y,t)$ of the n^{th} mode is governed by a forced, first-order wave equation (Gill and Schumann, 1974, Clarke, 1977):

$$c_n^{-1} Y_{nt} + Y_{ny} + (c_n T_f)^{-1} Y_n = b_n \tau(y,t), \quad (\text{II.7.1})$$

where the subscripts (y,t) denote partial differentiation, c_n is the free-wave phase speed of the n^{th} mode, b_n a constant dependent on the mode structure and topography, and T_f the friction time scale. Free wave solutions to the homogeneous equation propagate toward $+y$ at speed c_n , or along the characteristic line in $y-t$ space given by $y - c_n t = \text{constant}$.

We assume that fluctuations in ζ are dominated by the lowest mode and drop the subscripts. We then compare the observed alongshore-time behavior of ζ to Y predicted by (II.7.1) using observed (calculated) $\tau(y,t)$ as the forcing function. The solution of (II.7.1) at y and t is an integral of wind stress along the characteristic through y,t weighted by an exponential function due to friction

$$Y = b \int_0^{\infty} \exp(-r/cT_f) \tau(y-r, t-r/c) dr. \quad (\text{II.7.2})$$

The influence of τ equatorward of y decreases exponentially with increasing separation. We predict time series of ζ at the CODE analysis grid points by numerically integrating (II.7.2). This is similar to the procedures used by Hamon (1976), who tested (II.7.1) by predicting ζ at one location on the east coast of Australia, and Clarke (1977), who predicted ζ at Depoe Bay, Oregon for a 34 day period during summer 1972.

Numerical integrations of (II.7.2) are performed along the characteristics using constant c , T_f , and b . Since the southern boundary of the τ grid (26°N) is considerably farther south than the southernmost ζ point (33°N), we approximate the infinite integral (II.7.2) for Y , which neglects an exponentially-damped contribution from ζ at the southern boundary. The predicted time series of ζ begin at 0000 on 16 June, which provides sufficient time for the initial ζ distribution to propagate through the analysis domain. Predictions are made only for locations poleward of Point Conception ($y=-540$ km), since the southern boundary contribution will make the predictions relatively inaccurate equatorward of the point. Thus, the prediction consists entirely of fluctuations forced within the study domain after 3 June.

We first estimate values of c , T_f , and b that give the best predictions of ζ within the most energetic alongshore subdomain of

the wind-driven northern ζ mode, essentially the Washington and Oregon coast. To determine these parameters, trial predictions of ζ are made at four sea level stations: NBA, Toke Point (TKP), SBC, and Umpqua River (UMP), using different values of c and T_f in the range $250 \leq c \leq 400 \text{ cm s}^{-1}$ and $2.5 \leq T_f \leq 6.0$ days. The values of these parameters and of b that maximize the fraction of total variance explained by the prediction at these four stations are then determined. The best predictions, which explain 64% of the total variance at these stations, are obtained using $c = 325 \text{ cm s}^{-1}$, $T_f = 4.25$ days, and $b = 1.19 \times 10^{-7} (\text{dy cm}^{-2})^{-1}$. These values are used in the subsequent analysis. This value of c is smaller than the observed phase speed of the northern ζ mode which dominates ζ fluctuations along Oregon and Washington. These phase speeds probably differ for several reasons:

1. observed ζ fluctuations consist of both forced and free wave energy;
2. both observed phase speeds and theoretical free wave phase speeds are not constant along the coast; and
3. more than one coastally-trapped wave mode may be present.

The quality of these test predictions is not very sensitive to the parameter T_f , with the fraction of total variance explained changing by less than one percent for $2.5 \leq T_f \leq 6.0$ days at $c = 325 \text{ cm s}^{-1}$. Squared correlation coefficients between ζ predicted at these four stations and ζ at SDO are no larger than 0.023, indicating that the neglect of ζ fluctuations propagating

into the analysis domain through the southern boundary does not significantly effect the prediction of ζ poleward of the northern forcing region.

The quality of predicted ζ at SBC may be seen in Fig. II.18. The zero-lag correlation coefficient between the measured and predicted time series is 0.83, while the zero-lag correlation between measured ζ and local τ is 0.72.

We determine the quality of the prediction poleward of Point Conception by computing the fraction of the variance of measured ζ explained by predicted ζ at each station (Fig. II.19). Between Cape Mendocino and Point Conception ($0 > y > -575$ km) and along most of the British Columbia coast ($y > 1200$ km), less than half of the variance is explained by the prediction. In between, up to 70% of the variance is explained by the prediction. The higher quality of the prediction along the Washington and Oregon coast occurs partly because we used constant values of c , T_f , and b set to give the best prediction for this segment of the coast, and partly because it is located north of the strongest forcing region. However, the prediction does explain a larger fraction of the ζ variance at all loctions than local τ alone.

Predicted ζ is contoured along with calculted τ for the selected τ events in Figs. II.16 and II.17. The predicted ζ response to these four events are qualitatively very similar to the observed responses. Wind stress event 4 has a much smaller predicted ζ response than event 5 (Fig. II.16), smaller than would

be expected by just considering the smaller amplitude of τ event 4. This is expected theoretically since the τ extremum associated with event 5 propagates poleward at about 500 cm s^{-1} , and should more effectively force ζ fluctuations than event 4, which propagates equatorward. The predicted ζ maximum for event 5 occurs at the poleward edge of the event, as did the measured ζ maximum, although the measured amplitude is somewhat smaller. The predicted ζ responses to the two τ events in Fig. II.18 are very similar to the measured responses, although the predicted response to the first event is smaller in amplitude than the measured response.

Differences in the measured and predicted amplitudes of ζ cannot be considered critical, since they may be due to alongshore variations in the coefficient b or to errors in the calculated wind field. The choice of 325 cm s^{-1} for the phase speed may have maximized the percent variance explained by the prediction along the Oregon and Washington coast, but the ζ response to individual events did not always propagate poleward at that speed. For example, the response to event 5 propagates poleward at about 500 cm s^{-1} .

We conclude that the first-order, forced coastally-trapped wave dynamics provide a fairly good description of the observed ζ fluctuations. The errors in predicted ζ can be attributed to several possible factors. In addition to the three factors listed earlier to explain the differences between c and the observed phase speeds, there are:

1. the parameters T_f and b are not constant along the coast;
2. the parameters c , T_f , and b depend on factors such as stratification and may be variable in time;
3. imperfect winds are used to represent the wind stress forcing function;
4. noise and local geographical effects affect measured ζ ; and
5. dynamical processes other than wind-forced large-scale coastally-trapped waves may influence ζ fluctuations.

II.8 DISCUSSION

During summer 1973, the dynamics of large-scale coastally-trapped waves explained a large fraction of the observed ζ variance along the coast from northern Baja California to British Columbia. Atmospheric forcing was not uniform along the coast, and the most effective forcing was confined primarily to two regions. The northern California and Oregon coast was the region of strongest forcing, while northern Baja California was a region of significant but weaker forcing. The forced fluctuations of ζ propagated poleward from these forcing regions. Local forcing was so weak along the British Columbia coast that ζ fluctuations were apparently dominated by free wave energy propagating poleward from the northern forcing region. Fluctuations forced in the southern region were detectable poleward to northern Washington.

Forcing within the northern region was very strong for two reasons: first, the strongest τ fluctuations existed along the Northern California coast; and second, poleward-propagating fluctuations in τ were apparently more energetic than equatorward-propagating fluctuations. The variance of τ was an order of magnitude larger near Cape Mendocino than at locations more than a few hundred kilometers poleward and equatorward of the Cape. We also observed that poleward propagating τ events more effectively forced ζ fluctuations than equatorward-propagating events. Since most of the τ variance in the northern forcing region was uncorrelated with τ at other locations, forced fluctuations of ζ both within and poleward of this forcing region were poorly correlated with fluctuations of ζ equatorward of the region. Most of the ζ variance was therefore explained by two EOFs in both the time and frequency domains, each dominating the ζ fluctuations along different segments of the coast, with the dividing zone located near CCY. The dividing zone was not an insurmountable barrier, since ζ fluctuations driven along Northern Baja California could still be weakly detected along the Oregon and Washington coast. The northern forcing zone was so effective that ζ fluctuations poleward of CCY that were driven in this zone strongly dominated the ζ fluctuations from the southern forcing region that propagated poleward past CCY.

The northern ζ fluctuations propagated poleward at about 600 cm sec^{-1} , and the southern ζ fluctuations propagated poleward at

about half that speed in the most energetic frequency bands. Observed wavelengths were greater than 1000 km along the entire coast, and the most energetic fluctuations had wavelengths greater than 2000 km. A frequency-domain EOF representing the northern ζ fluctuations had an amplitude maximum near 0.086 cpd, and a frequency-domain EOF representing the southern ζ fluctuations had an amplitude maximum at lower frequencies. A period equal to or greater than four months was visually evident in the amplitude time series of the corresponding southern time-domain EOF.

We observed that ζ fluctuations at a given location y along the coast are most highly correlated with τ earlier in time and equatorward of y , with the space and time lags dependent on location, since the effectiveness of τ forcing was not uniform along the coast. If y was located within a forcing region, the lags ranged from 100 to 500 km equatorward of y and 1 to 2 days earlier in time. If y was located away from a forcing region, both lags were larger. For example, ζ at BBL was most highly correlated with τ along the Oregon coast (about 900 km equatorward of BBL) about 3 days earlier in time. Knowledge of large-scale processes can therefore be important to shelf circulation studies in determining how ζ and therefore currents, are driven by τ . Wind stress data should be collected more than 1000 km away from the study region in the direction from which coastally-trapped waves propagate to be sure that important forcing regions, and the ζ fluctuations forced in those regions, are included in the analyses.

During the summer of 1973, τ calculated from FNOC pressure fields was as well correlated with ζ as the best available measured τ . Therefore, calculated τ proved to be a satisfactory forcing function for the purposes of this study. The calculated τ vector series were not aligned with measured τ along the entire alongshore domain except near Point Conception, and had to be rotated additionally an average of 50 degrees counterclockwise to correct this misalignment. This correction also approximately maximized the correlation between the alongshore component of τ and ζ , and therefore improved the quality of the results obtained in this study. Whenever calculated winds or wind stress are to be used in a study along the west coast of North America (and probably other regions as well), tests of the alignment of these winds should be conducted and the vector winds rotated if necessary.

Table II.1. Meteorological station information and basic statistics of measured τ .

Station	Symbol	Latitude (deg min)	Longitude (deg min)	y* (km)	Geographical coast orientation (deg)	Variable		Stations selected for analyses	Measured τ statistics (dyn cm ⁻²)	
						p	Wind		Mean	Std dev
Quillayute, Wa	QUI	47 57 N	123 32 W	1055	110	Yes	Yes	*	0.01	0.08
Hoquiam, WA	HOQ	46 58	123 56	942	95	Yes	Yes			
Westport, WA Columbia River	WSP	46 55	124 06	935	95	No	Yes			
Lightship	CLL	46 11	124 11	854	90	Yes	No	*	0.03	0.56
Astoria, WA	AST	46 09	123 53	850	90	Yes	Yes			
Newport, OR	NEW	44 38	124 03	683	82	Yes	Yes	*	-0.05	0.53
North Bend, OR	NOB	43 25	124 15	547	73	Yes	Yes	*	-0.02	0.37
Crescent City, CA	CCY	41 47	124 14	362	103	No	Yes	*	-0.09	0.34
Arcata, CA	ACA	40 59	124 06	270	75	No	Yes			
Humboldt Bay, CA	HUM	40 46	124 14	246	75	No	Yes	*	-0.12	0.07
Bodega Marine Lab, CA	BML	38 20	123 04	-46	133	No	Yes	*	-0.23	0.35
Bodega Bay, CA	BDB	38 19	123 04	-48	133	No	Yes			
San Francisco, CA	SFO	37 37	122 23	-142	105	Yes	No			
Pillar Point, CA	PIL	37 30	122 30	-156	105	No	Yes	*	-0.15	0.34
Fort Ord, CA	FOR	36 41	121 46	-264	110	No	Yes			
Monterey, CA	MRY	36 35	121 51	-278	110	No	Yes			
Point Piedras Blancas, CA	PPB	35 40	121 17	-401	130	No	Yes			
Diablo Canyon, CA	DIA	35 14	120 50	-464	120	No	Yes	*	-0.39	0.40
Vandenberg AFB, CA	VAN	34 43	120 52	-528	90	No	Yes			
Point Mugu, CA	MUG	34 07	119 07	-678	155	Yes	Yes	*	-0.03	0.05
Los Angeles, CA	LOS	33 56	118 24	-757	150	Yes	Yes			
Long Beach, CA	LBC	33 49	118 09	-785	150	Yes	Yes	*	0	0.04
San Diego, CA	SDO	32 44	117 10	-936	105	Yes	Yes	*	-0.02	0.12
Imperial Beach, CA	IMP	32 34	117 07	-954	105	Yes	Yes			

Table II.2. Coastal points of the CODE analysis grid and basic statistics of calculated τ .

Grid Point	Latitude (deg min)	Longitude (deg min)	y* (km)	Geographical coast orientation (deg)	Calculated τ statistics (dyn cm ⁻²)	
					Mean	Std dev
16	52 10 N	128 19 W	1620	115	0.04	0.40
15	50 32	127 13	1440	100	0.08	0.47
14	49 23	126 06	1260	125	-0.07	0.39
13	48 11	124 42	1080	115	-0.09	0.27
12	46 36	124 05	900	95	-0.12	0.28
11	44 58	124 03	720	85	-0.23	0.42
10	43 12	124 20	540	73	-0.35	0.58
9	41 46	124 12	360	103	0.82	0.90
8	40 12	124 18	180	130	-1.20	1.12
7	38 41	123 27	0	133	-1.09	0.85
6	37 18	122 24	-180	102	-0.50	0.35
5	35 59	121 31	-360	128	-0.74	0.42
4	34 35	120 39	-540	90	-0.72	0.43
3	34 01	118 53	-720	150	-0.94	0.49
2	33 00	117 21	-900	110	-0.45	0.22
1	31 27	116 44	-1080	110	-0.42	0.22
35	20 00	115 54	-1260	115	-0.33	0.23
34	28 47	114 51	-1440	130	-0.35	0.24
33	27 20	113 52	-1620	130	-0.24	0.19
32	26 07	112 40	-1800	130	-0.18	0.16

Table II.3. Coastal sea level information and standard deviation of ζ .

Station	Symbol	Latitude (deg min)	Longitude (deg min)	y* (km)	Station or grid point numbers for atmospheric pressure used in forming adjusted sea level	Standard deviation of ζ (cm)
Bella Bella, BC	BBL	52 10	128 08	1608	CG16	5.08
Tofino, BC	TOF	49 09	125 55	1232	CG14	4.83
Neah Bay, WA	NBA	48 22	124 37	1100	CG13	5.3
Toke Point WA	TKP	46 42	123 58	911	CG12	7.57
Astoria, OR	AST	46 10	123 46	852	Astoria	6.45
Garibaldi, OR	GAR	45 25	123 55	770	Astoria-Newport*	6.99
Unpqua River OR	UMP	43 42	124 10	579	North Bend	5.8
Port Orford, OR	POR	42 45	124 30	469	North Bend	5.94
Crescent City, CA	CCY	41 45	124 11	359	CG09	5.40
San Francisco, CA	SFO	37 48	122 28	-126	San Francisco	4.61
Monterey, CA	MRY	36 36	121 53	-276	CG05-CG06*	3.87
Port San Luis, CA	PSL	35 10	120 45	-473	Calculated**	2.84
Rincon Island, CA	RIS	34 21	119 27	-650	Pt. Mugu	3.51
Long Beach, CA	LBC	33 45	118 13	-785	Long Beach	3.54
San Diego, CA	SDO	32 45	117 10	-938	San Diego	3.44

Table II.4. Summary of the two comparisons of calculated and measured vector winds. Since integral correlation time scales vary for different time series, statistically significant correlations range between 0.31 and 0.38 to a 90% level of confidence.

Table II.4a. The inner correlation and phase.

Grid Point	Measurement station	Correlation	Phase (deg)
2	IMP	0.77	60
2	SDO	0.69	53
3	LBC	0.65	59
3	LOS	0.86	76
3	MUG	0.74	58
4	VAN	0.88	-11
4	DIA	0.88	12
5	PPB	0.48	19
5	MRY	0.86	50
6	MRY	0.85	59
6	FOR	0.90	70
6	PIL	0.68	41
7	BDB	0.79	40
7	BML	0.80	47
8	HUM	0.70	68
9	ARC	0.58	57
9	CCY	0.60	67
10	NOB	0.89	19
11	NEW	0.75	23
12	AST	0.66	56
12	CLL	0.83	35
12	WSP	0.80	45
12	HOQ	0.87	60
13	QUI	0.76	57

Table II.4b. Comparison of both wind sets to sea level.

Measurement station or grid point	ζ station	Orientation (deg).	Correlation
1	SDO	74	0.42
5	MRY	65	0.57
6	SFO	37	0.55
PIL	SFO	85	0.59
7	CCY	48	0.56
BDB	CCY	115	0.54
BML	CCY	115	0.54
8	CCY	22	0.58
HUM	CCY	92	0.55
9	CCY	35	0.57
ARC	CCY	89	0.54
CCY	CCY	103	0.59
10	UMP	42	0.79
NOB	UMP	66	0.71
11	SBC	44	0.79
NEW	SBC	62	0.74
12	AST	45	0.78
AST	AST	68	0.50
CLL	AST	70	0.51
WSP	AST	86	0.47
13	NBA	73	0.42

Table II.5. Computation of the alongshore component of calculated wind stress. The average inner phase difference and the average difference between wind orientations most correlated with sea level are computed from the data in

Grid Point	Difference (calculated minus measured) between inner phases		Average difference between wind orientations most correlated with ζ (calculated minus measured)		Geographical orientation of the coast (deg).	Estimated correction angle to align calculated wind with true wind at the coast (deg)
	Average (deg)	Number of wind measurement stations	Difference in angles (deg)	Number of wind measurement stations		
1	-	0	-	0	110	60
2	57	2	-	0	110	60
3	64	3	-	0	150	60
4	0	2	-	0	90	0
5	35	2	-	0	128	38
6	57	3	48	1	102	52
7	44	2	67	2	133	58
8	68	1	70	1	130	70
9	62	2	61	2	103	58
10	19	1	24	1	73	18
11	23	1	18	1	85	20
12	49	4	30	3	95	40
13	57	1	-	0	115	55
14	-	0	-	0	125	55
15	-	0	-	0	100	55
16	-	0	-	0	115	55

Table II.6. Summary of the space and time lagged correlation analyses between ζ at each of six selected stations and τ at all grid points. Correlation maxima relative to each ζ station are numbered sequentially from north to south and are marked by the solid dots in Fig. II.12. The y locations plus the space and time lags (δy and δt) of each maximum are given, from which a characteristic speed (with error estimates in parentheses based on a ± 6 hr uncertainty in lag time) is estimated.

ζ Station No.	Correlation maxima	y (km)	δy (km)	δt (days)	$\delta y/\delta t$ (cm s ⁻¹)
BBL 1	0.48	720	-888	-3.00	368 (314-371)
NBA 1	0.68	540	-560	-1.75	368 (322-429)
NBA 2	0.25	-1080	-2180	-5.75	436 (418-456)
SBC 1	0.79	540	-138	-0.75	212 (159-317)
SBC 2	0.28	-1080	-1758	-4.75	426 (404-449)
CCY 1	0.68	-180	-539	-1.50	413 (354-495)
CCY 2	0.49	-1080	-439	-4.00	414 (389-441)
MRY 1	0.51	-360	-84	-1.00	97 (77-129)
MRY 2	0.43	-900	-624	-3.00	239 (220-261)
LBC 1	0.45	-1260	-475	-0.50	1092 (728-2185)

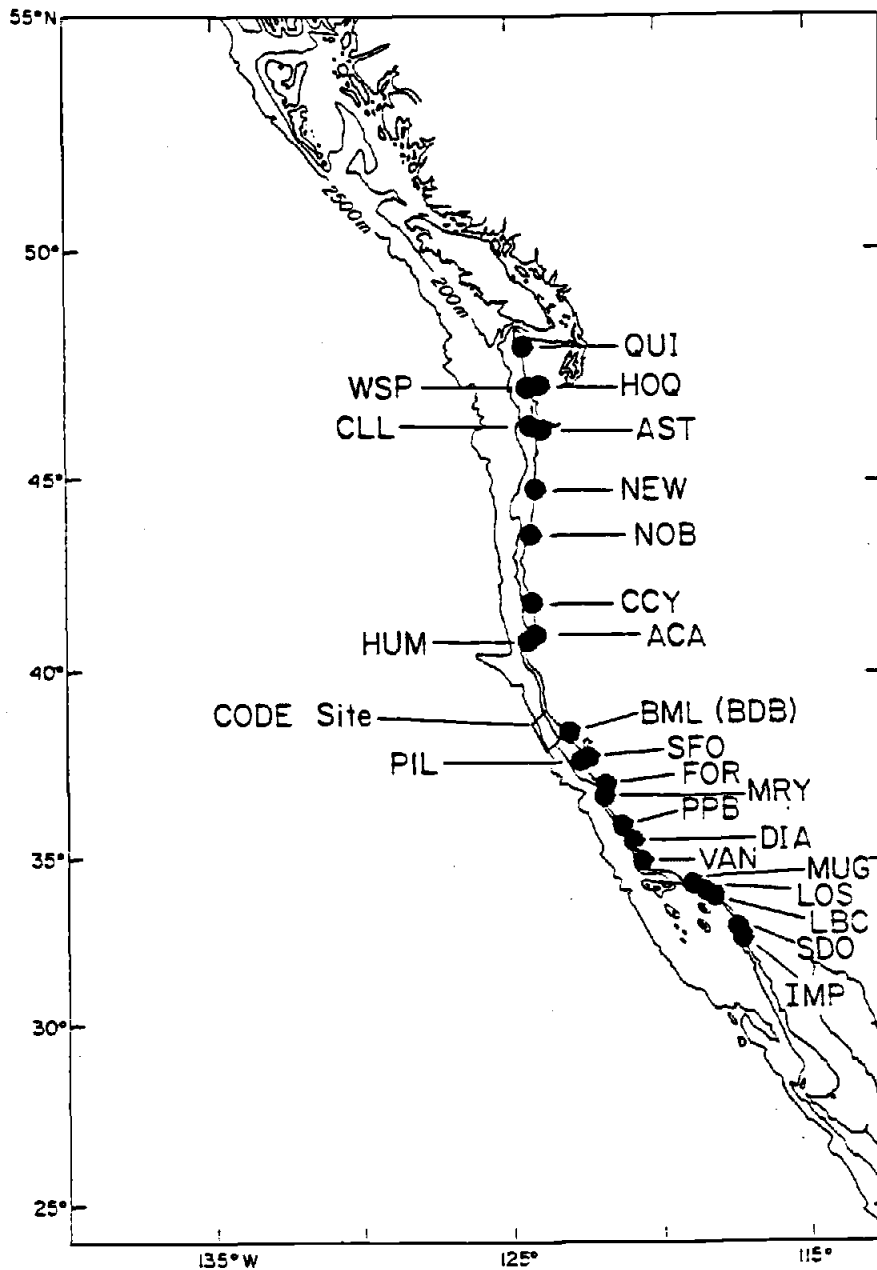


Fig. II.1: Coastal meteorological stations available during summer 1973. If more than one station is present at a given location, the other station abbreviations are shown in parentheses. The location of the CODE experimental site centered near latitude $38^{\circ}41'N$ is shown. Station information is summarized in Table II.1.

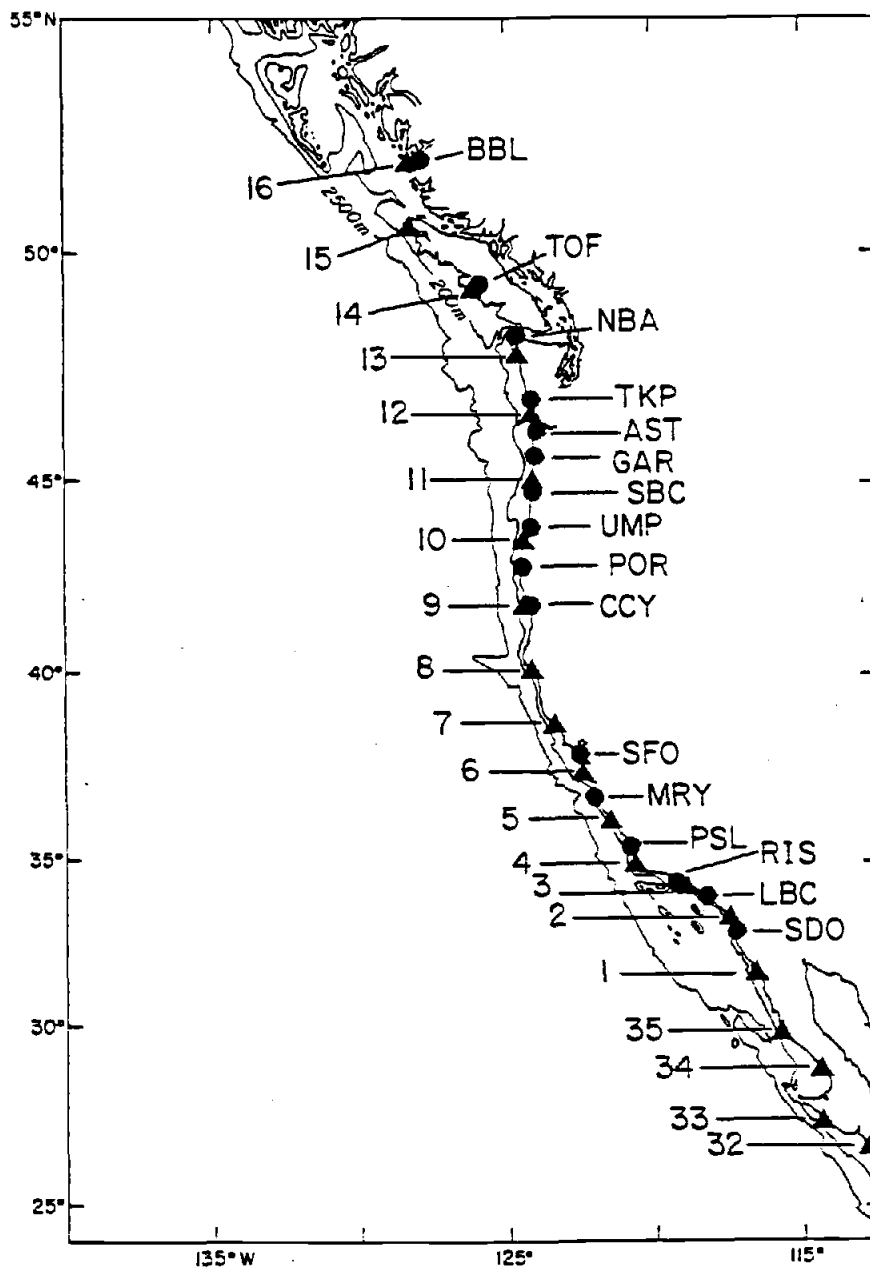
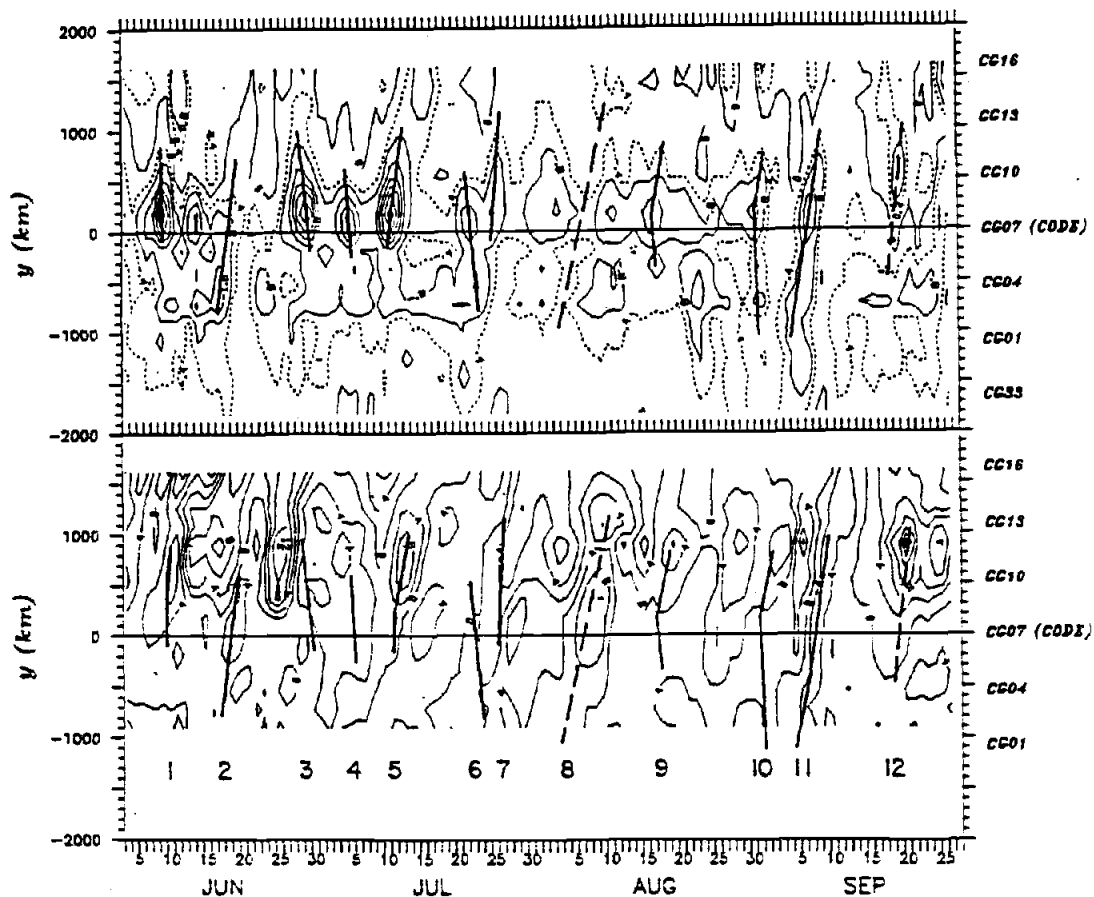


Fig. II.2: Coastal points of the CODE large-scale analysis grid (triangles) and sea level stations (circles). Grid points 17 through 31, most of which are located offshore, are not shown. Grid point information is summarized in Table II.2, and the sea level station information is summarized in Table II.3.



1973

Fig. II.3: Space-time contours of (top) daily averaged calculated τ and (bottom) daily averaged demeaned gridded ζ for summer 1973. Twelve τ events are numbered sequentially, and time lines denoting the locations and times of the τ extrema associated with these events are shown in both panels. These time lines are solid for τ minima (maximum equatorward τ) and dashed for τ maxima. The contour intervals for the solid contours are 0.8 dyn cm^{-2} for τ and 4 cm for ζ . Intermediate contours are dashed.

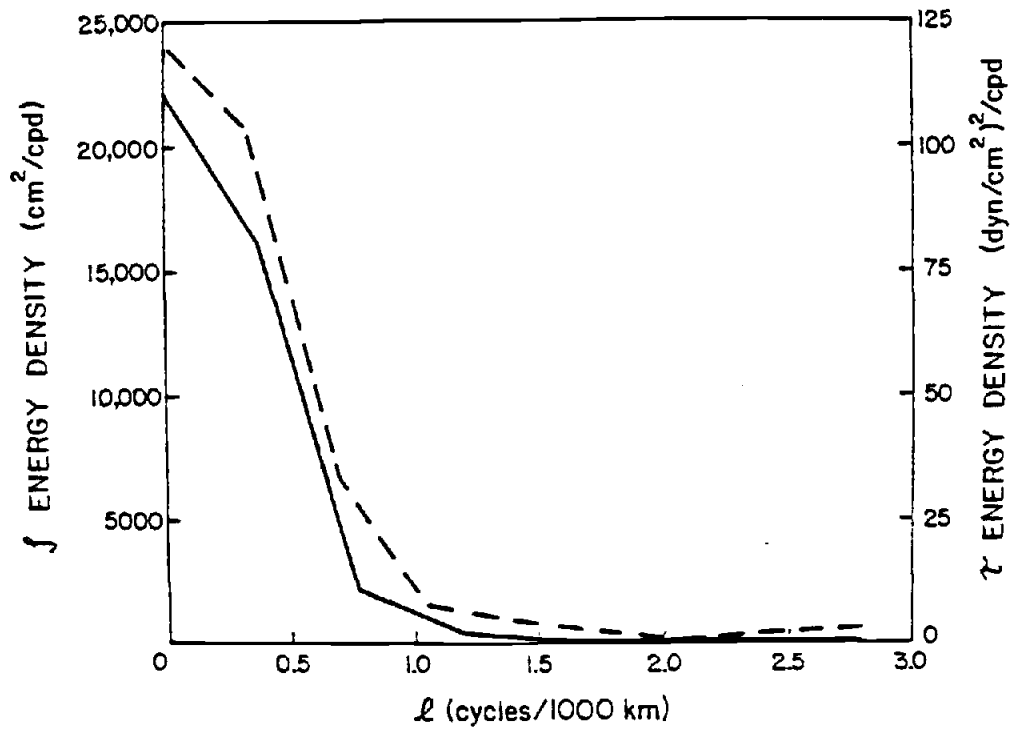


Fig. II.4: Wavenumber autospectra of gridded ζ (solid line) and calculated τ (dashed line), ensemble averaged over 4 months from six-hourly autospectra. Based on average integral time scales (Davis, 1976), the ζ spectrum has approximately 30 degrees of freedom, and the τ spectrum has approximately 37 degrees of freedom.

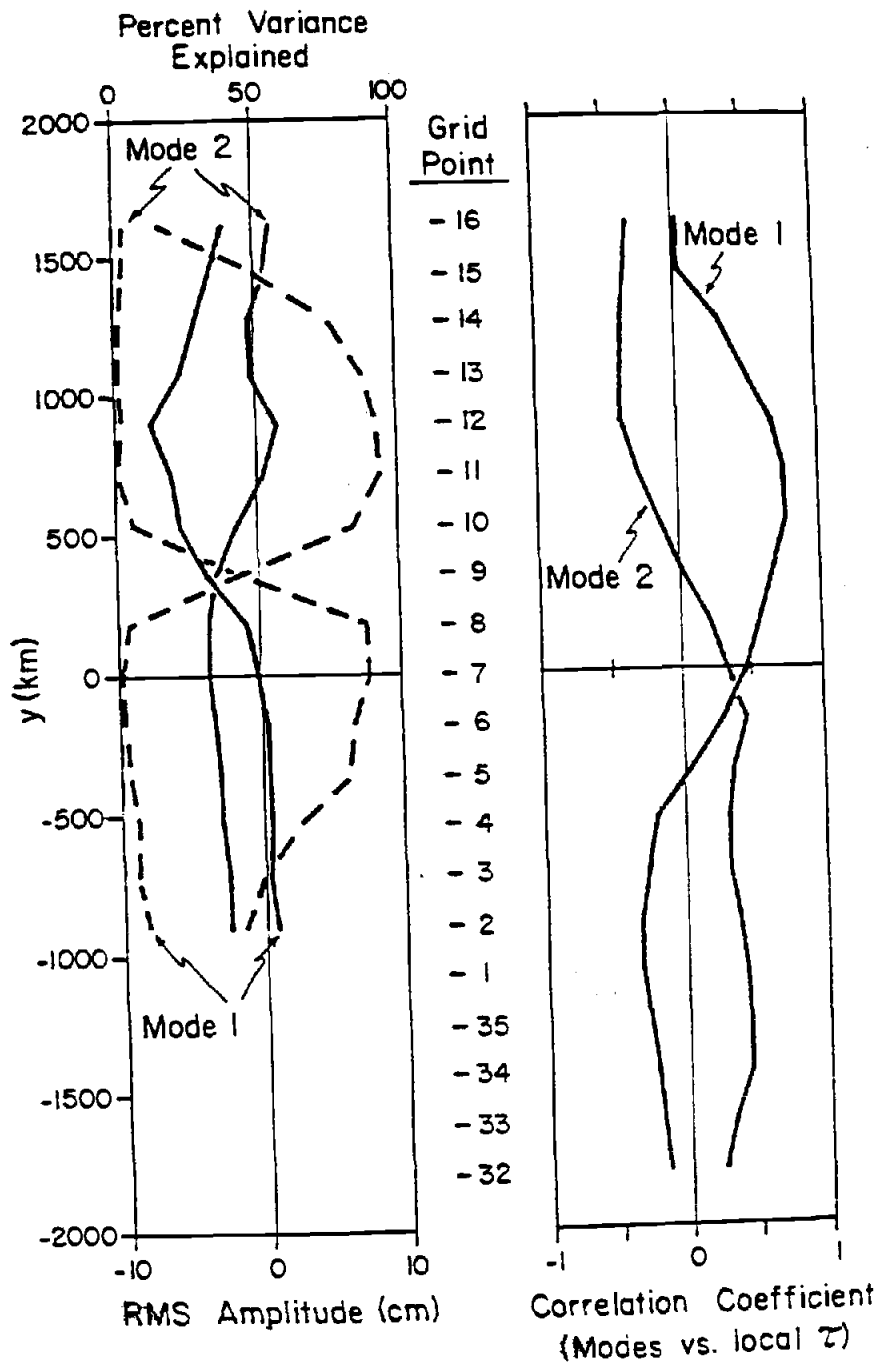


Fig. II.5: The two most significant time-domain EOFs of gridded z : (left) rms amplitudes (solid lines) and percent variance explained (dashed lines); and (right) correlation with local calculated τ that has been lagged by one day to approximately maximize the local correlation. The modes account for 56 and 23% of the total variance, respectively.

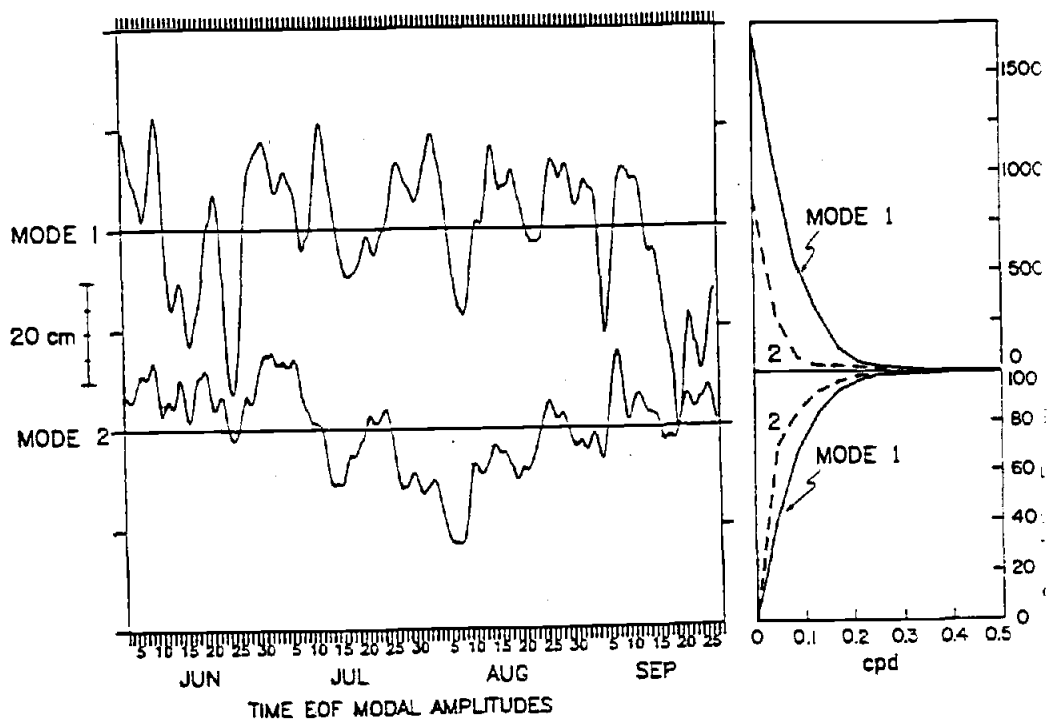


Fig. II.6: Time-varying amplitudes of the two most significant EOFs of gridded ζ from Fig. II.5 (left) and autospectra of these amplitudes graphed as energy density (right top) and as cumulative energy density in percent (right bottom). The autospectra were computed with a frequency bandwidth of 0.043 cpd, resulting in 10 degrees of freedom.

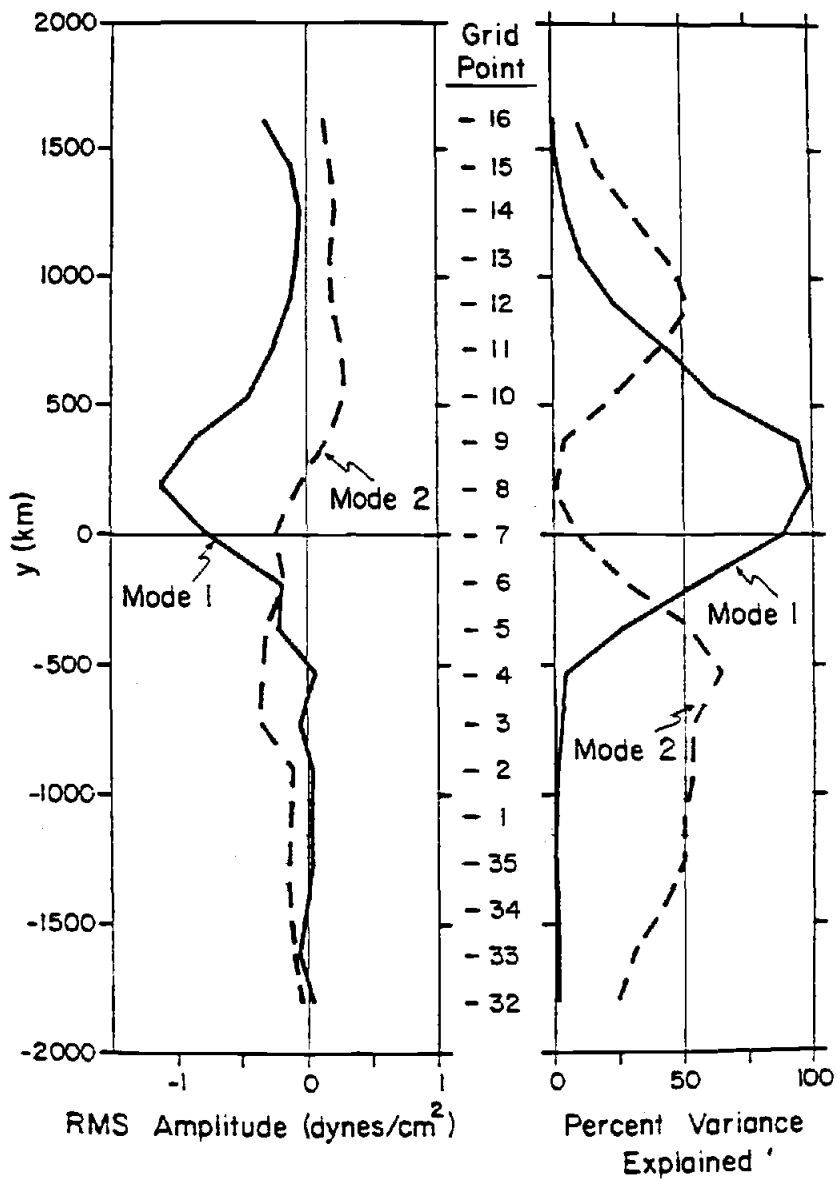


Fig. II.7: The two most significant time-domain EOFs of calculated τ : (left) rms amplitude and (right) percent variance explained. The modes account for 66 and 17% of the total variance, respectively.

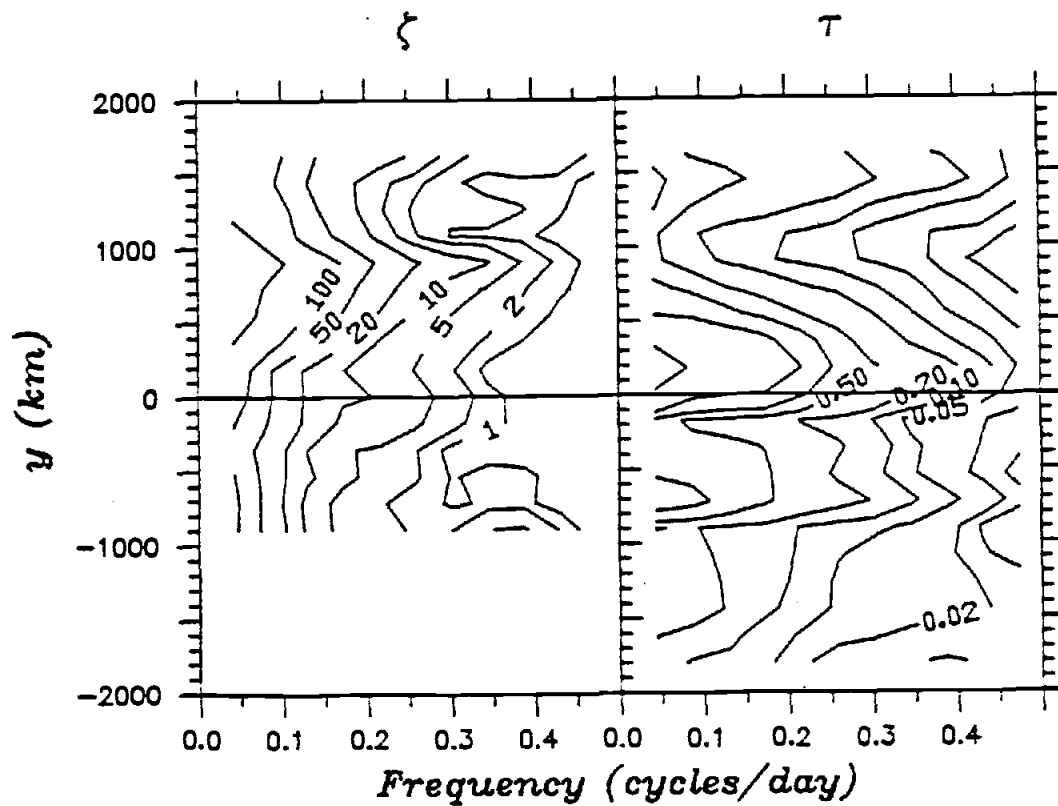


Fig. II.8: Autospectra of ζ and calculated τ contoured as a function of frequency, and y . The spectra are in units of $\text{cm}^2 \text{cpd}^{-1}$ and $(\text{dyn cm}^{-2})^2 \text{cpd}^{-1}$, respectively. The frequency bandwidth is 0.043 cpd, resulting in 10 degrees of freedom.

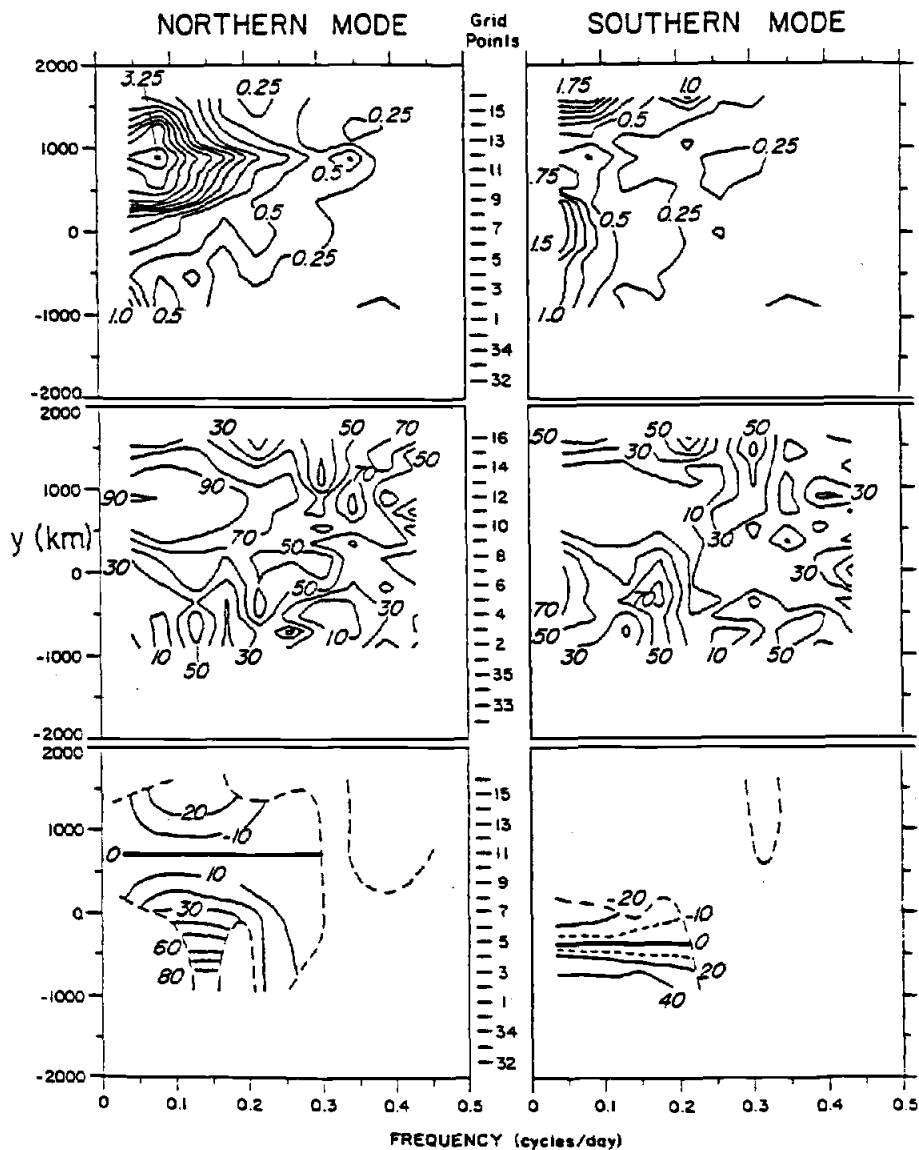


Fig. II.9: The northern and southern frequency-domain EOFs of gridded ζ contoured as a function of frequency and y : (top) rms amplitude in cm; (middle) percent variance explained; and (bottom) phase lag in hr. The frequency bandwidth is 0.043 cpd, resulting in 10 degrees of freedom. Phase is contoured only over that part of the y -frequency domain where the coherence squared between the modes and gridded ζ is greater than 0.3. The y locations of the zero phase contours are the same over all frequencies for each mode and are arbitrarily chosen to be located near the middle of the alongshore subdomains where the modes are energetic.

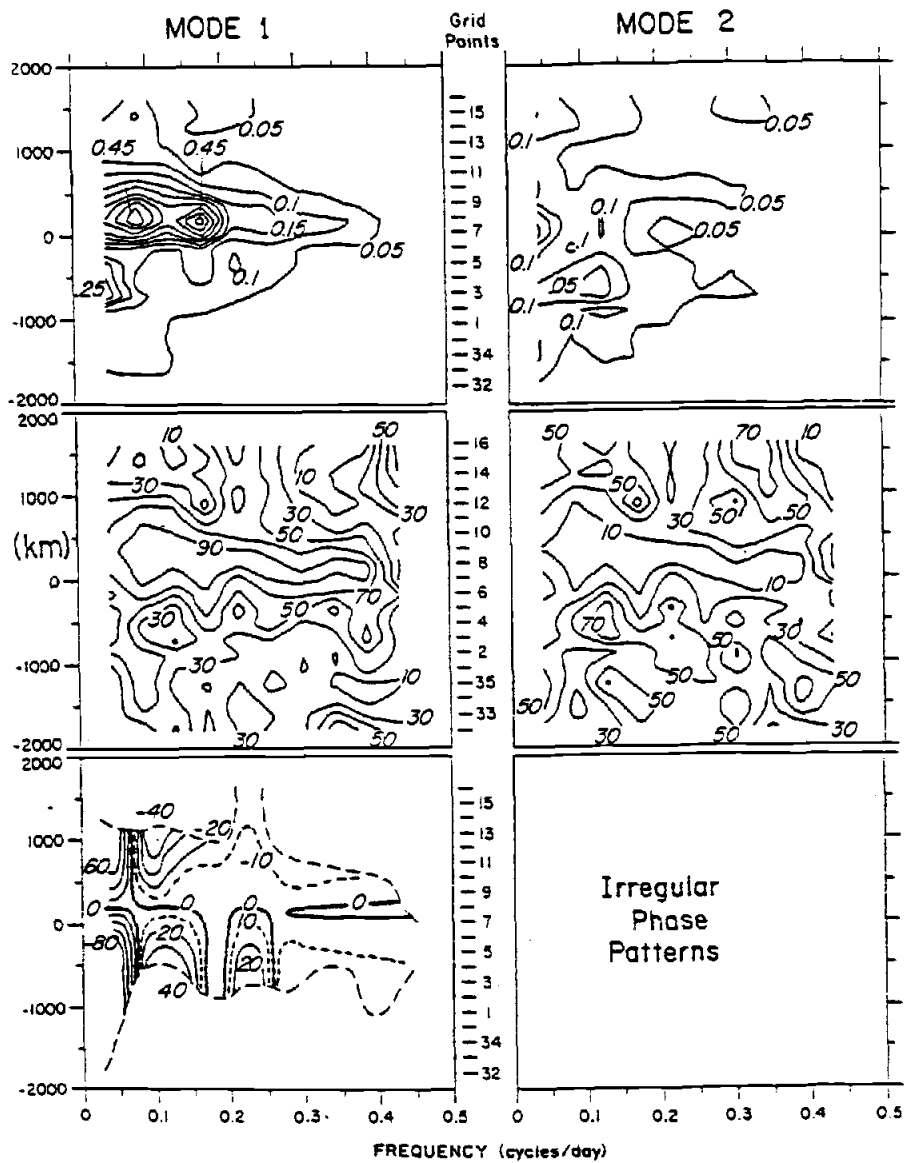


Fig. II.10: As in Fig. II.9 for the two most significant frequency-domain EOFs of calculated τ .

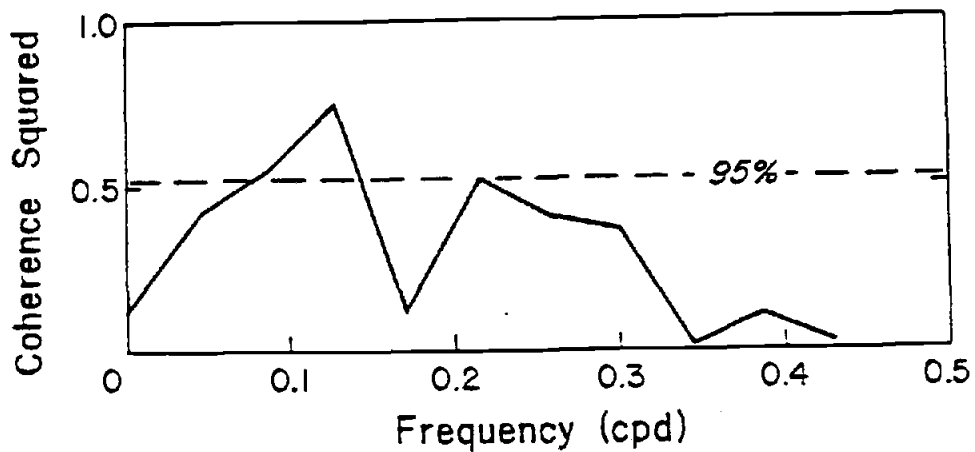


Fig. II.11: Coherence squared between the northern frequency-domain EOF of gridded ζ and the most significant frequency-domain EOF of calculated τ . The frequency bandwidth is 0.043 cpd, resulting in 10 degrees of freedom. The 95% significance level is shown.

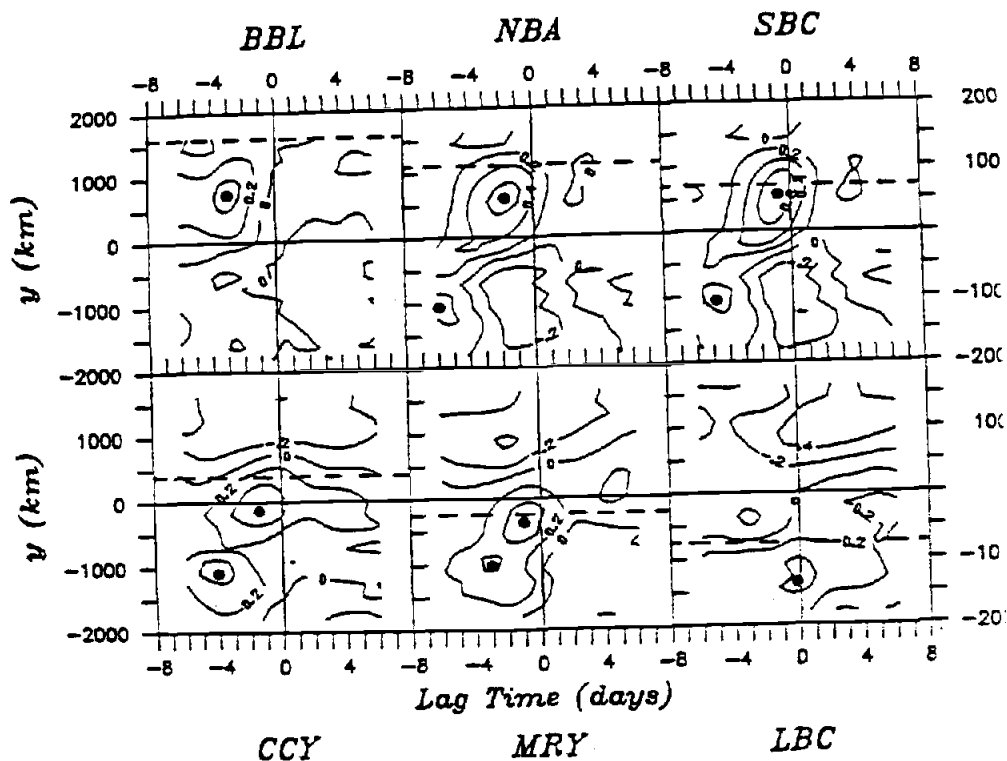


Fig. II.12: Contours of the space and time lagged correlation of ζ at each of six selected measurement stations with calculated τ at all grid points. The alongshore location of the ζ stations are shown by the horizontal dashed lines; therefore, the correlations are spatially lagged with respect to these lines. The alongshore locations and lag times of the correlation maxima at the two forcing regions are shown by the solid dots. Lag distances and lag times for these maxima are summarized in Table II.6. The integral time scales (Davis, 1976) vary for different time series: in general, statistically significant cross-correlations between ζ and τ are ≥ 0.33 to a 95% level of confidence.

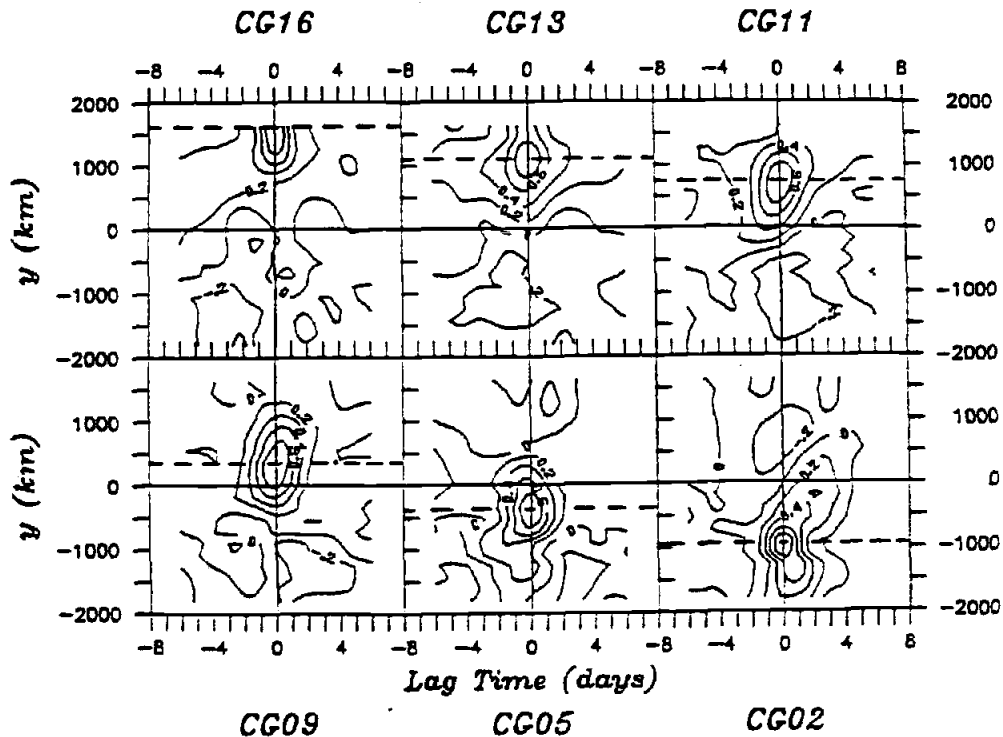


Fig. II.13: Contours of the space and time lagged correlation of calculated τ at each of the six grid points nearest to the six ζ stations in Fig. II.12 with calculated τ at all grid points. The alongshore locations of the grid points are shown by the horizontal dashed lines; therefore, the correlations are spatially lagged with respect to these lines. Statistically significant correlations are ≥ 0.32 to a 95% level of confidence.

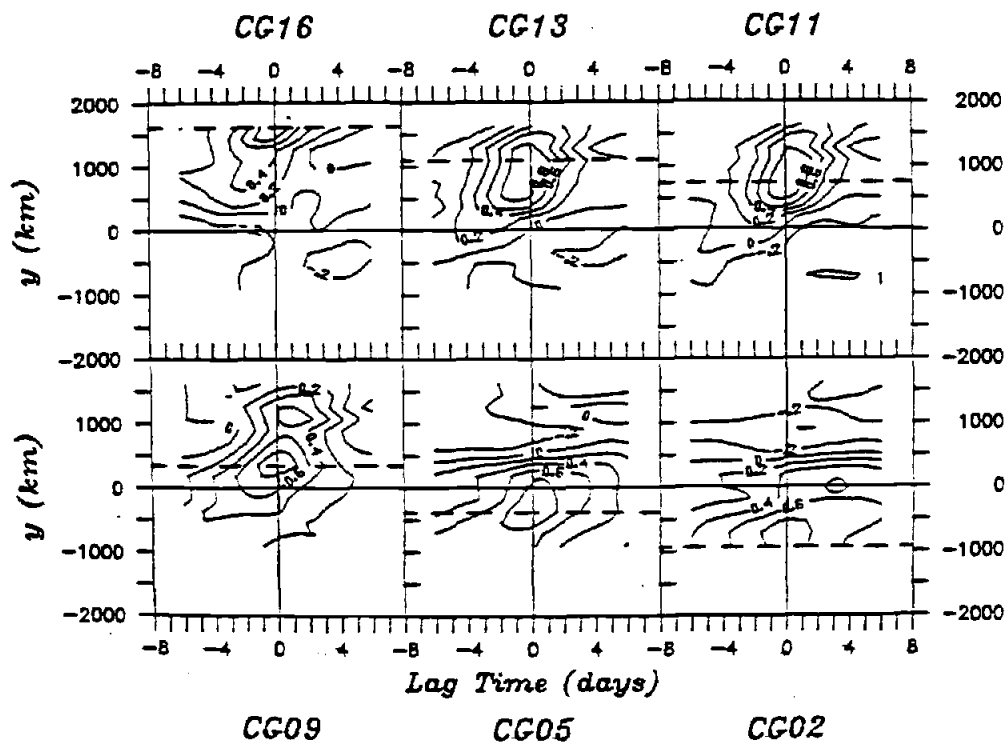


Fig. II.14: As in Fig. II.13 for gridded ζ . Statistically significant correlations are ≥ 0.38 equatorward of CCY and ≥ 0.32 poleward of CCY to a 95% level of confidence.

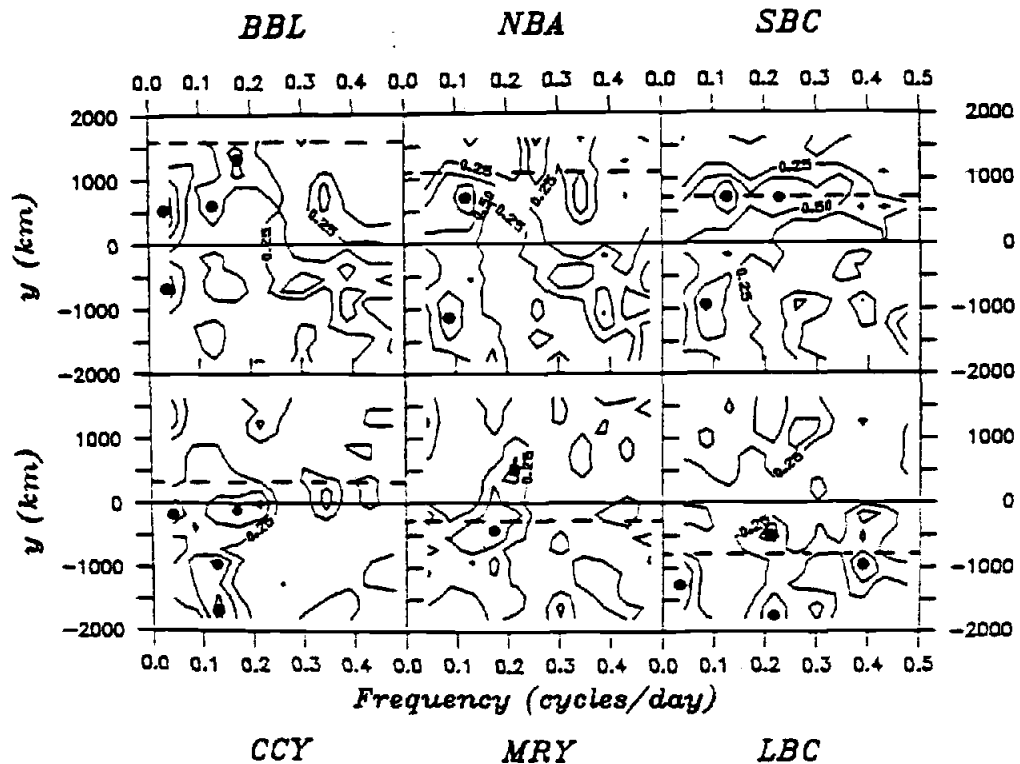


Fig. II.15: Contours of the space lagged coherence squared of ζ at the six measurement stations used in the correlation analysis with calculated τ at all grid points. The alongshore locations of the ζ stations are shown by the horizontal dashed lines; therefore, the coherences are spatially lagged with respect to these lines. The alongshore locations and frequencies of the coherence maxima at the two forcing regions (see Fig. II.12) are shown by the solid dots. The frequency bandwidth is 0.043 cpd, resulting in 10 degrees of freedom. Squared coherences of 0.52 are statistically significant to a 95% level of confidence. The contour interval is 0.25.

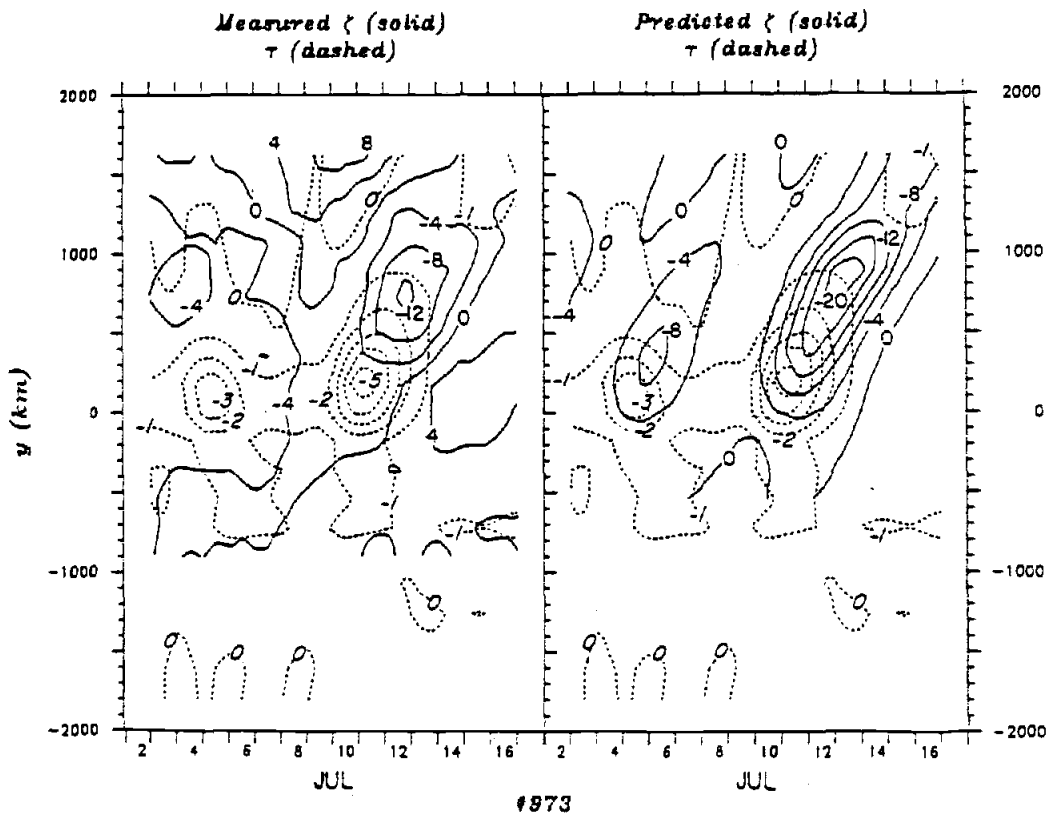


Fig. II.16: Space-time contours of six-hourly calculated τ in dy cm^{-2} (dashed) and six-hourly gridded z in cm (solid) for 3 July through 19 July 1973, spanning τ events 4 and 5. The observed z response to τ is shown on the left, and the response predicted by (II.7.2) is shown on the right.

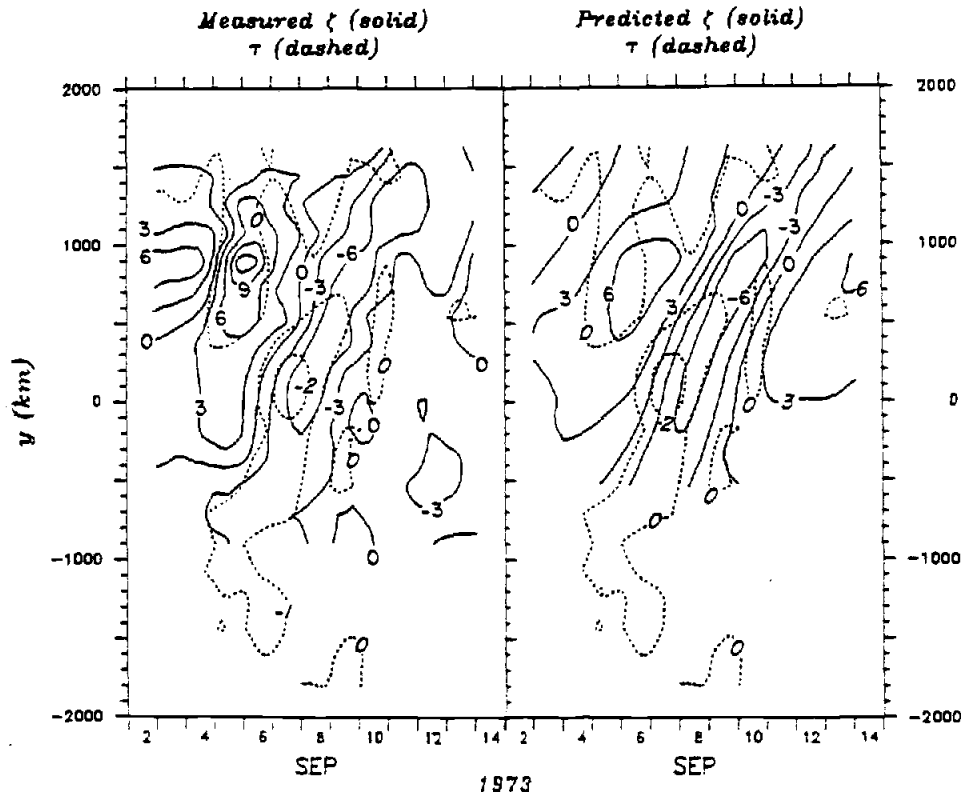


Fig. II.17: As in Fig. II.16 but for the time interval of 3-13 September 1973, spanning τ event 11. Also shown is a preceding τ event (not numbered in Fig. II.3) which forced the large ζ maximum on 5 and 6 September.

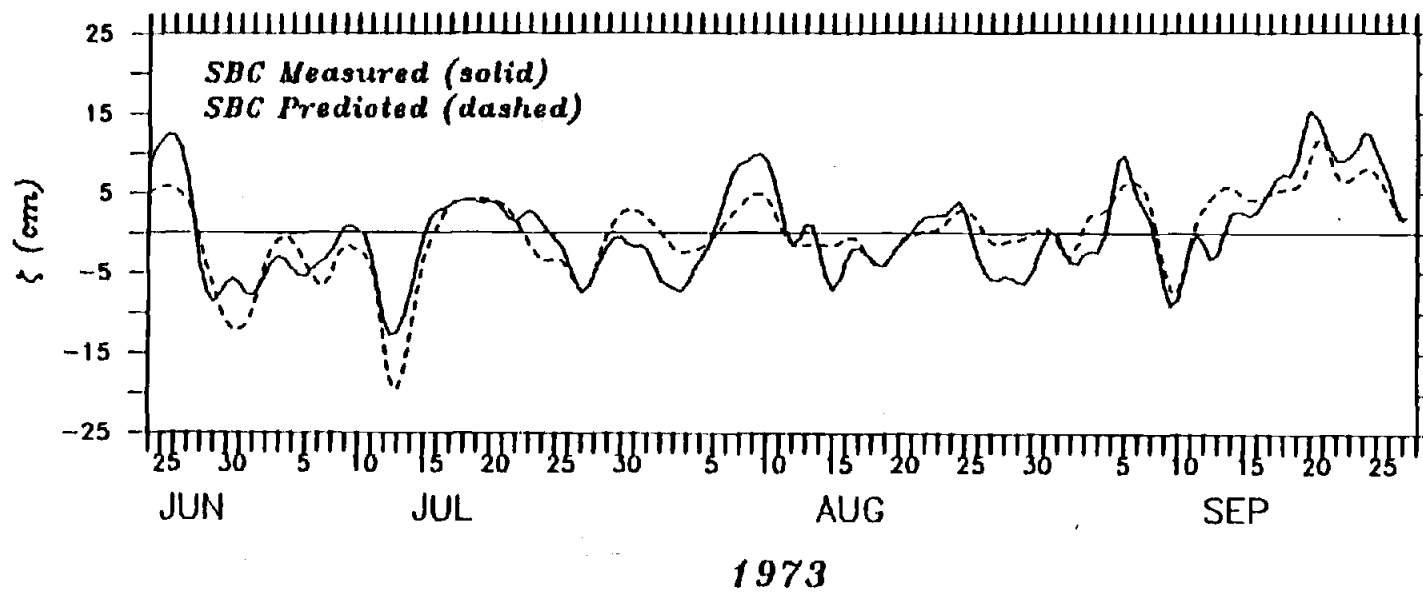


Fig. II.18: Time series of measured and predicted ζ at SBC.

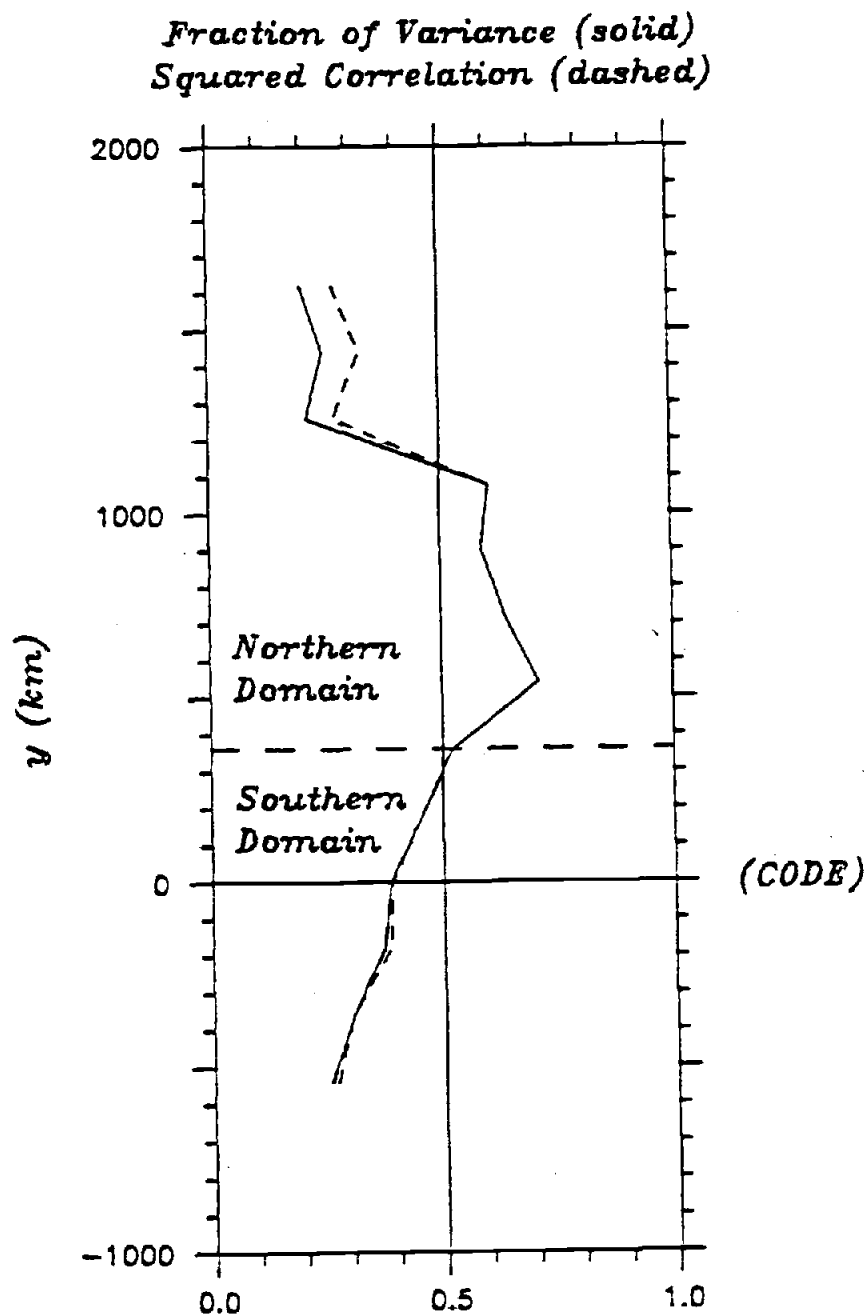


Fig. II.19: The fraction of the total variance of gridded ζ explained by the prediction from (II.7.2) (solid line) and the squared correlation coefficients between measured and gridded ζ (dashed line). The squared correlation is greater than the fraction of variance explained because a single transfer coefficient b was obtained by maximizing total variance explained at four stations along the Oregon and Washington coasts.

CHAPTER III

The Large-scale Coastal Wind Field Along the
West Coast of North America, 1981-82

ABSTRACT

We study the statistical properties of the coastal wind field along the west coast of North America for two summers, 1981 (CODE-1) and 1982 (CODE-2), and the intervening winter using measured winds and geostrophic winds calculated from FNOC atmospheric pressure analyses. Summer wind fluctuations are driven primarily by the interaction between two relatively stationary pressure systems, the North Pacific subtropical high and southwest U.S. thermal low, and by their interactions with propagating atmospheric systems to the north. In particular, propagating cyclones and associated fronts are often followed by a northeastward intensification of the high, producing strong upwelling events along the California coast. This summer event sequence occurs more frequently, and is displaced farther to the south on average, during summer 1981. Winter wind fluctuations are primarily driven by propagating cyclones and anticyclones, and they tend to have larger variance and space scales than in summer. A preference for poleward (equatorward) propagation exists in summer (winter), and the largest time scales are observed in summer 1982. Coastal atmospheric boundary layer processes substantially modify

winds within 100-200 km of the coast. Consequently, measured wind fluctuations are strongly polarized in the alongshore direction, and have means and rms amplitudes that can vary considerably between nearby stations along the coast. Calculated wind fluctuations are less polarized in the alongshore direction, and have alongshore correlation scales about 60% larger, than for measured winds. They represent fluctuations with alongshore wavelengths ≥ 900 km rather well, but poorly represent those with smaller wavelengths and those due to coastal atmospheric boundary layer effects.

III.1 INTRODUCTION

A major goal of the large-scale component of the Coastal Ocean Dynamics Experiment (CODE) is to study the large-scale response (alongshore scales \gg shelf/slope width) of continental shelf currents and coastal sea level to atmospheric forcing along the west coast of North America. The alongshore component of wind stress is an important forcing mechanism for this response, which in simple theories takes the form of forced coastally trapped waves (Gill and Schumann, 1974; Clarke, 1977). The large-scale wind fluctuations that effectively drive this current and sea level response (Halliwell and Allen, 1986b) are primarily caused by synoptic-scale atmospheric pressure systems (cyclones and anticyclones) that have space scales larger than several hundred kilometers and time scales longer than about 2 days. Execution of

CODE large-scale component studies therefore requires coastal wind data to be collected along several thousand kilometers of the west coast of North America.

In this paper, we study the properties of large-scale coastal wind fluctuations during the two intensive field experiments CODE-1 (summer 1981) and CODE-2 (summer 1982), and during the intervening winter. We focus on properties that are important for driving coastal currents, and document seasonal variations of these properties. In summer, large-scale wind fluctuations are driven primarily by the variable pressure gradient between two relatively stationary pressure systems: the North Pacific subtropical high, typically located between 20° and 50° N over the eastern North Pacific, and the interior thermal low which is normally centered over the southwestern U.S. These wind fluctuations can be substantially modified in the coastal atmospheric boundary layer over the continental shelf and slope (Beardsley, et al., 1986; Mass, et al., 1986; Dorman, 1985, 1986). In summer, a strong temperature inversion caps a surface layer of cool marine air within the domain of the North Pacific subtropical high (Neiburger, et al., 1961). The inversion layer slopes downward toward the coast and intersects the coastal mountains throughout most of the CODE large-scale domain. This blocks the across-shore component of low-level winds, inhibiting geostrophic adjustment to the near-surface atmospheric pressure field when isobars are not parallel to the coast. Coastal winds can therefore have a

substantial ageostrophic component, and coastally trapped baroclinic pressure and wind fluctuations may exist. In winter, coastal wind fluctuations are driven primarily by propagating pressure systems (cyclones and anticyclones), and the existence of the marine inversion layer is often interrupted by the strong winds generated by these systems (Neiburger, et al., 1961; Beardsley, et al., 1986). Consequently, seasonal cycles in the properties of both synoptic-scale atmospheric pressure systems and the coastal marine boundary layer contribute to the observed seasonal changes in coastal wind properties.

We analyze two representations of the coastal wind field: The first is a set of wind measurements from stations located at or near the coast and from buoys moored on the adjacent continental shelf. The second is a set of geostrophic winds calculated from the six-hourly surface atmospheric pressure analyses of the Fleet Numerical Oceanography Center (FNOC) (Bakun, 1975), which are hereafter referred to as calculated winds. A simple boundary layer correction is performed on these winds, consisting of a 30% reduction in speed and a 15° anticlockwise rotation. The data from which the pressure analyses are constructed are sampled at both ships and fixed land and buoy stations. This input data consists of both surface pressure and equivalent pressure gradient calculated from surface winds assuming geostrophic balance. These data are blended with an initial best-guess surface pressure field determined from previous analyses to generate the new pressure

analysis. This procedure is described in detail by Holl and Mendenhall (1972).

Measured winds should ideally be used to calculate the wind stress forcing function for shelf currents, but they have numerous problems, including topographic influence, data gaps, irregular sampling times, and sometimes human subjectivity in reading fluctuating anemometer analog displays. The problems with calculated winds include a spatial sampling resolution that restricts their use to studies of large-scale variability only, decreasing accuracy in the geostrophic approximation with decreasing latitude, variable spatial and temporal coverage with ship pressure and wind observations, and an inaccurate boundary layer correction in coastal regions (Section III.2.2; Halliwell and Allen, 1984). We therefore analyze both wind sets to characterize the large-scale, low-frequency properties of the coastal wind field. We also compare both wind sets with each other to assess the differences between their properties. The evaluation of the two wind sets as atmospheric forcing functions is presented in our studies of the coastal sea level response to wind stress (Halliwell and Allen; 1984, 1986b).

We first describe the data sets and discuss the boundary layer correction for calculated winds (Section III.2). We present the basic statistical properties of the coastal wind field, emphasizing interannual and seasonal similarities and differences (Section III.3). We document frequency domain and

wavenumber-frequency domain properties of wind fluctuations using spectrum analysis (Section III.4). We relate these statistical properties to those of wind events and synoptic-scale atmospheric systems by studying alongshore-time contour plots of calculated and measured winds and surface atmospheric pressure charts (Section III.5). We focus primarily on the properties of the alongshore component of the wind, since this is theoretically the most important component for driving large-scale coastally trapped waves, and since Halliwell and Allen (1984) noted that the component of measured vector wind stress within the CODE large-scale domain that is most correlated with sea level is oriented approximately alongshore. Analyses of the vector and across-shore winds are also presented wherever they illustrate important properties of the wind field.

III.2 THE DATA SET

III.2.1 Data and Data Processing

The CODE large-scale analysis domain extends from northern Baja California (26°N) to the Alaska border (54°N) to resolve the large alongshore scales of the wind field and the coastally trapped wave response. The coastal alongshore coordinate y is zero at the location of the CODE central line and positive poleward of that location. We use calculated winds that are interpolated to the locations of the CODE analysis grid (Fig. III.1, Table III.1), with

grid point 7 located at $y = 0$ km. The alongshore separation of the grid points is 180 km, and the grid spans 3600 km of coastline. The CODE experimental site (Winant, et al., 1986) is located approximately within the interval $-50 < y < 50$ km. Alongshore separations are estimated from coastal charts by measuring the distance following a smoothed shoreline, i.e., by ignoring deviations due to small bays and headlands that span less than about 20 km of coast.

We study three time intervals of four months duration:

1. 1200Z 3 April to 1800 Z 31 July 1981 (119.5 days),
2. 0000Z 1 December 1981 to 1800Z 31 March 1982 (121 days),
and
3. 0000Z 1 May to 1800Z 31 August 1982 (123 days).

The first four-month interval was shortened by 2.5 days at the beginning because of missing data. We refer to these intervals as summer 1981, winter 1981-82, and summer 1982. The two summer seasons are chosen both to coincide with the intensive instrument deployments of the CODE-1 and CODE-2 experiments (Winant, et al., 1986) and to span the period of strongest coastal upwelling. Therefore, the seasonal differences in wind field properties that we document in this study represent those between the periods of strongest upwelling and strongest downwelling over the continental shelf. The winter season is essentially centered about the period of strongest winter storminess in the atmosphere, but the two summer seasons are not centered on the summer minimum in

storminess. Consequently, we do not document the full seasonal range of properties of the coastal wind field in this study.

Measured winds are available at over 70 locations along the coast during the CODE experiment. These measurements are obtained from numerous sources, with information about them, including discussions of the editorial procedures used and the basic statistical properties of all of the data, documented in Halliwell and Allen (1983, 1985) and Halliwell, et al. (1986). The basic editorial steps performed on both measured and calculated winds include conversion of winds to north-south and east-west (u and v) components, conversion to common units of m s^{-1} , and deletion of obviously bad data points. All gaps less than 12 hr in length are filled by linear interpolation. The resulting time series are low-pass filtered (half-amplitude period = 40 hr) and have a sampling rate of six hours. Linear trends are removed from the time series prior to performing all statistical analyses.

We select the subset of wind measurement stations analyzed in this study by choosing the best possible stations that have alongshore separations as close as possible to the separation between CODE grid points ($\Delta y = 180 \text{ km}$). National Data Buoy Center (NDBC) offshore buoy winds are used wherever possible. For the remaining stations, the best are identified by studying the basic wind statistics to determine if local effects, such as topography, influence the wind, then by comparing measured and calculated winds under the assumption that the measured winds best correlated with

calculated winds are least influenced by local effects. The alongshore spacing of the selected stations is reasonably good along the U.S. coast, but is too large along the British Columbia coast because of an insufficient number of good stations (Fig. III.1 and Table III.2). Due to the presence of long data gaps, the identical set of stations could not be used for all three seasons. Several shorter gaps in the selected stations have been filled by linear regression from nearby stations not used in the analyses:

1. GRH, 06Z 22 August to 18Z 31 August 1982, filled using HOQ,
2. CCY, 00Z 1 May to 06Z 5 May 1982, filled using PSG,
3. B22, 00Z 1 December 1981 to 06Z 21 January 1982, filled using ACA, and
4. B12, 06Z 24 January to 18Z 31 March 1982, filled using FIG.

The additional stations used in these interpolations are also listed in Table III.1. For the integral correlation space and time scale analysis in Section III.3.6 and the wavenumber-frequency spectrum analyses in Section III.4.2, measured wind components are interpolated to the CODE large-scale analysis grid by a cubic spline interpolation in the alongshore direction at each sampling time.

III.2.2 The Rotation Correction for Calculated Winds.

Several studies have determined that the 15° anticlockwise rotation performed as part of the original boundary layer correction is not sufficient. These include the study of Halliwell and Allen (1984) for the west coast of North America, plus the wind analyses of Thomson (1983) for the British Columbia coast and Hsueh and Romea (1983) for the East China Sea. (Hsueh and Romea calculated geostrophic winds using pressure from surface meteorological charts.) Because of this, Halliwell and Allen (1984) rotated calculated winds to align their fluctuations with those of measured winds prior to calculating the alongshore component of the calculated winds. Since we have assembled a much-improved measured wind set for the CODE study that also includes winter measurements, we recalculate the rotation corrections here and determine if they have seasonal variability. This correction was performed prior to computing the along- and across-shore components of the calculated winds used in these analyses. However, all analyses of calculated vector wind components u and v , which include basic statistics, principal axes, complex correlations, and rotary auto- and cross-spectra, are performed using the original, uncorrected winds, since the effects of the misalignment between calculated and measured wind fluctuations are directly recovered by these analyses.

We estimate the rotation correction at a grid point for each of the three seasons by calculating complex inner correlation coefficients between the calculated wind at that point and all available measured winds that are within ± 90 km alongshore and have at least 50% good data. The inner phases of the complex correlation coefficients, which measure the average misalignment between fluctuations of two vector series (Kundu, 1976), are then averaged over all measurement stations near each grid point where the winds are significantly correlated with the calculated wind. At least one good measurement station is available near grid points 2 through 17, excluding point 14 (Fig. III.2). Since we rotate calculated winds by the negative of the inner phase to align with measured winds, we refer to the negative of these averaged inner phases as the rotation correction for calculated winds.

The rotation corrections calculated here have values similar to those calculated for summer 1973 (Halliwell and Allen, 1984), and the estimates along the British Columbia coast are consistent with the observations of Thomson (1983). They are positive throughout the CODE large-scale domain in all three seasons, indicating that calculated winds must be rotated anticlockwise, and they fluctuate in magnitude between about 5° and 50° over alongshore scales of a few hundred kilometers (Fig. III.2). Seasonal differences are small, so we average the rotation corrections for all three seasons at each grid point (Fig. III.2, right panel), then rotate the calculated winds by these averaged

angles. For grid point 14, we linearly interpolate the correction between points 13 and 15 (Fig. III.2). For grid points 32 to 35 and 1, we use the correction angle of 45° , which is approximately the average observed within the Southern California Bight at points 2 and 3. Because of this uncertainty in the correction along the Baja California coast, we do not use calculated alongshore winds equatorward of grid point 2 in any analyses that quantify the space-time properties of the wind fields throughout the CODE large-scale domain.

III.3 BASIC STATISTICAL PROPERTIES OF THE WIND FIELD

III.3.1 Seasonal Means

In summer, calculated and measured wind vector means (Fig. III.3) point primarily alongshore and equatorward south of the Oregon-Washington border (46°N). During summer 1981, they point increasingly onshore with increasing y poleward from this border, pointing almost directly onshore at the northern end of the CODE large-scale domain. This anticyclonic mean flow pattern essentially outlines the northeastern and eastern side of the North Pacific subtropical high. During summer 1982, the vector means point approximately alongshore and equatorward everywhere along the coast, primarily because the subtropical high extends farther to the north on average than it did during summer 1981 (Section III.5). Measured and calculated wind vector means point

in roughly the same direction throughout the domain, except in the Southern California Bight (32° to 34.5° N). Calculated wind vector means tend to vary smoothly along the coast in both amplitude and direction, while those for measured wind vary more irregularly.

Both wind sets have the largest vector mean amplitudes $(\langle u \rangle^2 + \langle v \rangle^2)^{1/2}$, where angle brackets $\langle \rangle$ denote time average, along the California coast south of Cape Mendocino (40° N), with the exception of measured winds in the Southern California Bight.

The summer calculated alongshore wind means (Fig. III.4) are relatively large and negative (equatorward) along nearly the entire California coast ($-1000 < y < 400$ km), while the same is true for the measured winds only between Cape Mendocino ($y \approx 200$ km) and Point Conception ($y \approx -550$ km). These maxima are more distinct during summer 1981 than during summer 1982. The measured means are sharply reduced in the Southern California Bight ($-1000 < y < -550$ km) compared to those poleward of the Bight in both summers. The mean equatorward alongshore wind tends to decrease less rapidly with increasing y poleward of California ($y > 400$ km) during summer 1982 because the subtropical high extends farther to the north on average than it did during summer 1981 (cf. Fig. III.3).

In winter, the directions of calculated and measured vector means point northward (southward) to the north (south) of the CODE experimental site (Fig. III.3). The calculated wind vector mean amplitudes exceed those of the measured wind everywhere except near the latitude of the reversal. The measured wind vector mean

amplitudes are generally smaller in winter than in summer throughout the domain, but those of the calculated winds are larger in winter than in summer to the north of the California-Oregon border (42°N). The measured and calculated wind vector means tend to point in the same direction throughout the domain, including the Southern California Bight (32° to 34.5°N). A major winter discrepancy exists near CSJ (52°N), where the CSJ mean points toward the east while the calculated wind mean at grid point 17 is substantially stronger and points toward the northwest.

The measured alongshore wind means in winter change sign near the site of the CODE experiment, while calculated means change sign about 200 km equatorward of the site (Fig. III.4). The calculated means change gradually between the California-Oregon border ($y \approx 400$ km) and northern Baja California ($y < -1000$ km), but the measured means change sign more abruptly near the CODE site. Measured means are substantially smaller than calculated means except near the location of the wind reversal. Unlike in summer, measured means within the Southern California Bight ($-1000 < y < -550$ km) are similar to measured means poleward of the Bight.

III.3.2 Seasonal RMS Amplitudes

In summer, rms principal axis ellipses (Fig. III.5) demonstrate that the measured wind fluctuations are strongly polarized in the alongshore direction, with the greatest

polarization located along the California coast poleward of Point Conception (34.5°N to 42°N). The calculated winds (unrotated) are substantially less polarized, but the major axes still have some tendency to align along the coast. The calculated wind ellipses would have to be rotated anticlockwise to align with the measured wind ellipses at most locations along the shelf, which is consistent with the statistically determined misalignment between calculated and measured wind fluctuations (Fig. III.2). One notable exception to this is at NEW (44.6°N) (Fig. III.5), where the major axis of the measured wind has a substantial across-shelf component, possibly due to local topography in the Yaquina Bay area. However, caution must be exercised in comparing measured and calculated wind principal axis ellipses since measured winds are constrained to fluctuate primarily in the alongshore direction by coastal mountain barriers, while calculated winds are not. The calculated wind vector rms amplitudes $[\langle(u-\langle u \rangle)^2\rangle + \langle(v-\langle v \rangle)^2\rangle]^{1/2}$ generally decrease from north to south by a factor of two within the large-scale domain, which is a pattern substantially different from that of the mean wind (Fig. III.3). (We hereafter refer to wind rms amplitude simply as wind amplitude.) The measured wind vector amplitudes vary more irregularly along the coast, and are relatively large between Cape Mendocino (40°N) and Point Conception (34.5°N) during both summers.

The summer calculated alongshore wind amplitudes (Fig. III.4) decrease by nearly a factor of three from north to south. A

relative maximum exists near Cape Mendocino ($y \approx 200$ km) during summer 1982. For measured alongshore winds, the amplitudes are relatively large between Cape Mendocino and Point Conception ($y \approx -550$ km). They are larger than those for calculated winds within this subdomain in both summers, but the difference is substantially larger in summer 1982. Outside of this subdomain, the measured wind amplitudes are about equal to or less than those of the calculated winds, except at CSJ ($y = 1760$ km).

In winter, the measured and calculated wind fluctuations are substantially less polarized than in summer (Fig. III.5), resulting largely from the passage of stronger synoptic-scale atmospheric systems (Section III.5) that can drive stronger across-shore winds past the coastal mountain barrier. The measured wind major axes are oriented in the alongshore direction, except at NEW (44.6°N), where the orientation is the same as in summer, and at GRH (46.9°N), where the across-shore winds are more energetic than the alongshore winds, probably due to the relatively low coastal mountain barrier at that location. Other than at GRH, there is generally little difference between winter and summer in both the measured and calculated wind major axis orientations. As in summer, the calculated winds are less polarized than the measured winds, and the major axes of the calculated wind ellipses tend to be rotated clockwise from those of the measured winds. The calculated wind vector amplitudes are larger than those of the measured wind everywhere, are larger everywhere in winter than they

are in summer, and decrease by a factor of three from north to south, with most of the decrease occurring equatorward of Cape Mendocino (40°N). Measured wind vector amplitudes have a relative maximum between Cape Mendocino and Point Conception (34.5°N), which was also observed for the two summers.

The winter calculated alongshore wind amplitudes (Fig. III.4) decrease from north to south by a factor of three between the relative maximum centered near Cape Mendocino ($y \approx 200 \text{ km}$) and the southern end of the CODE large-scale domain. The measured wind amplitudes are relatively large between Cape Mendocino and Point Conception ($y \approx -550 \text{ km}$), where they approximately equal those of the calculated winds. Elsewhere, the measured wind amplitudes are substantially smaller than those of the calculated winds, except at CSJ ($y = 1760 \text{ km}$).

III.3.3 The Coastal Boundary Layer Influence on Wind Properties

The mean and rms amplitude of coastal measured wind fluctuations vary considerably over scales small compared to synoptic-scale atmospheric pressure systems. Most of this variability can be attributed to several coastal atmospheric boundary layer processes, not all of which are independent. We now qualitatively discuss the effects of these processes, and how they probably contribute to the observed differences in measured and calculated wind statistics.

The coastal mountain blocking causes wind measurements to be strongly polarized in the alongshore direction. Although they are not directly affected by this blocking, calculated winds are still polarized in roughly the alongshore direction after the additional boundary layer rotation is made (Section III.2.2), but not as strongly as measured winds. Other processes may therefore contribute to the preference for alongshore polarization. For example, surface isobars in summer tend to parallel the coast between the subtropical high and thermal low (see Section III.5), so fluctuations in the strength of these systems will cause wind to fluctuate primarily in the alongshore direction. However, calculated winds remain slightly polarized in the alongshore direction in winter, so this seasonal pattern does not fully explain the polarization.

The presence of coastal mountains and a stratified atmosphere allows pressure and wind fluctuations to exist at scales substantially smaller than those of synoptic-scale systems. For example, poleward-propagating coastally trapped pressure fluctuations with across-shore scales of 100-200 km (Dorman, 1985, 1986; Mass, et al., 1986) can exist, the effects of which we discuss in Sections III.4 and III.5. Other dynamical processes permit the existence of pressure and wind fluctuations that have spatial scales equal to or smaller than the shelf width [$O(1)$ to $O(10)$ km]. For example, Beardsley, et al. (1986) and Friehe and Winant (1982, 1984) observe changes in wind speed of more than a

factor of 3, and changes in wind direction of more than 20° , over spatial separations of several kilometers on the continental shelf at the CODE site during CODE-1 and CODE-2. Also, when the spring/summer equatorward winds blow, some regions of relatively strong or weak winds tend to persist in the same locations. Consequently, the amplitude of measured wind fluctuations is probably sensitive to small changes in the location of a station.

The measured wind data set consists of a mixture of coastal land stations and offshore buoys, and three boundary layer processes may contribute to differences between these winds. Surface friction is larger over land than over water, so the measured land winds at the coast will tend to have smaller amplitude than those over water. Also, the topography at the coast may locally steer the wind, affecting both speed and direction. Brink, et al. (1984) note that winds at the coast near Point Conception ($y = -550$ km) tend to be stronger near headlands than at other alongshore locations. Finally, the diurnal (land breeze-sea breeze) cycle can influence daily-averaged wind velocity, since the daytime sea breeze and nighttime land breeze velocities are usually not equal, and this will affect seasonal mean winds. Low-frequency wind fluctuations may be affected since low-frequency changes in the strength of the diurnal cycle exist at the CODE site (Beardsley, et al., 1986). The diurnal cycle at the CODE site is strong at coastal land stations, but weak at buoys on the outer continental shelf, and may therefore contribute to the observed

differences between land and offshore winds. We therefore expect that the observed alongshore changes in measured wind statistics are influenced by the mixture of land stations and offshore buoys.

With so many processes influencing measured winds within the coastal atmospheric boundary layer, measured wind amplitudes differ substantially from those of calculated winds at many locations along the coast, and it is difficult to determine a consistent alongshore distribution of wind amplitude. For example, relatively large measured wind amplitudes exist in both summer and winter between Cape Mendocino ($y \approx 200$ km) and Point Conception ($y \approx -550$ km), but this regional maximum does not appear in the calculated winds. This maximum may be partly enhanced in all seasons because most of the measurements in this region are from offshore buoys. However, the few coastal stations in the region (SUR for all three seasons and ARL and DIA during winter 1981-82) all have larger fluctuations than the coastal stations outside of the region, indicating that this maximum in the measured wind field is at least partly real. Also, the dominance of land stations in the northern part of the CODE large-scale domain may be at least partly responsible for the reduced measured wind amplitudes there. For example, QUI ($y = 1055$ km), where wind amplitude is relatively small, is located several kilometers inland.

III.3.4 Can Land Winds be Adjusted to Equal Offshore Winds?

We determine if it is possible to adjust winds at land stations to equal winds offshore. Based on land and sea wind measurements from several coastal regions (not including the continental shelf in the CODE large-scale domain), Hsu (1981, 1986) recommends that coastal land vector wind speed be adjusted by the following formula to represent offshore vector wind speed:

$$\hat{U}_O = 1.62 + 1.17U_L, \quad (\text{III.3.1})$$

where U_L is the measured land speed and \hat{U}_O is the estimated offshore speed, all in units of m s^{-1} . This relationship is tested in all three seasons by regressing offshore buoy wind speed on nearby coastal wind speed in the CODE large-scale domain (Table III.3). The additional stations used in this comparison are listed in Table III.1. The regression coefficients vary substantially along the coast for a given season, and vary substantially between summer and winter and also between both summers. Calculating the mean of all regression coefficients listed in Table III.3, we obtain

$$\hat{U}_O = 2.19(\pm 1.35) + 1.00(\pm 0.38)U_L, \quad (\text{III.3.2})$$

with the standard deviations given in parentheses, and with \hat{U}_O and U_L given in m s^{-1} . Although these coefficients are statistically indistinguishable from those recommended by Hsu (1986), we do not correct our coastal land winds using this formula

because of both the large uncertainty in the coefficients and the apparent variability of the coefficients in space and time.

We also test if we can simply adjust the rms amplitudes of coastal land alongshore winds by a constant factor to represent offshore alongshore winds. A tabulation of the ratios of the alongshore wind amplitudes at offshore stations to those of nearby coastal land stations for the three seasons (Table III.3) reveals that they also vary with both alongshore location and time. For example, near Point Conception (represented by stations B11-DIA), wind amplitude is slightly smaller offshore in summer and larger offshore in winter, and the ratio is smaller during summer 1982 than summer 1981. In contrast, the wind amplitudes along the California coast between Monterey and the CODE site (represented by stations C3-SRA, B13-BML, and B12-PIL) are larger offshore during all seasons, and the ratios are substantially larger during summer 1982 than during both summer 1981 and the intervening winter, especially near the CODE site (C3-SRA). As a result, we cannot simply adjust coastal land alongshore wind amplitudes by a constant factor to represent offshore alongshore winds.

The inability to devise a simple correction for land winds may be caused by factors such as the large-amplitude, small-scale structure observed in the wind field (Beardsley, et al., 1986) and the topographic influence on coastal land winds. The small-scale structure may have a seasonal cycle caused by seasonal cycles in synoptic-scale atmospheric variability and in the properties of the

coastal marine boundary layer.

III.3.5 Effects of the RMS Amplitude Distribution on Statistical Analyses

The different representations of wind amplitude along the coast provided by the measured and calculated wind fields can have a major effect on some statistical analyses. Consider a true wind field $v(y,t)$, with zero mean at all y and the rms amplitude distribution $s(y) = \langle v^2(y,t) \rangle^{1/2}$. Now consider a sample of this wind field, $\hat{v}(y,t)$, that differs from the true field only in rms amplitude distribution $\hat{s}(y) = \langle \hat{v}^2(y,t) \rangle^{1/2}$. The sampled wind field is then given in terms of the true field by $\hat{v}(y,t) = \xi(y)v(y,t)$, where $\xi(y) = \hat{s}(y)/s(y)$. The function $\xi(y)$ represents the y -dependent error ratio in the rms amplitudes of the sampled wind field, which differs substantially between the calculated and measured wind fields. These amplitude errors will affect the results of many of our statistical analyses, and since we cannot correct for them, we must attempt to understand how they influence the interpretation of these analyses.

We employ the following strategy to accomplish this: We form an additional data set by adjusting the measured wind amplitude at each station to equal the calculated wind amplitude at that alongshore location. Defining the mean measured alongshore winds as

$$\bar{v}_m(y) = \langle v_m(y, t) \rangle, \quad (\text{III.3.3})$$

we then define

$$v_a(y, t) = \xi_{cm}(y)(v_m(y, t) - \bar{v}_m(y)) + \bar{v}_m(y), \quad (\text{III.3.4})$$

with

$$\xi_{cm}(y) = \frac{s_c(y)}{s_m(y)}, \quad (\text{III.3.5})$$

where v_m and v_a are the measured and adjusted measured winds, and s_c and s_m are the calculated and measured wind rms amplitudes. We linearly interpolate s_c alongshore to the location of the measurement stations. We use the vector rms amplitude $[\langle (v_e - \langle v_e \rangle)^2 \rangle + \langle (v_n - \langle v_n \rangle)^2 \rangle]^{1/2}$, where v_e and v_n are east and north wind components, to calculate $\xi_{cm}(y)$ for adjusting vector winds. We also form additional data sets by normalizing both the measured and calculated winds to unit amplitude. Analyses are performed for measured winds, adjusted measured winds, normalized measured winds, calculated winds, and normalized calculated winds. The results of these analyses are then compared to determine what part represents true features of the wind field and what part represents the influence of changes in the alongshore distribution of wind amplitude. For all analyses, we present the results for measured and calculated winds. For the analyses influenced by wind amplitudes, we also present the results for adjusted measured

winds, and occasionally present the results for normalized winds. Adjusting measured wind amplitudes to equal those of calculated winds does not mean that we believe calculated winds better represent the true wind amplitudes along the coast. We do this only to assess the impact of changing the alongshore distribution of wind amplitude, and hence the impact of rms amplitude errors in the calculated and measured wind sets, on our analyses.

III.3.6 Correlation Scales and Wind Field Correlations

We use the space-time averaged correlation function to estimate integral correlation space and time scales. For a wind field sampled at N evenly-spaced points, $v(y_i, t)$, $i = 1, N$, this function is given by

$$R(\eta_n, \tau) = \frac{\sum_{i=1}^J \langle v(y_i, t) v(y_i + \eta_n, t + \tau) \rangle}{\left[\sum_{i=1}^J \langle v^2(y_i, t) \rangle \right]^{1/2} \left[\sum_{i=1}^J \langle v^2(y_i + \eta_n, t + \tau) \rangle \right]^{1/2}}, \quad (\text{III.3.6})$$

where

$$\begin{aligned} I = 1, \quad J = N - n & \quad \text{for } n \geq 0, \\ I = |n| + 1, \quad J = N & \quad \text{for } n < 0, \quad |n| \leq |N - 1|, \end{aligned} \quad (\text{III.3.7})$$

η_n is the lag distance, and τ is the lag time. To calculate the integral correlation time scale, the function $R(0, \tau)$ is integrated over $\tau \geq 0$ out to the first zero crossing of R . For the space

scale, $R(\eta_n, 0)$ is integrated over η_n for $n \geq 0$ out to the first zero crossing of R . We use measured winds interpolated to the CODE grid points (Section III.2.1) in this analysis.

The correlation time scales (Table III.4) between grid points 4 and 13 typically range between 1 and 2 days. This alongshore subdomain is selected to avoid both the Southern California Bight and the poor alongshore resolution of measured winds along the British Columbia coast. The scales are similar for summer 1981 and winter 1981-82, but are substantially larger for summer 1982. Calculated winds tend to have slightly larger time scales than measured winds. Adjusting or normalizing measured wind amplitudes and normalizing calculated wind amplitudes cause only small changes in the estimated time scales. The correlation space scales (Table III.4) are typically 400 to 800 km in summer and 600 to 1000 km in winter, showing the dominance of large scales in the wind fluctuations. Calculated wind space scales exceed the measured wind scales by about 60% during all three seasons, presumably due to the poor representation of smaller-scale wind fluctuations by the calculated winds. However, even the measured wind space scales exceed the typical station spacing by a substantial margin (Fig. III.1, Table III.2), indicating that we have sampled the measured winds at sufficiently small alongshore intervals to resolve the large-scale fluctuations. Winter space scales exceed summer scales by about 20%, and changes in the space scales due to adjusting or normalizing the time series are relatively small.

The zero time-lagged spatial correlation matrices of calculated and measured alongshore winds (Fig. III.6) illustrate the alongshore dependence of spatial correlation scales. The horizontal (vertical) axes represent the alongshore locations of the columns (rows) of the matrices. These locations are evenly spaced for the CODE grid points, but not for the measurement stations. The locations of the rows and columns representing each station or grid point are shown by the tic marks on the diagonals of the matrices. To determine the correlation between a given station and stations to the south (north), start at the tic mark and follow a straight line vertically down (horizontally toward the left) from the mark. If the correlation contours bunch close to the diagonal at a given location, then winds poleward and equatorward of that location are poorly correlated with each other.

During both summers, the calculated wind correlation coefficients become insignificant (< 0.35 , see Appendix C) for spatial separations averaging between 600 and 800 km, with a tendency for this scale to decrease from north to south. During winter, the calculated wind correlation coefficients become insignificant over scales ranging from 1200 km in the north to 600 km in the south. In all seasons, correlations become insignificant over smaller spatial separations for the measured winds than for the calculated winds. The rate of decrease of correlation with spatial separation tends to vary more smoothly along the coast for calculated winds than for measured winds. The only exception to

this is during summer 1981 and winter 1981-82, where calculated winds at grid point 2 are poorly correlated with those poleward of that location, which is probably related to the large changes in coastline orientation there. During both summers, measured winds poleward of Point Conception ($y \geq -550$ km) tend to be poorly correlated with those equatorward, consistent with our observations that winds behave differently in the Southern California Bight ($-1000 < y < -550$ km). Also, measured winds poleward of the California-Oregon border ($y \geq 400$ km) tend to be poorly correlated with those equatorward.

The amplitude of the inner correlation coefficients between measured and calculated vector winds, and the correlation coefficients between measured and calculated alongshore winds (Fig. III.7), are statistically significant (> 0.35 , see Appendix C) throughout the large-scale domain in all seasons, except in the Southern California Bight during summer where only MUG ($y = -678$ km) vector and alongshore winds in 1981 are significantly correlated with the calculated winds. The alongshore winds tend to be slightly better correlated than the vector winds in all seasons, and these correlations are slightly smaller during summer 1982 than summer 1981. The phases of the vector inner correlations (not shown) are consistent with the misalignment discussed in Section III.2.2. The across-shore wind correlations (Fig. III.7) are substantially smaller in magnitude than the alongshore wind correlations in all seasons, except along the Washington coast

(near $y = 1000$ km) in summer, along the Washington and Oregon coasts in winter, and in the Southern California Bight ($-1000 < y < -550$ km) in summer. Along the California coast outside of the Bight ($-550 < y < 400$ km), the alongshore components are much better correlated than the across-shore components during both summer and winter, probably due to the blocking of the across-shore components by relatively tall coastal mountains. Within the Bight, however, the across-shore components of the two wind sets are better correlated than the alongshore components.

III.3.7 The Coastal Boundary Influence on Alongshore Wind Statistics

After correcting the calculated geostrophic winds for the boundary layer rotation, good correlations are observed between calculated and measured alongshore winds poleward of the Southern California Bight ($y \geq -550$ km). This result indicates that the coastal boundary layer primarily influences the rms amplitude of the fluctuations. In contrast, the quality of the across-shore wind component is severely affected by the coastal boundary in most of the large-scale domain, but it is probably not important in driving large-scale coastally trapped waves.

Strong coastal boundary effects must be present in the Southern California Bight in summer, since mean measured alongshore winds differ substantially from mean calculated alongshore winds, and since measured and calculated alongshore winds are poorly

correlated with each other. Measured and calculated across-shore winds are better correlated than alongshore winds there. This indicates that summer measured winds in the Bight are not closely related to gradients of the synoptic-scale atmospheric pressure field. The coastal mountains abruptly turn from a north-south to east-west orientation near Point Conception ($y \approx -550$ km), and the nearshore wind velocity consequently changes abruptly at this location (Brink, et al., 1984). Another mechanism that could suppress the summer alongshore wind correlations is the "Catalina Eddy" events in the wind field (Bosart, 1983). These cyclonic wind eddies essentially fill the entire Bight over time intervals of around 2 days, and produce poleward alongshore coastal winds within the Bight at the same time that equatorward alongshore coastal winds exist poleward of Point Conception. If these mesoscale wind eddies and the resulting coastal alongshore wind reversals within the Bight are not well represented in the calculated wind field, the correlation coefficients between measured and calculated alongshore winds within the Bight could be reduced as observed (see Section III.5). The influence of the Bight is not as great in winter, when relatively strong propagating pressure systems drive the wind field there.

III.4 SPECTRUM ANALYSIS OF THE WIND FIELD

III.4.1 Frequency Domain Properties

We study the frequency domain properties of the wind field using auto- and cross-spectrum analysis of calculated, measured, and adjusted measured winds. We discuss autospectra $[S(y, \omega)]$ of alongshore winds (Fig. III.8), the rotary coefficients $[S_r(y, -\omega) - S_r(y, +\omega)] / [S_r(y, +\omega) + S_r(y, -\omega)]$, where S_r indicates rotary autospectrum (Gonella, 1972, Mooers, 1973)] of vector winds (Fig. III.9), coherences between measured and calculated vector and alongshore winds (Fig. III.10), and spatial coherence scales of alongshore winds (Fig. III.11). The total rotary autospectra $S_r(y, +\omega) + S_r(y, -\omega)$ are not presented because the spectral shapes are very similar to those for alongshore wind.

Both the calculated and adjusted measured alongshore winds have similar distributions of variance density in (y, ω) space in all three seasons (Fig. III.8). They are red throughout the large-scale domain, and have no distinct maxima or minima in summer 1982. In most of the alongshore subdomain $y > -1000$ km during summer 1981, a relative minimum exists near 0.11 cycles per day (cpd) and a relative maximum exists near 0.19 cpd. In the alongshore subdomain $-500 < y < 500$ km during winter 1981-82, a relative minimum exists near 0.26 cpd and a relative maximum exists near 0.34 cpd. The variance density generally decreases from north to south at all frequencies in all seasons, with almost all of the

winter decrease occurring equatorward of Cape Mendocino ($y < 200$ km). The calculated wind variance density increases toward the south along the Baja California coast ($y < -1000$ km) in both summers. Wind variance is largest in winter, and is larger in summer 1981 than summer 1982. Wind autospectra tend to be more red in summer 1982 than in either summer 1981 or winter 1981-82, in agreement with the larger integral correlation time scales observed.

Some minor differences are observed, however, between the spectral shapes of calculated and adjusted measured alongshore winds in all seasons (Fig. III.8). We test the hypothesis that the true adjusted measured wind spectrum estimates $S_a(y, \omega)$ equal the true calculated wind spectrum estimates $S_c(y, \omega)$. At each (y, ω) , we form the null hypothesis $S_a = S_c$, then test it against the alternate hypothesis $S_a \neq S_c$. We use the statistical F-test, since the estimates \hat{S}_a and \hat{S}_c are χ^2 random variables. Because adjusted measured wind estimates are calculated at the measurement stations, we use a cubic spline interpolation in the alongshore direction at each frequency to obtain estimates at the y -locations of the CODE grid points. Applying the F-test, we find that $\log_{10} \hat{S}_a$ must differ by at least 0.43 from $\log_{10} \hat{S}_c$ to reject the null hypothesis that $S_a = S_c$ to a 95% level of confidence. We find significant differences between S_a and S_c only within the Southern California Bight ($-1000 < y < -550$ km) in the two summers, and at the highest frequency resolved (0.49 cpd) along the remainder of

the coast during winter 1981-82 and summer 1982. Elsewhere in (y, ω) space, fewer significant differences are observed than would be expected by chance in all seasons. We conclude that poleward of the Bight in summer and everywhere in winter, we cannot reject the hypothesis $S_a = S_c$ at frequencies ≤ 0.41 cpd, and the observed minor differences in spectral shapes are not statistically significant. This result agrees with other comparisons between calculated and measured wind autospectra for $\omega < 0.5$ cpd: Thomson (1983) for the British Columbia coast, Hsueh and Romea (1983) for the East China Sea, and Rienecker and Mooers (1983) for three open-ocean NDBO buoys in the northeast Pacific.

The measured alongshore wind variance is relatively large both along the California coast poleward of Point Conception ($y > -550$ km) and at CSJ ($y = 1760$ km) during all seasons (Fig. III.8). The variance is substantially reduced along the Washington coast, primarily due to the relatively small variance at QUI ($y = 1055$ km). Despite the large changes in measured alongshore wind variance along the coast, the analysis above indicates that the spectral shape for these winds is not significantly different from that of the calculated alongshore winds poleward of the Southern California Bight for $\omega \leq 0.41$ cpd. This provides additional support for our contention that the coastal atmospheric boundary layer effects primarily change the variance of alongshore wind measurements without seriously distorting other temporal statistical properties.

From the rotary coefficients (Fig. III.9), cyclonic variance dominates the calculated vector wind fluctuations in winter when propagating synoptic-scale atmospheric systems are strong and pass the coast frequently (Section III.5). During summer 1981, cyclonic variance exceeds anticyclonic in most of (y, ω) space poleward of Baja California ($y > -1000$ km) at frequencies > 0.2 cpd, while during summer 1982, this is true only along the California and southern Oregon coast ($-1000 < y < 600$ km) at frequencies > 0.2 cpd. During both summers, cyclonic variance exceeds anticyclonic at CSJ ($y = 1760$ km) over nearly the entire frequency band. For measured winds, there is less preference for cyclonic rotation than in the calculated winds during winter, and there is little preference for either rotation direction during both summers. The suppression of across-shore winds by coastal mountains apparently inhibits the rotation preference that is imposed by the fluctuating surface atmospheric pressure gradients caused by synoptic-scale systems.

The squared coherences between measured and calculated alongshore and vector winds (Fig. III.10) are largest during winter, are larger during summer 1981 than summer 1982, and are very small in the Southern California Bight ($-1000 < y < -550$ km) in summer. In winter, large alongshore wind coherence exists across the entire frequency band poleward of the Southern California Bight ($y > -550$ km), with the exception of the northern Oregon and southern Washington coast ($y \approx 900$ km), and coherence

within the Bight is not as small as in summer. Alongshore wind coherence decreases more rapidly with frequency during summer than during winter, and the summer decrease is more rapid during 1982. Coherence tends to be large in those parts of (y, ω) space where variance density is relatively large. For vector winds, the squared rotary coherences tend to be larger for the cyclonic component ($+\omega$) than for the anticyclonic component in all three seasons, which may be related to the larger cyclonic variance that is observed primarily in the calculated winds.

During winter, relatively small coherence is observed between measured and calculated alongshore and vector (cyclonic component only) winds within ± 400 km of the CODE site near 0.26 cpd (Fig. III.10). The preference for cyclonic rotation in winter does not exist in this region of (y, ω) space (Fig. III.9). This reduced cyclonic variance produces a relative minimum in the contoured autospectra of both alongshore winds (Fig. III.8) and vector winds (not shown), and reduces the coherence between the cyclonic components of calculated and measured vector wind. We do not have a plausible explanation for this observation.

We use space-averaged squared coherence functions to estimate alongshore coherence scales as a function of ω . For a given wind field $v(y_i, t)$ sampled at N evenly-spaced points, this function is given by

$$\gamma^2(\eta_n, \omega) = \frac{\left| \sum_{i=I}^J \{\bar{v}^*(y_i, \omega) \bar{v}(y_i + \eta_n, \omega)\} \right|^2}{\left[\sum_{i=I}^J \{\bar{v}^*(y_i, \omega) \bar{v}(y_i, \omega)\} \right] \left[\sum_{i=I}^J \{\bar{v}^*(y_i + \eta_n, \omega) \bar{v}(y_i + \eta_n, \omega)\} \right]} \quad (\text{III.4.1})$$

where I and J are given by (III.3.7), the overbars denote Fourier transforms, the asterisks denote complex conjugate, and the brackets denote frequency band averaging. We calculate these functions over grid points 4 through 13 (Fig. III.11). Without spatial averaging, a γ^2 of 0.16 is statistically significant to a 95% level of confidence. At the maximum η_n (1260 km), the function is averaged over three points, or over an alongshore distance much smaller than the correlation space scales (Table III.4). Since we gain no additional degrees of freedom by this averaging, we estimate the coherence space scale as the alongshore separation at which the squared coherence decreases to 0.16. The calculated and measured wind coherence space scales tend to be either constant over all ω or decrease slightly with increasing ω . The scale equals or exceeds 1000 km for calculated winds during summer 1981 and winter 1981-82, and for $\omega < 0.11$ cpd during summer 1982, while it is about 700 to 800 km for $\omega \geq 0.11$ cpd during summer 1982. In contrast, the measured wind scales are substantially smaller than calculated wind scales in all seasons. The measured wind scale exceeds 1000 km only for $\omega = 0.041$ cpd in summer 1982. Otherwise, measured wind scales are typically between 400 and 600 km in summer

and between 500 and 800 km in winter.

III.4.2 Wavenumber-Frequency Domain Properties

We study the wavenumber-frequency (ℓ, ω) domain properties of the alongshore wind field along the coast using auto- and cross-spectrum analysis (Figs. III.12 through III.15). The autospectrum functions $S(+\ell, \omega)$ [$S(-\ell, \omega)$] represent poleward-propagating [equatorward-propagating] variance density, and they are computed over grid points 4 through 13 using the two-dimensional Fourier transform method as outlined in Halliwell and Allen (1986b). The Nyquist wavenumber is $2.78 \cdot 10^{-3}$ cycles per kilometer (cpkm), but all spectrum functions are presented only for $-2.2 \cdot 10^{-3} \leq \ell \leq 2.2 \cdot 10^{-3}$ cpkm since calculated winds poorly represent fluctuations at larger ℓ , and since measured winds may also not represent these fluctuations well because the alongshore spacing between some measurement stations is > 180 km.

The variance density in (ℓ, ω) space for calculated, adjusted measured, and measured winds decreases with increasing ℓ and ω for all three seasons (Fig. III.12). The decrease with increasing ℓ is more rapid for calculated than adjusted measured winds, resulting from the poor representation of smaller-scale fluctuations by calculated winds. The variance density distributions of all wind sets are similar in each season at $\ell \leq 1.1 \times 10^{-3}$ cpkm (wavelengths ≥ 900 km). (We select this particular value of ℓ as the boundary between the energetic large scales and the much less energetic

small scales because it is one at which spectrum estimates are computed - see Fig. III.14.) From the results of a statistical F-test similar to that performed in Section III.4.1, significant differences between calculated and adjusted measured wind spectrum estimates exist only in those parts of (ℓ, ω) space where the calculated wind autospectra are roughly within the following ranges: $\log_{10} S < 3.6$ during summer 1981, $\log_{10} S < 4$ during winter 1981-82, and $\log_{10} S < 3.2$ during summer 1982. Therefore, these distributions of calculated wind variance density in (ℓ, ω) space for the three seasons are not significantly different from those of adjusted measured wind, except at the largest ℓ and ω (roughly $\ell \geq 1.2 \times 10^{-3}$ cpkm and $\omega \geq 0.3$ cpd) where very little wind variance exists. This is true despite the large variability along the coast in measured alongshore wind variance (Fig. III.8). The (ℓ, ω) autospectra indicate that the distribution of variance density in the wavenumber domain is also not changed significantly by adjusting the measured wind variance. Apparently the function $\xi_{cm}(y)$ in (III.3.5) has the property that it does not significantly alter the distribution of the variance of $v_a(y, t)$ in (ℓ, ω) space from that of $v_m(y, t)$.

The basic patterns in the contours of propagating autospectra of calculated, adjusted measured, and measured winds (Fig. III.13) are similar to each other in all seasons. Equatorward-propagating variance exceeds poleward in winter, with the greatest excess at $\ell \leq 1.1 \times 10^{-3}$ cpkm. In the two summers, poleward-propagating

variance generally exceeds equatorward for $\lambda \leq 1.1 \times 10^{-3}$ cpkm and $\omega \leq 0.41$ cpd (excluding 0.11 cpd) in summer 1981 and $\omega < 0.26$ cpd in summer 1982.

The spectral shapes in the λ and ω domains are illustrated by integrating the (λ, ω) autospectra over ω and λ , respectively (Fig. III.14). From the λ autospectra, the dominance of wind fluctuations with $\lambda \leq 1.1 \times 10^{-3}$ cpkm is evident in all three wind sets for all three seasons. Over 90% of calculated wind variance and about 80% of adjusted measured wind variance is due to fluctuations with $\lambda \leq 1.1 \times 10^{-3}$ cpkm in all seasons (Table III.5). Adjusting or normalizing the wind fields only slightly decreases these percentages. The spectral shapes for both measured and adjusted measured winds are very similar (Fig. III.14). There is little difference in the percentage of total variance with $\lambda \leq 1.1 \times 10^{-3}$ cpkm among the three seasons (Table III.5), but relatively more variance is observed at $\lambda = 0$ (essentially representing wavelengths > 2000 km) during winter 1981-82 than during the two summers. The distributions in λ space are skewed toward equatorward propagation (larger variance density for $-\lambda$) in winter and toward poleward propagation in the two summers.

The integrated ω autospectra have similar spectral shapes for all three seasons (Fig. III.14). They decrease monotonically with increasing ω , with two exceptions: In summer 1981, a relative minimum exists near 0.11 cpd and a relative maximum exists near 0.19 cpd. In winter 1981-82, a relative minimum exists near 0.26

cpd and a relative maximum exists near 0.34 cpd. These extrema are all evident in the (y, ω) autospectra of alongshore wind (Fig. III.8). The variance density decreases by two orders of magnitude over the entire frequency band ($0.04 \leq \omega \leq 0.48$ cpd) in summer 1982, and it decreases by one order of magnitude in the other seasons, with the smallest decrease occurring in winter 1981-82. Summer 1981 variance density exceeds that in summer 1982 for $\omega > 0.11$ cpd.

Squared coherences between calculated winds and both adjusted measured and measured winds (Fig. III.15) are large only for $\ell \leq 1.1 \times 10^{-3}$ cpkm in all seasons. The variation of coherence with ℓ , ω , and season tends to follow that of wind variance density, with high coherence generally found where the variance density is relatively large. The coherence decays more rapidly with increasing ω in the two summers than in winter, which is probably related to the relatively large winter variance density at higher frequencies. In winter, coherence is larger for equatorward-propagating variance than for poleward-propagating. In summer, there is a slight tendency for the poleward-propagating variance to be more coherent. It is again remarkable to observe the strong similarity of coherence patterns (Fig. III.15) between calculated winds and both adjusted measured and measured winds despite the large alongshore variability in measured alongshore wind variance. The coherence decays slightly more rapidly with increasing $|\ell|$ for measured winds than for adjusted measured winds

in all seasons. Alongshore errors in wind variance therefore have very little effect on (λ, ω) spectrum analyses.

III.5 CHARACTERISTICS OF WIND FLUCTUATION EVENTS

III.5.1 Space-Time Contour Plots of Alongshore Wind

We use space-time contour plots of alongshore wind to visually characterize the basic properties of alongshore winds, and to illustrate how these properties change among seasons, with alongshore location, and with time within a given season. We compare the representation of wind events by the calculated and measured wind sets, and we utilize National Weather Service surface atmospheric pressure charts to establish the basic relationships of surface synoptic-scale atmospheric pressure systems to observed wind event properties.

To illustrate typical characteristics of alongshore wind fluctuations, they are contoured for three 45-day subintervals, one from each of the four-month seasons, for calculated winds, adjusted measured winds, and measured winds (Figs. III.16 through III.18). We refer to extrema of equatorward (poleward) wind as upwelling (downwelling) events. The variance adjustment of the measured winds visually enhances the amplitudes of wind extrema poleward of the Oregon-California border ($y > 400$ km). Adjusted measured winds are visually correlated with calculated winds, and this visual correlation is substantially enhanced by removing the mean wind

prior to contouring (not shown), especially in summer.

Substantial differences in wind event properties exist between winter and summer. During the winter subinterval, strong wind events of 2 to 4 days duration dominate the fluctuations, most of which are either in-phase along the coast or tend to propagate equatorward (Fig. III.17). Some of these winter events affect the entire CODE large-scale domain. During the two summer subintervals, strong equatorward mean winds exist along the California coast ($-1000 < y < 400$ km) and wind events are typically confined within 1000 to 1500 km alongshore subdomains (Figs. III.16 and III.18). This seasonal difference in the alongshore scales of wind fluctuations is also found in the alongshore correlation space scales (Table III.4), the alongshore coherence scales (Fig. III.11), and the integrated wavenumber autospectra (Fig. III.14, where a larger percentage of total variance in winter is due to fluctuations with alongshore wavelengths > 2000 km). A preferred propagation direction for wind fluctuations is not visually evident in summer, although (ℓ, ω) autospectra indicate that the preferred direction is poleward, especially at low frequency (Fig. III.13).

III.5.2 Winter Event Properties

During the winter subinterval (Fig. III.17), equatorward-propagating alongshore wind fluctuations occur between 15 and 27 February 1982. A downwelling event occurs essentially

in-phase along the coast throughout the entire CODE large-scale domain on 1 March. Poleward-propagating wind fluctuations occur from 3 to 9 March, followed by equatorward-propagating fluctuations from 10 to 18 March. Smaller-amplitude, lower-frequency fluctuations exist after 18 March, which tend to occur in-phase or propagate equatorward. The interval from 3 to 9 March is the longest one in winter 1981-82 where poleward propagation dominates. In-phase or equatorward-propagating fluctuations dominate during most of that winter.

Propagating surface synoptic-scale pressure systems are responsible for these observed properties. For example, the in-phase downwelling event of 1 March 1982 is caused by a large cyclone that moves directly onshore near Vancouver Island ($1110 < y < 1470$ km) and has closed pressure contours that affect the entire large-scale domain poleward of Baja California ($y > -1000$ km). (When we refer to a cyclone, we include the fronts associated with them.) The winds become poleward almost simultaneously in the entire coastal region affected by the cyclone as it approaches the coast with its anticlockwise wind circulation. The wind then subsides along the coast as the cyclone both moves inland and weakens rapidly. The event persists for an extra day along the coast between northern California and southern British Columbia ($200 < y < 1400$ km) (Fig. III.17). Between 3 and 9 March, atmospheric cyclones and anticyclones propagate from southwest to northeast, first affecting the southern and central California

coast, then the Oregon, Washington, and British Columbia coasts. Between 10 and 18 March, a series of cold fronts and anticyclones propagate from northwest to southeast from the Gulf of Alaska across the northwest U.S. coast. These systems become weaker and occur less frequently after 18 March. Over time scales on the order of several days, the properties of winter propagating synoptic-scale systems can differ substantially from seasonal mean properties.

A typical example of the equatorward alongshore progression of winter weather systems is shown for the interval 11 to 14 March (Fig. III.19). Two cold fronts, separated by an anticyclone, propagate rapidly from northwest to southeast during this time interval, and two equatorward-propagating pulses of strong equatorward winds follow the frontal passages (Fig. III.17). These winter cold fronts trailing to the south or southwest from the cyclone centers usually propagate toward the east or southeast, giving the propagation an equatorward alongshore component, even when the parent cyclone propagates to the north of due east. Southeastward-propagating fronts are common in winter and probably produce the preference for equatorward propagation in the winter wind field. Halliwell and Allen (1986b) show that equatorward propagation dominates in all four winters from 1980-81 to 1983-84.

III.5.3 Summer Event Properties

In the two summer subintervals (Figs. III.16 and III.18), some individual wind events have a preferred propagation direction, but preferred directions usually do not persist over several-day intervals as is often observed during winter. Cyclones often generate strong downwelling events in the northern part of the CODE large-scale domain during the summer subintervals. These events are usually separated by two to six days in both the summer 1981 subinterval (Fig. III.16) and the first half of the summer 1982 subinterval (Fig. III.18), and affect the coast farther to the south on average during summer 1981. In particular, downwelling events penetrate equatorward to the CODE site on 18 May and 8 to 9 June 1981. Upwelling events along the U.S. coast ($-1000 < y < 1100$ km) often occur 2 to 4 days after the passage of these cyclones (Figs. III.16 and III.18), and they are usually strongest along the California coast ($-1000 < y < 400$ km), excluding the Southern California Bight ($-1000 < y < -550$ km) for measured winds. These upwelling events also tend to be centered farther to the south in summer 1981 than in summer 1982.

During the summer 1981 subinterval, the strongest upwelling events occur on 30 to 31 May, 9 to 11 June, 13 to 15 June, and 26 to 28 June. Based on surface weather charts, all four of these events follow the passage of cyclones in the northern half of the CODE large-scale domain, although the cyclones that precede the last two events weaken very rapidly as they reach the coast and do

not produce strong downwelling events (Fig. III.16). The cyclone preceding the 13 to 15 June upwelling event causes poleward alongshore winds on 12 to 13 June primarily along the Oregon coast only (centered near $y = 600$ km), and the cyclone preceding the 26 to 28 June upwelling event causes poleward alongshore winds on 24 to 25 June along the extreme northern British Columbia coast ($y > 1400$ km) in the calculated wind field only. In the event cycle from 28 to 31 May (Fig. III.20), a cyclone approaches the British Columbia coast on 28 and 29 May, and the trailing cold front has passed the coast southward to northern California by 30 May. The North Pacific subtropical high has intensified northeastward toward the U.S. coast by 31 May, increasing the pressure gradient and coastal wind speed between the high and the thermal low over the southwest U.S. The pressure gradient at the California coast south of Cape Mendocino (40° N) is about twice as strong on 31 May as on 28 May, and the measured alongshore wind speed near the CODE site (Fig. III.16) has also about doubled.

During the summer 1982 subinterval, the strongest upwelling events occur on 3 to 4 May, 8 to 9 May, 17 to 18 May, 22 to 23 May, and 26 to 27 May 1982, and they all follow cyclones that induce strong downwelling events (Fig. III.18). These event cycles are similar to those observed in summer 1981, except for being shifted to the north on average. In the event cycle from 15 to 18 May (Fig. III.21), the cyclone strikes the British Columbia coast on 16 May and the associated cold front passes the northwest U.S. coast

by 17 May. During the two days after frontal passage, the subtropical high intensifies northeastward, producing strong equatorward winds. The coastal pressure gradient near the CODE site on 18 May 1982 is about 40% stronger than three days earlier (Fig. III.21), which is about the percentage increase of measured alongshore wind speed near the CODE site. Mass, et al. (1986) study similar summer event cycles in great detail, emphasizing how they drive onshore surges of cool marine air along the northwest U. S. and Canadian coasts. They show that as the cyclones and associated fronts approach the coast, coastally trapped pressure systems are generated which drive coastal gravity currents that enhance the poleward alongshore wind in the northern part of the large-scale domain caused by the synoptic-scale systems.

Downwelling events centered along the California coast occasionally follow these upwelling events in both summers. These downwelling events are clearly represented in the measured wind contour plots, but are poorly represented in the calculated wind contour plots (Figs. III.16 and III.18). The strongest of these events during the two summer subintervals occur on 28 to 30 June 1981, 4 to 6 May 1982, and 24 to 26 May 1982. These events are evidently associated with coastally trapped atmospheric pressure disturbances (Dorman, 1985, 1986). Since the atmospheric internal Rossby radius of deformation is about 150 km along the California coast, these disturbances have an across-shore scale substantially smaller than the alongshore scale, probably causing the calculated

winds to poorly resolve them. To crudely determine how well the calculated wind field reproduces the event of 4 to 6 May, we compare the maximum changes in calculated and measured alongshore wind speeds caused by the event at both grid point 6 and B12 (near $y = -180$ km), the approximate location of the largest speed change. The measured alongshore wind changes from -10 to $+6$ m s^{-1} between 3 and 5 May, while the calculated wind changes from -9 to -2 m s^{-1} , or only 44% of the measured wind change.

During the last third of the summer 1982 subinterval (following about 28 May), calculated alongshore wind fluctuations are relatively small, and event cycles such as the ones we have discussed for both 1981 and 1982 are not evident (Fig. III.18). This relatively quiet pattern dominates most of the remainder of the four-month summer 1982 season, and a similar quiet period occurs after 10 July in the four-month summer 1981 season. Quiet intervals dominate about 20% of summer 1981 and nearly two-thirds of summer 1982. No propagating cyclones or associated fronts are evident in the surface pressure field during a typical quiet interval (28 to 31 May 1982, Fig. III.22). The subtropical high extends much farther to the north during this interval, and cyclones remain far to the north of the CODE large-scale domain. Although propagating systems are not evident at the surface, the pressure field does not remain steady between 28 and 31 May (Fig. III.22) because the subtropical high weakens and the thermal low builds northward to cover nearly the entire western U.S. over

this four-day interval. During intervals when propagating systems are very weak or absent, oscillations in the relative strengths and positions of the subtropical high and thermal low may still have an important influence on coastal surface winds.

Measured alongshore wind fluctuations are substantially larger than those for calculated alongshore wind during these quiet intervals (Fig. III.18), which may be partly caused by coastal boundary layer processes. For example, propagating atmospheric systems (troughs and ridges) that have a very weak pressure signal at the surface still exist in the middle troposphere during these quiet intervals. Passage of these systems can raise or lower the marine inversion layer, indirectly affecting coastal winds (Beardsley, et al., 1986). Strong equatorward measured winds exist near the latitude of the CODE site between 1 and 8 June, 1982, but this event is not as evident in the calculated wind field (Fig. III.18). During this interval, enhanced northwest winds to the west of a pressure trough at the 700 mb level (height = 3 km) in the atmosphere change the across-shore structure of the marine inversion layer by raising it near the coast, making the actual equatorward alongshore winds at the coast stronger than could be accounted for by the synoptic-scale pressure gradient alone (Beardsley, et al., 1986).

We can visually assess the characteristics of the summer measured alongshore winds within the Southern California Bight ($-1000 < y < -550$ km), and see how they differ from the calculated

winds there, by inspecting wind events (Figs. III.16 and III.18). Several time intervals can readily be identified where measured alongshore wind in the Bight opposes the measured alongshore wind poleward of the Bight. These include most of the interval from 5 to 13 June 1981, 5 and 6 May 1982, 17 to 20 May 1982, and most of the interval from 2 to 7 June 1982. In contrast, the calculated alongshore wind in the Bight does not oppose the calculated alongshore wind poleward of the Bight during these time intervals. From surface weather charts, wind patterns within the Bight resemble cyclonic Catalina eddy events (Bosart, 1983) during the 5 to 13 June 1981 and 17 to 20 May 1982 intervals.

III.6 DISCUSSION

The properties of coastal wind fluctuations along the west coast of North America vary over a wide range of time scales. The wind properties have a large seasonal cycle due to changes in the properties of both synoptic-scale pressure systems and the coastal marine boundary layer. Winter winds are primarily driven by propagating cyclones and anticyclones, so the statistical properties of wind fluctuations depend strongly on the size, strength, propagation speed and direction, and frequency of occurrence of these systems. These properties often remain relatively constant for several days, then change abruptly. The summer situation is more complicated due to the continuous existence of a strong inversion layer in the coastal marine

boundary and to the existence of two permanent pressure systems: the North Pacific subtropical high and the southwest U.S. thermal low. The interaction between propagating surface cyclones, which are weaker on average than in winter, and these stationary systems has an important influence on summer winds. In particular, the subtropical high often builds northeastward toward the coast after a cyclone passes to the north of the high, causing strong upwelling events along the California coast. The high occasionally builds far to the north for days to weeks at a time, keeping propagating cyclones far to the north of the CODE large-scale domain. During these intervals, oscillations in the strength and position of the subtropical high and thermal low, plus coastal boundary layer processes, have an important influence on coastal winds. Coastally trapped atmospheric disturbances can enhance downwelling events ahead of cyclones approaching the coast and cause relaxations or reversals in the mean equatorward wind along the California coast.

These properties of atmospheric systems and the coastal marine boundary layer lead to the following seasonal similarities and differences in measured wind statistics along the west coast of North America: Mean summer winds have an equatorward alongshore component throughout the domain, except at the northern end during summer 1981, and are relatively strong along the California coast. The largest mean exists near the CODE experimental site northwest of San Francisco. Mean winter winds have a poleward component north of the CODE site and an equatorward component to the south.

Wind fluctuations are strongly polarized in the alongshore direction in all seasons, but less so in winter. Wind fluctuations are relatively large near the CODE site in summer, near Cape Mendocino in winter, and at the northern end of the large-scale domain (northern British Columbia) in both seasons. Winter fluctuations have larger amplitudes and larger space scales than in summer. They have a strong tendency to propagate equatorward at all frequencies, while summer fluctuations have a tendency to propagate poleward. In summer, poleward-propagating coastally trapped pressure disturbances may contribute to the directional preference. In all seasons, about 80% to 85% of measured wind variance is due to fluctuations with wavelengths greater than 900 km. Coastal atmospheric boundary layer processes appear to primarily influence the variance of measured alongshore wind without seriously affecting other statistical properties.

Wind variance is larger, and wind autospectra are less red, in summer 1981 than summer 1982. The subtropical high extends far to the north, preventing propagating cyclones from affecting the large-scale domain at all, for nearly two-thirds of summer 1982. This pattern exists for only about 20% of summer 1981. Winds tend to fluctuate at lower frequency and have smaller amplitudes under these conditions, which probably accounts for much of the observed differences in wind statistics between the two summers. Denbo and Allen (1986) report substantial differences in wind stress properties in two 64-day intervals in summer 1981 (8 May to 11

July) and summer 1982 (26 May to 29 July). From the study of surface pressure charts here, we find that the influence of propagating cyclones and anticyclones is much weaker during most of their summer 1982 interval than during their summer 1981 interval, and this is presumably a major cause of the observed differences in wind stress properties.

The statistical properties of wind fluctuations therefore differ substantially between winter and summer and between different years for the same season. Within a given season, properties such as the fluctuation amplitude, the frequency of the fluctuations, and the propagation direction can be relatively constant over time intervals of several days to several weeks. These intervals are separated from one another by abrupt changes in some or all of these properties. Studies of the response of coastal currents to wind forcing during one season, or a small subset of one season, may not represent typical conditions for that season.

The calculated and measured alongshore wind sets are very coherent for wavelengths ≥ 900 km throughout the large-scale domain, except within the Southern California Bight in summer. Calculated alongshore winds poorly represent fluctuations with wavelengths < 900 km. They represent fluctuations caused by coastal boundary layer processes, but with less than half the amplitude of the measured winds. Outside of the Bight, the primary difference between the two alongshore wind sets for wavelengths

≥ 900 km is in the representation of wind variance as a function of alongshore location. For example, a large maximum in measured alongshore wind variance exists along the northern California coast in both summer and winter, which does not exist in the calculated alongshore winds. However, we found that many statistical analyses are not sensitive to errors in the distribution of wind variance along the coast. We conclude that, poleward of the Southern California Bight in summer and everywhere along the coast in winter, both wind sets should perform reasonably well as forcing functions for wavelengths ≥ 900 km and $\omega < 0.5$ cpd in studying properties of the coastal ocean response that do not depend on the absolute magnitude of wind variance.

Table III.1. Coastal points of the CODE large-scale analysis grid (bottom). Coast orientation is measured in degrees anticlockwise from due east. Data from odd points between 1 and 17 and from 32 and 34 are used in Figs. III.3 and III.5.

<u>Station or Point Number</u>	<u>Lat.</u>	<u>Lon.</u>	<u>y (km)</u>	<u>Coast Orient.</u>
17	54 09N	130 20W	1800	120
16	52 10	128 19	1620	115
15	50 32	127 13	1440	100
14	49 23	126 06	1260	128
13	48 11	124 42	1080	120
12	46 36	124 05	900	95
11	44 58	124 03	720	85
10	43 21	124 20	540	73
09	41 46	124 12	360	103
08	40 12	124 18	180	130
07	38 42	123 27	0	133
06	37 18	122 24	-180	102
05	35 59	121 31	-360	128
04	34 35	120 39	-540	90
03	34 01	118 53	-720	150
02	33 00	117 21	-900	110
01	31 27	116 44	-1080	110
35	30 00	115 54	-1260	115
34	28 47	114 41	-1440	130
33	27 20	113 52	-1620	130
32	26 07	112 40	-1800	130

Table III.2. Wind measurement stations used in the analysis of wind field properties (top). Stations from which data are plotted in Figs. III.3 and III.5 are marked by asterisks under Time Periods Used. Additional wind measurement stations used in the filling of data gaps (Section III.2.2) and in the comparison of land to offshore winds (Section III.3.4) are listed at the bottom. Coast orientation is measured in degrees anticlockwise from due east.

<u>Station or Point Number</u>	<u>Abbrev.</u>	<u>Lat.</u>	<u>Lon.</u>	<u>y (km)</u>	<u>Coast Orient.</u>	<u>Time Periods Used</u>
Cape St James, BC	CSJ	51 56N	131 01W	1760	115	All *
Cape Scott, BC	CSC	50 47	128 26	1467	134	W81-2, S82 *
Quillayute, WA	QUI	47 57	124 32	1055	110	All *
Grays Harbor, WA	GRH	46 55	124 06	936	95	All *
Newport, OR	NEW	44 38	124 03	683	82	All *
North Bend, OR	NOB	43 25	124 15	547	73	All
Crescent City, CA	CCY	41 47	124 14	362	103	All *
Humboldt Bay, CA	HUM	40 46	124 14	246	75	S81
NDBC 46022	B22	40 46	124 31	240	75	W81-2, S82
NDBC 46014	B14	39 13	123 58	71	100	S81, S82 *
Point Arena Lt., CA	ARL	38 57	123 44	41	110	W81-2 *
NDBC 46013	B13	38 14	123 18	-61	133	All
NDBC 46012	B12	37 22	122 39	-171	105	All *
Point Sur, CA	SUR	36 18	121 53	-301	115	All
Diablo Canyon, CA	DIA	35 14	120 50	-464	120	W81-2 *
NDBC 46011	B11	34 53	120 52	-506	90	S81, S82 *
Point Mugu, CA	MUG	34 07	119 07	-678	155	All *
San Diego, CA	SDO	32 44	117 10	-936	105	All *
Hoquiam, WA	HOQ	46 58	123 56	942	95	
Point St. Geo., CA	PSG	41 47	124 16	362	103	
Arcata, CA	ACA	40 59	124 06	270	75	
Sea Ranch	SRA	38 41	123 26	0	133	
CODE Met. Buoy C3	C3	38 36	123 28	0	133	
Bodega Marine Lab.	BML	38 19	123 04	-46	133	
Pillar Point, CA	PIL	37 30	122 30	-156	105	
Pigeon Point, CA	PIG	37 11	122 24	-191	102	

Table III.3. Regression of offshore vector wind speed U_o on nearby land vector wind speed U_l , $U_o = a + bU_l$, and the variance ratio of buoy alongshore winds to nearby land alongshore winds.

<u>Time Interval</u>	<u>Stations</u>		<u>Regression</u>		<u>Correl. Coeff.</u>	<u>RMS Ampl. Ratio</u>	<u>% Common Good Data</u>
	<u>Buoy</u>	<u>Land</u>	<u>Coefficients</u>				
			<u>(m s⁻¹)</u>				
			<u>a</u>	<u>b</u>			
Apr - Jul 81	B14	ARL	1.21	1.08	0.76	1.22	100
	C3	SRA	2.93	1.05	0.81	1.26	88
	B13	BML	5.30	0.86	0.62	1.35	100
	B12	PIL	2.88	0.50	0.68	1.07	81
	B11	DIA	1.71	0.93	0.89	0.97	89
	B22	HUM	3.27	0.66	0.50	1.76	95
Dec 81 - Mar 82	B14	ARL	1.01	1.12	0.90	1.36	87
	C3	SRA	3.60	0.95	0.55	1.43	39
	B12	PIL	3.38	0.39	0.59	1.07	89
	B11	DIA	2.51	0.88	0.79	1.20	15
	B22	HUM	0.26	1.49	0.72	1.74	95
May - Aug 82	B14	ARL	0.59	1.25	0.80	1.27	100
	C3	SRA	1.42	1.98	0.85	2.14	70
	B13	BML	2.63	1.13	0.70	1.57	100
	B12	PIL	1.64	0.78	0.76	1.38	98
	B11	DIA	0.76	0.93	0.88	0.80	100

Table III.4. Integral correlation alongshore space scales and time scales for coastal alongshore winds between grid points 4 (34.6°N; y = -540 km) and 13 (48.2°N; y = 1080 km).

<u>Wind Field</u>	<u>Integral Correlation Scale</u>					
	<u>Apr - Jul 81</u>		<u>Dec 81 - Mar 82</u>		<u>May - Aug 82</u>	
	<u>Space</u> <u>(km)</u>	<u>Time</u> <u>(days)</u>	<u>Space</u> <u>(km)</u>	<u>Time</u> <u>(days)</u>	<u>Space</u> <u>(km)</u>	<u>Time</u> <u>(days)</u>
Calculated	824	1.44	1036	1.36	746	2.06
Normalized Calculated	776	1.56	1042	1.27	768	1.95
Measured	436	1.27	592	1.13	452	1.98
Adjusted Measured	556	1.09	662	1.28	442	1.91
Normalized Measured	474	1.20	658	1.19	496	1.80

Table III.5. Percentage of total variance due to alongshore wind fluctuations with wavelengths ≥ 900 km determined from wavenumber-frequency autospectra integrated over frequency (Fig. III.14).

<u>Wind Set</u>	<u>Time Interval</u>		
	<u>Apr - Jul 81</u>	<u>Dec 81 - Mar 82</u>	<u>May - Aug 82</u>
Calculated	93	92	94
Normalized Calculated	91	91	89
Measured	83	85	85
Adjusted Measured	80	82	79
Normalized Measured	80	81	80

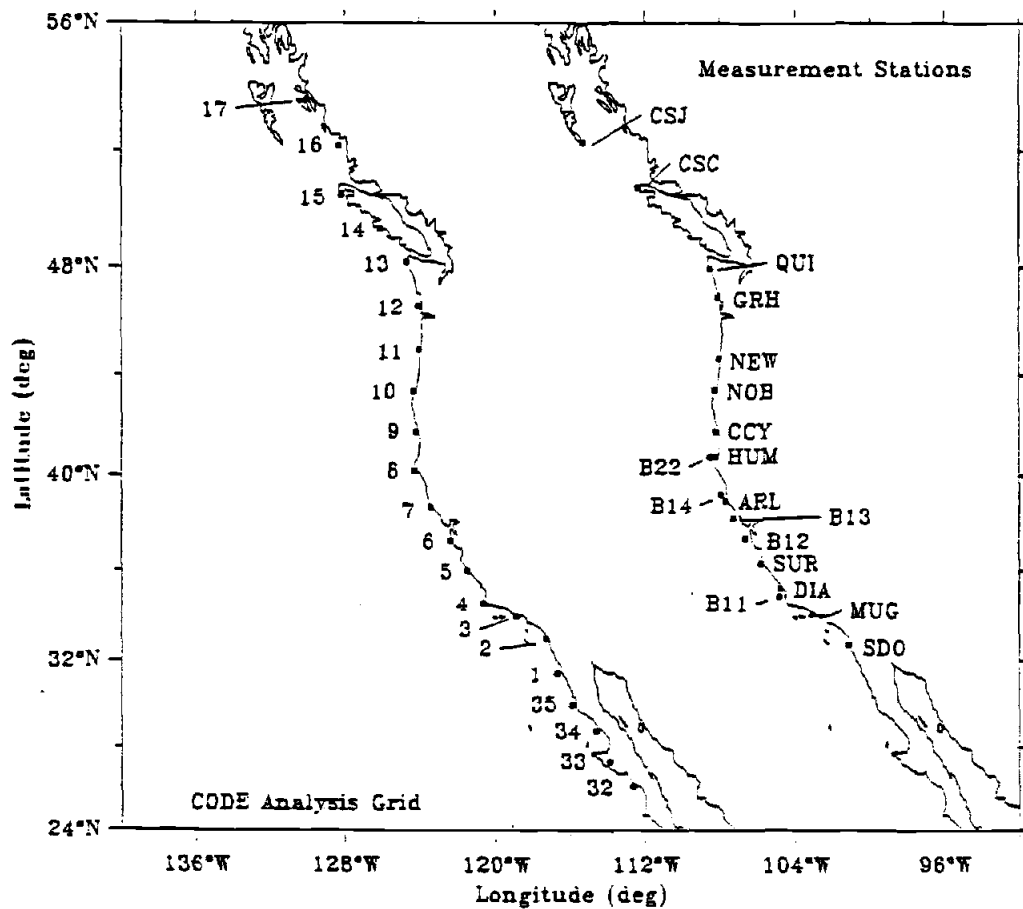


Fig. III.1: The coastal points of the CODE analysis grid (left coastline) and the wind measurement stations used in this study (right coastline). The longitude axis is correct for the left coastline. Information on the stations and grid points is summarized in Tables III.1 and III.2.

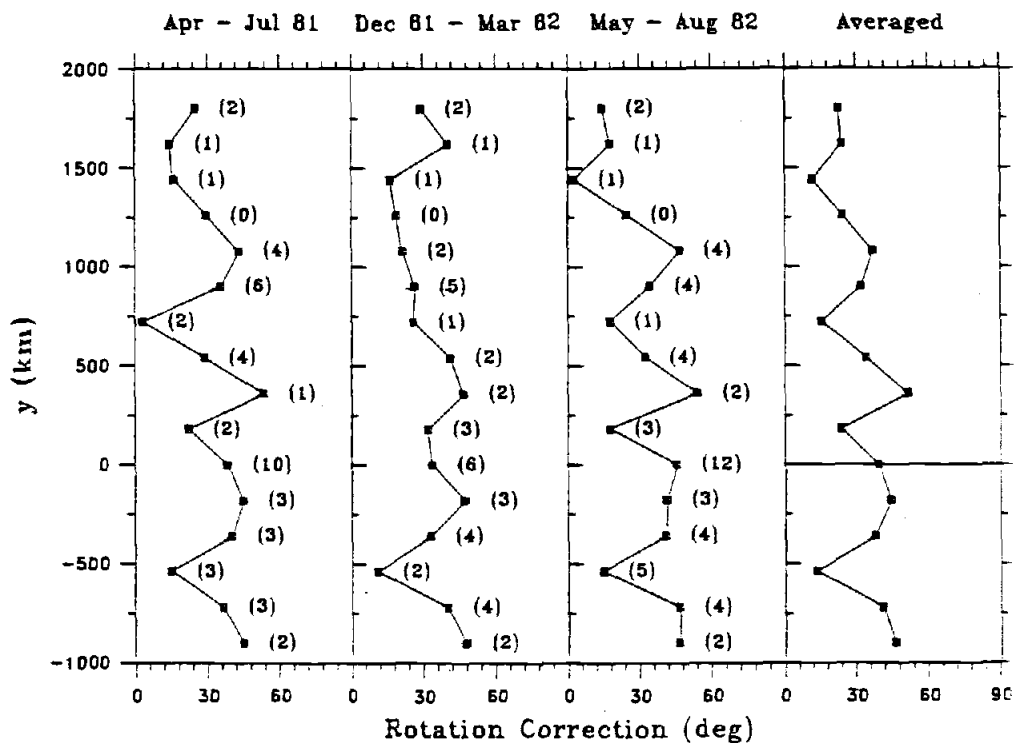


Fig. III.2: The rotation correction required to align the calculated wind fluctuations with measured wind fluctuations for grid points 2 through 17 for the three seasons. A positive correction means that the calculated winds must be rotated anticlockwise to be aligned with the measured winds. The number of measurement stations available near each grid point is in parentheses.

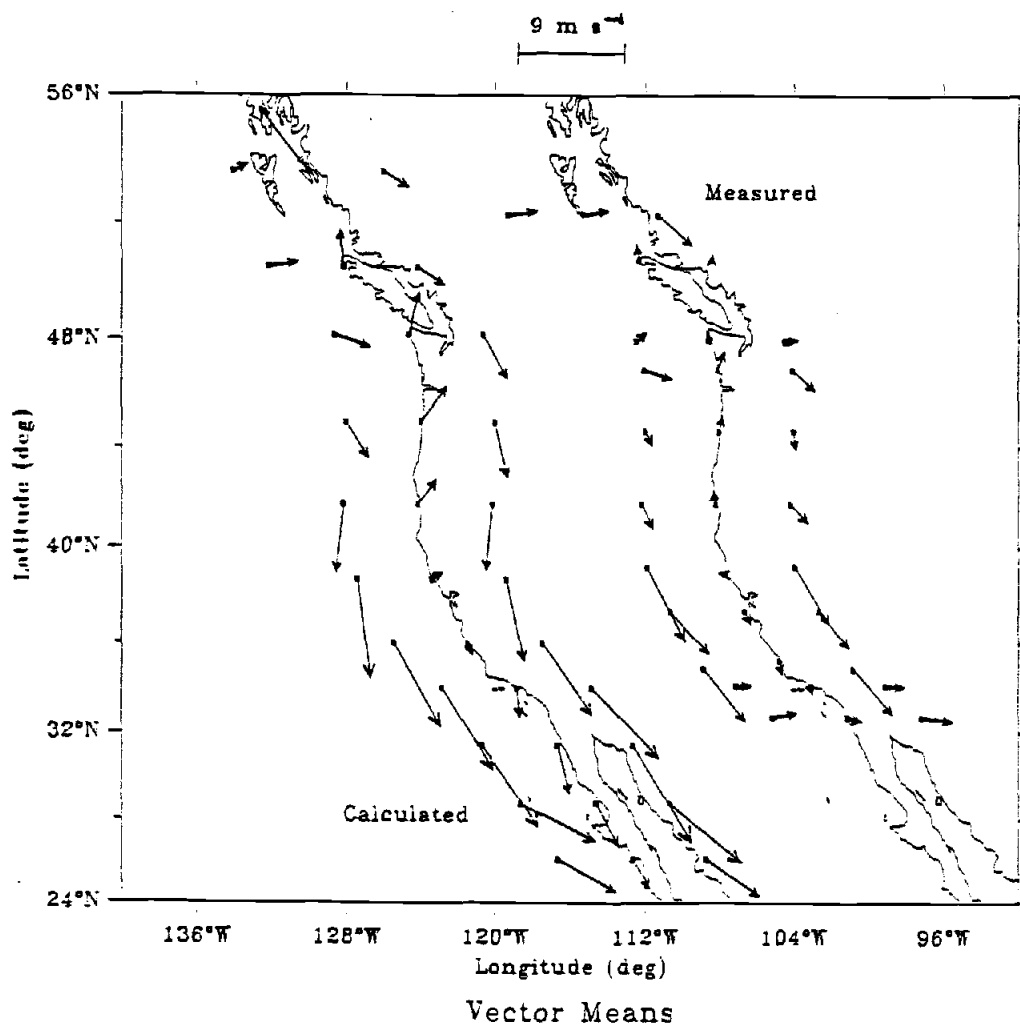


Fig. III.3: Mean vectors for calculated (left coastline) and measured (right coastline) winds. For each coastline, the vectors to the left are for Apr - Jul 81; the vectors at the coast are for Dec 81 - Mar 82, and the vectors to the right are for May - Aug 82. The origins of the vectors are at the appropriate CODE grid point or measurement station. The mean vectors for the summer seasons are displaced $\pm 4^\circ$ longitude from each coast. Calculated wind means are shown for every other grid point centered at point 7 (the CODE site). Measured wind means are shown for most stations (see Table III.2). The calculated winds have not been rotated. The longitude axis is correct for the left coastline.

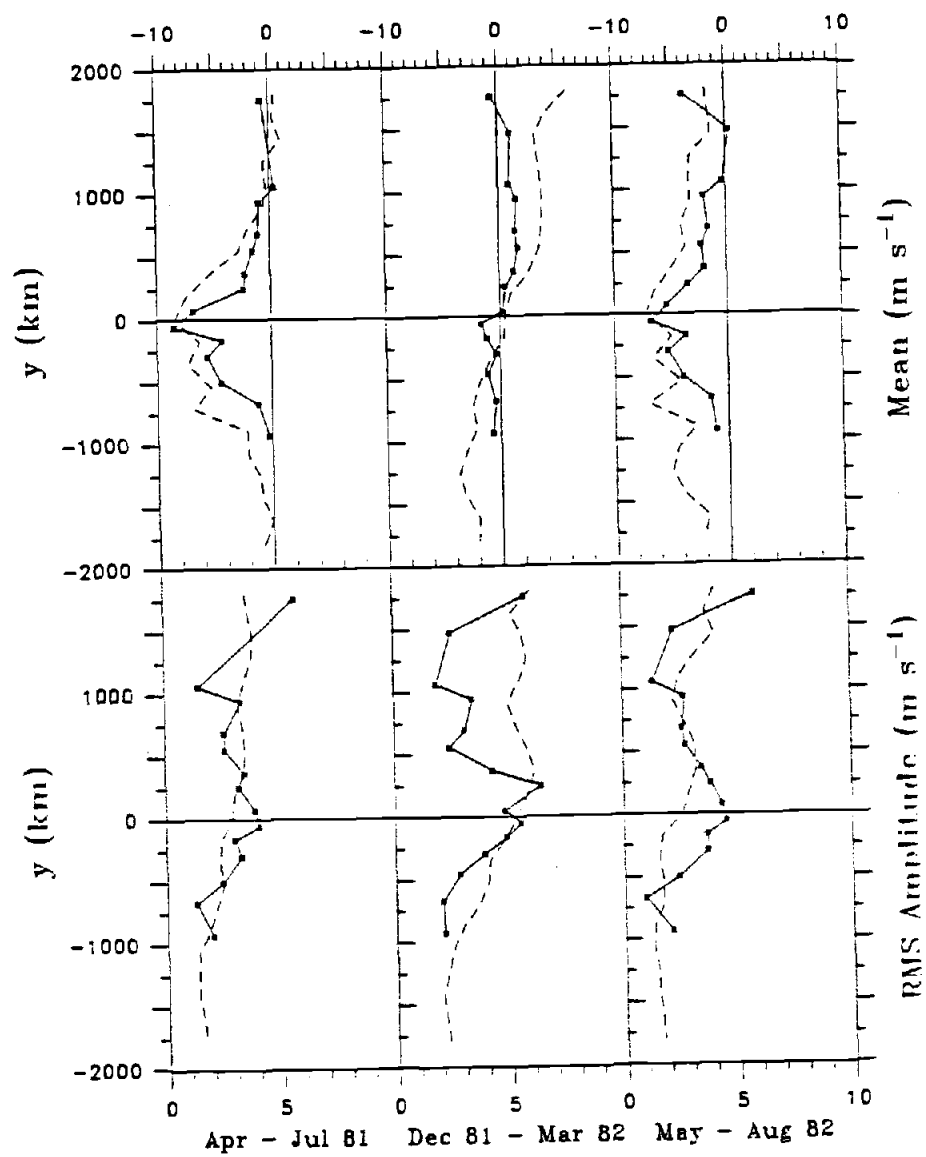


Fig. III.4: The means and rms amplitudes of the calculated (dashed) and measured (solid) alongshore winds as a function of y for the three seasons.

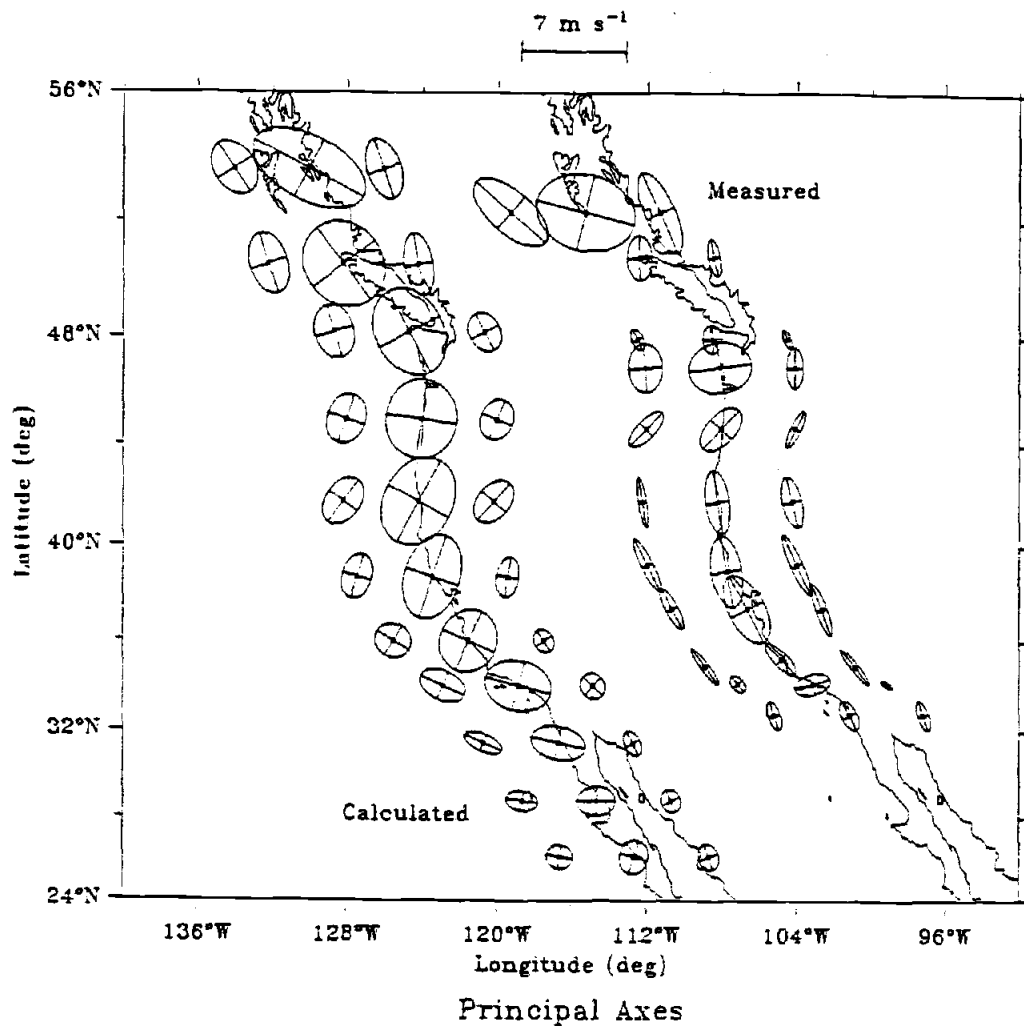


Fig. III.5: Same as Fig. III.3, except for rms principal axis ellipses.

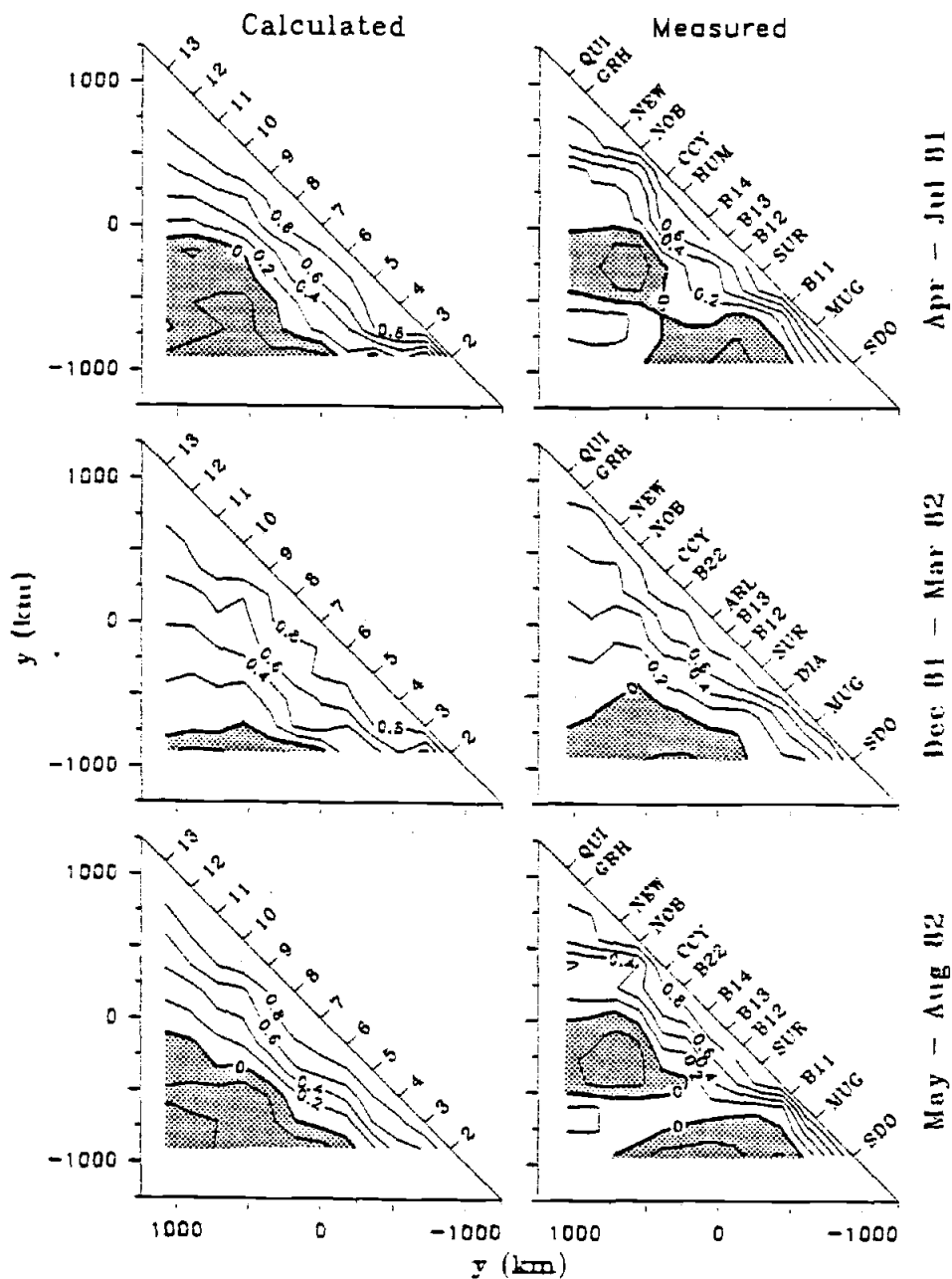


Fig. III.6: Zero time-lagged correlation matrices for calculated and measured winds contoured as a function of alongshore separation. Correlation coefficients > 0.35 are statistically significant to a 95% level of confidence (see Appendix C). The matrices are calculated for the U.S. coast only, where measurement station spacing is relatively uniform. Negative correlations are shaded.

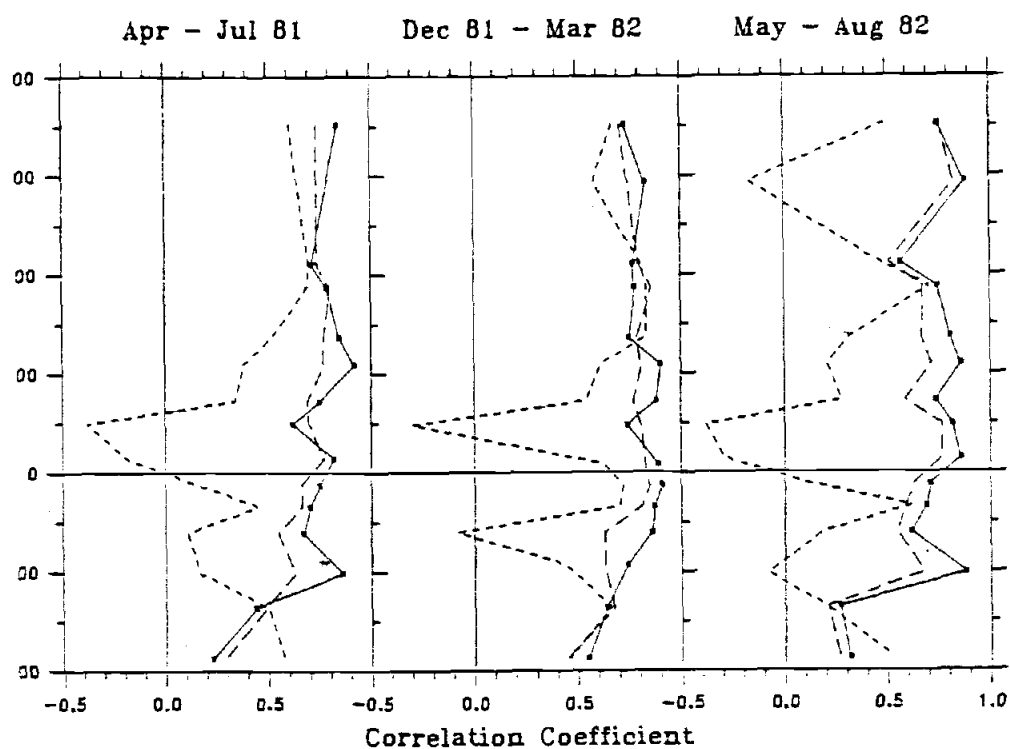


Fig. III.7: Correlation coefficients between measured and calculated winds. The correlation coefficients of alongshore wind (solid), across-shore winds (short dashes), and the inner correlation coefficients of vector winds (long dashes), are plotted as a function of y for the three seasons. Correlation coefficients > 0.35 are statistically significant to a 95% level of confidence (see Appendix C).

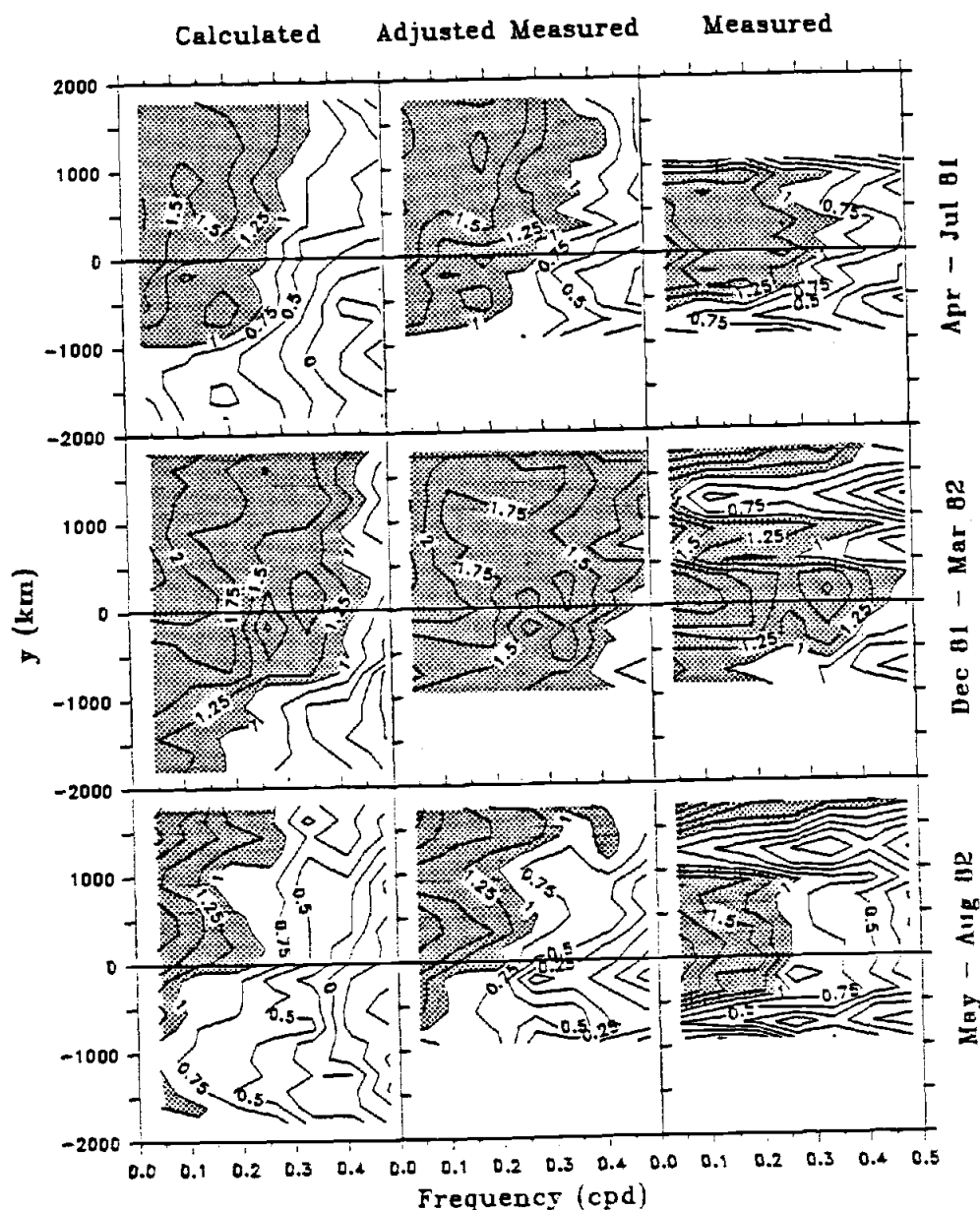


Fig. III.8: Autospectra of calculated, adjusted measured, and measured alongshore winds for the three seasons. The contours are of $\log_{10}[S(y, \omega)]$, with S in units of $\text{m}^2 \text{s}^{-2} \text{cpd}^{-1}$. The number of degrees of freedom is 18. The 95% confidence limits are between $\log_{10}S - 0.24$ and $\log_{10}S + 0.34$ at all y and ω . The autospectra are shaded where $S(y, \omega) > 10^1$. Autospectra for measured winds north of QUI ($y = 1055$ km) are not contoured due to the large data gap between QUI and CSJ ($y = 1760$ km). The frequencies at which spectrum estimates exist are shown in Fig. III.14.

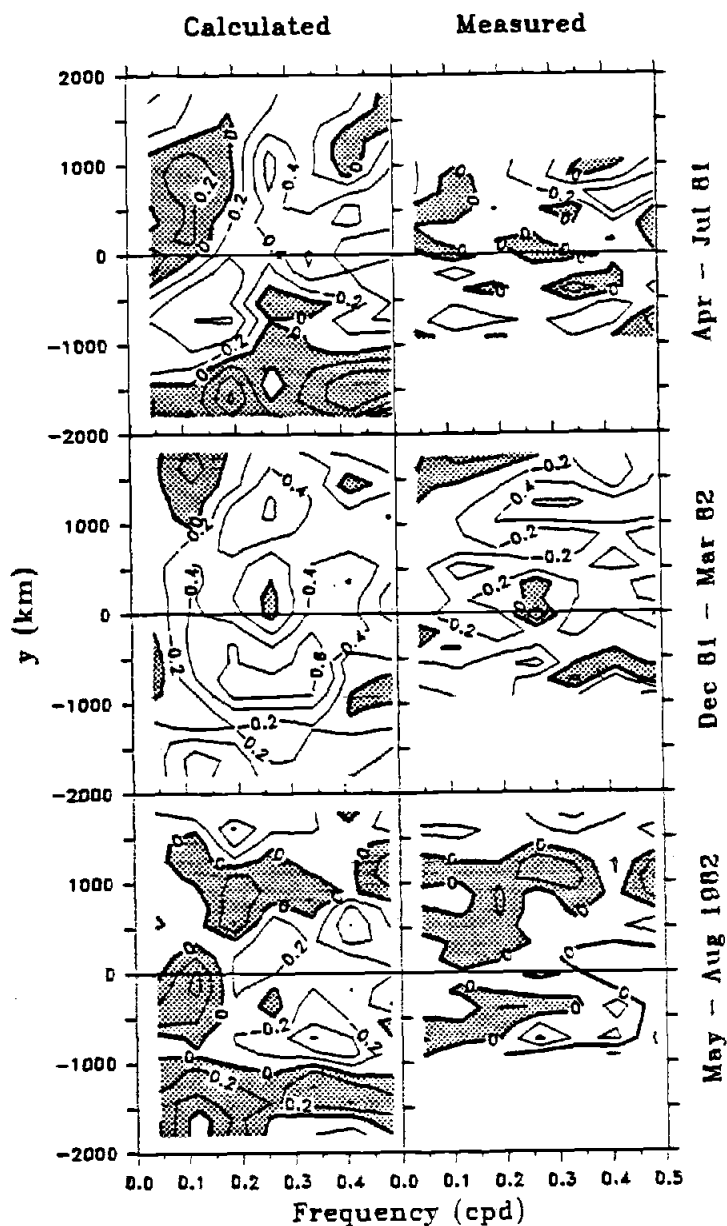


Fig. III.9: Contours of rotary coefficients $[S_r(y, -\omega) - S_r(y, +\omega)] / [S_r(y, -\omega) + S_r(y, +\omega)]$ for calculated and measured vector winds for the three seasons. The coefficients for adjusted measured winds are identical to those for measured winds. Positive coefficients (anticyclonic variance exceeds cyclonic) are shaded. A rotary coefficient of +1 (-1) indicates that cyclonic (anticyclonic) variance is zero. The frequencies at which estimates exist are shown in Fig. III.14.

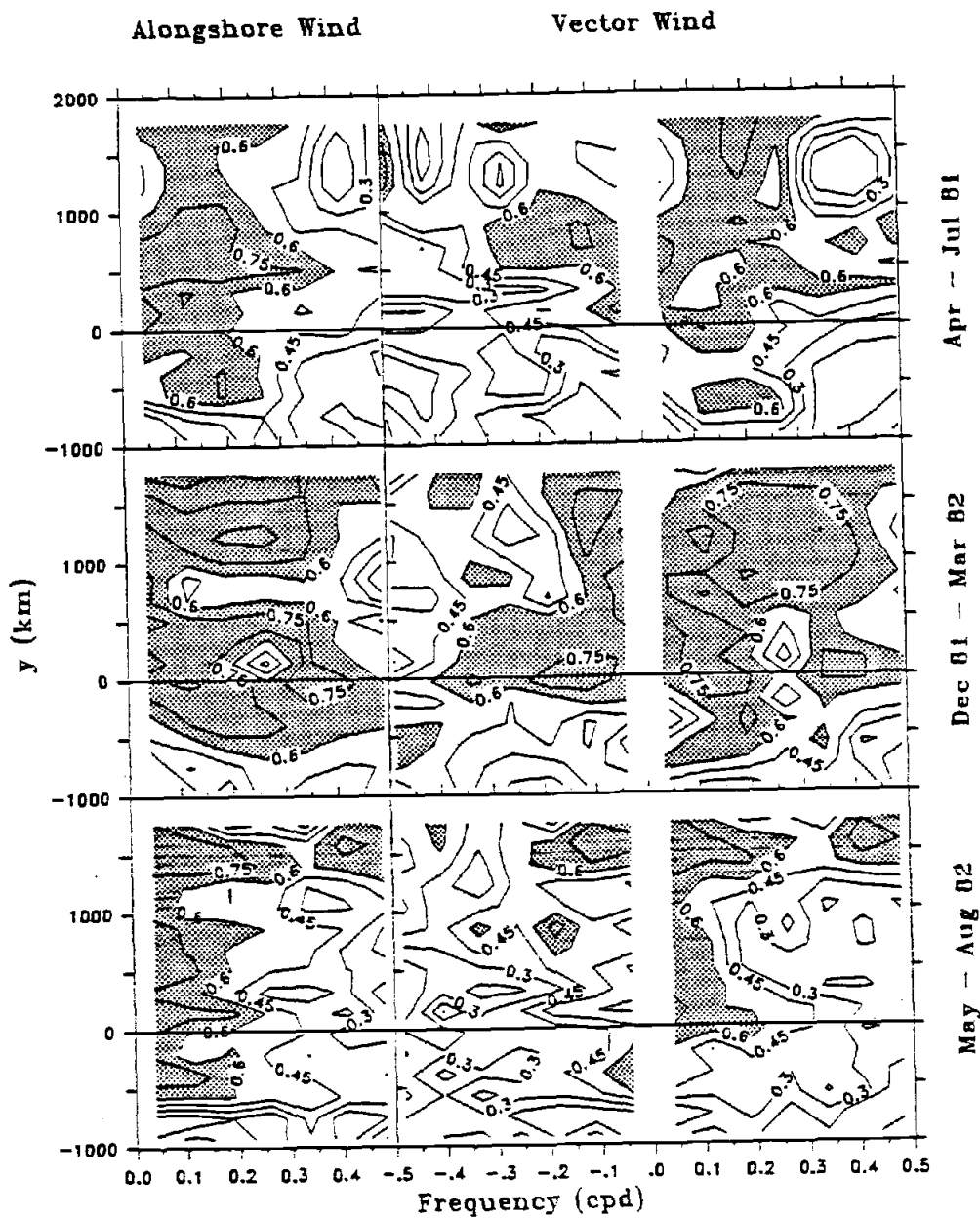


Fig. III.10: The squared coherences between measured and calculated alongshore winds and squared rotary coherences between measured and calculated vector winds contoured as a function of frequency and y for the three seasons. Squared coherences greater than 0.6 are shaded, and those greater than 0.16 are statistically significant to a 95% level of confidence. The frequencies at which coherence estimates exist are shown in Fig. III.14.

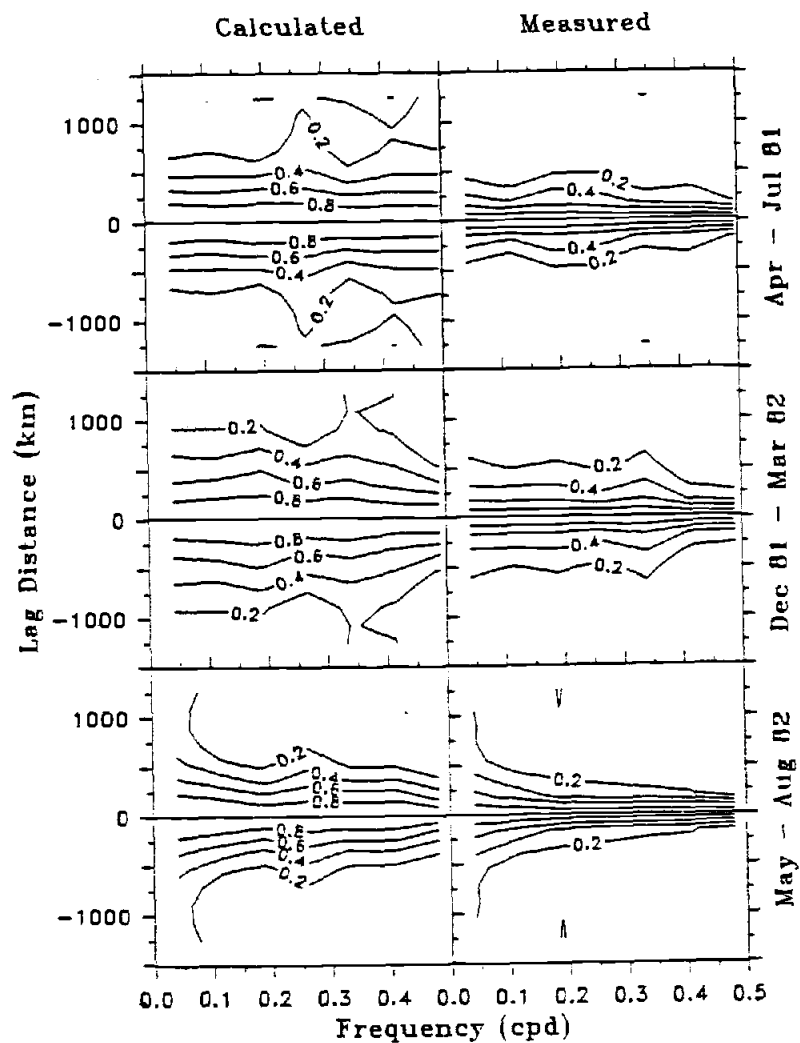


Fig. III.11: The space-frequency squared coherence γ^2 , calculated from space-averaged autospectra and cross-spectra [Eq. (4.1)] for calculated and measured alongshore winds over grid points 4 through 13 for the three seasons. The frequencies at which estimates exist are shown in Fig. III.14;

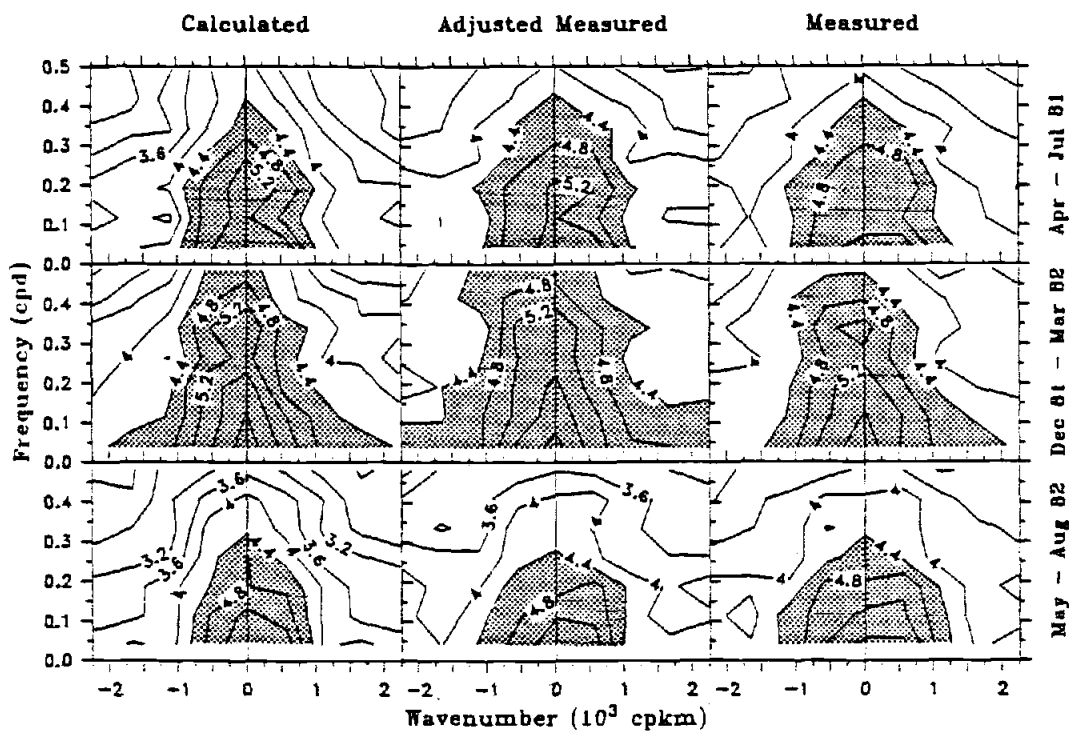


Fig. III.12: Wavenumber-frequency autospectra of calculated, adjusted measured, and measured alongshore winds over grid points 4 through 13 for the three seasons. The contours are of $\log_{10}[S(\pm l, \omega)]$, with S in units of $m^2 s^{-2} cpd^{-1} cpkm^{-1}$. The autospectra have been band-averaged over nine frequency bands only, so the resulting number of degrees of freedom is 18 (Halliwell and Allen, 1986). The 95% confidence limits are between $\log_{10} S - 0.24$ and $\log_{10} S + 0.34$ at all l and ω . The autospectra are shaded where $S(\pm l, \omega) > 10^{4.4}$. The wavenumbers and frequencies at which spectrum estimates exist are shown in Fig. III.14.

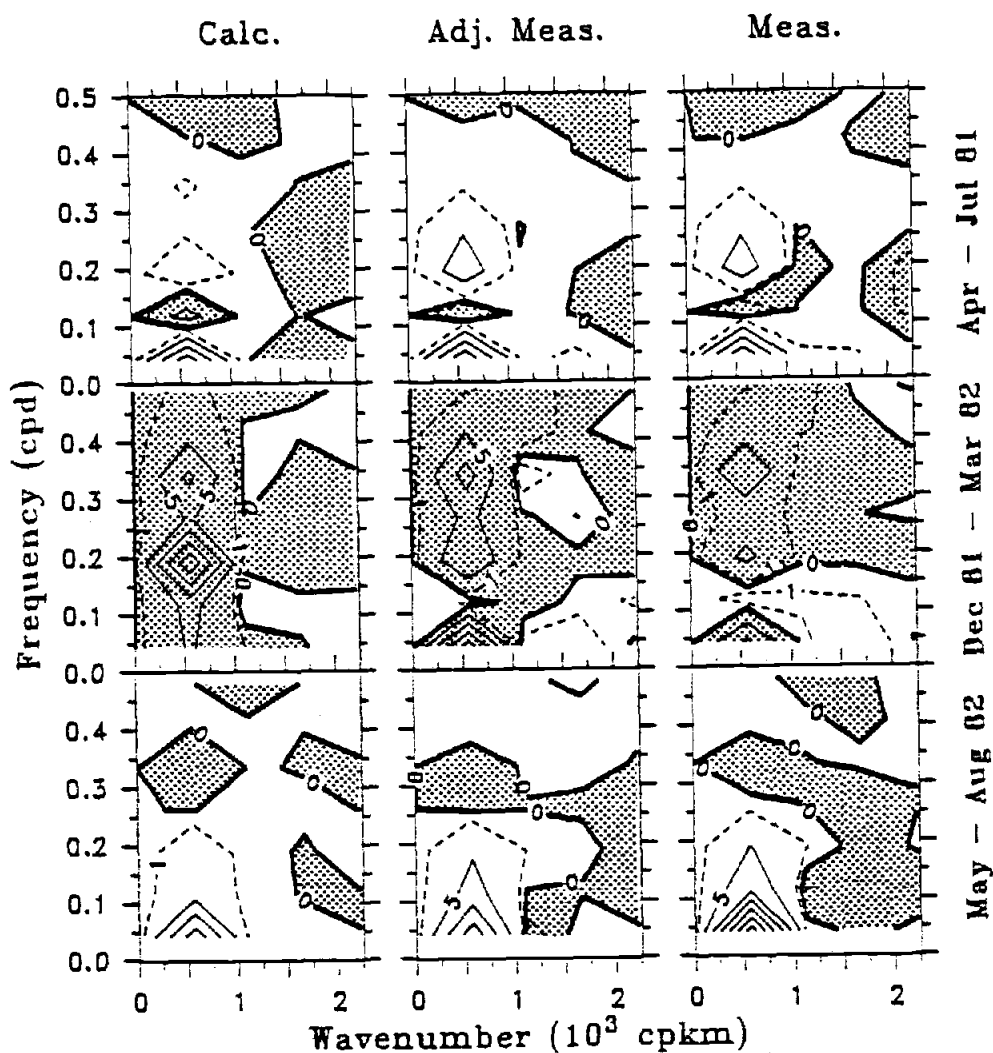


Fig. III.13: Wavenumber-frequency propagating autospectra of calculated, adjusted measured, and measured alongshore winds over grid points 4 through 13 for the three seasons. The contours are of $10^{-4}[S(+l, \omega) - S(-l, \omega)]$, with S in units of $m^2 s^{-2} cpd^{-1} cpkm^{-1}$. The number of degrees of freedom is 18. Negative (equatorward-propagating) autospectra are shaded. The wavenumbers and frequencies at which spectrum estimates exist are shown in Fig. III.14.

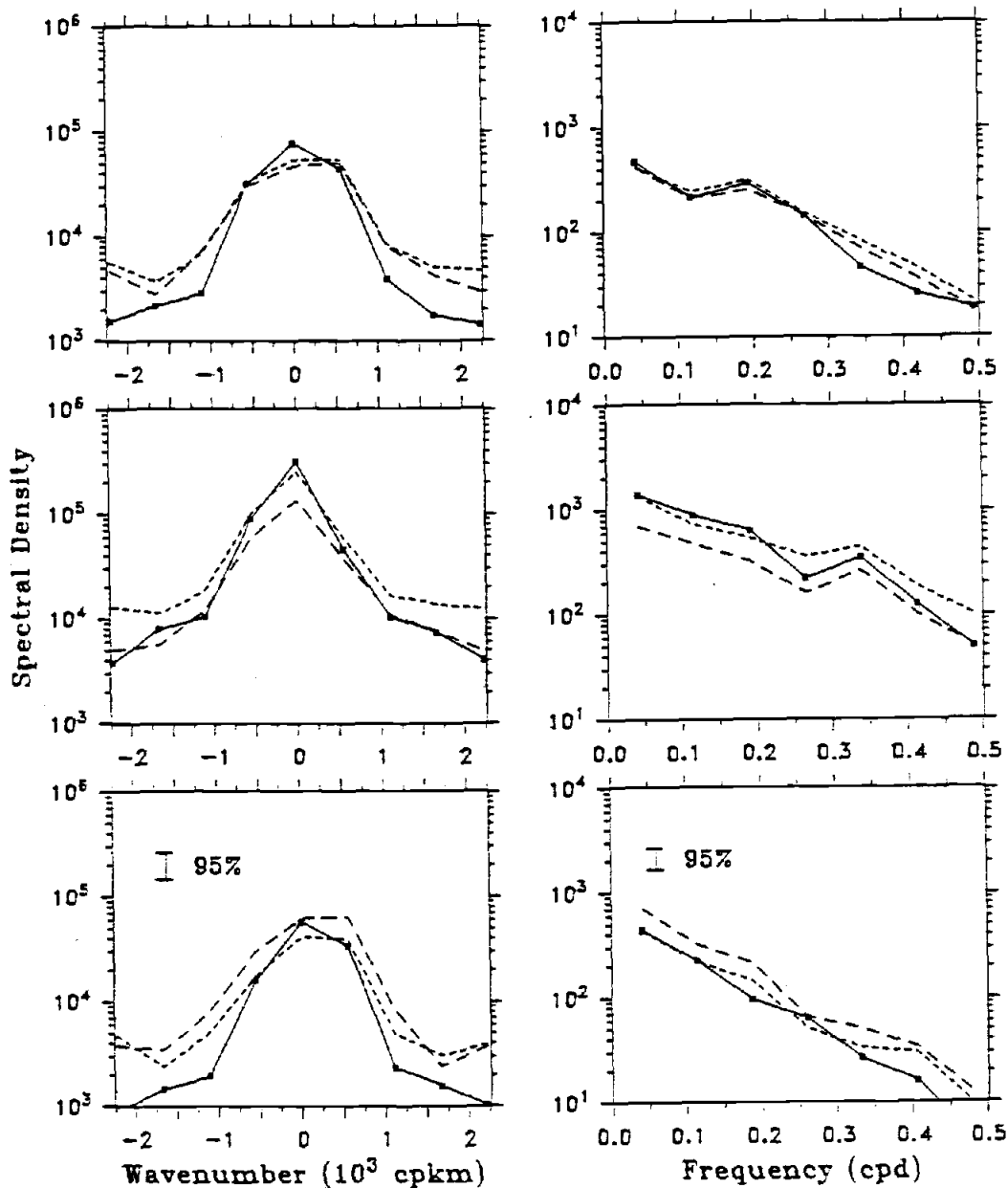


Fig. III.14: Integrated wavenumber autospectra (left) and integrated frequency autospectra (right) for calculated (solid), adjusted measured (short dashes), and measured (long dashes) alongshore winds over grid points 4 through 13 for the three seasons. The integrated wavenumber (frequency) autospectra are computed with 126 (198) degrees of freedom. 95% confidence bands are shown.

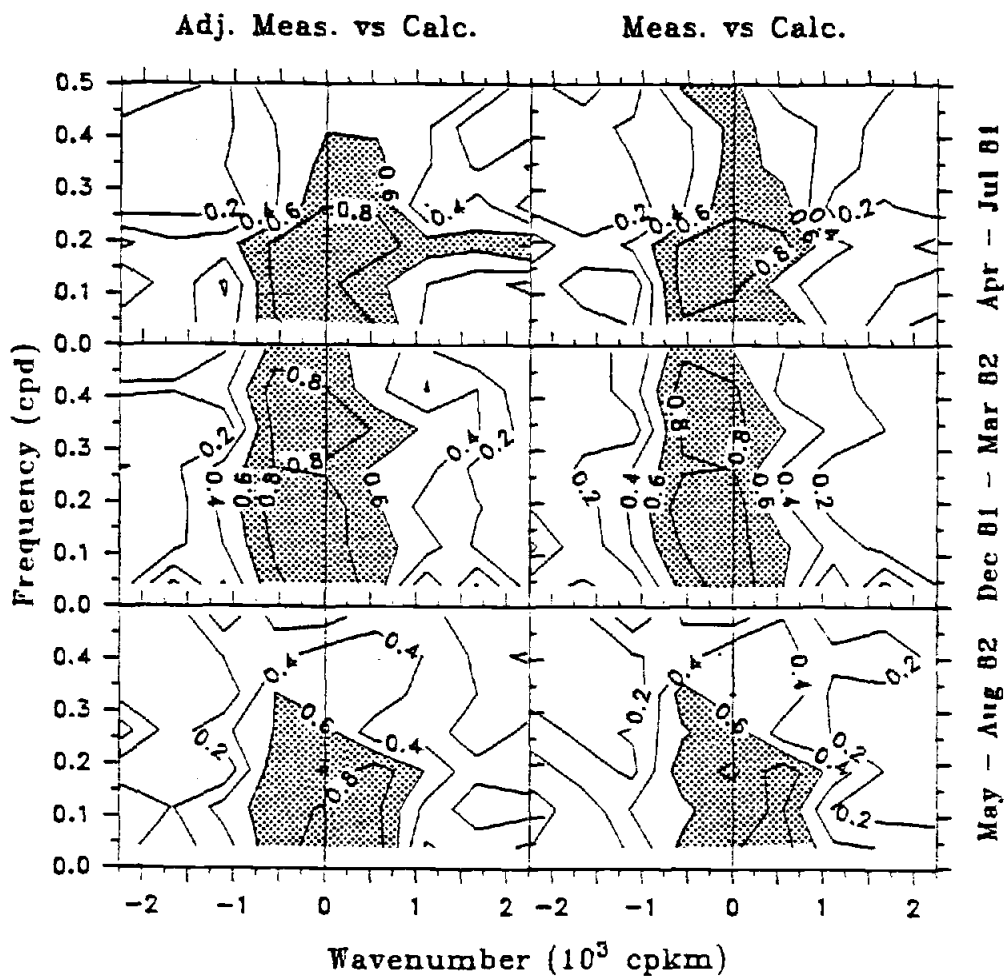


Fig. III.15: Wavenumber-frequency squared coherences between adjusted measured and calculated, and between measured and calculated, alongshore winds, over grid points 4 through 13 for the three seasons. Squared coherences greater than 0.6 are shaded. Squared coherences greater than 0.16 are significant to a 95% level of confidence. The wavenumbers and frequencies at which coherence estimates exist are shown in Fig. III.14.

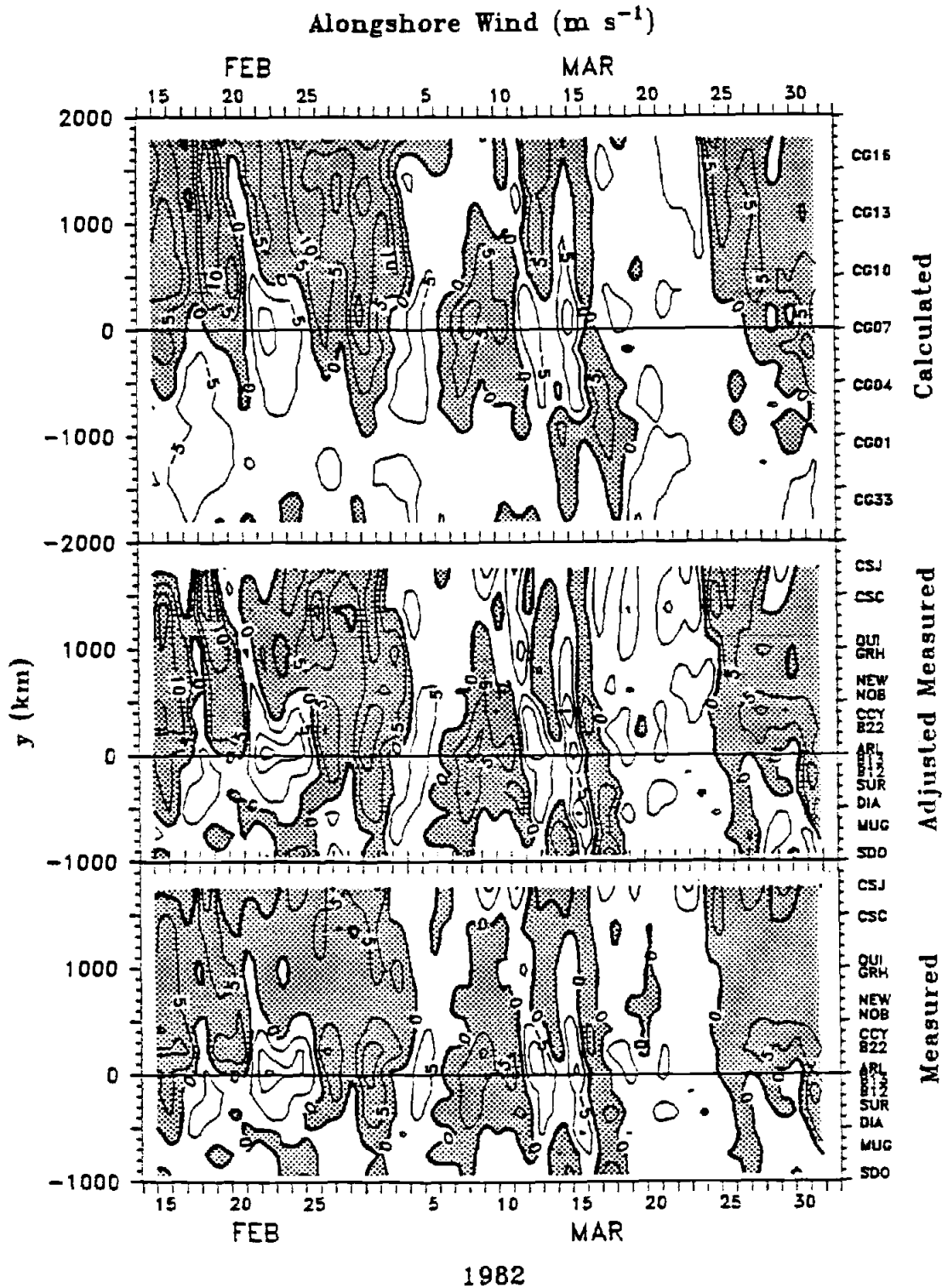
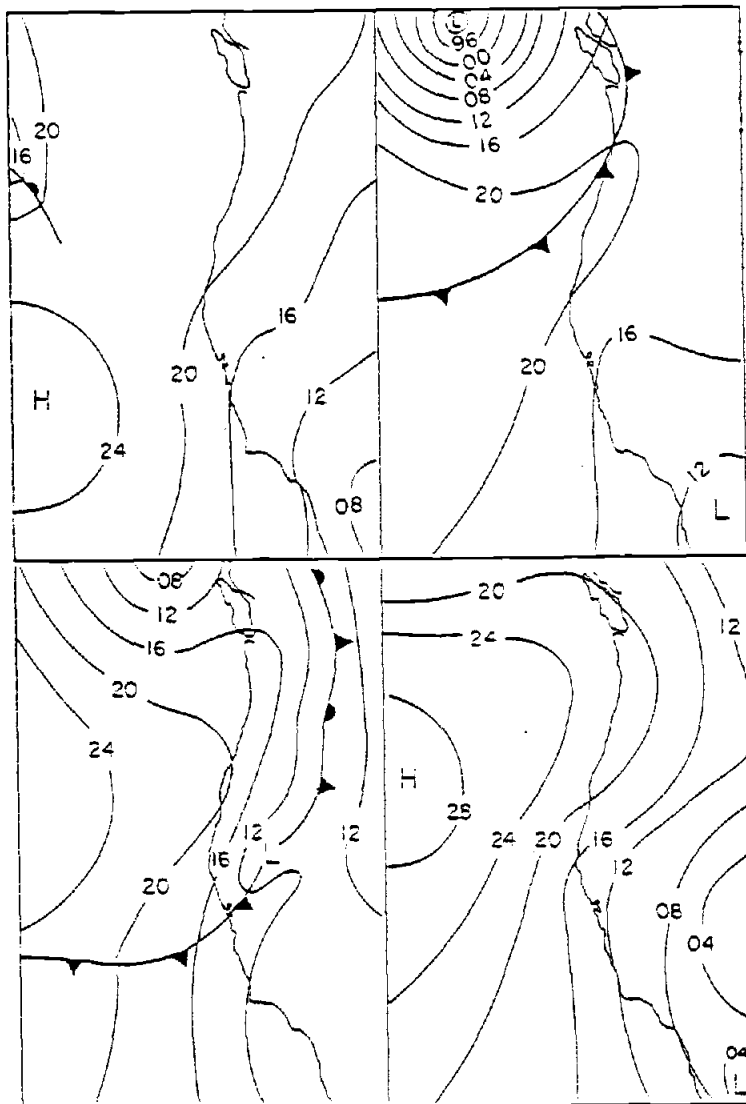


Fig. III.17: As in Fig. III.16, except for 15 February through 31 March 1982. The contour interval here is $5 m s^{-1}$.

12Z 15 May 12Z 16 May



09Z 17 May 12Z 18 May
1982

Fig. III.19: Surface atmospheric pressure charts for 11 to 14 March 1982 (from National Weather Service surface meteorological charts).

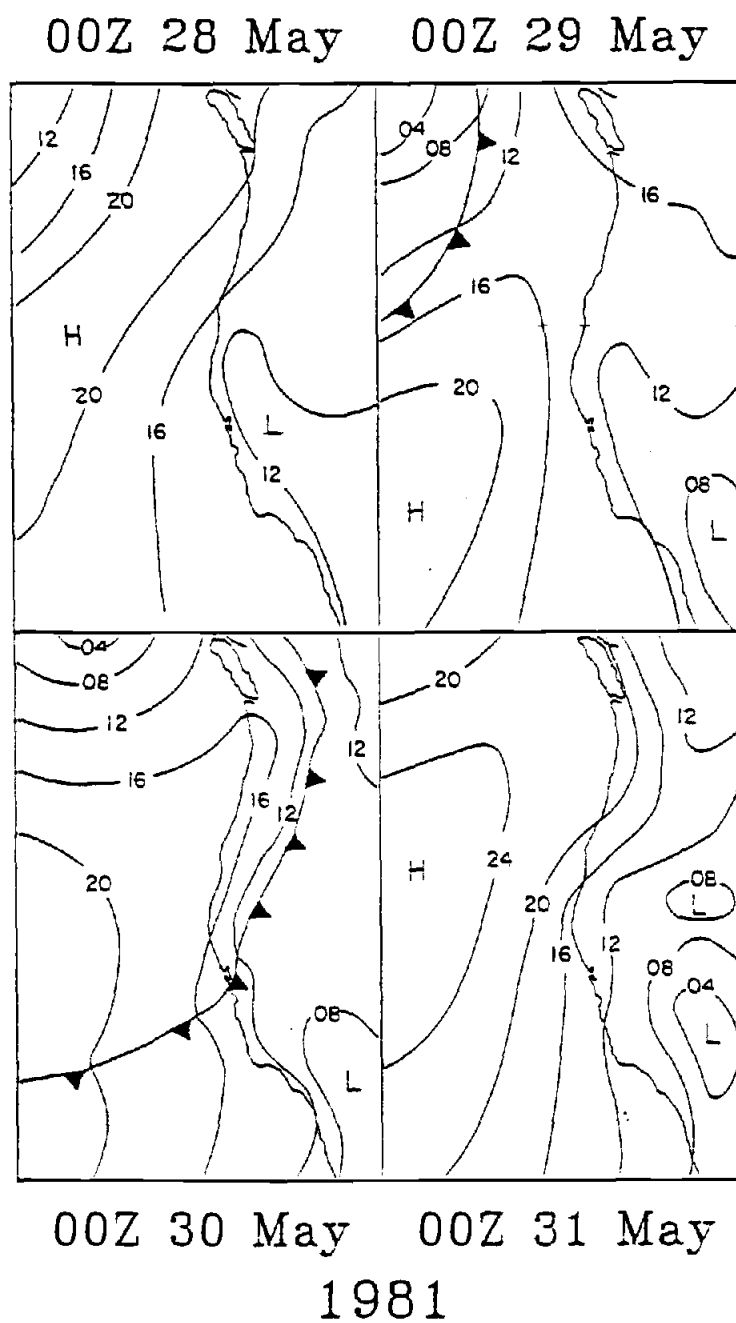


Fig. III.20: As in Fig. III.19, except for 28 to 31 May 1981.

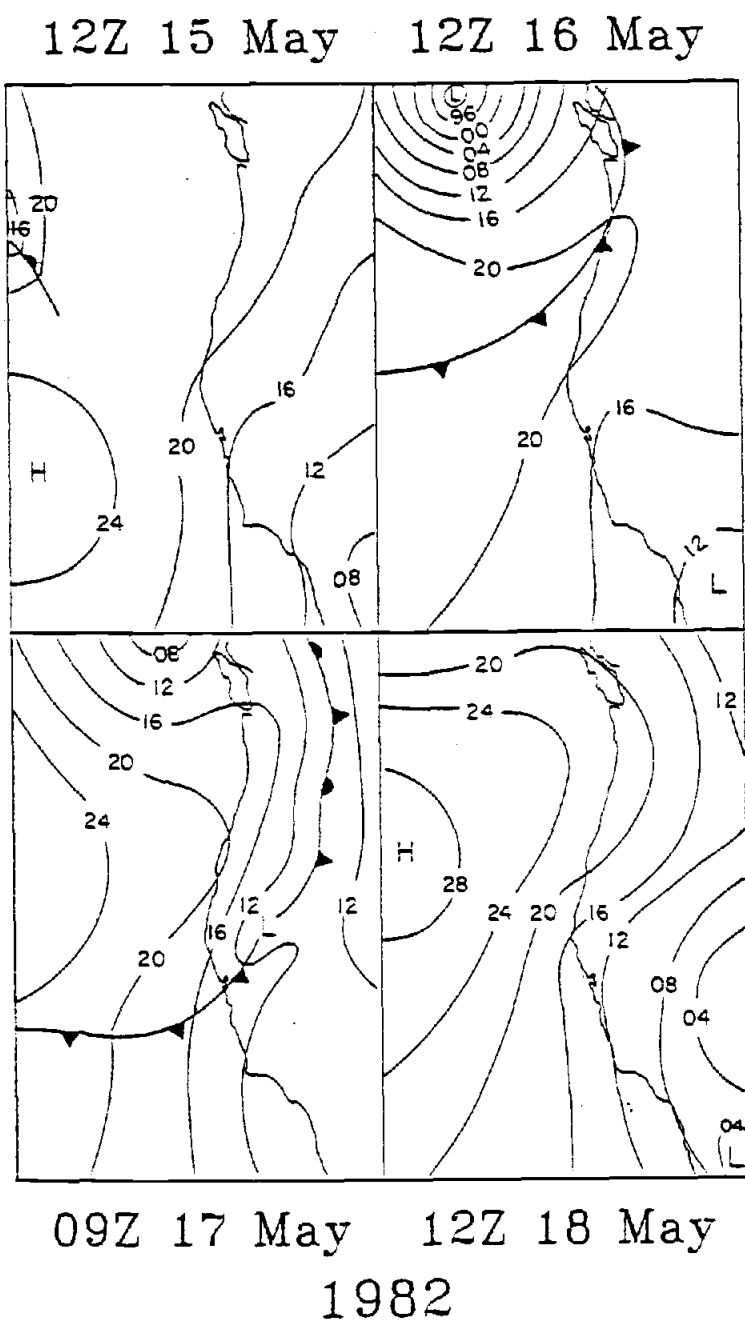


Fig. III.21: As in Fig. III.19, except for 15 to 18 May 1982.

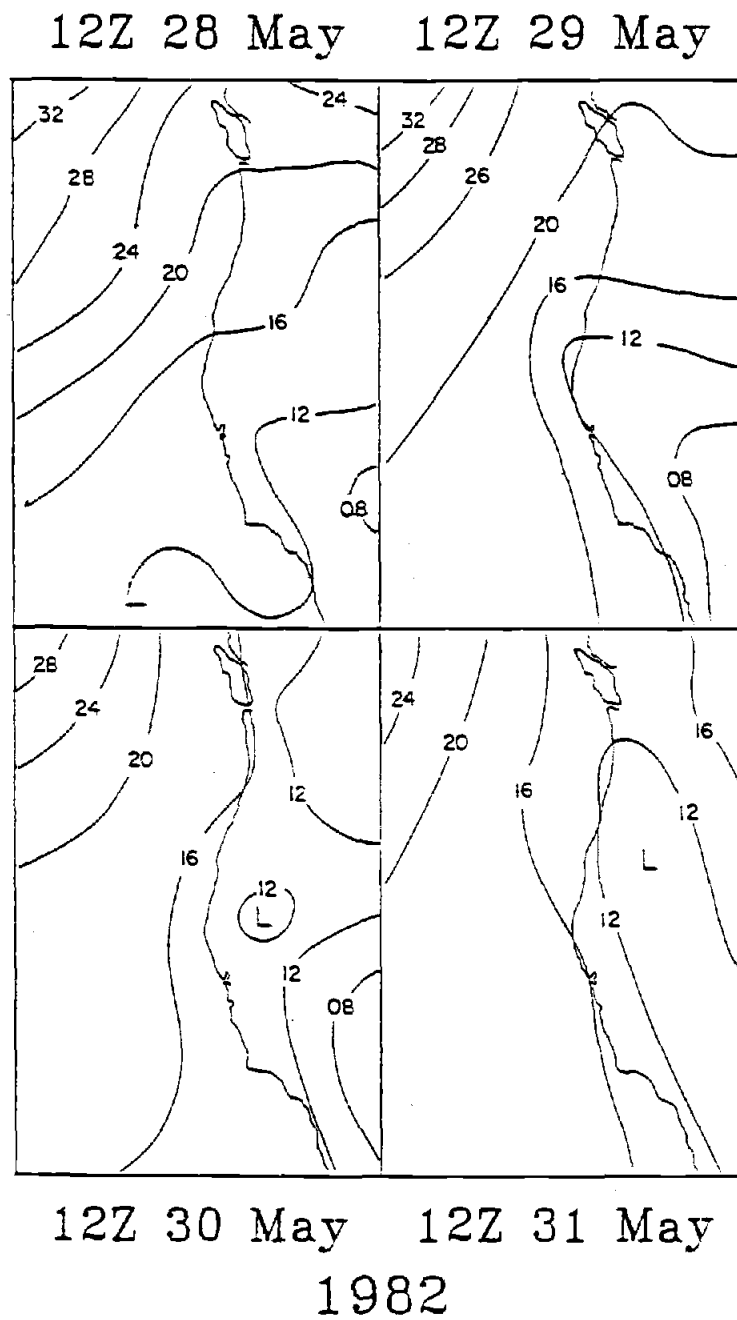


Fig. III.22: As in Fig. III.19, except for 28 to 31 May 1982.

CHAPTER IV

Wavenumber-Frequency Domain Properties of Coastal Sea
Level Response to Alongshore Wind Stress Along the West
Coast of North America, 1980-84

ABSTRACT

Fluctuations in alongshore wind stress (τ) calculated from FNOG geostrophic winds along the west coast of North America are relatively energetic at alongshore wavenumbers $|\ell| \leq 1.1 \times 10^{-3}$ cpkm and frequencies $0.025 < \omega < 0.5$ cpd, and they effectively drive a coastal sea level (ζ) response within this (ℓ, ω) band. Equatorward propagation ($\ell < 0$) dominates the winter τ fluctuations for $\omega < 0.35$ cpd, and poleward propagation ($\ell > 0$) dominates the summer τ fluctuations for $\omega < 0.1$ cpd. In contrast, poleward propagation strongly dominates the ζ fluctuations in both seasons, but more so in summer. The largest coherence between ζ and τ is observed in that part of (ℓ, ω) space where τ is most energetic; i.e., for $0 \leq \ell \leq 1.1 \times 10^{-3}$ cpkm in summer and $-1.1 \times 10^{-3} \leq \ell < 0$ cpkm in winter. Results are compared with predictions from theoretical models for wind-driven coastally trapped waves. The observed transfer functions show evidence for near-resonant ζ response in both seasons, with the maximum gain occurring along a single ridge of approximately constant poleward phase speed, along

which the response is approximately in-phase with τ . This behavior is consistent with a response dominated by one coastally trapped wave mode governed by a forced, first-order wave equation with a linear friction term. The maximum gain decreases substantially along this ridge with increasing l and ω in both seasons, and the resulting region where the largest gain is observed is confined to smaller l and ω in winter than in summer. This observed decrease in maximum gain is not predicted by a single wave equation. It is shown that the contribution of higher wave modes to the total ζ response may explain a part of this observed decrease.

IV.1. INTRODUCTION

Considerable observational and theoretical evidence has accumulated indicating that free perturbations in current and pressure over a continental shelf propagate alongshore with the coast to the right (left) in the Northern (Southern) Hemisphere (e.g., Allen, 1980). Based on scaling arguments in the equations of motion, the alongshore component of wind stress at the coast (τ) is the most important atmospheric forcing variable for perturbations with large alongshore scales (\gg shelf/slope width). Halliwell and Allen (1984) showed that the coastal ocean response tends to be larger for τ disturbances that propagate alongshore in the same direction as free coastal sea level (ζ) perturbations as opposed to τ disturbances that remain stationary or propagate in the opposite direction. The coastal ocean response therefore

depends in part on the alongshore wavenumber and frequency domain properties of the τ field. The properties of this response have never been studied in wavenumber-frequency space.

As part of the large-scale component of the Coastal Ocean Dynamics Experiment (CODE), we characterize properties of the τ and ζ fields, and of the ζ response to τ , during four spring/summer upwelling seasons and four winter seasons between May 1980 and March 1984. In this paper, we focus primarily on the large scale (small wavenumber) properties of these fields in wavenumber-frequency space determined using auto- and cross-spectrum analysis. We describe these observed properties and relate them to predictions from simple coastal circulation models.

The simplest linear models predict that the coastal circulation response to variable alongshore wind stress with large alongshore scales consists of an infinite number of coastally trapped wave modes, with the alongshore-time variability of each mode governed by a forced, first-order wave equation with a linear friction term. Given an alongshore-time (y,t) coordinate system, where y is positive poleward along the west coast of North America, the wave equation for mode n of a given coastal circulation response variable $Y_n(y,t)$ is

$$c_n^{-1} Y_{nt} + Y_{ny} + (c_n T_{fn})^{-1} Y_n = b_n \tau, \quad (\text{IV.1.1})$$

where c_n are the free wave phase speeds, T_{fn} are the friction time scales, and b_n are the transfer coefficients. These modal

equations (without the friction term) were first derived by Gill and Schumann (1974) for a barotropic fluid over a continental shelf and by Gill and Clarke (1974) for coastal Kelvin waves in a stratified fluid. Clarke (1977) derives similar frictionless equations for a continental shelf with horizontally uniform basic stratification. Major simplifying assumptions, such as neglecting the alongshore dependence of bottom topography, must be made in these derivations. The linear friction term in (IV.1.1) is added in an ad hoc manner in these early studies. Brink (1982) shows that if friction is sufficiently strong, each mode becomes frictionally coupled to all other modes.

In previous studies where one mode was assumed to dominate the response, (IV.1.1) was found to predict the ζ response at a given location along the coast with reasonably good accuracy (Hamon, 1976; Clarke, 1977; and Halliwell and Allen, 1984). It was also found to predict the nature of certain observed statistical relationships between the response and τ (Allen and Denbo, 1984). In the present study, we determine that (IV.1.1) qualitatively predicts many of the observed properties of the ζ response to τ in wavenumber-frequency space. More importantly, however, we find response properties that are not predicted, revealing limitations to (IV.1.1) that were not detected in the earlier studies.

We first describe the τ and ζ data sets and discuss certain properties of these sets that may affect our analyses (Section IV.2). We then discuss the basic statistical properties

of the τ and ζ fields in summer and winter, comparing some of these properties to those observed by Halliwell and Allen (1984) during summer 1973 and predicted from (IV.1.1) by Allen and Denbo (1984) (Section IV.3). We then present the ζ and τ wavenumber-frequency autospectra (Section IV.4), and discuss the observed properties of the ζ response to τ in wavenumber-frequency space (Section IV.5). In these wavenumber-frequency space analyses, we discuss the similarities and differences in the observed properties of the forcing and response between summer and winter, plus the interannual variability in these properties for each season. Finally, we compare the observed response properties in wavenumber-frequency space to those predicted by (IV.1.1) (Section IV.6).

IV.2. THE DATA

We analyze the response of ζ to τ within a 2700 km domain along the west coast of North America, stretching approximately from San Diego (32.7°N) to near the Alaska/British Columbia border (54.1°N). We use an alongshore-time (y,t) coordinate system, with the $y = 0$ km coordinate located at the central line of the intensive CODE experiments (38.7°N) (Winant, *et al.*, 1986), and analyze data interpolated to points of the CODE analysis grid (Fig. IV.1, Table IV.1). Grid point 7 is located at $y = 0$ km and the alongshore spacing of the points is $\Delta y = 180$ km. Our common analysis domain for both ζ and τ includes grid points 2 through 17

($-900 \leq y \leq 1800$ km) since no coastal sea level data were available from point 1 south. However, τ is also available at grid points south to central Baja California (grid point 32; $y = -1800$ km). We study four spring/summer (hereafter referred to as summer) and four winter seasons, all of which are 121 days long:

1. 1 May to 29 August 1980,
2. 4 April to 2 August 1981 (CODE-1 experiment),
3. 1 May to 29 August 1982 (CODE-2 experiment),
4. 1 May to 29 August 1983,
5. 25 November 1980 to 25 March 1981,
6. 1 December 1981 to 31 March 1982,
7. 1 December 1982 to 31 March 1983, and
8. 27 November 1983 to 26 March 1984.

We refer to the individual seasons as summers 1980 through 1983 and winters 1980-81 through 1983-84. All summer seasons begin after the spring transition (Strub, et al., 1986), which occurs between late March and mid-April. All winter seasons are chosen to terminate before the transition, which explains their staggered times. All summer seasons begin on 1 May except for summer 1981, which is shifted to better coincide with the extensive instrument deployments of the CODE-1 experiment (Winant, et al., 1986).

Coastal sea level data are obtained at several stations (Fig. IV.1 and Table IV.2) for all eight seasons. Sea level time series are checked for bad values and datum shifts (Pittock, et al., 1982). Details of the remaining editorial procedure are

contained in Halliwell, et al. (1986). To create ζ time series, sea level heights are adjusted to represent coastal subsurface pressure by adding FNOC surface atmospheric pressure in mb from the nearest CODE grid point to sea level in cm if that point is within 30 km of the sea level station. If it is farther away, atmospheric pressure linearly interpolated between the two nearest grid points is used. The mean ζ is removed from all time series for each individual season. We use ζ as the response variable because it is available over a sufficiently large alongshore domain to resolve some of the large scales present in the coastal ocean response along the west coast of North America.

We compute τ time series using geostrophic winds obtained from the Fleet Numerical Oceanography Center (FNOC) (Bakun, 1975; Halliwell and Allen, 1986a) and interpolated to the CODE analysis grid. We hereafter refer to this field as calculated τ . The coarse spatial resolution of calculated τ effectively restricts its use to represent fluctuations with wavelengths greater than several hundred kilometers. Calculated τ is used for the four-year study interval because the highest quality CODE large-scale measured wind data set exists primarily for 1981-82, and because calculated winds are readily obtainable over a larger alongshore domain than measured winds. The properties of, and relationships between, the calculated and measured wind fields are discussed by Halliwell and Allen (1986a). To assess the effects of using calculated τ in the present analysis, we study properties of wavenumber-frequency auto-

and cross-spectra of calculated τ , measured τ , and ζ using measured winds from several stations (Fig. IV.1 and Table IV.3) for summers 1981 and 1982, plus winter 1981-82 (Sections IV.4.3 and IV.5.3). Information on the measured wind stations and details of wind data processing are presented in Halliwell and Allen (1983, 1985) and Halliwell, et al. (1986).

Vector wind stress is computed from vector wind 10 m above the surface (\vec{V}_{10}) in units of m s^{-1} using the bulk aerodynamic formula with the drag coefficient determined from the regression formula of Large and Pond (1981):

$$\vec{\tau} = \rho_a C_d |\vec{V}_{10}| \vec{V}_{10} \quad (\text{IV.2.1})$$

with

$$10^3 C_d = \begin{cases} 1.2 & |\vec{V}_{10}| \leq 11 \text{ m s}^{-1} \\ 0.49 + 0.065 |\vec{V}_{10}| & |\vec{V}_{10}| > 11 \text{ m s}^{-1} \end{cases} \quad (\text{IV.2.2})$$

where ρ_a is the air density and C_d is the drag coefficient. Where necessary, measured winds are adjusted to represent 10 m winds assuming neutral stability (Halliwell, et al., 1986). We assume that the calculated winds received from FNOC represent 10 m winds. Before computing the alongshore component of the wind stress, the calculated vector wind stress is rotated as described in Halliwell and Allen (1986a) to improve the boundary layer correction of Bakun (1975). We use the geographical alongshore component of the

measured vector wind stress. All τ and ζ time series are low-pass filtered with a half-amplitude period of 40 hr, and the time sampling rate is $\Delta t = 0.25$ days.

Wind velocity usually varies in the across-shore direction over the continental shelf, and may also be directly influenced by local topography at the coast. Partly because the measured wind set consists of a mixture of coastal land stations and offshore buoys, the variance of measured and calculated alongshore winds differ substantially at many locations along the coast. Halliwell and Allen (1986a) found that it was not possible to adjust measured coastal land winds to represent winds over the outer continental shelf within the CODE large-scale domain in a consistent manner. They also found, however, that the wavenumber-frequency auto- and cross-spectra of alongshore wind were not sensitive to the distribution of wind variance along the coast.

Since τ is a nonlinear function of \bar{V}_{10} , and since the drag coefficient is a function of wind speed if it exceeds 11 m s^{-1} , any differences in alongshore wind variance will be amplified in τ . In this paper, we roughly evaluate the influence of the distribution of τ variance along the coast on our analyses by including analysis results for adjusted measured τ wherever we compare analysis results for calculated τ to those of measured τ . To form adjusted measured τ , we simply scale the amplitude of measured τ so that its variance equals the calculated τ variance at that alongshore location. (We do not intend to imply by this choice that the

calculated τ field represents the alongshore distribution of τ variance more accurately than the measured τ field.) These results essentially show that the wavenumber-frequency auto- and cross-spectrum analyses presented in this paper are also not sensitive to the distribution of τ variance along the coast.

IV.3. BASIC STATISTICAL PROPERTIES OF THE WIND STRESS AND SEA LEVEL FIELDS

IV.3.1 Means and RMS Amplitudes

Substantial differences in the basic statistics of the τ and ζ fields exist between summer and winter. (We always use τ to refer to calculated τ . We will use the phrase "calculated τ " only when it must be distinguished from measured τ .) The mean of τ is negative (equatorward) within the entire CODE large-scale domain in summer, but is negative only for $y \leq -360$ km in winter (Fig. IV.2). The magnitude of the summer mean is largest within the alongshore subdomain $-720 < y < 180$ km, where it typically exceeds 1 dy cm^{-2} equatorward. The summer mean calculated τ does not accurately represent the actual mean within the Southern California Bight ($-1000 < y < -575$ km) since calculated alongshore and vector wind means differ substantially from the corresponding measured wind means within the Bight in summer (Halliwell and Allen, 1986a). The winter equatorward means for $y < -360$ km are relatively small ($|\tau| \leq 0.35 \text{ dy cm}^{-2}$), but the poleward means are substantially

larger for $y \geq 180$ km, exceeding 2 dy cm^{-2} at the northern end of the CODE large-scale domain. The observed properties of seasonal mean τ generally agree with seasonal differences in the properties of the alongshore component of monthly mean wind stress near the coast computed from ship reports for 1° squares (Nelson, 1977). The one major difference is that mean calculated τ changes sign in winter near $y = -360$ km, while Nelson's data indicate the sign change is near Cape Mendocino ($y \approx 200$ km) during winter months.

For summer, the largest rms amplitude of τ exists in the subdomain $-720 < y < 180$ km, the same subdomain where mean equatorward τ is largest (Fig. IV.2). The maximum summer rms amplitude is 0.79 dy cm^{-2} at $y = 180$ km (near Cape Mendocino). The rms amplitude generally increases for increasing y in winter. The winter rms amplitude increases substantially poleward from $y = -900$ km (0.32 dy cm^{-2}) to a relative maximum at $y = 360$ km (1.72 dy cm^{-2}). It is approximately constant near 1.65 dy cm^{-2} in the subdomain $540 \leq y \leq 900$ km. It then increases rapidly poleward of $y = 900$ km to 3.48 dy cm^{-2} at $y = 1800$ km. The rms amplitude of ζ is also substantially greater in winter than in summer, but in contrast to τ , similar patterns in the alongshore distributions of ζ rms amplitudes are observed in both seasons (Fig. IV.2). In both summer and winter, the ζ amplitudes are roughly constant for $y < -360$ km, increase with increasing y for $-360 \leq y \leq 900$ km, then decrease with increasing y for $y > 900$ km. The summer poleward increase is from 2.91 cm at $y = -360$ km to 6.10 cm at $y = 900$ km.

The corresponding winter increase is from 4.27 cm to 10.15 cm.

The strikingly different seasonal changes in the rms amplitudes of τ and ζ are evident from the ratios of winter to summer rms amplitude plotted as a function of y (Fig. IV.3). Equatorward of the CODE site, the amplitude of τ is between 1 and 1.6 times larger, and the amplitude of ζ is between 1.35 and 1.5 times larger, in winter than in summer. Poleward of the CODE site, the ratio for ζ increases slightly to values typically between 1.6 and 1.75, but the ratio for τ increases very sharply, reaching 5.0 at a relative maximum at $y = 1080$ km, then reaching 7.4 at $y = 1800$ km. Therefore, the increases in τ and ζ rms amplitudes in winter over summer have similar magnitudes equatorward of the CODE site, but the τ increase becomes much larger than the ζ increase poleward of the CODE site. This winter increase depends substantially on the choice of C_d . Calculated wind speeds exceeding 11 m s^{-1} are uncommon in summer, but occur more frequently in winter, especially to the north of the CODE site. The ratio plotted in Fig. IV.3 for τ decreases by about 50% at grid point 17 ($y = 1800$ km) if a constant C_d is used. We address other possible causes of this y -dependent seasonal change in our discussion of the wavenumber-frequency spectrum analyses.

IV.3.2 Correlation/Coherence Scales and Alongshore Propagation

We estimate the correlation space and time scales, plus the alongshore propagation properties, of the τ and ζ fluctuations

using the spatially-averaged, space-time auto- and cross-correlation functions $R_{\tau\tau}(\eta_n, t_\ell)$, $R_{\zeta\zeta}(\eta_n, t_\ell)$, and $R_{\zeta\tau}(\eta_n, t_\ell)$, calculated for both summer (grid points 4 through 17) and winter (grid points 2 through 17) (Fig. IV.4). Grid points 2 and 3 are not included in summer since calculated winds poorly represent coastal winds in the Southern California Bight (Halliwell and Allen, 1986a). The methods used to calculate these functions and the integral correlation space and time scales are presented in Appendix D. The correlation space scales of τ are 699 km in summer and 988 km in winter (Table IV.4). The correlation time scales of τ are 1.36 days in summer and 1.21 days in winter. The τ space scale is 41% greater in winter than in summer and the τ time scale is 11% greater in summer than in winter. The space and time scales of ζ are both substantially larger than those of τ . The space scale of ζ is 1085 (1324) km in summer (winter), and the time scale of ζ is 3.48 (3.51) days in summer (winter). The ζ space scale is 22% greater in winter than in summer, but the ζ time scale is nearly equal in both seasons.

The orientation of the central correlation ridge of $R_{\tau\tau}$ is determined by the propagation characteristics of the τ field (Fig. IV.4). This ridge is symmetric about the lag time and lag distance axes in summer, and therefore no preferred propagation direction is evident. Along the major axis of the ridge in winter, the ratio of space lag to time lag is about -2500 cm s^{-1} , indicating that equatorward propagation of τ fluctuations is

dominant in winter. The central correlation ridges of $R_{\zeta\zeta}$ indicate that poleward propagation of ζ fluctuations is dominant in both summer and winter (Fig. IV.4). The ζ ridges are insufficiently elongated to make accurate estimates of propagation speeds, but since ζ fluctuations are partly a forced response, these estimates do not represent free wave phase speeds (Allen and Denbo, 1984).

The maxima of the cross-correlation functions $R_{\zeta\tau}$ are 0.51 (0.55) in summer (winter), and they occur at a space lag of -360 km in both seasons, and at a time lag of -1.25 (-0.75) days in summer (winter). Thus, ζ fluctuations at a given location along the coast are most highly correlated with τ fluctuations that occur equatorward and earlier in time in both summer and winter, consistent with the summer 1973 observations of Halliwell and Allen (1984). This correlation displacement results if one coastally trapped wave mode governed by (IV.1.1) dominates the ζ response (Allen and Denbo, 1984). Free wave phase speeds of ζ can be determined from the slope of the line connecting the origin (zero space and time lags) with the peak of $R_{\zeta\tau}$ (Allen and Denbo, 1984), yielding estimates here of 330 (230 to 460) cm s^{-1} in summer and 560 (360 to 830) cm s^{-1} in winter. The error ranges for these estimates are based on an uncertainty of ± 90 km in lag distance and ± 0.125 day in lag time of the location of the $R_{\zeta\tau}$ peak. The free wave phase speed is substantially larger in winter, but due to the large uncertainty in these estimates, we cannot conclude that this difference is statistically significant. Using (IV.1.1) for more

than one mode, Chapman and Brink (1986) note that the presence of higher modes can shift the peak of $R_{\zeta\tau}$ such that these speed estimates are smaller than the lowest-mode phase speed. Consequently, the speeds estimated above may be smaller than the actual first-mode phase speed.

The summer and winter correlation ridges of $R_{\zeta\tau}$ also have distinctly different shapes (Fig. IV.4). In winter, the ridge has an extension from the correlation peak toward positive space lag and negative time lag, giving the full ridge a teardrop shape. The slope of this extension is negative and approximately equals the slope of $R_{\tau\tau}$ in winter of -2500 cm s^{-1} . This indicates that at least part of the winter ζ response propagates alongshore at the same speed as τ disturbances.

Coherence scales and propagation characteristics of the τ and ζ fields can be studied in the frequency domain using the space-lagged squared coherences $\gamma_{\tau\tau}^2(\eta_n, \omega)$, $\gamma_{\zeta\zeta}^2(\eta_n, \omega)$, and $\gamma_{\zeta\tau}^2(\eta_n, \omega)$, and phase functions $\theta_{\tau\tau}(\eta_n, \omega)$, $\theta_{\zeta\zeta}(\eta_n, \omega)$, and $\theta_{\zeta\tau}(\eta_n, \omega)$. These functions are contoured in Figs. IV.5 and IV.6, and the methods of calculating them are presented in Appendix D. We use the alongshore separation at which γ^2 decreases to its minimum significant value (0.041 - see Appendix D) as the coherence scale. It exceeds 2000 km for τ at all ω in both seasons, for ζ at $\omega < 0.15$ cycles per day (cpd) in both seasons, and for ζ near $\omega = 0.26$ cpd in summer (Fig. IV.5). The scale for ζ decreases to < 1000 km for $\omega \geq 0.34$ cpd. These scales will be substantially

smaller for measured τ than calculated τ . Halliwell and Allen (1986a) calculated γ_{vv}^2 for measured and calculated alongshore wind v and determined that measured v alongshore coherence scales were 30% to 50% smaller than those for calculated v . The same calculation made using measured and calculated τ (not shown) shows a similar decrease.

The width of the central coherence ridge for $\gamma_{\tau\tau}^2$ is nearly constant over the entire ω band (0.041 to 0.48 cpd) in summer (Fig. IV.4). If we define the coherence ridge as that part of (y, ω) space where the squared coherence is > 0.4 , then the half-width of this ridge is about 400 km in summer. In winter, the half-width is larger and decreases from about 700 km to 500 km with increasing ω over the entire ω band. In contrast, the half-widths of the central coherence ridges for $\gamma_{\zeta\zeta}^2$ vary with ω by a large amount, decreasing from 700 to 150 km (800 to 150 km) with increasing ω in summer (winter). A decrease such as this is qualitatively predicted by (IV.1.1) for one mode (Allen and Denbo, 1984).

The maximum coherence ridges for $\gamma_{\zeta\tau}^2$ are displaced toward negative space lag. In summer, the maximum coherence is at $\eta_n = -360$ km for $\omega \leq 0.11$ cpd, at $\eta_n = -180$ km for $0.11 < \omega \leq 0.26$ cpd, and at $\eta_n = 0$ km for $\omega = 0.34$ cpd. The maximum coherence is small (< 0.1) for $\omega > 0.34$ cpd. This decrease in space lag with increasing ω is predicted by (IV.1.1) (Allen and Denbo, 1984). In winter, however, the largest coherences are observed at $\eta_n = -360$

km for $\omega < 0.19$ cpd, and at $\eta_n = -180$ km for $\omega \geq 0.19$ cpd. The maximum winter squared coherences decrease to 0.1 only at the largest ω resolved (0.48 cpd).

The propagation characteristics of the τ field, as illustrated by the phase function $\Theta_{\tau\tau}(\eta_n, \omega)$ and propagation speed function $c_{\tau\tau}(\eta_n, \omega)$ (Appendix D) differ substantially between summer and winter (Fig. IV.6). Poleward propagation dominates in summer for $\omega \leq 0.11$ cpd, and $c_{\tau\tau}$ decreases from > 1000 cm s^{-1} at $\omega = 0.11$ cpd to about 400 cm s^{-1} at the smallest ω resolved (0.041 cpd). In winter, however, equatorward propagation exists for $\omega \leq 0.34$ cpd, with $c_{\tau\tau}$ approximately constant at -2500 cm s^{-1} (the same speed estimated from the correlation function $R_{\tau\tau}$). The winter τ fluctuations are evidently due to spatially-coherent propagating disturbances (cyclones, anticyclones, and fronts) that generate τ fluctuations over a broad ω band, consistent with the results from the wind analysis of Halliwell and Allen (1986a). This does not seem to be true in summer since $c_{\tau\tau}$ is strongly frequency dependent. The propagation characteristics of the ζ field differ substantially from those of the τ field in both summer and winter. Poleward propagation dominates at all ω , and $c_{\zeta\zeta}$ (not to be interpreted as a free wave phase speed) increases with increasing ω from about 500 cm s^{-1} (1000 cm s^{-1}) at $\omega = 0.041$ cpd to about 900 cm s^{-1} (1800 cm s^{-1}) near $\omega = 0.19$ cpd in summer (winter). Increasing $c_{\zeta\zeta}$ with increasing ω is predicted from (IV.1.1) by Allen and Denbo (1984).

From the phase function $\theta_{\zeta\tau}$, we can quantify the local phase lag of ζ to τ in units of time or degrees. In summer, the local time lag (Fig. IV.6) is roughly constant near 1 day for $\omega < 0.26$ cpd. In winter, however, the local lag time decreases substantially with increasing ω , from about 2 days to < 0.5 days over the entire ω band. It is interesting to note that the constant local time lag in summer corresponds to a local phase lag in degrees that increases with increasing ω , an effect predicted by Allen and Denbo (1984) from (IV.1.1). In winter, however, the decreasing local time lag with increasing ω corresponds to a local phase lag that is approximately constant near 60° over all ω except the smallest (0.041 cpd), where it is near 30° . The time lag increases with increasing equatorward space lags ($\eta_n < 0$ km) in both seasons, consistent with a ζ response that tends to propagate poleward.

IV.4. WAVENUMBER-FREQUENCY AUTOSPECTRA OF WIND STRESS AND SEA LEVEL

IV.4.1 Summer and Winter Autospectra of τ and ζ

Autospectra of τ and ζ [$S_\tau(\pm\lambda, \omega)$ and $S_\zeta(\pm\lambda, \omega)$] for summer (grid points 4 through 17) and winter (grid points 2 through 17) (Fig. IV.7, top) are calculated using the two-dimensional Fourier transform method described in Appendix E. The spectrum estimates for $\lambda > 0$ represent poleward-propagating variance, and those for

$l < 0$ represent equatorward-propagating variance. The total variance of the τ and ζ fields for both seasons, which in each case equals the sum of the total variances of the individual seasons, is listed in Table IV.5.

Most of the variance of τ and ζ exists for $|l| \leq 1.1 \times 10^{-3}$ cpkm (wavelengths ≥ 900 km) (Fig. IV.7, top). For τ , the variance density decreases by about a factor of 10 for $|l|$ increasing from 0 to 1.1×10^{-3} cpkm over all frequencies resolved (0.025 to 0.48 cpd) in both seasons. For ζ , the corresponding decrease is greater for negative l than positive l , and becomes smaller for increasing ω . It exceeds a factor of 10 only for $\omega < 0.27$ (< 0.15) cpd for negative (positive) l in summer, and only for $\omega < 0.36$ (< 0.15) cpd for negative (positive) l in winter. This wavenumber asymmetry results from the strong tendency for ζ fluctuations to propagate poleward. The preferred propagation direction in (l, ω) space is best illustrated by contouring the propagating autospectra $[S(+l, \omega) - S(-l, \omega)]$ of ζ and τ (Fig. IV.7, bottom). In summer, poleward propagation dominates for τ over all l for $\omega \leq 0.066$ cpd, and the excess of poleward-propagating variance is greatest for $l < 10^{-3}$ cpkm. Equatorward-propagating variance slightly exceeds poleward-propagating variance at higher frequencies. In winter, equatorward propagation dominates for τ in most of (l, ω) space, with the largest excess of variance existing for $l < 0.6 \times 10^{-3}$ cpkm and $\omega < 0.36$ cpd. In contrast to τ , poleward propagation dominates ζ fluctuations in both summer and winter at nearly all l

and ω , with the greatest excess existing for $\lambda \leq 1.1 \times 10^{-3}$ cpkm and $\omega \leq 0.19$ cpd in summer and ≤ 0.15 cpd in winter. The largest excess of poleward-propagating ζ variance for both seasons is found at the smallest λ resolved (0.40×10^{-3} cpkm in summer and 0.35×10^{-3} cpkm in winter), and at $\omega = 0.025$ cpd in summer and 0.066 cpd in winter.

The overall distributions of variance density as functions of λ and ω separately are illustrated by integrating $S_{\tau}(\pm\lambda, \omega)$ and $S_{\zeta}(\pm\lambda, \omega)$ over ω and λ , respectively. It is evident from the resulting λ and ω autospectra (Fig. IV.8) that the increase of τ variance in winter over summer is much greater than the corresponding increase of ζ variance (Table IV.5). We noted earlier that this winter increase is a function of y (Section IV.3.1, Fig. IV.3).

The λ autospectra illustrate the dominance of large wavelengths for the τ and ζ fluctuations. In summer, 94.1% (92.5%) of the τ (ζ) variance is at $|\lambda| \leq 1.1 \times 10^{-3}$ cpkm (Table IV.5). In winter, this percentage of τ variance decreases to 88.8 while the percentage of ζ variance increases to 94.1. The asymmetry of the λ autospectra illustrates the preferred propagation direction of the fluctuations. In summer, 53.4% (60.8%) of the total τ (ζ) variance is due to poleward-propagating fluctuations (Table IV.5). In winter, this percentage of τ variance decreases to 46.4 and this percentage of ζ variance decreases to 56.0. The ω autospectra for τ decrease monotonically with increasing ω in both seasons, with

the summer autospectrum being slightly more red. The ω autospectra for ζ are more red than those for τ in both seasons, which was predicted from (IV.1.1) by Allen and Denbo (1984). In winter, the autospectrum for ζ is more red for $\omega < 0.15$ cpd than it is for larger ω .

IV.4.2 Interannual Variability in the Autospectra of τ and ζ

The (ℓ, ω) autospectra for the individual four summers (grid points 4 through 17) and four winters (grid points 2 through 17) are contoured for τ in Fig. IV.9 and ζ in Fig. IV.10, and propagating autospectra of both τ and ζ for the individual seasons are contoured in Fig. IV.11. Although the summer and winter distributions of variance density for both τ and ζ appear qualitatively similar from year to year in Figs. IV.9 and IV.10, some interannual variability does exist for both seasons.

For τ in summer, the total variance over grid points 4 through 17 ranges from $3.29 \text{ (dy cm}^{-2}\text{)}^2$ in summer 1983 to $5.18 \text{ (dy cm}^{-2}\text{)}^2$ in summer 1981 (CODE-1) (Table IV.5). Well over 90% of the total variance is due to fluctuations with $\ell \leq 1.1 \times 10^{-3}$ cpkm in all four summers (Table IV.5). The large excess of poleward-propagating variance observed for $\omega < 0.1$ cpd in the ensemble-averaged propagating autospectra (Fig. IV.7, bottom) results primarily from the large excess observed in summers 1981 and 1982 (CODE-1 and CODE-2) (Fig. IV.11). Most of the excess poleward-propagating variance at small ℓ is distributed over a

larger ω band ($\omega < 0.35$ cpd) in summer 1983. Little preference for either poleward or equatorward propagation is observed in summer 1980. Only 49.4% of the total variance propagates poleward in summer 1980, while between 53.4% and 56.3% propagates poleward in the other summers. The largest excess is observed in summer 1982 (CODE-2) (Table IV.5).

For ζ in summer, the total variance over grid points 4 through 17 ranges from 169 cm^2 in summer 1980 to 460 cm^2 in summer 1983 (Table IV.5). The total variance does not appear related to either the total τ variance or the percentage of τ variance that propagates poleward. For example, the largest ζ variance and the smallest τ variance both occur in summer 1983, and the largest percentage of poleward-propagating τ variance and the second-smallest ζ variance both occur in summer 1982. The percentage of total variance due to fluctuations with $|\ell| \leq 1.1 \times 10^{-3}$ cpkm ranges from 89.7 during summer 1981 (CODE-1) to 94.3 during summer 1980. The largest excess of poleward-propagating variance exists at the smallest ℓ resolved (0.40×10^{-3} cpkm in summer and 0.35×10^{-3} cpkm in winter) and essentially for $\omega \leq 0.19$ cpd in all four years (Fig. IV.11). The magnitudes of these excesses varies substantially from year to year, with the largest observed during summer 1982 (CODE-2), where 64.7% of the total variance propagates poleward (Table IV.5). The smallest excess (58.4%) occurs during summer 1981 (CODE-1).

For τ in winter, the total variance over grid points 2 through 17 ranges from 22.0 (dy cm^{-2})² in winter 1983-84 to 69.0 (dy cm^{-2})² in winter 1982-83. The percentage of total variance due to fluctuations with $|\ell| \leq 1.1 \times 10^{-3}$ cpkm ranges from 83.6 during winter 1981-82 to 91.9 during winter 1980-81.

Equatorward-propagating variance exceeds poleward-propagating in all four winters, and the excess is largest for the smallest nonzero $|\ell|$ resolved. The frequency bands where the excess is greatest shift substantially from year to year. During winter 1980-81, a small excess of poleward-propagating variance exists for $\omega > 0.25$ cpd. During winters 1982-83 and 1983-84, small excesses of poleward-propagating variance exist only at the smallest ω resolved (0.041 cpd). The percentage of total variance that propagates poleward ranges from 45.2 in winter 1981-82 to 47.2 in winter 1983-84 (Table IV.5).

For ζ in winter, The total variance over grid points 2 through 17 ranges from 612 cm^2 in winter 1983-84 to 1393 cm^2 in winter 1982-83. These are the same winters where the τ variance is smallest and largest, respectively. The total variance does not appear related to the percentage of τ variance that propagates poleward. The percentage of total variance due to fluctuations with $|\ell| \leq 1.1 \times 10^{-3}$ cpkm ranges from 91.4 in winter 1983-84 to 95.7 in winter 1982-83. The excess of poleward-propagating variance is largest at the smallest nonzero $|\ell|$ resolved, and spans all or nearly all of the entire frequency band resolved in all

winters except 1981-82, where equatorward propagation dominates for $\omega > 0.2$ cpd. This indicates that a substantial part of the ζ response propagated alongshore along with the τ disturbances during this winter, which also had the largest percentage excess of equatorward-propagating τ variance. The percentage of total variance that propagates poleward ranges from 53.7 in winter 1981-82 to 58.1 in winter 1983-84 (Table IV.5).

IV.4.3 Comparison of Measured and Calculated τ Autospectra

We test the reliability of calculated τ autospectra by comparing them to measured τ autospectra for summers 1981 and 1982, plus winter 1981-82 (Fig. IV.12), and calculated over grid points 4 through 13 only. Since calculated and measured τ have substantially different variance at many locations along the coast, it is important to assess how much this problem will contribute to observed differences between calculated and measured τ autospectra. We therefore also compare autospectra of measured τ to autospectra of adjusted measured τ (Section IV.2).

Similar distributions of variance density in (ℓ, ω) space are observed for both measured and adjusted measured τ (Fig. IV.12). If the differences in total variance are taken into account, then based on the statistical F-test as described in Halliwell and Allen (1986a), adjusted measured τ spectrum estimates do not differ significantly (to 95% confidence) from those of measured τ throughout (ℓ, ω) space in all three seasons, except for

$\ell < -1.5 \times 10^{-3}$ and $\omega > 0.35$ cpd in winter 1981-82. The similarities in the distributions of variance density are evident by inspecting integrated ℓ and ω autospectra (Fig. IV.13). The variance of measured and calculated τ differs by an order of magnitude at some locations along the coast, yet the shape of the (ℓ, ω) autospectra of measured τ are not significantly distorted when the variance of this field is adjusted to equal that of calculated τ . Uncertainties in the representation of τ variance by the calculated and measured τ fields therefore do not significantly influence the results of our (ℓ, ω) autospectrum analyses. We can compare calculated τ autospectra directly to those of either measured or adjusted measured τ to characterize similarities and differences between (ℓ, ω) autospectra of the calculated and measured τ fields.

Significant differences do exist between the distributions of calculated and measured τ variance densities in (ℓ, ω) space. Comparing the calculated and adjusted measured τ autospectra in Fig. IV.12, calculated τ variance density decreases much more rapidly with increasing $|\ell|$ than it does for measured τ . This difference is observed more clearly in the integrated ℓ autospectra in Fig. IV.13. The adjusted measured τ spectrum estimates are smaller than the calculated τ estimates at $\ell = 0$ in all seasons, but more so in both summers. These estimates are about equal at the smallest nonzero $|\ell|$ resolved (0.55×10^{-3} cpkm) in all seasons, but for larger $|\ell|$ the estimates for calculated τ decrease

much more rapidly with increasing $|\lambda|$ than those for adjusted measured τ . For $|\lambda| = 2.2 \times 10^{-3}$, the differences are about a factor of 5 in summer 1981, a factor of 3.5 in winter 1981-82, and a factor of 10 in summer 1982. Typically between 75% and 80% of measured and adjusted measured τ variance, and over 90% of calculated τ variance, is due to fluctuations with $|\lambda| \leq 1.1 \times 10^{-3}$ cpkm (Table IV.6). In contrast, the distributions of variance density as a function of ω are very similar for both calculated and adjusted measured τ (Fig. IV.13). Comparing the (λ, ω) autospectra of calculated and adjusted measured τ using the F-test indicates that for all three seasons, the spectrum estimates are not significantly different (to 95% confidence) for $|\lambda| \leq 1.1 \times 10^{-3}$ cpkm within the frequency band $\omega < 0.34$ cpd, and for $|\lambda| \leq 0.55 \times 10^{-3}$ cpkm within the frequency band $0.34 \leq \omega \leq 0.48$ cpd.

The calculated τ field underestimates the magnitude of poleward-propagating τ variance in summer, more so in summer 1982 than summer 1981 (Table IV.6). The probable cause is the relatively poor representation of wind fluctuations caused by coastally trapped poleward-propagating atmospheric pressure disturbances along the California coast (Dorman, 1985, 1986) by the calculated wind field, as documented by Halliwell and Allen (1986a). These disturbances were more common in summer 1982 than summer 1981.

Both adjusted measured and measured τ are very coherent with calculated τ at small $|\ell|$ for the three seasons (Fig. IV.14). (The method of calculating these squared coherence functions is presented in Appendix E.) Similar coherence patterns with calculated τ are observed for both measured and adjusted measured τ , with slightly larger coherence observed for adjusted measured τ in both summer 1981 and winter 1981-82, and for measured τ in summer 1982. Consequently, the coherence between the calculated and measured τ fields is not significantly influenced by large differences in the alongshore distribution of measured and calculated τ variance. Coherence is larger for $\ell > 0$ in summer and for $\ell < 0$ in winter, so it tends to be largest at those ℓ and ω where τ variance is largest. Based on these auto- and cross-spectrum analyses, we conclude that the calculated τ field represents fluctuations with $|\ell| \leq 1.1 \times 10^{-3}$ cpkm with reasonable accuracy for the purpose of (ℓ, ω) autospectrum analysis.

IV.5. OBSERVED SEA LEVEL RESPONSE PROPERTIES IN WAVENUMBER-FREQUENCY SPACE

IV.5.1 Summer and Winter Response of ζ to τ

Properties of the response of ζ to τ in (ℓ, ω) space are illustrated by the coherence squared between τ and ζ [$\gamma_{\tau\zeta}^2(\pm\ell, \omega)$], and by the gain and phase of the transfer function of the ζ response to τ [$G_{\tau\zeta}(\pm\ell, \omega)$ and $\theta_{\tau\zeta}(\pm\ell, \omega)$] (Fig. IV.15). These

functions are calculated from (λ, ω) auto- and cross-spectra as described in Appendix E. In both seasons, relatively large coherence is only observed for $|\lambda| \leq 1.1 \times 10^{-3}$ cpkm (Fig. IV.15). In summer, $\gamma_{\tau\zeta}^2$ is relatively large for $\lambda > 0$ and $\omega < 0.3$ cpd, while in winter, it is relatively large for $\lambda < 0$ and $\omega < 0.4$ cpd. The shift of large coherence toward negative λ in winter likely occurs because equatorward propagation dominates the τ fluctuations.

In contrast, the gain of the ζ response tends to be larger for positive λ in both seasons (Fig. IV.15). The largest gain is observed for the smallest positive λ resolved in both seasons (0.40×10^{-3} cpkm in summer and 0.35×10^{-3} cpkm in winter), but at the lowest frequency resolved (0.025 cpd) in summer and at the second-lowest frequency resolved (0.066 cpd) in winter. These are the same values of λ and ω where the largest excesses of poleward-propagating ζ variance are observed (Fig. IV.7, bottom). A ridge of relatively large gain extends approximately along a line of constant ω/λ . The gain decreases along this ridge for increasing λ and ω to $< 50\%$ of the maximum at approximately $\omega = 0.25$ cpd and $\lambda = 0.75 \times 10^{-3}$ cpkm in summer. It decreases more rapidly with increasing λ and ω in winter, causing the largest gain to be concentrated at smaller λ and ω than it is in summer. The gain is substantially larger in summer than in winter. For a given total variance of τ fluctuations, the winter ζ response will be smaller than in summer for two reasons: the smaller gain

throughout (ℓ, ω) space, and the dominance of equatorward propagation in the τ fluctuations, which causes τ variance in winter to exist farther from the ridge of large gain in (ℓ, ω) space.

The corresponding phase functions for both summer and winter change sign on either side of an approximately straight line that roughly follows the ridges of maximum gain in (ℓ, ω) space. Consequently, the ζ response is nearly in-phase with τ at those ℓ and ω where the largest gain is observed. The zero phase contour is not as well defined in winter as it is in summer, but this is largely because the winter coherence is small in that part of (ℓ, ω) space. The largest possible response for a given τ disturbance will therefore occur if that disturbance propagates alongshore at speed $c = \omega/\ell$ as defined by the ridge of large gain, and this response will be nearly in-phase with the forcing. Most τ and ζ variance is found in that part of (ℓ, ω) space where the phase is negative, so that the ζ response at a given y will lag the τ forcing in time.

Integrated ℓ and ω coherence squared, gain, and phase functions (Fig. IV.16) are calculated from the (ℓ, ω) auto- and cross-spectra that have been integrated over ω and ℓ , respectively. The integrated ℓ coherence is larger for $\ell > 0$ in summer and $\ell < 0$ in winter, and is relatively small for $|\ell| > 1.1 \pm 10^{-3}$ cpkm. In contrast, the gain is larger for $\ell > 0$ in both seasons, relatively more so in summer, and is substantially larger for all ℓ in summer.

For $\lambda \leq 0$, the phase generally ranges between -45° and -90° (ζ lags τ) in both seasons. As λ increases from 0, the phase increases rapidly to exceed 0° (ζ leads τ) in summer and approximately equal zero in winter. The integrated ω coherence tends to decrease with increasing ω (Fig. IV.16). The strong bias toward small ω in the ζ response is evident in the gain for both seasons. In summer, it decreases rapidly with ω to 0.35 cpd, then is approximately constant for larger ω . In winter, it decreases rapidly with ω to 0.23 cpd, then is approximately constant for larger ω . The phase for both seasons is generally negative over all ω , tends to decrease with increasing ω to 0.19 cpd, and is roughly constant for larger ω . In summer, it is near 0° at the smallest ω resolved (0.025 cpd).

IV.5.2 Interannual Variability in the Response of ζ to τ

The coherence squared between τ and ζ , and the gain and phase of the ζ response to τ , are contoured in Figs. IV.17 through IV.19 for the eight individual seasons. While there are some differences in the details of the coherence patterns from year to year, the fundamental seasonal differences between the ensemble-averaged summer and winter patterns observed in Fig. IV.15 are also observed for the individual seasons in Fig. IV.17. The largest summer coherence is observed for $\lambda > 0$ in all summers except for summer 1981 (CODE-1). The largest winter coherence is observed for $\lambda < 0$, but much less so during winter 1980-81 than during the other

winters.

The gain functions (Fig. IV.18) show substantial year-to-year variability, while the phase functions (Fig. IV.19) generally do not. In particular, the rate of decrease of maximum gain with increasing ℓ and ω differs among the individual seasons. During summer 1980, the gain first increases with increasing ℓ and ω following the ridge, then decreases. The gain generally decreases along the ridge in the other three summers, with the largest decrease observed during summer 1983. The decrease is somewhat smaller during winter 1980-81 than the other winters. The change in the sign of the phase near the dispersion curve is present in all eight seasons, although it is poorly detected during the winters due to poor coherence in that part of (ℓ, ω) space.

IV.5.3 The Response of ζ to Measured and Calculated τ

We test if the observed response properties are significantly biased in any manner because we use calculated τ as the forcing function. We compare the ζ response to calculated τ with the ζ response to both measured and adjusted measured τ for three seasons, which also allows us to determine if differences in the alongshore distribution of τ variance influences the observed response properties. The coherence squared, gain, and phase functions are computed from auto- and cross-spectrum functions for grid points 4 through 13. These functions are contoured for summer 1981, winter 1981-82, and summer 1982 in Figs. IV.20 through IV.22.

The coherence squared, gain, and phase functions for the ζ response to measured τ are very similar to those for the ζ response to adjusted measured τ , the only notable exception being differences in the magnitude of the gain function, especially in winter 1981-82, where it is substantially larger for measured τ . The large differences in the alongshore distribution of variance in the measured and calculated τ fields do not significantly influence the observed (λ, ω) -dependent properties of the ζ response. The uncertainty about which τ field best represents τ variance along the coast affects only our ability to determine the magnitude of the gain, not our ability to qualitatively determine the dependence of gain and other response properties on λ and ω . In the subsequent discussion, we therefore compare the response of ζ to both calculated and measured τ without considering adjusted measured τ .

The coherences squared between ζ and both calculated and measured τ have similar patterns in (λ, ω) space for all three seasons, but coherence with measured τ is somewhat larger (Figs. IV.20 through IV.22). Although the squared coherence is generally statistically significant (> 0.16 to 95% confidence) in most of (λ, ω) space, it is relatively low for $|\lambda| > 1.1 \times 10^{-3}$ cpm, and little improvement occurs at these $|\lambda|$ when measured τ is used instead of calculated τ , even though measured τ is expected to represent τ fluctuations at these $|\lambda|$ much more accurately. The wind-driven response of ζ is apparently weak at larger $|\lambda|$, and can

at best be marginally detected.

The patterns of the gain of the ζ response to both calculated and measured τ are similar for each season, with the tendency for a ridge of large gain to exist on the positive k side of the spectrum (Figs. IV.20 through IV.22). The decrease in gain along the ridge for increasing k and ω exists whether calculated or measured τ is used as the forcing function, and the decrease tends to be larger for measured wind. This decrease is therefore not an artifact of using calculated τ as the forcing function, and if anything, the decreases observed for both summer and winter (Fig. IV.15) are underestimated by using calculated τ . The phase functions for calculated and measured τ also have qualitatively similar patterns in each season. The results of our analyses are not seriously distorted by using calculated τ to represent the forcing.

IV.6. PREDICTED SEA LEVEL RESPONSE PROPERTIES IN WAVENUMBER-FREQUENCY SPACE

IV.6.1 Response Properties Predicted by (IV.1.1) for One Mode

The fundamental properties of the ζ response to τ in (k, ω) space predicted from basic coastally trapped wave theory can be studied using a transfer function derived from (IV.1.1) by assuming constant parameters along the coast and Fourier transforming it in two dimensions (Appendix F). To illustrate the predicted response properties for one mode, we contour the gain and phase of this

transfer function for two values of the friction coefficient: $T_f = 1$ and 3 days (Fig. IV.23). In these examples, we use $c = 350$ cm s^{-1} , a typical value observed by Halliwell and Allen (1984) during summer 1973, and the transfer coefficient $b = (cT_f)^{-1}$, the latter resulting in a maximum gain of 1 (Appendix F). The maximum gain and zero phase contours both follow the linear dispersion curve, so the slope of these contours is $c = \omega/l = 350$ cm s^{-1} . All other gain and phase contours are parallel to this dispersion curve. If the long wave assumption is not made, the dispersion curve will not be straight, but the deviation from a straight line is small within that part of (l, ω) space resolved in this study (Brink, et al., 1986).

The fundamental properties of the predicted response can be elucidated by considering the response generated by a τ disturbance at a particular $|l| > 0$ and $\omega > 0$ (a pure sine wave that propagates alongshore). The largest ζ response (also a pure propagating sine wave with the same l and ω as the forcing) will occur for a disturbance that propagates alongshore at speed $\omega/l = c_\tau = c$, and this response will be exactly in-phase with the τ disturbance. If c_τ differs from c , the phase, which can be characterized as either a space or time lag, will be nonzero. Positive (negative) phase indicates that the response wave is displaced alongshore from the τ wave in the direction toward (opposite from) which the τ wave is propagating, resulting in the ζ response leading (lagging) τ in time at a given y . Positive phase is observed for $0 \leq c_\tau < c$,

representing poleward propagation of the τ wave at a speed slower than the free wave phase speed and corresponding to the shaded regions of the phase plots in Fig. IV.23. Negative phase is observed for $c_\tau > c$, representing poleward propagation of the τ wave at a speed faster than the free wave phase speed and corresponding to the unshaded regions of the positive l side of the phase plots, and also for $c_\tau < 0$, representing equatorward propagation of the τ wave and corresponding to the negative l side of the phase plots. The response wave always propagates along the coast at the same speed as the τ wave, but the spatial (and resulting temporal) lag of the response depends on the difference between c_τ and c , with the lag equaling zero if $c_\tau = c$.

Increasing T_f has several effects. The maximum gain increases, since it equals $cT_f b$ (Appendix F). The response far from the dispersion curve in (l, ω) space becomes relatively smaller and has a larger phase lead or lag. In the limit as $T_f \rightarrow \infty$, the gain approaches infinity along the dispersion curve and zero elsewhere in (l, ω) space, and the phase approaches $\pm 90^\circ$ everywhere in (l, ω) space except on the dispersion curve. Increasing c will increase the slopes of the contours in Fig. IV.23, and will also increase the maximum gain since it is a linear function of c .

There are qualitative similarities between the observed gain and phase (Fig. IV.15) and the gain and phase predicted by (IV.1.1) for one mode. Both observed and predicted gain are largest along a ridge that follows a line of constant ω/l for $l > 0$, and both

observed and predicted phase change sign on opposite sides of this ridge although the observed winter sign change is poorly resolved due to low coherence in that part of (λ, ω) space. The prediction that a near-resonant response can occur due to τ disturbances that propagate poleward at speed $c = \omega/\lambda$ is confirmed by the data. The good coherence between τ and ζ at $|\lambda| \leq 1.1 \times 10^{-3}$ cpkm, coupled with the qualitative similarities between observed and predicted response properties, indicates that large-scale wind forcing of ζ is very important along the west coast of North America in both summer and winter, and that the response to this forcing has many properties that are predicted for forced large-scale coastally trapped waves.

At sufficiently small ω , coastally trapped wave energy can be propagated offshore by planetary Rossby waves as shown by a barotropic model by Dorr and Grimshaw (1986), so (IV.1.1) becomes invalid as $\omega \rightarrow 0$. Theoretical models that accurately describe the nature of this behavior for general stratified situations, however, evidently are not available. Thus, it is not clear at precisely what frequencies or in what form this breakdown of (IV.1.1) will occur. This process may influence the observed response properties in (λ, ω) space near the smallest ω resolved (Fig. IV.15). In particular, the decay rate of the forced wave response may be larger at these small ω , tending to decrease the amplitude of the response. The observed maximum in gain near the dispersion curve increases with decreasing ω down to the smallest ω resolved (0.025

cpd) in summer, and to the second-smallest ω resolved (0.066 cpd) in winter (Fig. IV.15). In addition, the observed maximum winter gain decreases only slightly from $\omega = 0.066$ cpd to $\omega = 0.025$ cpd. Consequently, offshore propagation of Rossby waves apparently does not have a clearly identifiable effect on the observed response.

Although we are analyzing the forced ζ response, free wave properties can also be deduced from the shape of the observed transfer functions (Fig. IV.15). Comparing Figs. IV.15 and IV.23, rough estimates of the average values of c and T_f along the coast in summer are 300 to 400 cm s^{-1} and between 1 and 3 days. Estimates are more difficult to make for winter since the observed ridge of large gain and the zero phase contours are not as well defined as in summer, but c appears larger and T_f appears roughly the same in winter as opposed to summer. Estimates of b cannot be made with confidence since calculated τ may not accurately represent the total τ variance along the coast. Since the gain is proportional to cbT_f , and since c does not appear to be smaller in winter, the winter decrease in gain must be caused by decreases in b or T_f . The magnitude of the transfer coefficient b depends on the basic stratification (Brink, 1982), and this stratification changes substantially between summer and winter. According to the analysis of Grant and Madsen (1979), the friction time scale T_f will probably be smaller in winter because of larger bottom stress due to increased storminess in the northeast Pacific and the resulting increase in surface gravity wave energy over the

continental shelf.

The fact that τ variance increases much more in winter over summer poleward of the CODE site ($y > 0$) than does ζ variance (Fig. IV.3) indicates that the winter decrease in gain may be y -dependent. Since winter storminess increases toward the north, larger bottom stress from increased surface gravity wave energy may produce a y -dependent winter decrease in T_f that could at least partly explain this y -dependence of the seasonal change in gain. However, we estimated in above that T_f has similar values in summer and winter. Our subsequent discussion of the limitations of using (IV.1.1) will show that the crude estimates of T_f made using Fig. IV.15 have a very large uncertainty, especially if more than one mode contributes to the total response, so T_f could still be substantially smaller in winter without being visually evident in Fig. IV.15. For reasons such as this, we do not try to obtain more accurate estimates of the parameters of (IV.1.1) by statistically fitting the predicted to observed transfer functions.

One major difference between the observed and predicted response properties does exist: The maximum predicted gain is constant along the dispersion curve $\omega/l = c$, while the observed gain decreases substantially along this line as l and ω increase. Possible mechanisms that may cause this observed decrease include the y -dependence of parameters in (IV.1.1), an (l, ω) -dependent friction that may exist if the linear friction term in (IV.1.1) is invalid, and a significant contribution to the response by higher

modes. The ζ response predicted by (IV.1.1) will have larger space and time scales than τ (Allen and Denbo, 1984), but our observations indicate that the scales of this response will be even larger than predicted by (IV.1.1).

The effects of y -dependent parameters were explored by numerically integrating (IV.1.1) for different $c(y)$, $T_f(y)$, and $b(y)$ with τ from winter 1981-82 and summer 1982 as the forcing functions, using the method described in Halliwell and Allen (1984) extended to handle y -dependent parameters, then computing the transfer functions for the numerical solutions. Variable parameters distort the gain and phase by only a small amount (not shown), and this mechanism appears incapable of accounting for the large observed decrease in maximum gain. This result is in agreement with Chapman (1986) who found that in integrations of (IV.1.1), predictions of a response variable at a given y show little difference in quality whether y -dependent or averaged parameters are used.

The responses predicted by two recent models illustrate that the effect of friction can depend on l and ω if the assumptions required to derive the linear friction term in (IV.1.1) are relaxed. The two-layer Kelvin wave model of Allen (1984) predicts an increasing gain with decreasing l and ω that is qualitatively consistent with observations, but most of the increase is confined to much smaller $|l|$ and ω than is observed. However, the stochastic model of the wind-driven response of a continuously

stratified continental shelf and slope presented by Brink, et al. (1986) predicts a decreasing resonant response with decreasing ω , not the increasing resonant response that is observed. The (l, ω) dependence of friction can therefore be strongly dependent on the model assumptions, and must be further studied.

IV.6.2 Response Predicted by (IV.1.1) for More Than One Mode

We consider the properties of the total ζ response in (l, ω) space that result if more than one coastally trapped wave contributes significantly to this response. Parameters of (IV.1.1) for ζ as the response variable, calculated using the model of Brink (1982) for the CODE site (Brink, personal communication) and also averaged along the west coast of the U.S. between San Diego ($y = -938$ km) and the CODE site ($y = 0$) (Chapman, 1986), are listed in Table IV.7 along with the maximum gain for each mode. In calculating these parameters, Brink and Chapman used a bottom friction coefficient $r = 0.05 \text{ cm s}^{-1}$ at all locations along the coast. For the CODE site, the maximum gain of modes 2 through 4 are 33%, 11%, and 6% of the maximum gain of mode 1. For the west coast, the corresponding percentages for modes 2 and 3 are 32% and 17%. These estimates indicate that modes two and three may make a substantial contribution to the total observed ζ response in the CODE large-scale domain.

The predicted response properties for multiple modes can be readily studied since the (l, ω) transfer function of the total

response is simply the sum of the individual transfer functions. These total transfer functions are calculated for the CODE site and the west coast using the parameters for all modes listed in Table IV.7, and the gain and phase of these functions are contoured in Fig. IV.24. Individual ridges of large gain are evident at large positive ℓ , each following a line given by $\omega/\ell = c_n$. At very small ω and ℓ , the ridges merge into one broader ridge and become indistinct from each other. Sharp phase changes are observed near the dispersion curves.

The ridges of large gain are substantially narrower, and the phase changes sharper, than are observed for the single mode (Fig. IV.23) because the T_{fn} in Table IV.7 are much larger than the T_f used for the single mode cases. These theoretically estimated T_f are also much larger than both the estimate of 1 to 3 made using Fig. IV.15 and the estimate of 4.25 days made by Halliwell and Allen (1984) for summer 1973. To illustrate the effects of changing T_{fn} on the multiple-mode response, we calculate gain and phase using the parameters in Table IV.7, but with T_{f1} set to 2.5 days (reduced to 45% of its estimated theoretical value for the CODE site and 26% of its estimated theoretical value for the west coast), and with the ratios T_{fn}/T_{f1} preserved (Fig. IV.25). With T_f reduced, the individual ridges of large gain are substantially broader and therefore blend together to appear as one broad ridge. The single ridge dominates for $\ell \leq 1.1 \times 10^{-3}$ cpkm, and the only apparent contribution from higher modes is to cause the gain to

decrease with increasing ω and λ , as observed in the data. The phase functions in Fig. IV.25 also better resemble the observed phase functions in Fig. IV.15 than do those in Fig. IV.24.

However, the predicted change in maximum gain along the ridge is not as large as the observed change, and we can conclude at most that contributions to the ζ response from higher modes may contribute to the observed decrease in gain with increasing ω and λ .

Since the (λ, ω) resolution in the data analyses is too coarse to define the narrow ridges of large gain and the very sharp phase changes predicted when large T_{fn} are assumed, we cannot use these (λ, ω) analyses to determine which values of T_f are most correct. The inability to detect strong gradients of gain and phase may be influenced by this resolution problem, and we cannot conclude that the smaller T_f inferred from Fig. IV.15 represents friction time scales that actually exist.

IV.6.3. One Dimensional Response Properties Predicted by (IV.1.1)

Using the observed winter and summer (λ, ω) autospectra of τ (Fig. IV.7), we calculate the one-dimensional squared coherence and gain as functions of λ and ω predicted by (IV.1.1) as described in Appendix F, assuming one mode dominates the response. We calculate these functions using $c = 350 \text{ cm s}^{-1}$, and $T_f = 1 \text{ day}$ (Fig. IV.26) and $T_f = 3 \text{ days}$ (Fig. IV.27), the parameters used to predict (λ, ω) transfer functions (Fig. IV.23). The coherence predicted by

(IV.1.1), which is a constant equal to one in (ℓ, ω) space, is generally less than one when calculated as a function of ℓ or ω (Appendix F). A similar reduction of coherence appears in the observed one-dimensional coherence functions (Fig. IV.16). For example, summer $\gamma^2(\ell, \omega)$ in Fig. IV.15 is greater than 0.45 at $\omega = 0.025$ cpd for $-1.5 \times 10^{-3} < \ell < 1.5 \times 10^{-3}$ cpkm, which contains most of the τ and ζ variance at that ω , yet summer $\gamma^2(\omega)$ in Fig. IV.16 is only 0.29 at $\omega = 0.025$ cpd. The predicted one-dimensional coherence (Fig. IV.26) is approximately constant as a function of ω , but it varies as a function of ℓ , with the smallest coherence found for $0 \leq \ell < 1.5 \times 10^{-3}$ cpkm. Both ℓ and ω coherence functions decrease with increasing T_f . The predicted and observed one-dimensional coherence functions differ substantially, primarily because "noise" in the τ and ζ data sets substantially reduces the observed coherence, particularly for $|\ell| > 1.1 \times 10^{-3}$ cpkm. Predicted coherence functions represent the coherence that would exist if the input and response data sets were noise-free.

The predicted ℓ gain functions (Figs. IV.26 and IV.27) tend to be relatively large for $\ell > 0$, and the ω gain functions decrease with increasing ω . The corresponding observed gain functions (Fig. IV.16) are larger than the predicted for the smallest positive ℓ resolved and for small ω . This is consistent with the inability of (IV.1.1) to predict the increase in maximum gain in (ℓ, ω) space for decreasing ℓ and ω observed in Fig. IV.15. Increasing T_f does not change the shape of the ℓ gain functions

very much. Increasing T_f from 1 to 3 days introduces a relative maximum to the predicted summer ω gain function for $\omega = 0.15$ cpd (Fig. IV.27), where a relative maximum is found in the observed summer gain (Fig. IV.16). Increasing T_f also increases the magnitude of the slope of the predicted winter ω gain function for small ω , in better agreement with the observed winter gain. The predicted phase functions are qualitatively very similar to the observed phase functions, changing sign for small positive ℓ and becoming increasingly negative for increasing ω . Increasing T_f increases the slope of the ℓ phase near the zero crossing, and shifts the ω phase toward larger negative values over all ω .

IV.7. DISCUSSION

Fluctuations in alongshore wind stress τ calculated from FNOC geostrophic winds along the west coast of North America are relatively energetic at alongshore wavenumbers $|\ell| \leq 1.1 \times 10^{-3}$ cpkm and frequencies $0.025 < \omega < 0.5$ cpd, and they effectively drive a coastal sea level ζ response within this (ℓ, ω) band. Winter τ fluctuations are generated primarily by spatially-coherent propagating weather systems (Halliwell and Allen, 1986a), and equatorward propagation dominates these fluctuations for $\omega < 0.35$ cpd. Poleward propagation strongly dominates the summer τ fluctuations for $\omega < 0.1$ cpd, and equatorward-propagating variance slightly exceeds poleward-propagating variance for larger ω . In contrast, poleward propagation dominates the ζ fluctuations in both

seasons, but more so in summer. The ζ response at a given location is most highly correlated with τ time series at lag distances 300 to 400 km equatorward of that location. Coherence analysis indicates that the lag distance is approximately -360 km for $\omega \leq 0.11$ cpd ($\omega < 0.19$ cpd) in summer (winter), and is approximately -180 km for larger ω in both seasons, except near $\omega = 0.34$ cpd, where it is approximately 0.

The largest coherence between ζ and τ as a function of (ℓ, ω) is observed where τ is most energetic; i.e., for $\ell > 0$ in summer and $\ell < 0$ in winter. The ζ response to τ is apparently very weak for $|\ell| > 1.1 \times 10^{-3}$ cpkm in both seasons since the coherence is small for all ω at these large ℓ . This result is not an artifact of using calculated τ as the forcing function because similar results are obtained using measured τ . The observed transfer functions indicate that a resonance exists in both seasons, with the largest gain occurring along a single ridge that approximately follows a straight line (dispersion curve) of constant poleward phase speed, and with ζ approximately in phase with τ along this ridge. The gain along this ridge decreases substantially with increasing ℓ and ω in both seasons, with the largest response confined to even smaller ℓ and ω in winter than in summer. The decrease is also not an artifact of using calculated τ as the forcing function, since it is also present, and even tends to be slightly larger, when measured τ is used. The interannual variability in this observed pattern of gain is large, with only

small decreases in maximum gain observed during some seasons, and very large decreases observed in others. The phase patterns are more similar among individual summer and winter seasons.

The ζ response is more effectively forced by τ in summer than in winter. The ratio of total ζ variance to total τ variance is nearly four times greater in summer. Two factors are responsible for this: First, the magnitude of the gain is substantially smaller in winter than in summer, which is probably due primarily to larger friction in winter. Second, the dominance of equatorward propagation in the winter τ field causes substantially more τ variance to exist in a region of (ℓ, ω) space away from the dispersion curve in locations where the gain is relatively small.

A single forced, first-order wave equation model with a linear friction term governing the (y, t) dependence of the response due to one coastally trapped wave mode predicts that a resonant response exists. A constant maximum in the predicted gain follows the straight dispersion curve $c = \omega/\ell > 0$ in (ℓ, ω) space, and the predicted phase lag of the response is zero along this curve. These predicted patterns are qualitatively consistent with the observed patterns, except for the observed decrease in maximum gain with increasing ℓ and ω along the dispersion curve. Since this decrease is not predicted by one wave equation, we attempted to find the causes of this decrease, but were less than completely successful.

Alongshore variations in the parameters for one wave equation (phase speed, friction time scale, and transfer coefficient) did not distort the predicted gain and phase patterns very much. Models with (ℓ, ω) -dependent friction did not successfully predict properties of the observed transfer functions. A significant contribution to the response from additional coastally trapped wave modes can increase the predicted maximum gain at small ℓ and ω . This occurs because the individual ridges of large gain merge and become indistinguishable at small ℓ and ω , and within this part of (ℓ, ω) space, the gain decreases with increasing ℓ and ω as observed. Based on theoretically determined wave equation parameters for the first several modes, the predicted decrease of maximum gain is substantially smaller than the observed decrease. Therefore, the presence of higher modes may contribute to the observed decrease, but evidently did not fully account for the magnitude of the decrease.

Table IV.1. Coastal points of the CODE large-scale analysis grid. Coast orientation is measured in degrees counter-clockwise from due east.

<u>Grid Point No.</u>	<u>Lat.</u>	<u>Lon.</u>	<u>y (km)</u>	<u>Coast Orientation</u>
17	54°09'N	130°20'W	1800	120
16	52 10	128 19	1620	115
15	50 32	127 13	1440	100
14	49 23	126 06	1260	128
13	48 11	124 42	1080	120
12	46 36	124 05	900	95
11	44 58	124 03	720	85
10	43 21	124 20	540	73
09	41 46	124 12	360	103
08	40 12	124 18	180	130
07	38 42	123 27	0	133
06	37 18	122 24	-180	102
05	35 59	121 31	-360	128
04	34 35	120 39	-540	90
03	34 01	118 53	-720	150
02	33 00	117 21	-900	110
01	31 27	116 44	-1080	110
35	30 00	115 54	-1260	115
34	28 47	114 41	-1440	130
33	27 20	113 52	-1620	130
32	26 07	112 40	-1800	130

Table IV.2. Coastal sea level stations used in this analysis.

<u>Station</u>	<u>Abb.</u>	<u>Lat.</u>	<u>Lon.</u>	<u>Y</u> <u>(km)</u>
Prince Rupert, BC	PRR	54°19'N	130°20'W	1883
Bella Bella, BC	BBL	52 10	128 08	1608
Zeballos, BC	ZBL	50 01	126 47	1349
Tofino, BC	TOF	49 09	125 55	1232
Neah Bay, WA	NBA	48 22	124 37	1100
Toke Point, WA	TKP	46 42	123 58	911
Astoria, OR	AST	46 10	123 46	852
South Beach, OR	SBC	44 38	124 03	683
Charleston, OR	CHR	43 20	124 19	538
Crescent City, CA	CCY	41 45	124 11	359
Trinidad Head, CA	TRH	41 03	124 09	277
North Spit, CA	NSP	40 45	124 14	244
Arena Cove, CA	ARC	38 55	123 43	37
Point Reyes, CA	PRY	38 00	122 58	-76
San Francisco, CA	SFO	37 48	122 28	-126
Monterey, CA	MRY	36 36	121 53	-276
Port San Luis, CA	PSL	35 10	120 45	-473
Santa Barbara, CA	SBA	34 25	119 41	-634
Rincon Island, CA	RIS	34 21	119 27	-650
Los Angeles, CA	LOS	33 43	118 16	-780
San Diego, CA	SDO	32 45	117 10	-938

Table IV.3. Wind measurement stations used in the inter-comparison with calculated winds. Coast orientation is in degrees counterclockwise from due east. NDBC stands for National Data Buoy Center.

<u>Station</u>	<u>Abbrev.</u>	<u>Lat.</u>	<u>Lon.</u>	<u>y</u> <u>(km)</u>	<u>Coast</u> <u>Orient.</u>	<u>Time</u> <u>Periods</u> <u>Used</u>
Quillayute, WA	QUI	47°57'N	124°32'W	1055	110	All
Grays Harbor, WA	GRH	46 55	124 06	936	95	All
Newport, OR	NEW	44 38	124 03	683	82	All
North Bend, OR	NOB	43 25	124 15	547	73	All
Crescent City, CA	CCY	41 47	124 14	362	103	All
Humboldt Bay, CA	HUM	40 46	124 14	246	75	S81
NDBC 46022	B22	40 46	124 31	240	75	W81-2,S82
NDBC 46014	B14	39 13	123 58	71	100	S81,S82
Point Arena Lt., CA	ARL	38 57	123 44	41	110	W81-2
NDBC 46013	B13	38 14	123 18	-61	133	All
NDBC 46012	B12	37 22	122 39	-171	105	All
Point Sur, CA	SUR	36 18	121 53	-301	115	All
Diablo Canyon, CA	DIA	35 14	120 50	-464	120	W81-2
NDBC 46011	B11	34 53	120 52	-506	90	S81,S82
Point Mugu, CA	MUG	34 07	119 07	-678	155	All
San Diego, CA	SDO	32 44	117 10	-936	105	All

Table IV.4. Integral space and time correlation scales for summer (grid points 4 through 17) and winter (grid points 2 through 17) determined from the space-time correlation functions described in Appendix D.

<u>Season</u>	<u>Space Scale (km)</u>		<u>Time Scale (days)</u>	
	<u>1</u>	<u>2</u>	<u>1</u>	<u>2</u>
All Summers	699	1085	1.36	3.48
All Winters	988	1324	1.21	3.51

Table IV.5. The total variance, the percentage of total variance with $|\lambda| \leq 1.1 \times 10^{-3}$ cpkm, and the percentage of total variance due to poleward-propagating fluctuations for summer (grid points 4 through 17) and winter (grid points 2 through 17) seasons.

<u>Season</u>	<u>Total Variance</u>		<u>Percentage For Percentage Poleward</u> <u>$\lambda \leq 1.1 \times 10^{-3}$ Propagating</u>			
	<u>$(dy^2 \frac{1}{cm^{-4}})$</u>	<u>$(\frac{1}{cm^2})$</u>	<u>1</u>	<u>2</u>	<u>1</u>	<u>2</u>
All Summers	16.0	1252	94.1	92.5	53.4	60.8
All Winters	190	3519	88.8	94.1	46.4	56.0
Summer 1980	3.63	169	93.8	94.3	49.4	59.2
Summer 1981	5.18	337	93.9	89.7	53.4	58.4
Summer 1982	3.94	286	95.0	93.3	56.3	64.7
Summer 1983	3.29	460	93.7	93.7	54.2	60.6
Winter 1980-81	54.0	738	91.9	93.2	46.8	55.1
Winter 1981-82	44.9	776	83.6	94.6	45.2	53.4
Winter 1982-83	69.0	1393	89.3	95.7	46.5	57.1
Winter 1983-84	22.0	612	89.6	91.4	47.2	58.1

Table IV.6. The percentage of total variance with wavelengths ≥ 900 km and the percentage of total variance due to poleward-propagating fluctuations for calculated, adjusted measured, and measured τ over grid points 4 through 13 for summers 1981 and 1982 plus winter 1981-82.

<u>Season</u>	<u>Wind Stress Set</u>	<u>Percentage With</u> <u>$\lambda \geq 900$ km</u>	<u>Percentage Poleward</u> <u>Propagating</u>
Summer 1981	Calculated	92.6	54.7
	Adjusted Measured	78.5	57.6
	Measured	74.4	55.9
Winter 1981-82	Calculated	90.4	47.8
	Adjusted Measured	77.8	46.8
	Measured	79.6	46.4
Summer 1982	Calculated	94.1	53.9
	Adjusted Measured	77.2	59.0
	Measured	78.5	58.9

Table IV.7. Parameters of (IV.1.1) calculated by Brink (personal communication) for the CODE site and Chapman (1986) for the west coast between San Diego and the CODE site using the model of Brink (1982). The values for the west coast are averaged over 17 subdomains along the west coast of North America as described by Chapman (1986).

<u>Location</u>	<u>Parameter</u>	<u>Mode No.</u>			
		<u>1</u>	<u>2</u>	<u>3</u>	<u>4</u>
CODE Site	c_n (cm s ⁻¹)	299	153	84	55
	$10^8 b_n$ (dy cm ⁻²) ⁻¹	5.85	3.41	1.34	0.92
	T_{fn} (days)	5.52	6.00	9.35	11.0
	Maximum Gain [cm (dy cm ⁻²) ⁻¹]	8.34	2.70	0.91	0.48
West Coast	c_n (cm s ⁻¹)	350	176	111	
	$10^8 b_n$ (dy cm ⁻²) ⁻¹	4.17	4.17	3.09	
	T_{fn} (days)	9.45	6.26	6.82	
	Maximum Gain [cm (dy cm ⁻²) ⁻¹]	11.9	3.97	2.02	

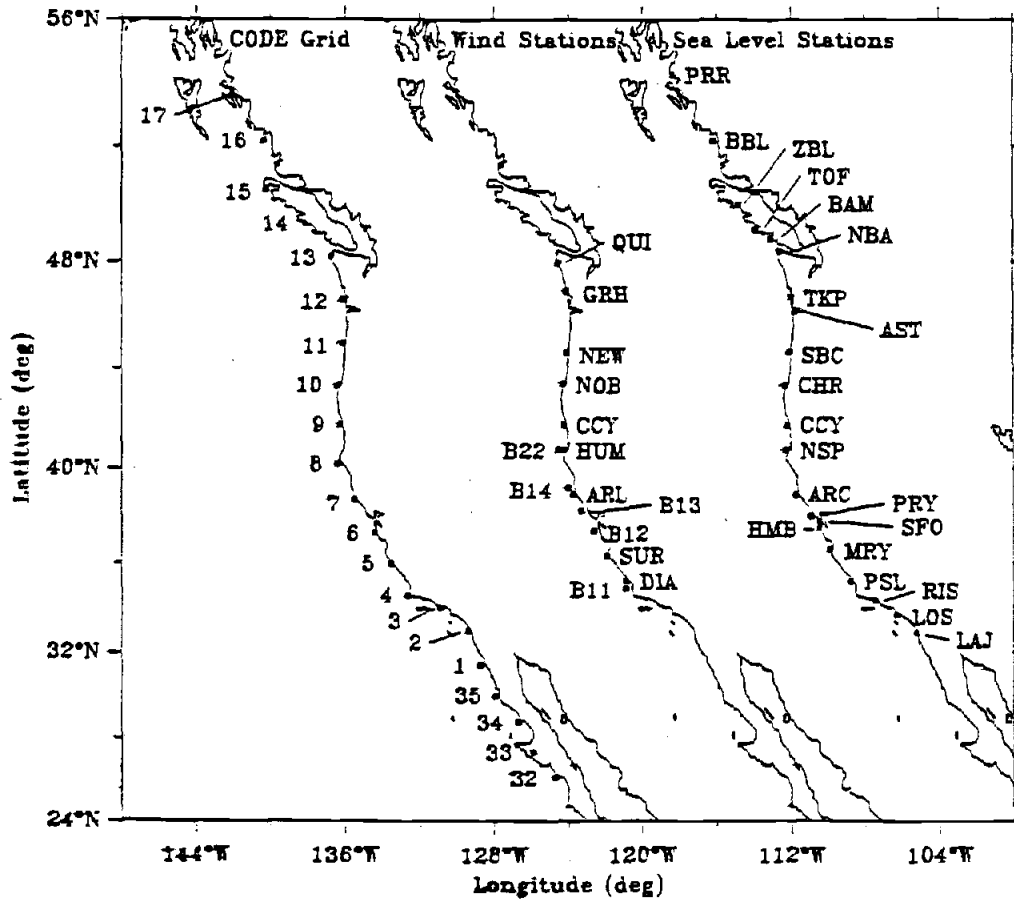


Fig. IV.1: The coastal points of the CODE analysis grid (left coastline), the wind measurement stations (middle coastline), and the coastal sea level stations (right coastline) used in this study. The longitude axis is correct for the middle coastline. Information on the stations and grid points is summarized in Tables IV.1 through IV.3.

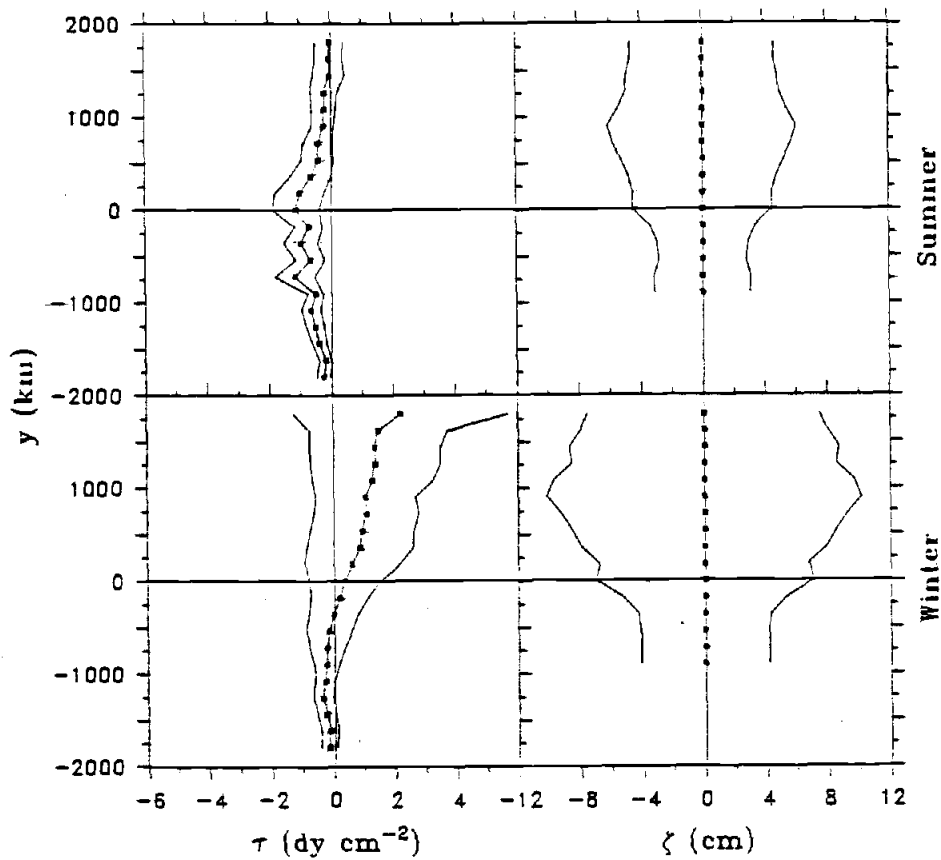


Fig. IV.2: The mean (solid line with squares) and rms amplitude envelopes of τ and ζ for summer and winter. The means and rms amplitudes for both seasons are the averages of the means and rms amplitudes of the individual summer and winter seasons. The τ statistics south of grid point 2 are also included, and ζ has been interpolated to the CODE grid points. The means of ζ have been removed.

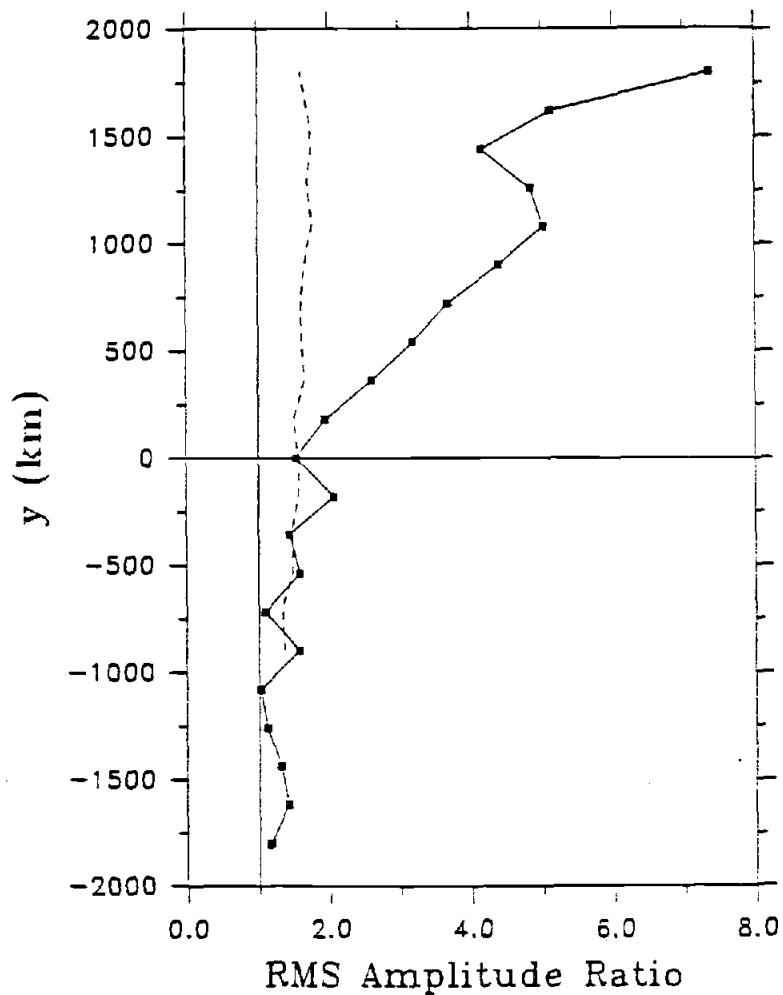


Fig. IV.3: The ratios of winter rms amplitude to summer rms amplitude for τ (solid line with squares) and ζ (dashed line) which has been interpolated to the CODE grid. A ratio of 1.0 is indicated by a vertical solid line.

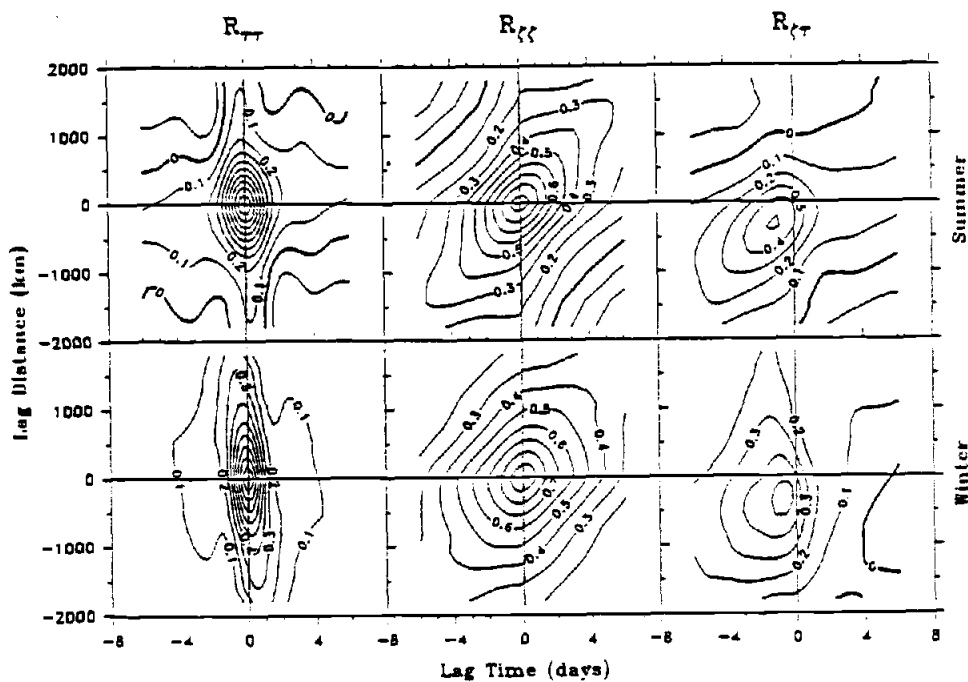


Fig. IV.4: The space-time correlation functions $R_{\tau\tau}(\eta_n, \tau_l)$, $R_{\zeta\zeta}(\eta_n, \tau_l)$, and $R_{\tau\zeta}(\eta_n, \tau_l)$, calculated from space-averaged covariances as described in Appendix D, ensemble-averaged over the four summers (grid points 4 through 17) and four winters (grid points 2 through 17).

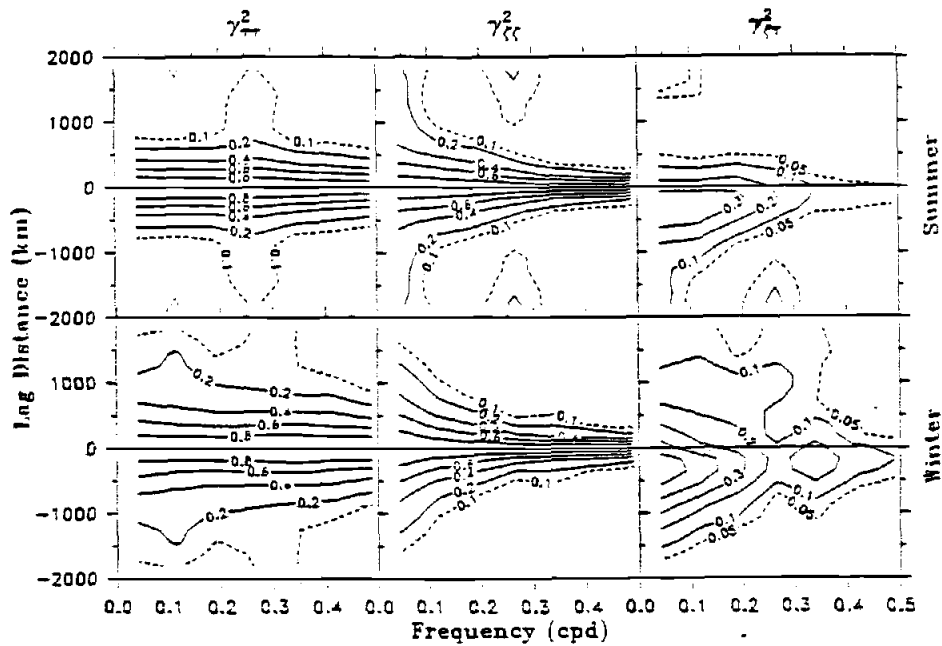


Fig. IV.5: The space-frequency coherence squared $\gamma_{\tau\tau}^2(\eta_n, \omega_l)$, $\gamma_{\zeta\zeta}^2(\eta_n, \omega_l)$, and $\gamma_{\tau\zeta}^2(\eta_n, \omega_l)$, calculated from space-averaged autospectra and cross-spectra and ensemble-averaged over the four summers (grid points 4 through 17) and four winters (grid points 2 through 17). A γ^2 of 0.041 is statistically significant to a 95% level of confidence (Appendix D).

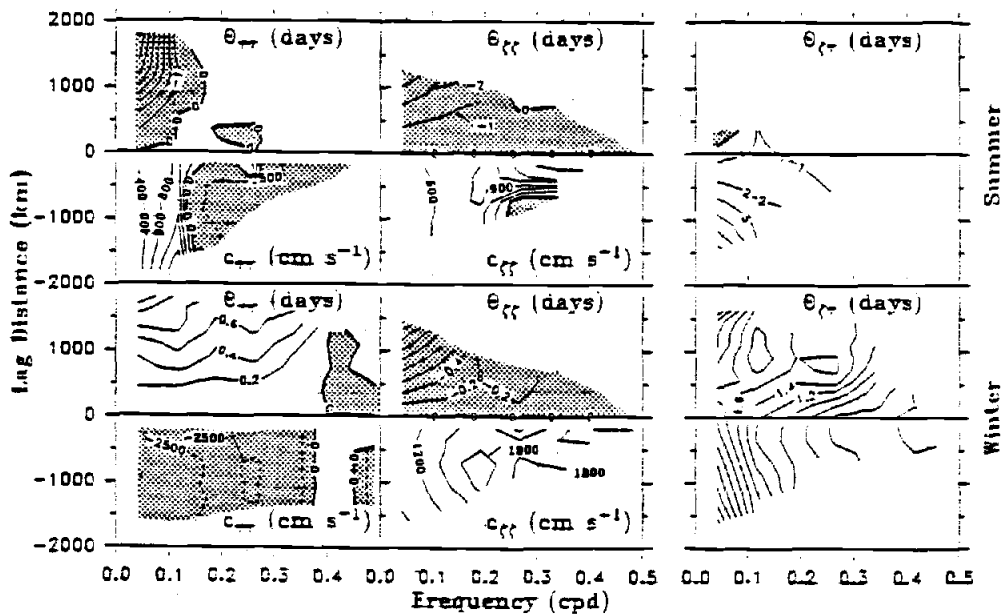


Fig. IV.6: The space-frequency phase lags $\theta_{\tau\tau}(\eta_n, \omega)$, $\theta_{\zeta\zeta}(\eta_n, \omega)$, and $\theta_{\tau\zeta}(\eta_n, \omega)$ contoured in days, and the phase speed functions $c_{\tau\tau}(\eta_n, \omega)$ and $c_{\zeta\zeta}(\eta_n, \omega)$ contoured in cm s^{-1} . Since they are symmetric, $\theta_{\tau\tau}$ is combined with $c_{\tau\tau}$, and $\theta_{\zeta\zeta}$ is combined with $c_{\zeta\zeta}$, in the same panels. Negative θ and c are shaded. The functions θ and c are not contoured where the corresponding γ^2 function (Fig. IV.5) is insignificant.

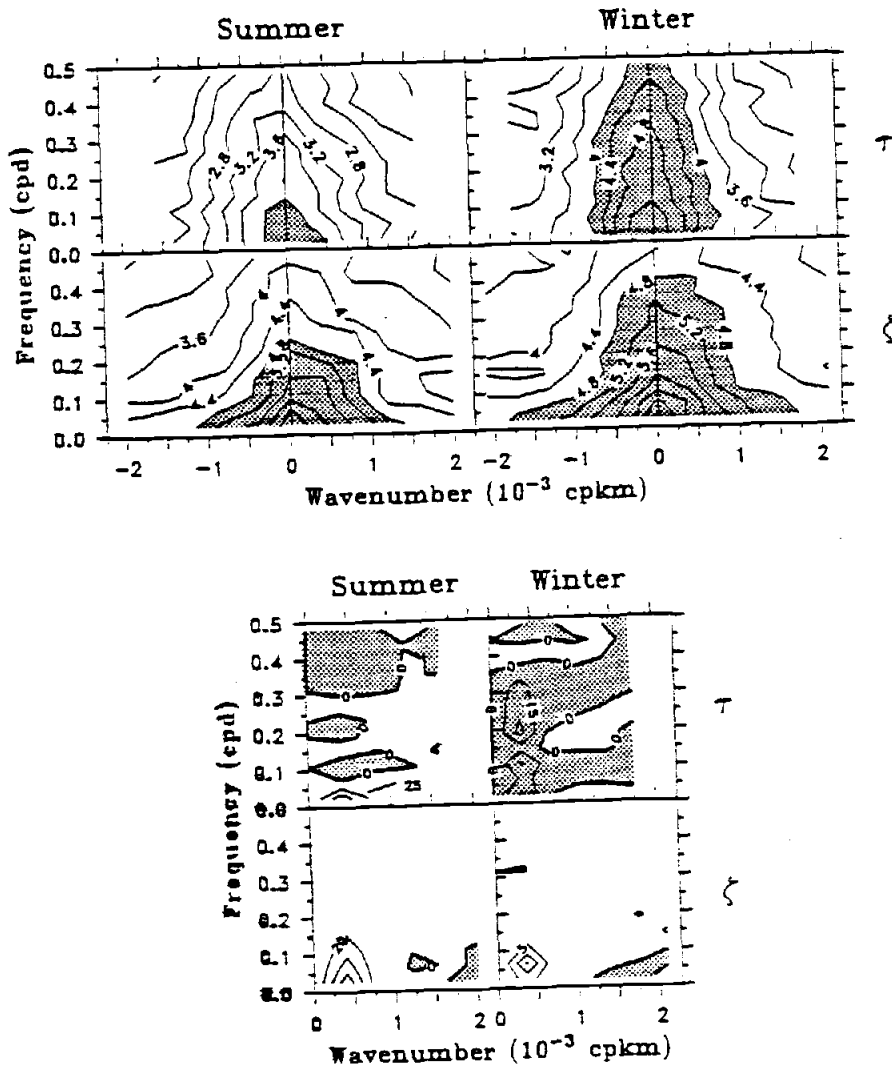


Fig. IV.7: Wavenumber-frequency autospectra (top) and propagating autospectra (bottom) of τ and ζ ensemble-averaged over the four summers (grid points 4 through 17) and four winters (grid points 2 through 17). The contours are of $\log_{10}[S(\pm l, \omega)]$ (top) and $P \cdot [S(+l, \omega) - S(-l, \omega)]$ (bottom), with S in $(\text{units})^2 \text{ cpd}^{-1} \text{ cpkm}^{-1}$, where $P = 10^{-2}$ for τ in summer, $P = 10^{-3}$ for τ in winter, $P = 10^{-4}$ for ζ in summer, and $P = 10^{-5}$ for ζ in winter. Spectrum estimates have been averaged over 5 frequency bands, excluding $\omega = 0$, and 4 seasons, so the number of degrees of freedom is 40 (Appendix E). The 95% confidence limits are between $\log_{10} S - 0.17$ and $\log_{10} S + 0.21$ at all l and ω . The autospectra (top) are shaded where $S_{\tau} > 10^4$ and $S_{\zeta} > 10^{4.8}$. Negative propagating autospectra (equatorward-propagating variance exceeds poleward-propagating variance) are shaded (bottom). The l_m and ω_n at which estimates are made are shown in Fig. IV.8.

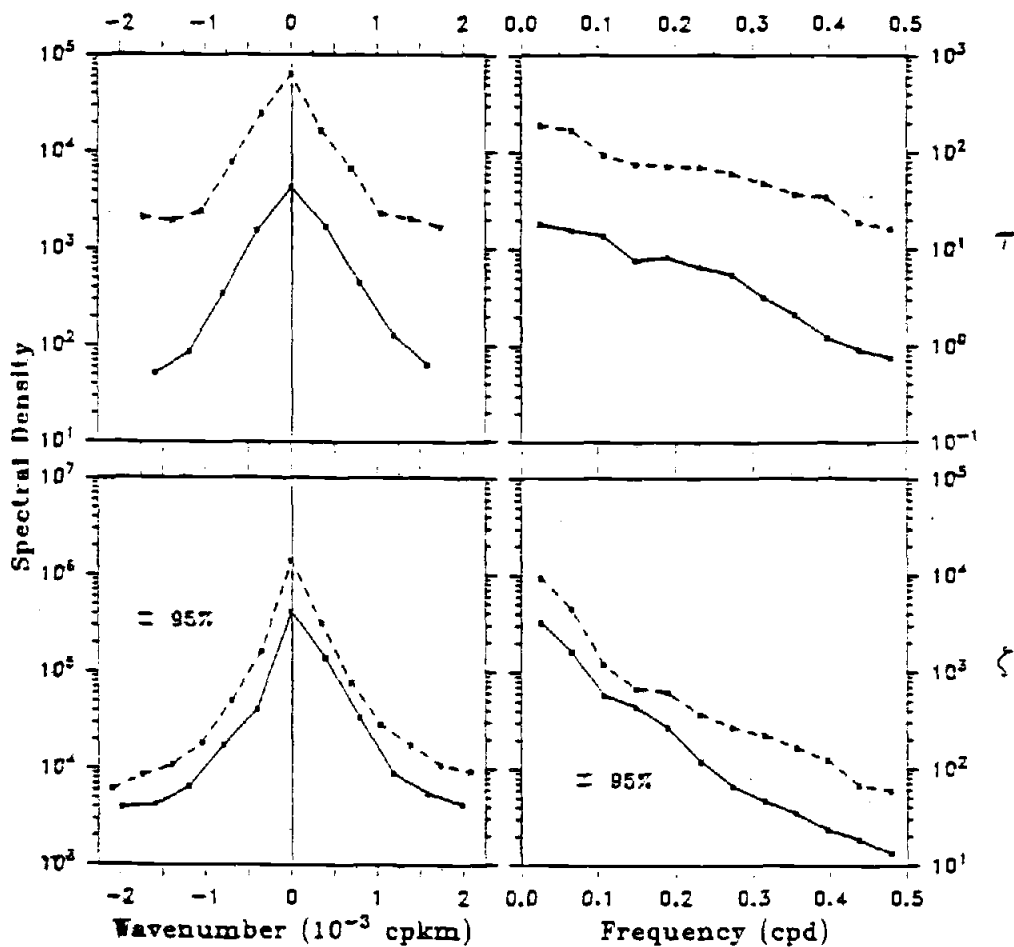


Fig. IV.8: Integrated wavenumber autospectra (left) and integrated frequency autospectra (right) for τ (top) and ζ (bottom), ensemble-averaged over the four summers (grid points 4 through 17; solid lines) and four winters (grid points 2 through 17; dashed lines). The wavenumber autospectra have 480 degrees of freedom in both seasons and the frequency autospectra have 600 (680) degrees of freedom for summer (winter). The 95% confidence band is shown.

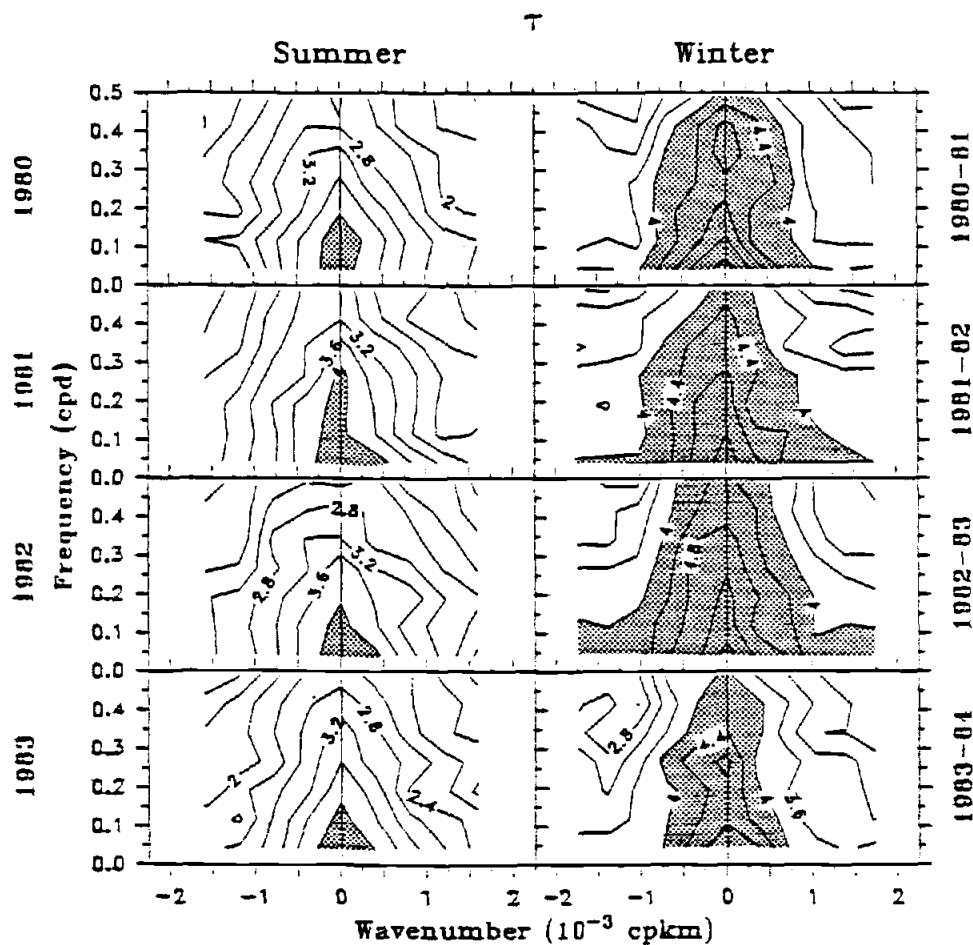


Fig. IV.9: Wavenumber-frequency autospectra of τ for the individual four summers (grid points 4 through 17) and four winters (grid points 2 through 17). The contours are of $\log_{10}[S(\pm l, \omega)]$, with S in $(\text{dy cm}^{-2})^2 \text{cpd}^{-1} \text{cpkm}^{-1}$. Spectrum estimates have been averaged over 9 frequency bands, excluding $\omega = 0$, so the number of degrees of freedom is 18. The 95% confidence limits are between $\log_{10} S - 0.24$ and $\log_{10} S + 0.34$ at all l and ω . The autospectra are shaded where $S(\pm l, \omega) > 10^4$. The $l_m(\omega_m)$ at which estimates are made are shown in Fig. IV.8 (Fig. IV.13).

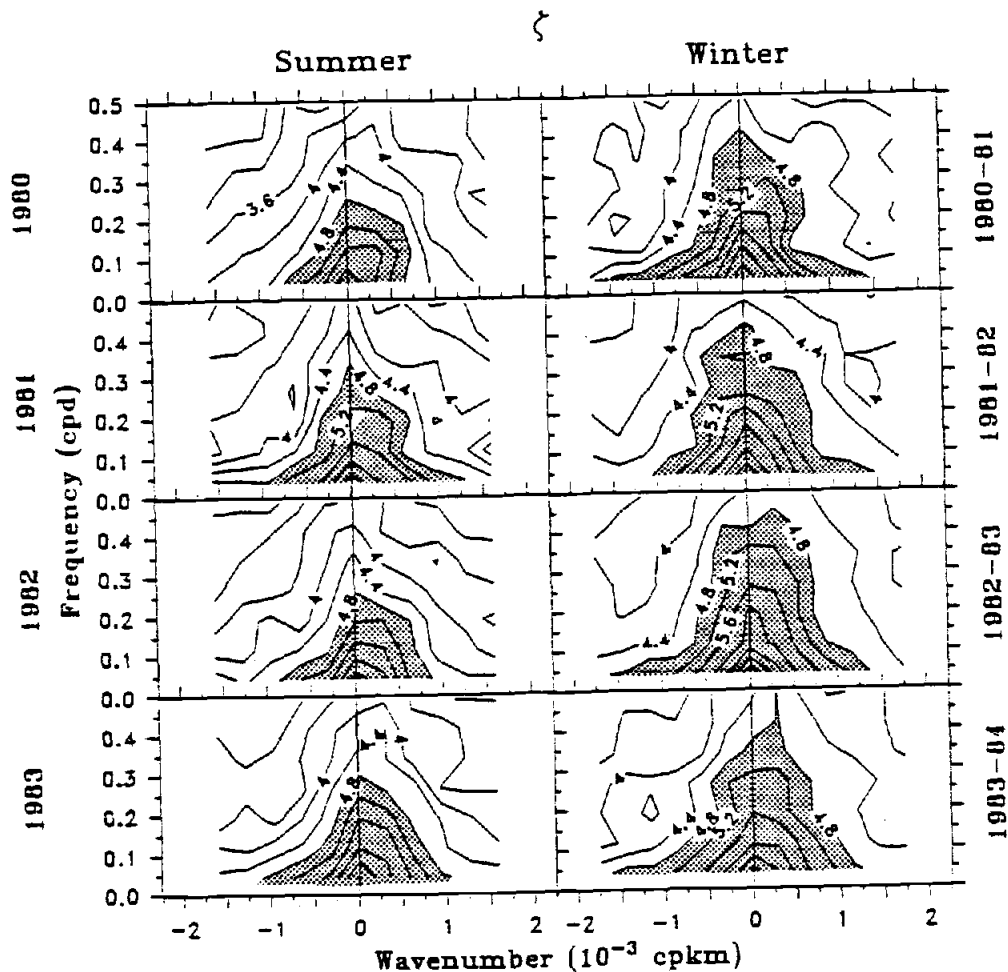


Fig. IV.10: Wavenumber-frequency autospectra of ζ for the individual four summers (grid points 4 through 17) and four winters (grid points 2 through 17). The contours are of $\log_{10}[S(\pm l, \omega)]$, with S in $\text{cm}^2 \text{cpd}^{-1} \text{cpkm}^{-1}$. The number of degrees of freedom is 18 (see Fig. IV.9). The 95% confidence limits are between $\log_{10} S - 0.24$ and $\log_{10} S + 0.34$ at all l and ω . The autospectra are shaded where $S(\pm l, \omega) > 10^{4.8}$. The $l_m(\omega_n)$ at which estimates are made are shown in Fig. IV.8 (Fig. IV.13).

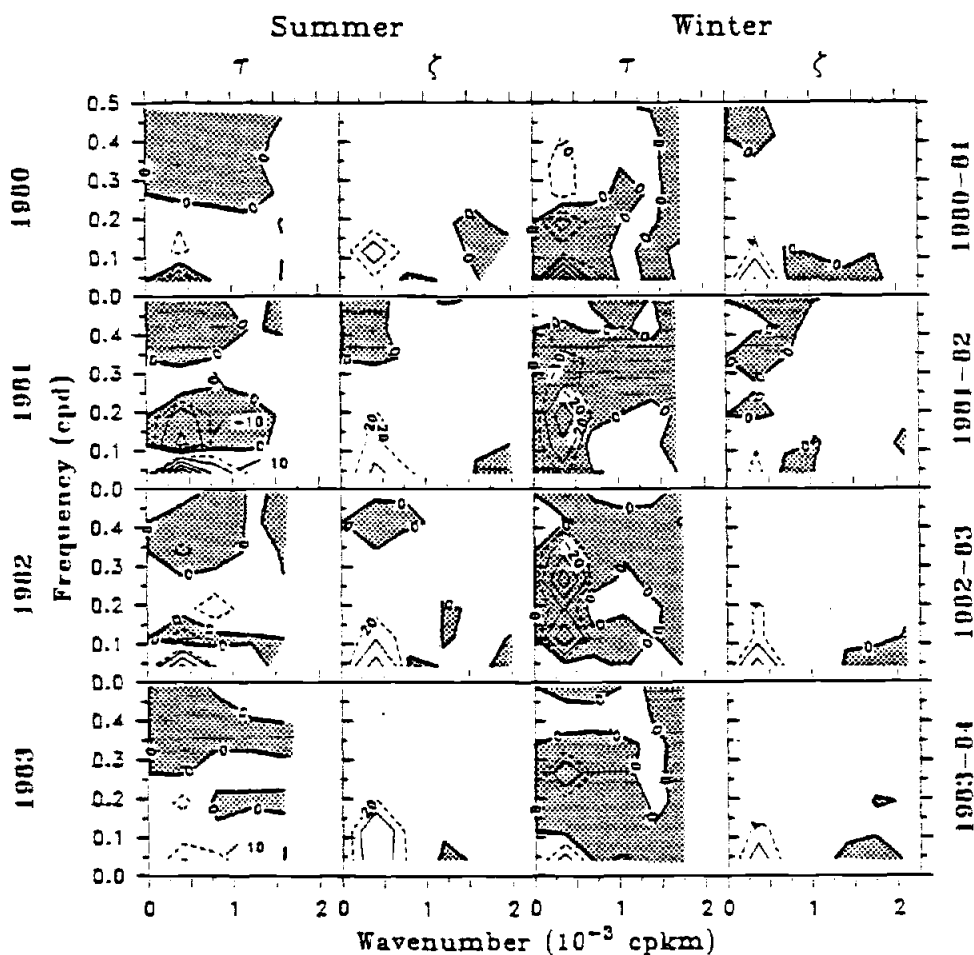


Fig. IV.11: Wavenumber-frequency propagating autospectra of τ and ζ for the individual four summers (grid points 4 through 17) and four winters (grid points 2 through 17). The contours are of $P \cdot [S(+l, \omega) - S(-l, \omega)]$ (bottom), with S in $(\text{units})^2 \text{ cpd}^{-1} \text{ cpkm}^{-1}$, where $P = 10^{-2}$ for τ in summer, $P = 10^{-3}$ for τ in winter, $P = 10^{-4}$ for ζ in summer, and $P = 10^{-5}$ for ζ in winter. The number of degrees of freedom is 18 (see Fig. IV.9). Negative propagating autospectra (equatorward-propagating variance exceeds poleward-propagating variance) are shaded. The $l_m(\omega_m)$ at which estimates are made are shown in Fig. IV.8 (Fig. IV.13).

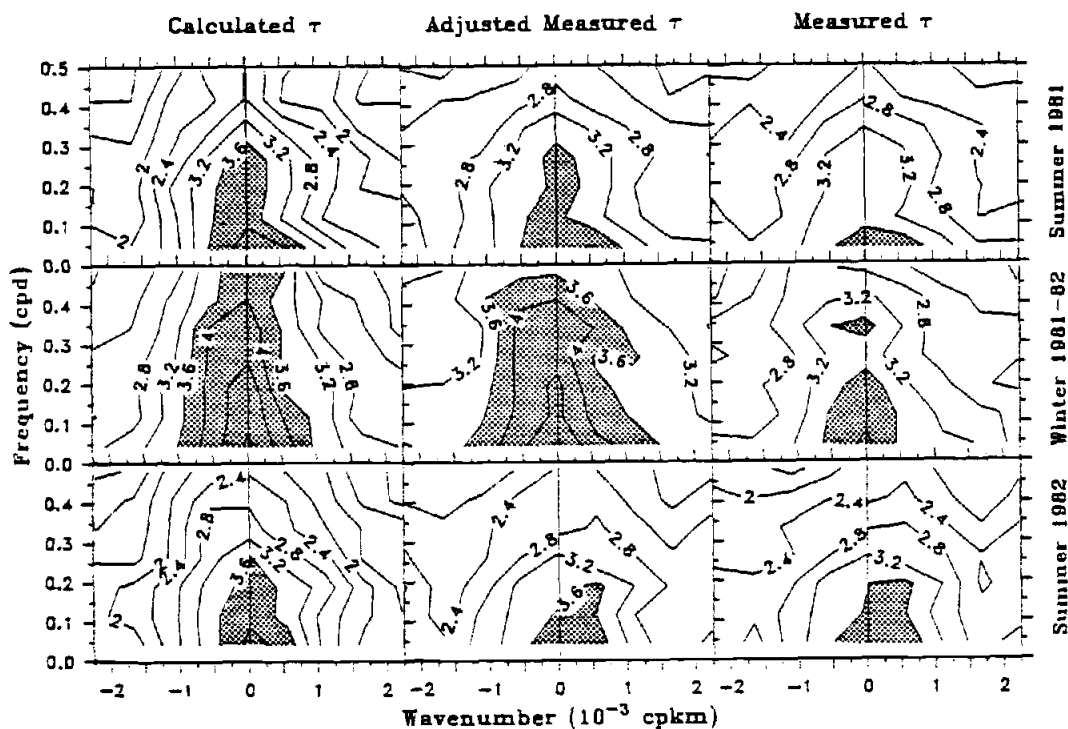


Fig. IV.12: Wavenumber-frequency autospectra of calculated, adjusted measured, and measured τ at grid points 4 through 13 for two summers and one winter. The contours are of $\log_{10}[S(\pm l, \omega)]$, with S in units of $m^2 s^{-2} \text{cpd}^{-1} \text{cpkm}^{-1}$. Spectrum estimates have been averaged over 9 frequency bands, excluding $\omega = 0$, so the number of degrees of freedom is 18. The 95% confidence limits are between $\log_{10} S - 0.24$ and $\log_{10} S + 0.34$ at all l and ω . The autospectra are shaded where $S(\pm l, \omega) > 10^{3.6}$. The l_m and ω_n at which estimates are made are shown in Fig. IV.13.

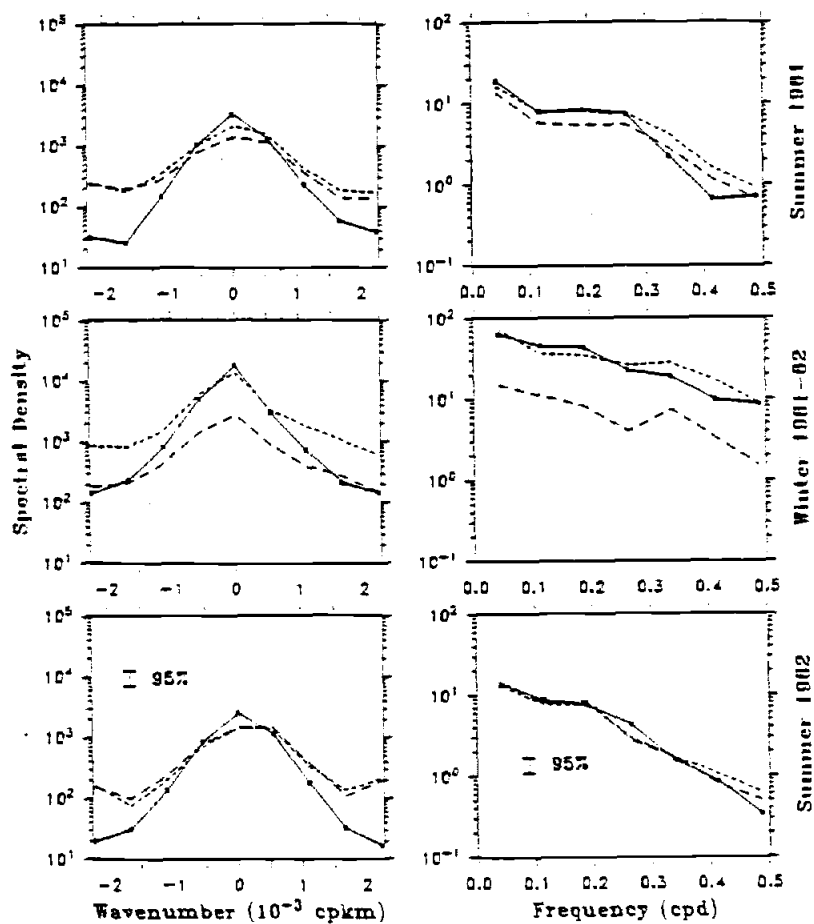


Fig. IV.13: Integrated wavenumber autospectra (left) and integrated frequency autospectra (right) for calculated winds (solid), adjusted measured winds (short dashes), and measured τ (long dashes) at grid points 4 through 13 for two summers and one winter. The integrated wavenumber (frequency) autospectra have 126 (198) degrees of freedom. The 95% confidence bands are shown.

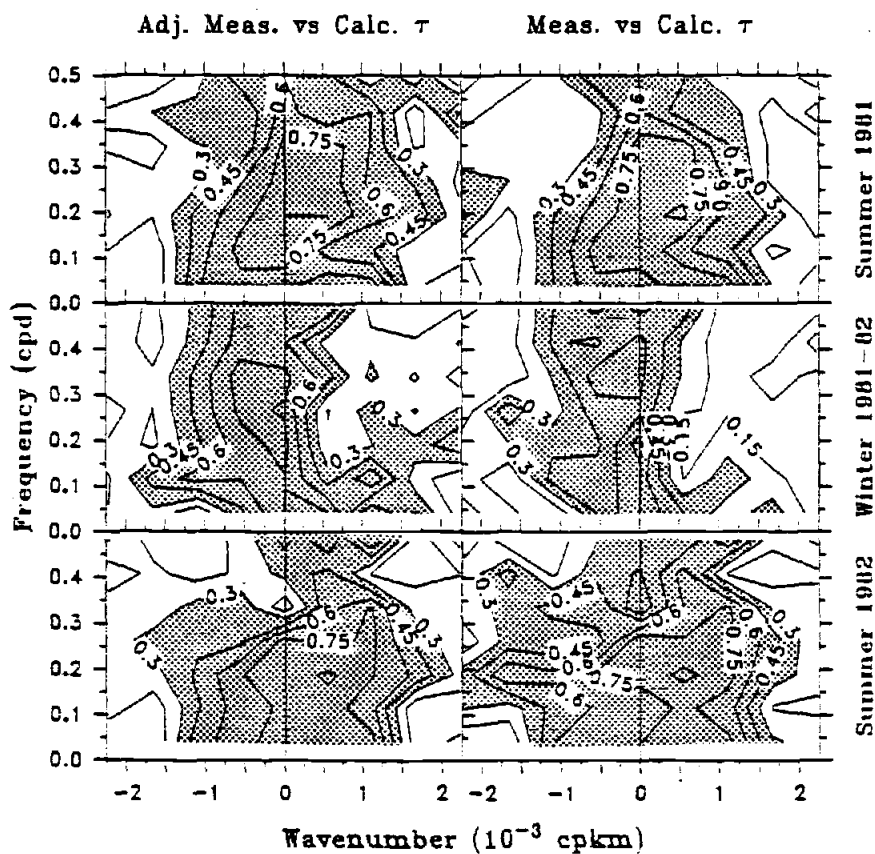


Fig. IV.14: Wavenumber-frequency coherence squared between adjusted measured and calculated τ , and between measured and calculated τ , at grid points 4 through 13 for two summers and one winter. The number of degrees of freedom is 18 (see Fig. IV.12). Squared coherences greater than 0.16 are significant to a 95% level of confidence. Squared coherences greater than 0.3 are shaded. The λ_m and ω_n at which estimates are made are shown in Fig. IV.13.

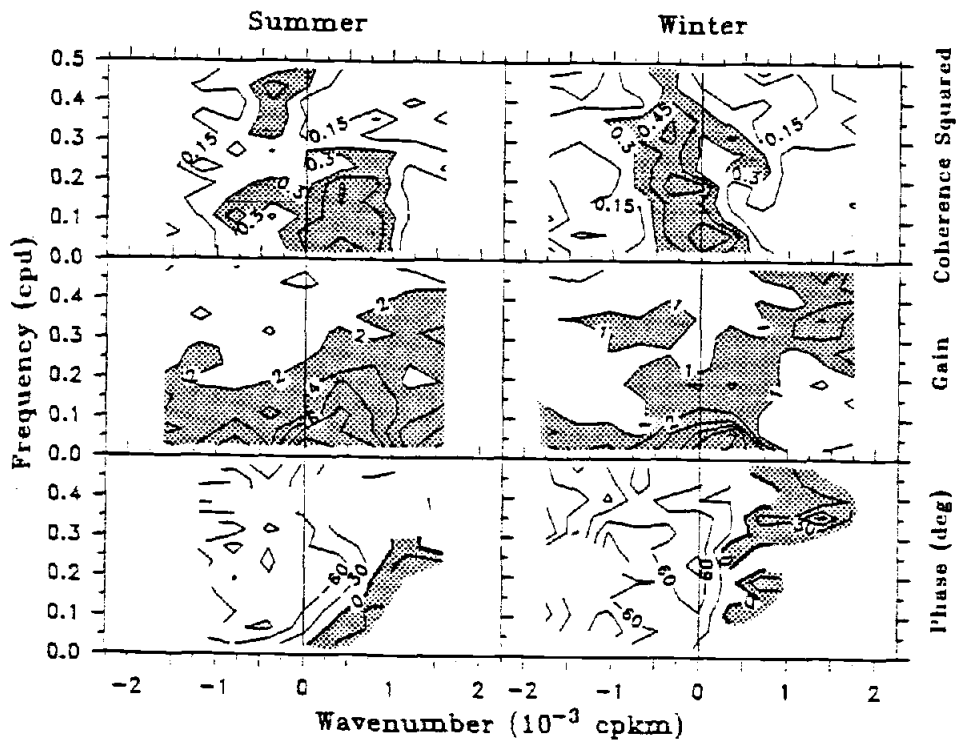


Fig. IV.15: Wavenumber-frequency coherence squared between τ and ζ , and the transfer function [gain in $\text{cm} (\text{dy cm}^{-2})^{-1}$ and phase in degrees] of the ζ response to τ , calculated from autospectra and cross-spectra ensemble-averaged over the four summers (grid points 4 through 17) and four winters (grid points 2 through 17). The number of degrees of freedom is 40 (see Fig. IV.7). Squared coherences greater than 0.074 are significant to a 95% level of confidence. Phase is contoured only in that part of (λ, ω) space where the coherence is statistically significant. Squared coherences greater than 0.3, gain larger than 2 (summer) and 1 (winter), and positive phase are shaded. The λ_m and ω_n at which estimates are made are shown in Fig. IV.8.

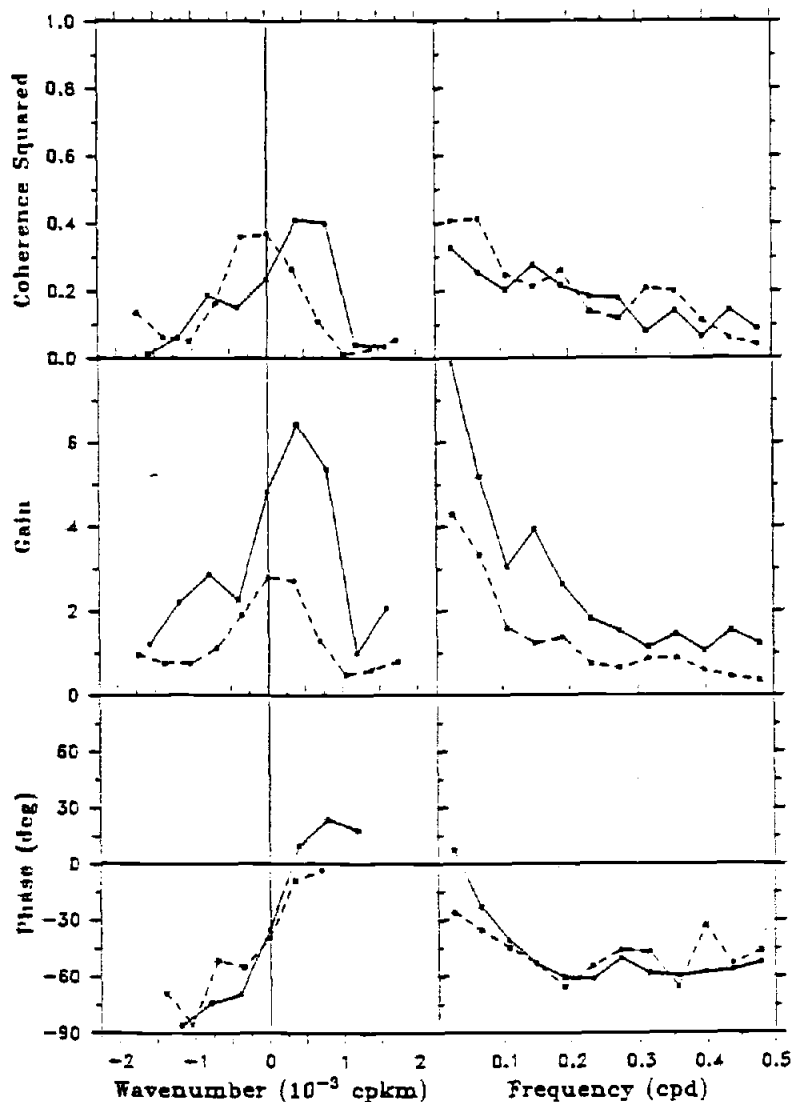


Fig. IV.16: Integrated wavenumber (left) and frequency (right) coherence squared between τ and ζ and the transfer function [gain in $\text{cm} (\text{dy cm}^{-2})^{-1}$ and phase in degrees] of the ζ response to τ , ensemble-averaged over four summers (grid points 4 through 17, solid lines) and four winters (grid points 2 through 17, dashed lines). The wavenumber autospectra have 480 degrees of freedom in both seasons and the frequency autospectra have 600 (680) degrees of freedom for summer (winter). Wavenumber (frequency) squared coherences > 0.006 (> 0.005) are statistically significant to a 95% level of confidence. Phase is graphed only where the coherence is significant.

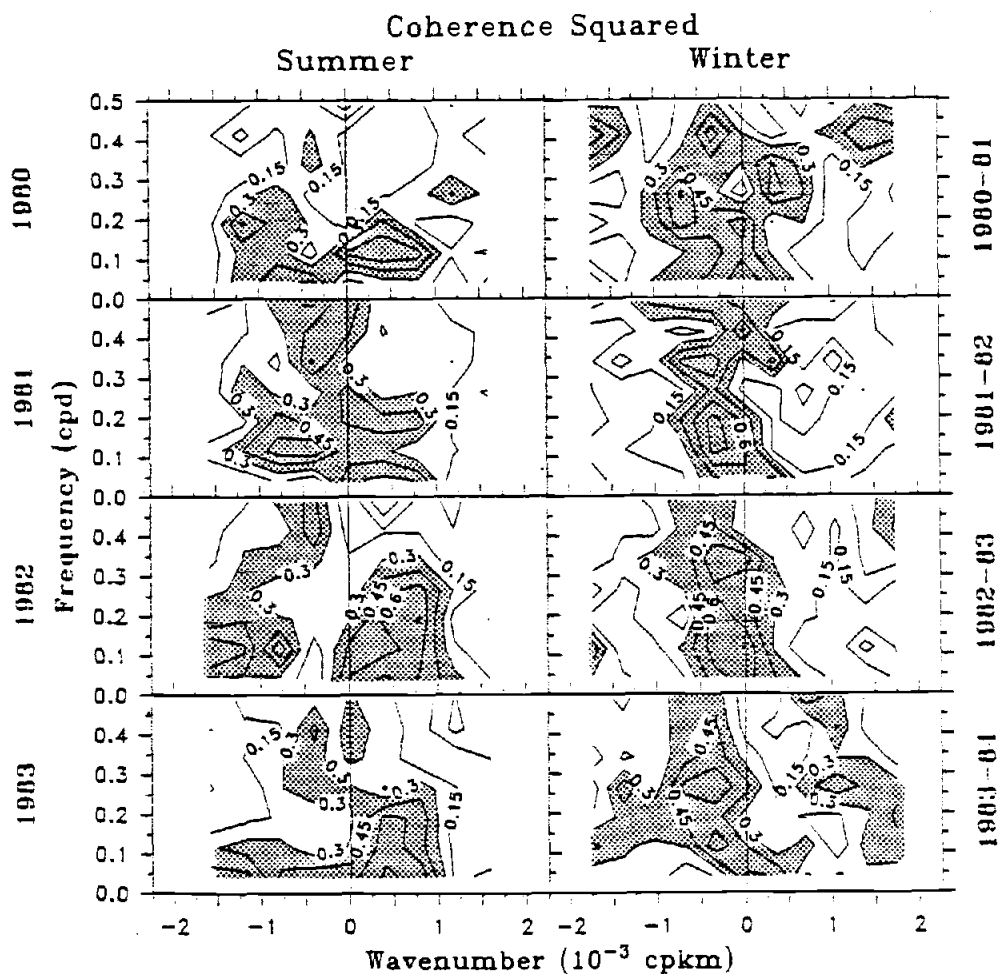


Fig. IV.17: Wavenumber-frequency coherence squared between τ and ζ for the individual four summers (grid points 4 through 17) and four winters (grid points 2 through 17). The number of degrees of freedom is 18 (see Fig. IV.9). Squared coherences greater than 0.16 are statistically significant to a 95% level of confidence, and those greater than 0.3 are shaded. The $k_m(\omega_m)$ at which estimates are made are shown in Fig. IV.8 (Fig. IV.13).

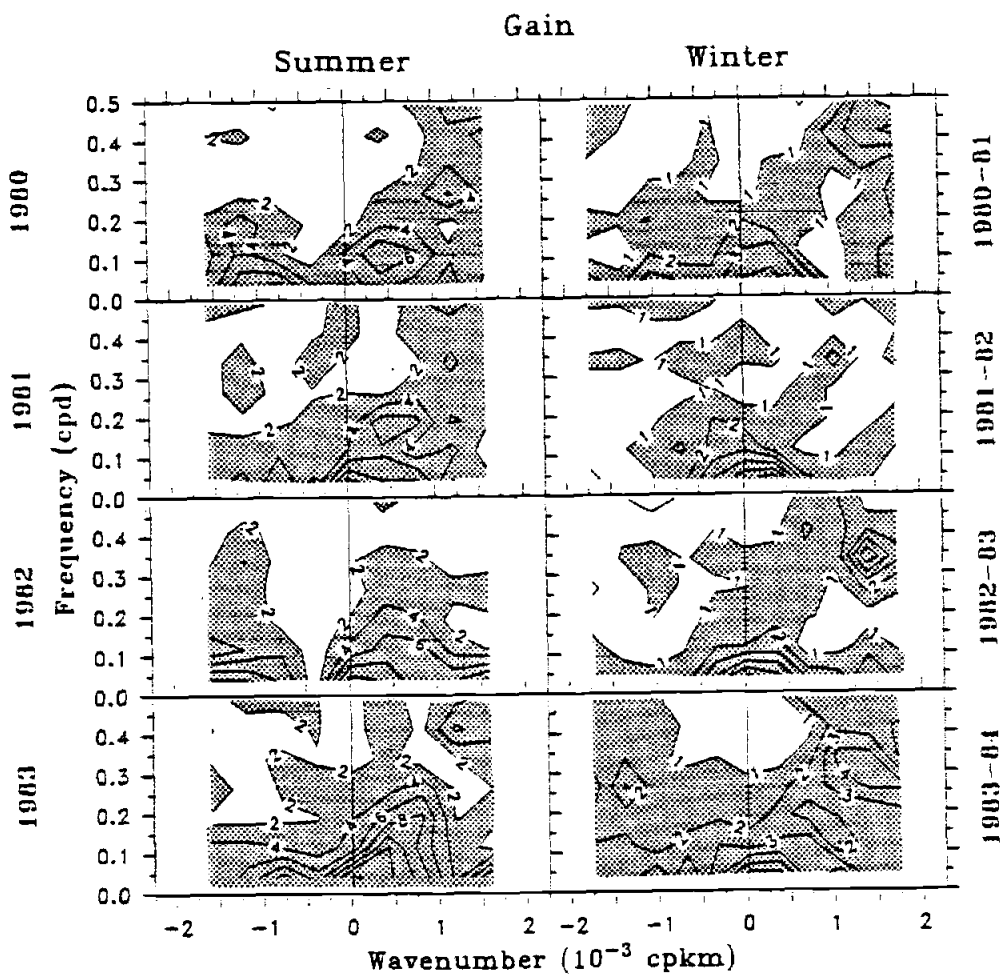


Fig. IV.18: Wavenumber-frequency gain in $\text{cm} (\text{dy cm}^{-2})^{-1}$ of the transfer function of the ζ response to τ for the individual four summers (grid points 4 through 17) and four winters (grid points 2 through 17). The number of degrees of freedom is 18 (see Fig. IV.9). Gain greater than 2 (summer) and 1 (winter) is shaded. The $\ell_m(\omega_m)$ at which estimates are made are shown in Fig. IV.8 (Fig. IV.13).

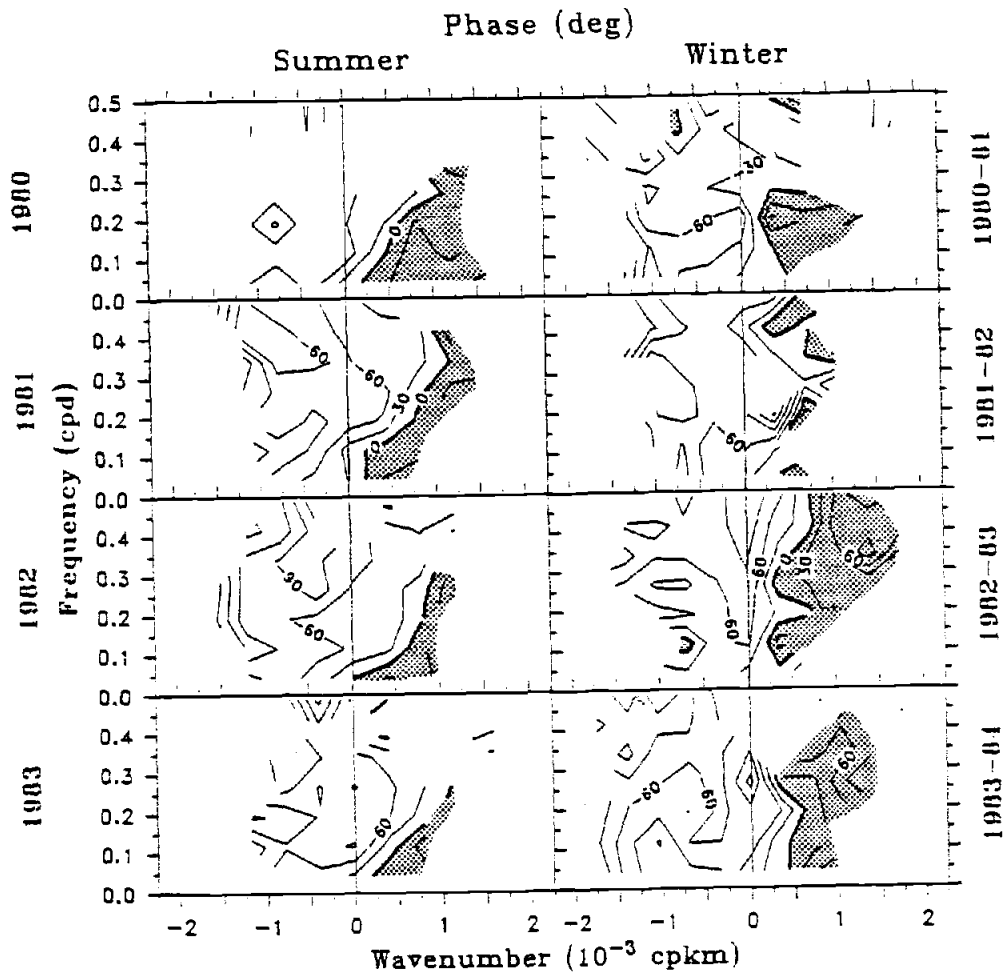


Fig. IV.19: Wavenumber-frequency phase in degrees of the transfer function of the ζ response to τ for the individual four summers (grid points 4 through 17) and four winters (grid points 2 through 17). The number of degrees of freedom is 18 (see Fig. IV.9). Phase is contoured only in that part of (ℓ, ω) space where the coherence is statistically significant. Phase greater than 0 (ζ leads τ) is shaded. The $\ell_m(\omega_n)$ at which estimates are made are shown in Fig. IV.8 (Fig. IV.13).

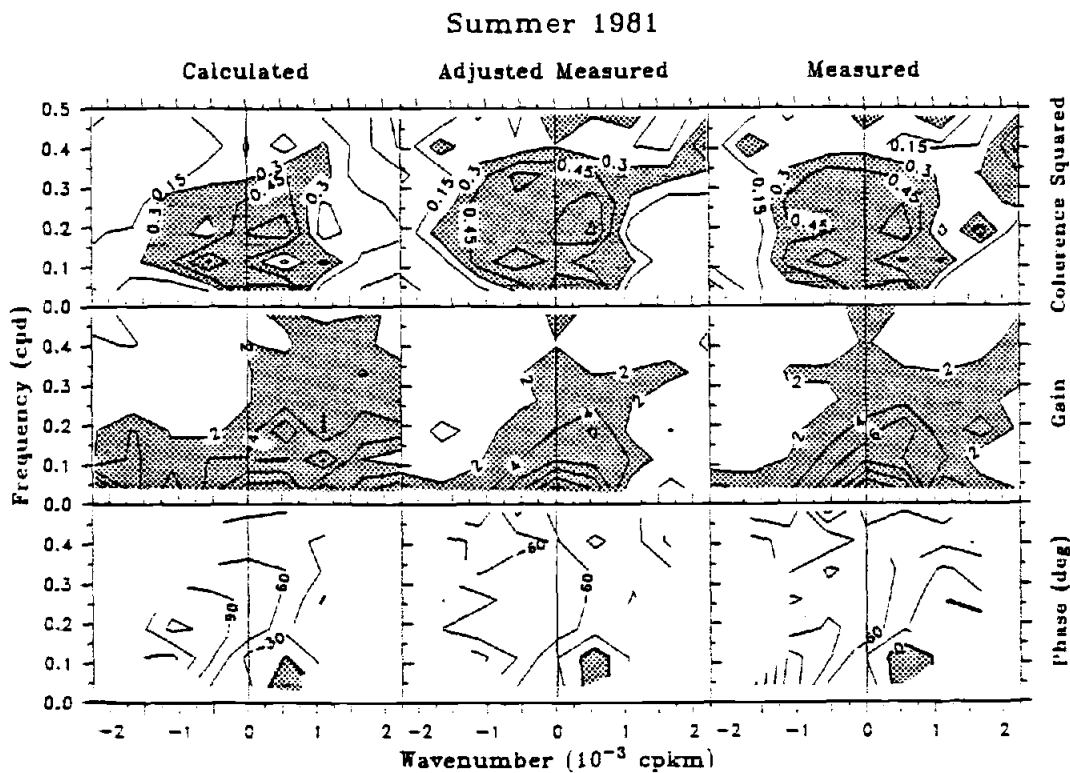


Fig. IV.20: Wavenumber-frequency coherence squared between τ and ζ , and transfer functions [gain in $\text{cm} (\text{dy cm}^{-2})^{-1}$ and phase in degrees] of the ζ response to τ , at grid points 4 through 13 for calculated, adjusted measured, and measured τ during summer 1981. The number of degrees of freedom is 18 (see Fig. IV.12). Squared coherences greater than 0.16 are significant to a 95% level of confidence. Phase is contoured only in that part of (ℓ, ω) space where the coherence is statistically significant. Squared coherences greater than 0.3, gain larger than 2, and positive phase (ζ leads τ) are shaded. The ℓ_m and ω_n at which estimates are made are shown in Fig. IV.13.

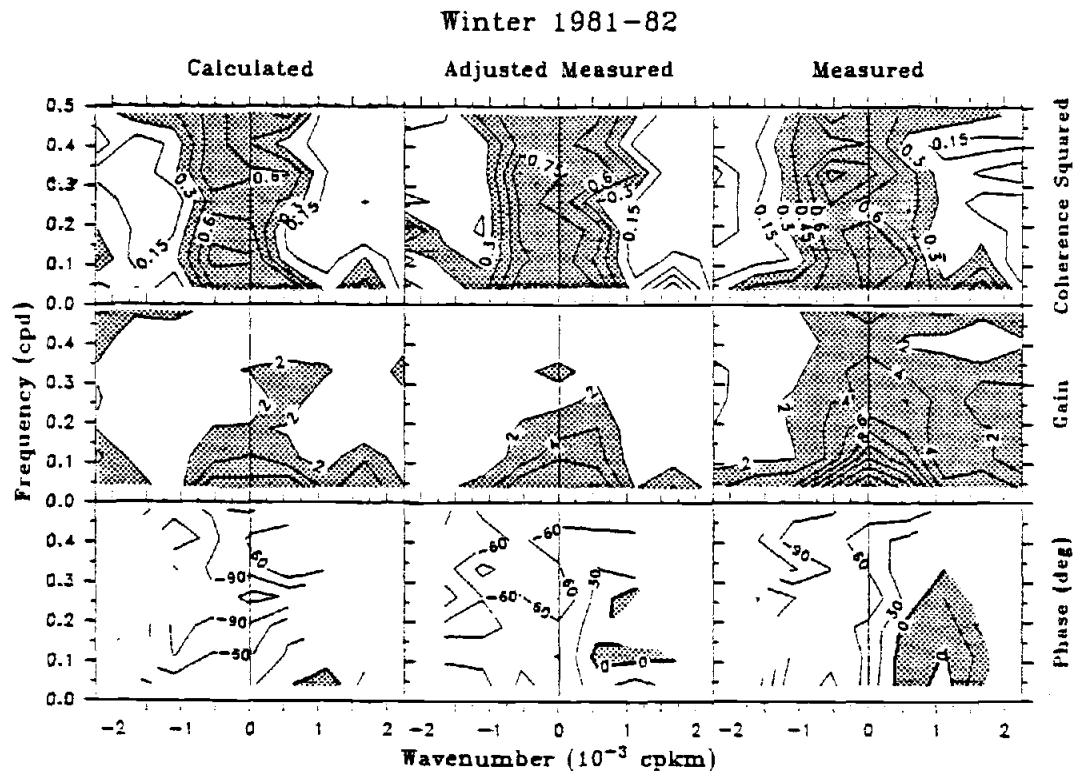


Fig. IV.21: Same as Fig. IV.20 for Winter 1981-82.

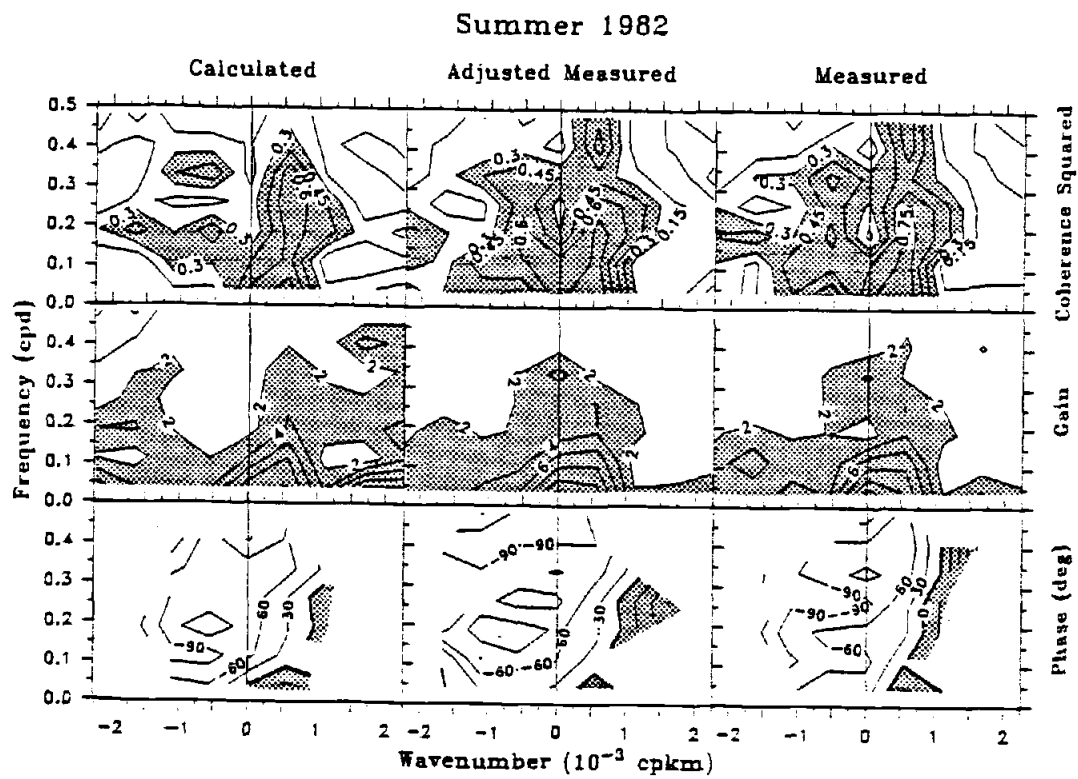


Fig. IV.22: Same as Fig. IV.20 for Summer 1982.

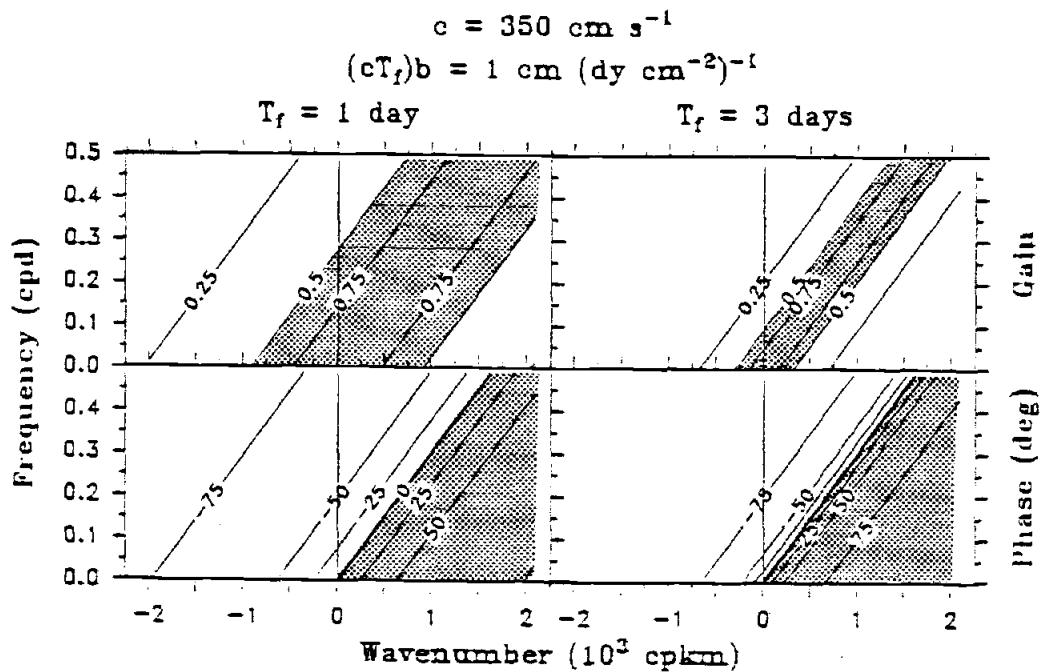


Fig. IV.23: Transfer functions (gain and phase) of the ζ response to τ in wavenumber-frequency space predicted by the forced, first-order wave equation with linear friction term (IV.1.1) for one coastally trapped wave mode. The transfer coefficient b is chosen so the maximum gain is $1 \text{ cm (dy cm}^2\text{)}^{-1}$. Values of gain > 0.5 and positive phase are shaded.

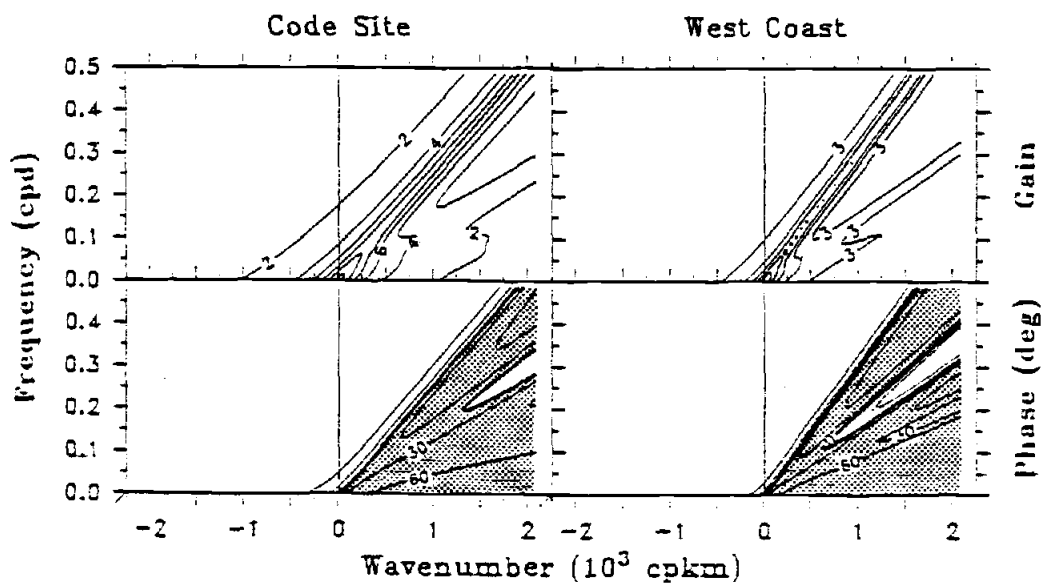


Fig. IV.24: Transfer functions (gain and phase) of the ζ response to τ in wavenumber-frequency space predicted by (IV.1.1) for several coastally trapped wave modes calculated using the parameters in Table IV.7. Positive phase is shaded.

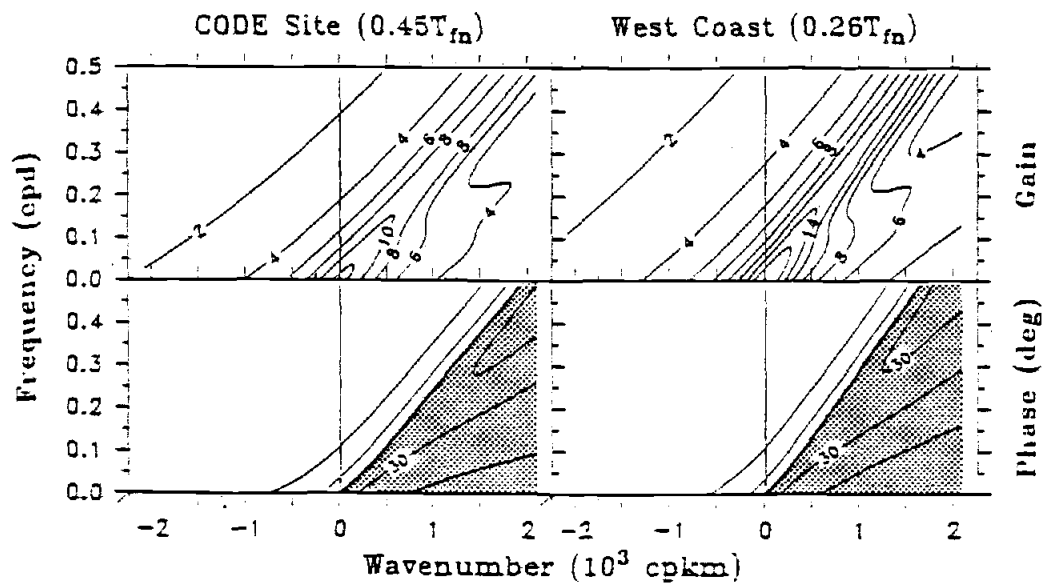


Fig. IV.25: Same as Fig. IV.24, except that the T_{fn} from Table IV.7 have been reduced in magnitude as shown. The maximum gain for each mode is the same as shown in Fig. IV.24. Positive phase is shaded.

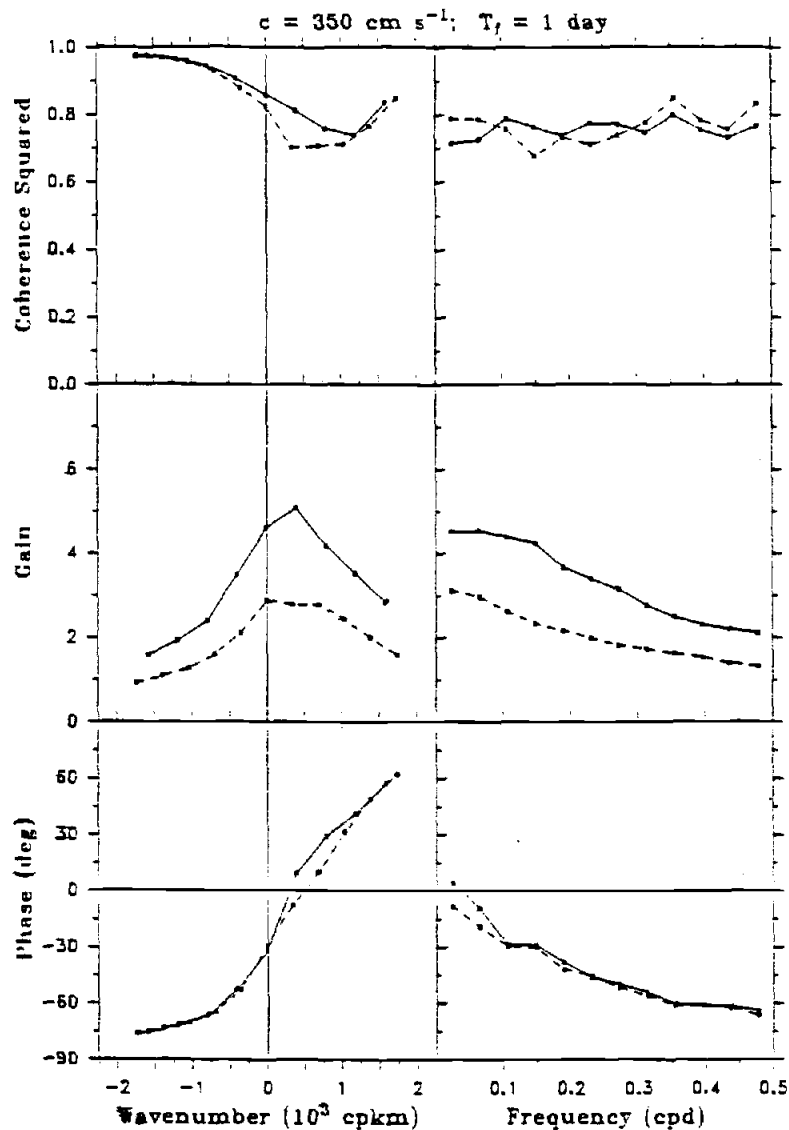


Fig. IV.26: Integrated wavenumber (left) and frequency (right) squared coherence between τ and ζ , and the transfer function [gain in $\text{cm} (\text{day cm}^{-2})^{-1}$ and phase in degrees] of the ζ response to τ , calculated from (IV.1.1) as described in Appendix F using the summer (solid lines) and winter (dashed lines) autospectra of τ presented in Fig. IV.7. For this calculation, we use $c = 350 \text{ cm s}^{-1}$ and $T_f = 1 \text{ day}$ to calculate the (k, ω) transfer function from (IV.1.1), and choose b so that the k gain functions in both seasons at $k = 0$ have the same magnitudes as those for the corresponding observed gain functions in Fig. IV.16.

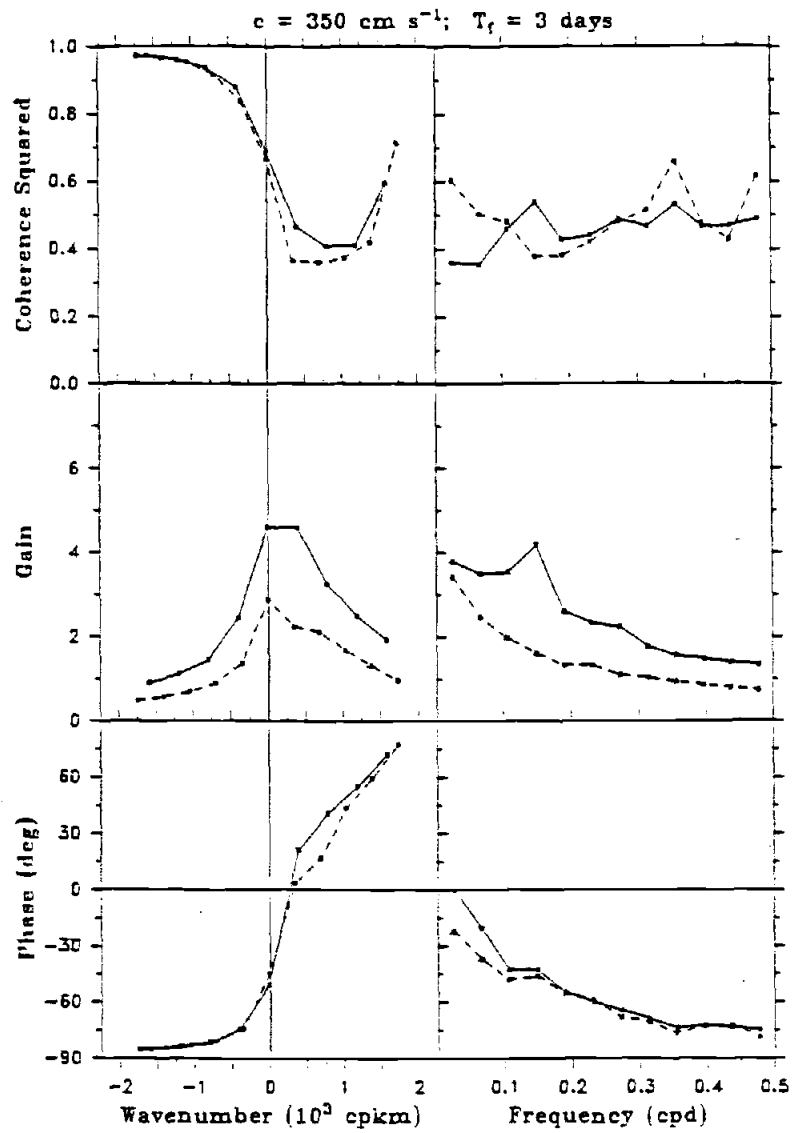


Fig. IV.27: Same as Fig. IV.26, except for using $T_f = 3$ days.

BIBLIOGRAPHY

- Allen, J. S., Models of wind-driven currents on the continental shelf, Ann. Rev. Fluid Mech., 12, 389-434, 1980.
- Allen, J. S., A simple model for stratified shelf flow fields with bottom friction, J. Phys. Oceanogr., 14, 1200-1214, 1984.
- Allen, J. S. and D. W. Denbo, Statistical characteristics of the large-scale response of coastal sea level to atmospheric forcing, J. Phys. Oceanogr., 14, 1079-1094, 1984.
- Allen, J. S., R. Beardsley, W. Brown, D. Cacchione, R. Davis, D. Drake, C. Friehe, W. Grant, S. Huyer, J. Irish, M. Janopaul, A. Williams and C. Winant, Coastal Ocean Dynamics Experiment (CODE), a preliminary program description, EOS, 64, 538-539, 1983.
- Bakun, A., Daily and weekly upwelling indices, west coast of North America, 1967-73, NOAA Tech. Rep. NMFS SSRF-693, National Marine Fisheries Service, Seattle, Washington, 114 pp., 1975.
- Bakun, A., Coastal upwelling indices, west coast of North America, 1946-71, NOAA Tech. Rep. NMFS SSRF-671, National Marine Fisheries Service, Seattle, Washington, 103 pp., 1975.
- Beardsley, R. C., C. E. Dorman, C. A. Friehe, and L. K. Rosenfeld, Local atmospheric forcing during CODE-1 and CODE-2, part 1: A description of the marine boundary layer and atmospheric conditions over a northern California upwelling region, Submitted to J. Geophys. Res., CODE issue, 1986. Service, Seattle, Washington, 114 pp., 1975.
- Bendat, J. S. and A. C. Piersol, Random Data: Analysis and Measurement Techniques, John Wiley, New York, 407 pp., 1971.
- Bosart, L. F., Analysis of a California Catalina eddy event, Mon. Wea. Rev., 111, 1619-1633, 1983.
- Brink, K. H., The effect of bottom friction on low frequency coastal trapped waves, J. Phys. Oceanogr., 12, 127-133, 1982.
- Brink, K. H., D. C. Chapman, and G. R. Halliwell, Jr., A stochastic model for wind-driven currents over the continental shelf, Submitted to J. Geophys. Res., 1986.

- Brink, K. H., D. W. Stuart, and J. C. Van Leer, Observations of the coastal upwelling region near $34^{\circ} 30'N$ off California: spring 1981, J. Phys. Oceanogr., 14, 378-391, 1984.
- Chapman, D. C., Application of wind-forced long coastal-trapped wave theory along the California coast, In preparation, 1986.
- Chapman, D. C. and K. H. Brink, Reconciling empirical and dynamical views of wind-forced, long, coastal-trapped waves, Submitted to J. Geophys. Res., 1986.
- Chelton, D. B. and R. E. Davis, Monthly mean sea level variability along the west coast of North America, J. Phys. Oceanogr., 12, 757-784, 1982.
- Clarke, A. J., Observational and numerical evidence for wind-forced coastal trapped long waves, J. Phys. Oceanogr., 7, 231-247, 1977.
- Davis, R. E., Predictability of sea surface temperature and sea level pressure anomalies over the North Pacific Ocean, J. Phys. Oceanogr., 6, 249-266, 1976.
- Denbo, D. W. and J. S. Allen, Rotary empirical orthogonal function analysis of currents near the Oregon coast, J. Phys. Oceanogr., 14, 35-46, 1984.
- Denbo, D. W. and J. S. Allen, Large-scale response to atmospheric forcing of shelf currents and coastal sea level off California and Oregon: May - July, 1981 and 1982, Accepted by J. Geophys. Res., 1986.
- Dorman, C. E., Evidence of Kelvin waves in California's marine layer and related eddy generation, Mon. Wea. Rev., 113, 827-839, 1985.
- Dorman, C. E., Possible role of gravity currents in Northern California's coastal summer wind reversals, Submitted to J. Geophys. Res., 1986.
- Dorr, A. and R. Grimshaw, Barotropic continental shelf waves on a β plane, J. Phys. Oceanogr., 16, 1345-1358, 1986.
- Enfield, D. B. and J. S. Allen, On the structure and dynamics of monthly mean sea level anomalies along the Pacific coast of North and South America, J. Phys. Oceanogr., 10, 557-578, 1980.

- Friehe, C. A. and C. D. Winant, Observations of wind and sea surface temperature structure off the northern California coast, in preprint volume, The First International Conference on Meteorology and Air-sea Interaction of the Coastal Zone, 10-14 May 1982, The Hague, Netherlands, 1982.
- Friehe, C. A. and C. D. Winant, Contoured aircraft survey data for CODE-1, 1981, SIO Ref. Ser., 84-20, University of California, Scripps Institution of Oceanography, La Jolla, California, 1984.
- Garrett, C. and B. Toulany, 1982, Sea level variability due to meteorological forcing in the northeast Gulf of St. Lawrence, J. Geophys. Res., 87, 1968-1978, 1982.
- Gill, A. E. and Schumann, E. H., The generation of long shelf waves by the wind, J. Phys. Oceanogr., 4, 83-90, 1974.
- Gill, A. E. and A. J. Clarke, Wind-induced upwelling, coastal currents, and sea level changes, Deep-Sea Res., 21, 325-345, 1974.
- Gonella, J., A rotary component method for analyzing meteorological and oceanographic time series, Deep-Sea Res., 19, 833-846, 1972.
- Grant, W. D. and O. S. Madsen, Combined wave and current interaction with a rough bottom, J. Geophys. Res., 84, 1797-1808, 1979.
- Halliwell, Jr., G. R. and J. S. Allen, CODE-1: Large-scale wind and sea level observations, In CODE-1: Moored array and large-scale data report, L. K. Rosenfeld, Ed., WHOI Tech. Rep. 82-23, 139-185, 1983.
- Halliwell, Jr., G. R. and J. S. Allen, Large-scale sea level response to atmospheric forcing along the west coast of North America, summer 1973, J. Phys. Oceanogr., 14, 864-886, 1984.
- Halliwell, Jr., G. R. and J. S. Allen, CODE-2: Large-scale wind and sea level observations, In CODE-2: Moored array and large-scale data report, R. Limeburner, Ed., WHOI Tech. Rep. 85-35, 181-234, 1985.
- Halliwell, Jr., G. R. and J. S. Allen, The large-scale coastal wind field along the west coast of North America, 1981-82, Accepted by J. Geophys. Res., 1986a.

- Halliwel, Jr., G. R. and J. S. Allen, Wavenumber-frequency domain properties of coastal sea level response to alongshore wind stress along the west coast of North America, 1980-84, Submitted to J. Geophys. Res., 1986b.
- Halliwel, Jr. G. R., H. L. Pittock, V. M. Halliwel, and J. S. Allen, The CODE large-scale meteorological, sea surface temperature, and coastal sea level data set, In preparation, 1986.
- Hamon, B. V., Generation of shelf waves on the east Australian coast by wind stress, Mem. Soc. Roy. Sci. Liège, 10, 359-367, 1976.
- Holl, M. M. and B. R. Mendenhall, Fields by information blending, sea level pressure version, Tech. Note. 72-2, Fleet Numerical Weather Central, Monterey, CA, 66pp., 1972. Numerical Weather Center, Meteorology International, Inc., Monterey, CA, 66 pp., 1971.
- Hsu, S. A., Models for estimating offshore winds from nearby onshore meteorological measurements, Bound.-Layer Meteor., 20, 341-351, 1981.
- Hsu, S. A., Correction of land-based wind data for offshore applications: a further evaluation, J. Phys. Oceanogr., 16, 390-394, 1986.
- Hsueh, Y. and R. D. Romea, A comparison of observed and geostrophically calculated wintertime surface winds over the East China Sea, J. Geophys. Res., 88, 9588-9594, 1983.
- Huyer, A., R. L. Smith, and E. J. C. Sobey, Seasonal differences in low frequency current fluctuations over the Oregon continental shelf, J. Geophys. Res., 83, 5077-5089, 1978.
- Kundu, P. K., Ekman veering observed near the ocean bottom, J. Phys. Oceanogr., 6, 238-242, 1976.
- Kundu, P. J., J. S. Allen, and R. L. Smith, Modal decomposition of the velocity field near the Oregon coast, J. Phys. Oceanogr., 5, 683-704, 1975.
- Large, W. G. and S. Pond, Open ocean flux measurements in moderate to strong winds, J. Phys. Oceanogr., 11, 324-336, 1981.
- Mass, C. F., M. D. Albright, and D. J. Brees, The onshore surge of marine air into a coastal region of complex terrain, Mon. Wea. Rev., In press, 1986.

- Mooers, C. N. K., A technique for the cross spectrum analysis of pairs of complex-valued time series, with emphasis on properties of polarized components and rotational invariants, Deep-Sea Res., 20, 1129-1141, 1973.
- Neiburger, M., D. S. Johnson, and C Chien, Studies of the structure of the atmosphere over the eastern Pacific Ocean in summer. I. The inversion over the eastern North Pacific Ocean, Univ. of California Publication Meteor., 1, 94 pp, 1961.
- Nelson, C. S., Wind stress and wind stress curl over the California Current, NOAA Tech. Rep. SSRF-714, National Marine Fisheries Service, 87 pp., 1977.
- Osmer, S. R. and A. Huyer, Variations in the alongshore correlation of sea level along the west coast of North America, J. Geophys. Res., 83, 1921-1927, 1978.
- Pittock, H. L., W. E. Gilbert, A. Huyer, and R. L. Smith, Observations of sea level, wind, and atmospheric pressure at Newport, Oregon, 1967-1980, Data Rep. 98, Oregon State University, Corvallis, OR, 158pp., 1982.
- Smith, R. L., A description of current, wind, and sea level variations during coastal upwelling off the Oregon coast, July-August, 1972, J. Geophys. Res., 79, 435-443, 1974.
- Strub, P. T., J. S. Allen, A. Huyer, and R. L. Smith, Large-scale structure of the spring transition, Accepted by J. Geophys. Res., 1986.
- Rienecker, M. M. and C. N. K. Mooers, Comparative spectrum analyses of surface wind stress fields based on NDBC winds and FNOC analyses, In Proc. 1983 Symposium on Buoy Technology, New Orleans, LA, Marine Technology Society, Washington, D. C., 281-285, 1983.
- Thomson, R. E., A comparison between computed and measured oceanic winds near the British Columbia coast, J. Geophys. Res., 88, 2675-2683, 1983.
- Thompson, R. O. R. Y., Coherence significance levels, J. Atmos. Sci., 36, 2020-2021, 1979.
- Wallace, J. M. and R. E. Dickinson, 1972, Empirical orthogonal representation of time series in the frequency domain, Part I: Theoretical consideration, J. Appl. Meteor., 11, 887-892, 1972.

Wang, D-P and C. N. K. Mooers, Long coastal trapped waves off the coast of the United States, summer 1973, J. Phys. Oceanogr., 7, 856-864, 1977.

Winant, C. D., R. C. Beardsley, and R. E. Davis, Moored current, wind, temperature, and current observations made during CODE-1 and CODE-2 over the northern California continental shelf and upper slope, Submitted to J. Geophys. Res., CODE issue, 1986.

APPENDICES

APPENDIX A

THE LARGE-SCALE RELATIONSHIP OF CUE-II CURRENTS TO
CALCULATED τ

In order to study the response of coastal circulation to large-scale wind forcing over an alongshore domain sufficiently large to resolve the structure of both the forcing and the response, coastal sea level must presently be used as the response variable. Earlier studies of currents along the Pacific Northwest coast, such as those of Smith (1974), Kundu, et al. (1975), and Huyer, et al. (1978) determined that alongshore currents v and empirical modes of v are very well correlated with ζ (typically ≥ 0.8 during summer), presumably due to the approximate geostrophic balance of v (e.g., Allen, 1980). These results strongly support the use of ζ as a proxy variable for v . Nevertheless, the question remains whether v has the same statistical relationship as ζ with the large-scale τ forcing field.

We therefore utilize the CUE-II current measurements off Oregon to test if v and ζ have the same statistical relationship with large-scale τ , first by inspecting the space and time lagged correlation patterns of both v and ζ with the calculated τ field, and second by comparing the quality of v and ζ predictions using (II.7.2). To represent the alongshore current, we use the

amplitude time series of the most significant u and v column EOF of 11 current meters in the CUE-II cross-shelf array as presented by Huyer, et al.. This EOF is computed for a one-month time interval (the maximum time of overlapping current measurements) from 1800 PST 25 July to 1200 PST 25 August 1973. It explains 72% of the total variance and has a maximum correlation coefficient with SBC ζ of 0.86.

Space and time lagged correlations of both SBC ζ and the CUE-II current EOF with calculated τ at all grid points along the coast for the one-month time interval (Fig. A.1) show a striking similarity in the patterns. The one-month correlation pattern for SBC ζ is also similar to the four-month pattern for SBC ζ (Fig. II.12, upper right panel), at least in the structure of the primary correlation peak. The maximum correlation between SBC ζ and τ is 0.75 for the one-month period and 0.79 for the four-month period. The maximum correlation between the current EOF and τ is 0.82, substantially greater than the maximum of 0.75 for SBC ζ , which indicates that the current EOF has primarily extracted the large-scale, wind-driven signal contained in the current data. This dominant current signal has an almost identical relationship to the large-scale τ field as ζ .

A prediction of ζ from (II.7.2) also represents a prediction of the time variability of the alongshore current v . Therefore, cross-correlation analysis between a prediction and both ζ and v can be used to determine if v is predicted as well as ζ . To

perform this comparison, we use measured and predicted ζ at CG11 (Section II.7), plus the amplitude of the CUE-II current EOF to represent the alongshore current. The zero-lag correlation is 0.78 between the prediction and ζ at CG11, and 0.87 between the prediction and the current mode. The higher correlation of the current mode is probably due again to the extraction of the large-scale, wind-driven signal by the EOF analysis. Most important, a prediction of the time variability of the first EOF of CUE-II currents is as good or better than the prediction of ζ , indicating that at this location the assumption of one wave mode is also useful for the prediction of v .

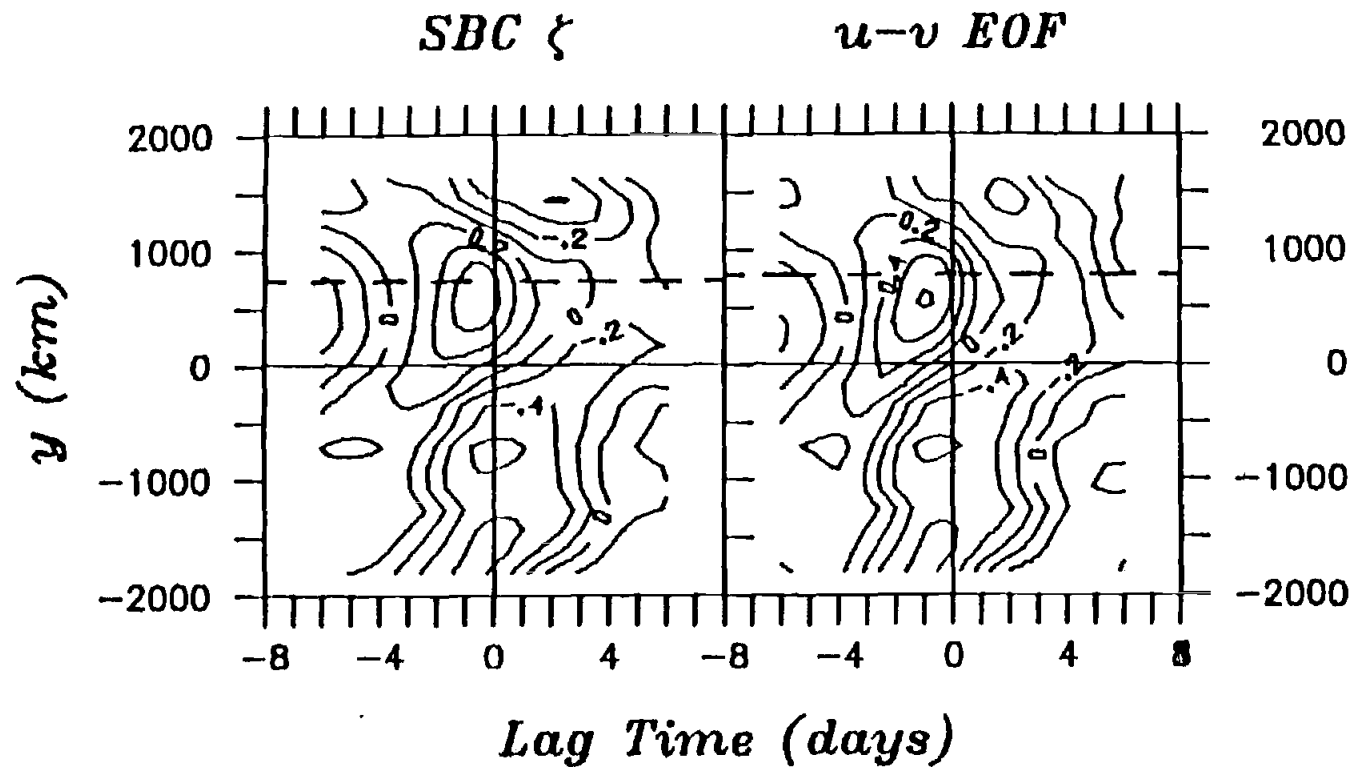


Fig. A.1: Contours of the space and time lagged correlations of (left) ζ at SBC with calculated τ at all grid points and (right) the most significant $u-v$ column time-domain EOFs of currents at the CUE-II cross-shelf array discussed by Huyer et al. (1978) with calculated τ at all grid points. The alongshore location of SBC and the current meter array are shown by the horizontal dashed lines; therefore, the correlations are spatially lagged with respect to these lines. The time interval for these calculations is 1800 PST 25 July 1973 to 1200 PST 25 August 1973. Since integral correlations time scales vary for different time series, a correlation coefficient of approximately 0.7 is statistically significant to a 95% level of confidence.

APPENDIX B

THE LARGE-SCALE RELATIONSHIP OF ζ TO MEASURED τ

Here we test if the statistical relationship between ζ and the large-scale τ field is adequately determined when calculated τ is used to represent this forcing. The correlation and coherence analyses in Figs. II.12 and II.15 are reproduced in Figs. B.1 and B.2 using measured τ at the 12 stations listed in Table II.1. The analyses with measured τ are restricted to a smaller alongshore domain than the analyses with calculated τ since no measured winds are available off British Columbia or Baja California.

The correlation patterns between ζ and measured τ (Fig. B.1) are very similar to the patterns between ζ and calculated τ (Fig. II.12), except that the Northern Baja California forcing region is not detected because of the lack of good measured winds in that region. The maximum correlation for BBL ζ is the same (0.48) with both measured and calculated τ . For the other five stations, the maximum correlation of ζ with calculated τ is slightly larger than with measured τ . The corresponding squared coherences with measured τ (Fig. B.2) also have similar patterns to the squared coherences with calculated τ (Fig. II.15). We therefore conclude that calculated τ is adequately representative of the large-scale forcing for the purposes of this study.

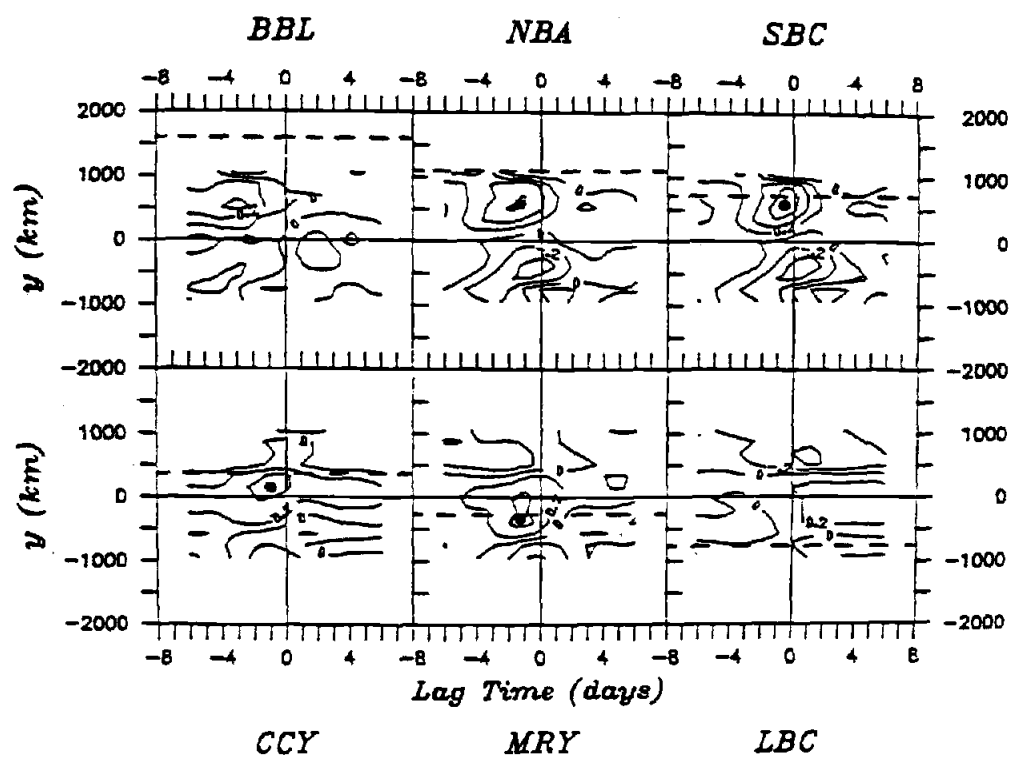


Fig. B.1: As in Fig. II.12 using measured τ at each of the 12 stations indicated in Table II.1.

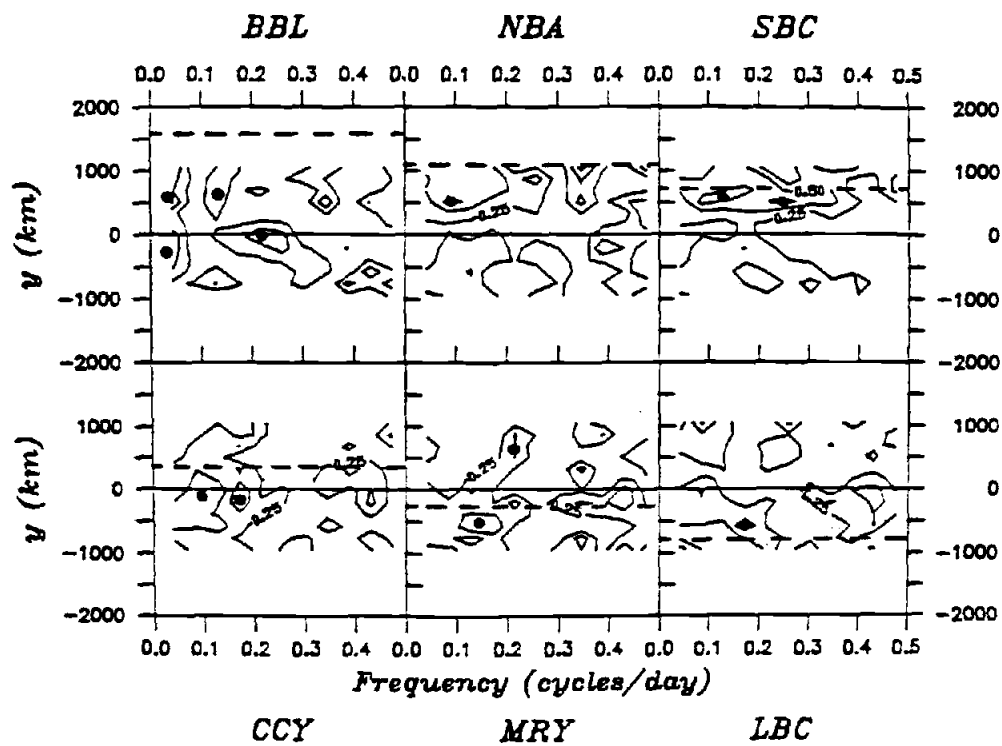


Fig. B.2: As in Fig. II.15 using measured τ at each of the 12 stations indicated in Table II.1.

APPENDIX C

CORRELATION SIGNIFICANCE LEVELS

We estimate the magnitude of the minimum correlation coefficient that is significantly different from zero using the number of degrees of freedom based on the independence time scale discussed by Davis (1976). These time scales vary with alongshore location and season, but for those stations with the largest time scales, the number of degrees of freedom is about 35, resulting in a "worst-case" estimate of 0.35 for the minimum significant correlation at the 95% level of confidence. We therefore use this value as the minimum significant correlation for all time series.

APPENDIX D.

SPACE-LAGGED CORRELATION, COHERENCE, AND PHASE FUNCTIONS

Given a set of N evenly-spaced time series sampled during M seasons, the space-lagged autorrelation function for the τ field ($R_{\tau\tau}$), and the space-lagged cross-correlation function between the τ and ζ fields ($R_{\zeta\tau}$), both seasonally-averaged over the M seasons, are calculated as follows:

$$R_{\tau\tau}(\eta_n, t_\ell) = \frac{\sum_{m=1}^M \sum_{i=1}^J \langle \tau(y_i, t) \tau(y_i + \eta_n, t + t_\ell) \rangle}{\left[\sum_{m=1}^M \sum_{i=1}^J \langle \tau^2(y_i, t) \rangle \right]^{1/2} \left[\sum_{m=1}^M \sum_{i=1}^J \langle \tau^2(y_i + \eta_n, t + t_\ell) \rangle \right]^{1/2}} \quad (D1)$$

and

$$R_{\zeta\tau}(\eta_n, t_\ell) = \frac{\sum_{m=1}^M \sum_{i=1}^J \langle \zeta(y_i, t) \tau(y_i + \eta_n, t + t_\ell) \rangle}{\left[\sum_{m=1}^M \sum_{i=1}^J \langle \zeta^2(y_i, t) \rangle \right]^{1/2} \left[\sum_{m=1}^M \sum_{i=1}^J \langle \tau^2(y_i + \eta_n, t + t_\ell) \rangle \right]^{1/2}}, \quad (D2)$$

where

$$\begin{aligned} I &= 1, \quad J = N - n && \text{for } n \geq 0, \\ I &= |n| + 1, \quad J = N && \text{for } n < 0, \quad |n| \leq |N - 1|. \end{aligned} \quad (D3)$$

The autocorrelation function for the ζ field, $R_{\zeta\zeta}(\eta_n, t_\ell)$, is

calculated in the same manner as $R_{\tau\tau}(\eta_n, t_\ell)$ using ζ in place of τ in (D1). The angle brackets signify time averaging, and the mean values of τ and ζ are assumed to be removed. Therefore, the terms in brackets in (D1) and (D2) are spatially- and seasonally-averaged covariance functions. The functions $R_{\tau\tau}$, $R_{\zeta\zeta}$, and $R_{\zeta\tau}$, are contoured in Fig. IV.4. We estimate integral correlation space scales of τ and ζ by integrating $R_{\tau\tau}(\eta_n, 0)$ and $R_{\zeta\zeta}(\eta_n, 0)$ over positive η_n out to the first zero crossing of R . We estimate correlation time scales of τ and ζ by integrating $R_{\tau\tau}(0, t_\ell)$ and $R_{\zeta\zeta}(0, t_\ell)$ over positive t_ℓ out to the first zero crossing of R . In estimating these scales, we integrated out to space or time lags larger than the maximum lags shown in Fig. IV.4, if necessary. In winter, the zero crossing of $R_{\zeta\zeta}(\eta_n, 0)$ is not reached by the maximum space lag that we integrated to ($\eta_n = 2520$ km), but $R_{\zeta\zeta}(\eta_n, 0)$ has decreased to less than 0.1 by this lag. If $R_{\zeta\zeta}(\eta_n, 0)$ is assumed to decrease linearly beyond this maximum lag, then the winter correlation space lag for ζ is underestimated by no more than 5%. All space and time scales are summarized in Table IV.4.

The seasonally-averaged space-lagged coherence squared function for the τ field, and the seasonally-averaged space-lagged coherence squared function between the ζ and τ fields, are given by

$$\gamma_{\tau\tau}^2(\eta_n, \omega) = \frac{\left| \sum_{m=1}^M \sum_{i=I}^J \{ \overline{\tau}^*(y_i, \omega) \overline{\tau}(y_i + \eta_n, \omega) \} \right|^2}{\left[\sum_{m=1}^M \sum_{i=I}^J \{ \overline{\tau}^*(y_i, \omega) \overline{\tau}(y_i, \omega) \} \right] \left[\sum_{m=1}^M \sum_{i=I}^J \{ \overline{\tau}^*(y_i + \eta_n, \omega) \overline{\tau}(y_i + \eta_n, \omega) \} \right]} \quad (D4)$$

and

$$\gamma_{\zeta\tau}^2(\eta_n, \omega) = \frac{\left| \sum_{m=1}^M \sum_{i=I}^J \{ \overline{\tau}^*(y_i, \omega) \overline{\zeta}(y_i + \eta_n, \omega) \} \right|^2}{\left[\sum_{m=1}^M \sum_{i=I}^J \{ \overline{\zeta}^*(y_i, \omega) \overline{\zeta}(y_i, \omega) \} \right] \left[\sum_{m=1}^M \sum_{i=I}^J \{ \overline{\tau}^*(y_i + \eta_n, \omega) \overline{\tau}(y_i + \eta_n, \omega) \} \right]}, \quad (D5)$$

where I and J are computed using (D3). The overbar denotes the Fourier transform, and an asterisk superscript denotes complex conjugate, and braces denote frequency band averaging. The coherence squared for the ζ field is calculated in the same manner as for the τ field using (D4). The phase functions for the τ field and between the τ and ζ fields are the arguments of the complex spatially- and seasonally-averaged cross-spectra in the numerators of (D4) and (D5). These are given by

$$\theta_{\tau\tau}(\eta_n, \omega) = \arg \left(\sum_{m=1}^M \sum_{i=I}^J \{ \overline{\tau}^*(y_i, \omega) \overline{\tau}(y_i + \eta_n, \omega) \} \right), \quad (D6)$$

and

$$\theta_{\zeta\tau}(\eta_n, \omega) = \arg \left(\sum_{m=1}^M \sum_{i=1}^J \{ \bar{\tau}^*(y_i, \omega) \bar{\zeta}(y_i + \eta_n, \omega) \} \right) . \quad (D7)$$

With θ in radians, the phase speed function for τ is given by

$$c_{\tau\tau}(\eta_n, \omega) = \omega \eta_n / \theta_{\tau\tau}(\eta_n, \omega) \quad (D8)$$

We band average over nine adjacent frequency bands, excluding $\omega = 0$, and ensemble average over 4 seasons, which would result in estimates with 72 degrees of freedom if no spatial averaging were performed. The spatial averaging will increase the number of degrees of freedom by an amount that is a function of η_n . The increase will be largest for $\eta_n = 0$, where the spectrum estimates are spatially-averaged over 2 to 3 spatial correlation scales (Section IV.3.2). At the largest space lags, the spatial averaging is only over one correlation space scale, so no additional degrees of freedom are gained. We therefore assume the estimates have 72 degrees of freedom, for which the minimum significant squared coherence is 0.041 (Thompson, 1979).

APPENDIX E.

CALCULATION OF THE WAVENUMBER-FREQUENCY SPECTRUM ESTIMATES

We use the Fourier transform method in two dimensions to estimate the wavenumber-frequency auto- and cross-spectra. Given the discrete data sets $\tau(y,t)$ and $\zeta(y,t)$ for a given season sampled at N points along the coast and L points in time with sampling rates Δy and Δt , raw (unaveraged) estimates of the autospectra of τ and ζ , and the cross-spectrum between τ and ζ , are given by

$$S_{\tau}(\ell_m, \omega_n) = B_{\ell} B_{\omega} \bar{\tau}^*(\ell_m, \omega_n) \bar{\tau}(\ell_m, \omega_n), \quad (E1)$$

$$S_{\zeta}(\ell_m, \omega_n) = B_{\ell} B_{\omega} \bar{\zeta}^*(\ell_m, \omega_n) \bar{\zeta}(\ell_m, \omega_n), \quad (E2)$$

and

$$S_{\tau\zeta}(\ell_m, \omega_n) = B_{\ell} B_{\omega} \bar{\tau}^*(\ell_m, \omega_n) \bar{\zeta}(\ell_m, \omega_n). \quad (E3)$$

where the overbar denotes two-dimensional Fourier transform, the asterisk superscript denotes complex conjugate, and where $B_{\ell} = (N\Delta y)^{-1}$ and $B_{\omega} = (L\Delta t)^{-1}$ are the wavenumber and frequency bandwidths for the raw estimates. The discrete two-dimensional Fourier transform of a function $f(y,t)$ is

$$\bar{f}(\ell_m, \omega_n) = \Delta y \Delta t \sum_{j=1}^N \sum_{k=1}^L f(y_j, t_k) e^{i(\ell_n y_j - \omega_n t_k)}, \quad (E4)$$

where the discrete wavenumbers and frequencies of the raw spectrum

estimates are given by

$$\hat{\lambda}_m = m(N\Delta y)^{-1} \quad \text{for} \quad -N/2 < m < N/2, \quad \text{and} \quad (\text{E5a})$$

$$\hat{\omega}_n = n(L\Delta t)^{-1} \quad \text{for} \quad 0 < n < L/2, \quad (\text{E5b})$$

Spectrum estimates at negative frequencies contain redundant information.

The raw spectrum estimates are χ^2 random variables with approximately two degrees of freedom. We must therefore average these estimates to increase their statistical stability. The averaged estimates are also χ^2 random variables, but with $2N_s$ degrees of freedom, where N_s is the total number of raw estimates that are averaged (Bendat and Piersol, 1971). The raw estimates may be band-averaged over wavenumber, band-averaged over frequency, and/or ensemble-averaged over two or more realizations (or in our case, seasons). The number of degrees of freedom will then be given by

$$n_{\text{dof}} = 2 n_\ell n_\omega n_r, \quad (\text{E6})$$

where n_ℓ is the number of wavenumber bands, n_ω is the number of frequency bands, and n_r is the number of realizations over which spectrum estimates are averaged. Due to limited resolution, we do not band average over wavenumber. To generate the average summer and winter spectrum estimates, we ensemble-average over 4 seasons.

We also corrected for leakage effects by prewhitening and postcoloring. Both the k and ω autospectra of ζ and τ are red, but leakage effects will be most severe in the space domain because the length of the alongshore domain has the same order of magnitude as the alongshore scales of τ and ζ disturbances. Because of this, we prewhitened and postcolored in the space domain only. Tests indicated that prewhitening τ and ζ in either the time or space domains had only a small effect on the spectral properties of these fields.

The coherence squared, gain, and phase are given by

$$\gamma_{\tau\zeta}^2(k_m, \omega_n) = \frac{|S_{\tau\zeta}(k_m, \omega_n)|^2}{S_{\tau}(k_m, \omega_n) S_{\zeta}(k_m, \omega_n)}, \quad (\text{E7})$$

$$G_{\tau\zeta}(k_m, \omega_n) = \frac{|S_{\tau\zeta}(k_m, \omega_n)|}{S_{\tau}(k_m, \omega_n)}, \quad (\text{E8})$$

and

$$\theta_{\tau\zeta} = \arg(S_{\tau\zeta}(k_m, \omega_n)), \quad (\text{E9})$$

where the braces denote the averaging performed.

APPENDIX F.

SEA LEVEL RESPONSE PREDICTED BY FORCED, FIRST-ORDER WAVE EQUATIONS

The forced, first-order wave equation with a linear friction term describing the alongshore-time dependence of the ζ response to τ , assuming one mode dominates this response, is

$$c^{-1}\zeta_t + \zeta_y + (cT_f)^{-1}\zeta = b\tau, \quad (\text{F1})$$

where c is the free wave phase speed, T_f is the friction time scale, and b is the transfer coefficient for the ζ response. Using the continuous two-dimensional Fourier transform

$$\bar{f}(\ell, \omega) = \int_{-\infty}^{\infty} \int_{-\infty}^{\infty} f(y, t) \exp[i(\ell y - \omega t)] dy dt, \quad (\text{F2})$$

and assuming constant coefficients, we find the transformed wave equation

$$[i\omega c^{-1} - i\ell + (cT_f)^{-1}]\bar{\zeta} = b\bar{\tau} \quad (\text{F3})$$

The predicted transfer function $H_{\tau\zeta}(\ell, \omega)$ is therefore given by

$$H_{\tau\zeta}(\ell, \omega) = \frac{cT_f b}{1 - iT_f(\ell c - \omega)} = G_{\tau\zeta} \exp(i\theta_{\tau\zeta}), \quad (\text{F4})$$

where the gain $G_{\tau\zeta}$ and phase $\theta_{\tau\zeta}$ are given by

$$G_{\tau\zeta}(\ell, \omega) = \frac{cT_f b}{[1 + T_f^2(\ell c - \omega)^2]^{1/2}}, \quad (\text{F5})$$

and

$$\theta_{\tau\zeta}(\ell, \omega) = \tan^{-1}[T_f(\ell c - \omega)]. \quad (\text{F6})$$

If additional modes contribute significantly to the response, the transfer function of the total response equals the sum of the transfer functions of the individual modes.

Given the autospectrum of τ , $S_\tau(\ell, \omega)$, the predicted cross-spectrum between τ and ζ , $S_{\tau\zeta}(\ell, \omega)$, and the predicted autospectrum of ζ , $S_\zeta(\ell, \omega)$, are given by

$$S_{\tau\zeta}(\ell, \omega) = H_{\tau\zeta}(\ell, \omega) S_\tau(\ell, \omega) \quad (\text{F7})$$

and

$$S_\zeta(\ell, \omega) = |H_{\tau\zeta}(\ell, \omega)|^2 S_\tau(\ell, \omega). \quad (\text{F8})$$

The squared coherence is

$$\gamma_{\tau\zeta}(\ell, \omega) = \frac{|S_{\tau\zeta}(\ell, \omega)|^2}{S_\tau(\ell, \omega) S_\zeta(\ell, \omega)} = 1 \quad (\text{F9})$$

for all ℓ and ω .

The squared coherence and transfer functions can be calculated as functions of ℓ or ω only, and we describe these calculations here for functions of ℓ . Given

$$S_{\tau}(\lambda) = \int_0^{\infty} S_{\tau}(\lambda, \omega) d\omega, \quad (\text{F10})$$

we can calculate $S_{\tau\zeta}(\lambda)$ and $S_{\zeta}(\lambda)$ by integrating (F7) and (F8) over ω , as was done for $S_{\tau}(\lambda)$ in (F10), then calculate the λ squared coherence and gain functions by

$$\gamma^2(\lambda) = \frac{|S_{\tau\zeta}(\lambda)|^2}{S_{\tau}(\lambda) S_{\zeta}(\lambda)} \quad (\text{F11})$$

and

$$H(\lambda) = \frac{S_{\tau\zeta}(\lambda)}{S_{\tau}(\lambda)}. \quad (\text{F12})$$

The squared coherence $\gamma^2(\lambda)$ is generally less than one. To calculate the one-dimensional squared coherence and transfer functions presented in Section IV.6.3, we numerically integrate (F7) and (F8) over ω , and numerically calculate the integral in (F10) using (F4) and observed values of $S_{\tau}(\lambda, \omega)$ (Fig. IV.7). We then calculate γ^2 and θ using (F11) and (F12). The numerical integrations are performed using the trapezoidal rule.